



HAL
open science

Plasticity and damage mechanisms in specific multiphased steels with bainitic matrix under various mechanical loading paths: influence of temperature

Pauline Martin

► **To cite this version:**

Pauline Martin. Plasticity and damage mechanisms in specific multiphased steels with bainitic matrix under various mechanical loading paths: influence of temperature. Solid mechanics [physics.class-ph]. Normandie Université, 2019. English. NNT: 2019NORMC227 . tel-02585794

HAL Id: tel-02585794

<https://theses.hal.science/tel-02585794v1>

Submitted on 15 May 2020

HAL is a multi-disciplinary open access archive for the deposit and dissemination of scientific research documents, whether they are published or not. The documents may come from teaching and research institutions in France or abroad, or from public or private research centers.

L'archive ouverte pluridisciplinaire **HAL**, est destinée au dépôt et à la diffusion de documents scientifiques de niveau recherche, publiés ou non, émanant des établissements d'enseignement et de recherche français ou étrangers, des laboratoires publics ou privés.



Normandie Université

THÈSE

Pour obtenir le diplôme de doctorat

**Spécialité MECANIQUE DES SOLIDES, GENIE MECANIQUE, PRODUCTIQUE,
TRANSPORT ET GENIE CIVIL**

Préparée au sein de l'Université de Caen Normandie

**Plasticity and damage mechanisms in specific multiphased steels
with bainitic matrix under various mechanical loading paths-
Influence of temperature**

**Présentée et soutenue par
Pauline MARTIN**

**Thèse soutenue publiquement le 14/11/2019
devant le jury composé de**

| | | |
|--------------------------------------|---|--------------------|
| M. ALAIN HAZOTTE | Professeur des universités, Université Metz Paul Verlaine | Rapporteur du jury |
| M. JEAN-BERNARD VOGT | Professeur des universités, Université Lille 1 Sciences Et Technolog | Rapporteur du jury |
| Mme ANNE-FRANÇOISE GOURGUES-LORENZON | Professeur des universités, ECOLE DES MINES DE PARIS | Président du jury |
| Mme ANNE-MARIE HABRAKEN | Directeur de recherche, Université de Liège - Belgique | Membre du jury |
| M. CLEMENT KELLER | Maître de conférences, INSA de Rouen Normandie | Membre du jury |
| Mme MAYERLING MARTINEZ | Maître de conférences, ENSICAEN | Membre du jury |
| M. ERIC HUG | Professeur des universités, Université Caen Normandie | Directeur de thèse |

**Thèse dirigée par ERIC HUG, Laboratoire de cristallographie et sciences des
matériaux (Caen)**



UNIVERSITÉ
CAEN
NORMANDIE



C'est de la folie de haïr toutes les roses parce qu'une épine vous a piqué,
d'abandonner tous les rêves parce que l'un d'entre eux ne s'est pas réalisé,
de renoncer à toutes les tentatives parce qu'on a échoué...

Le petit Prince, Antoine de Saint Exupéry

Acknowledgments

La thèse est présentée comme un travail de recherche individuel, heureusement dans cette solitude parfois ressentie de nombreuses personnes sont présentes au quotidien pour vous soutenir et vous accompagner. C'est pour cela que je souhaite mettre à l'honneur en ce début de thèse les personnes qui ont été présentes durant ces trois dernières années et grâce auxquels ce travail a pu être construit.

Au sein d'une entreprise comme dans le public tout projet commence par le budget, je souhaite donc dans un premier temps remercier Wilfried PRELLIER, directeur du laboratoire CRISMAT ainsi que Carey DILLIOTT, responsable actuel de l'équipe matériaux de Faurecia d'avoir permis le commencement ainsi que le bon déroulement de cette thèse.

Je souhaite ensuite remercier Mr VOGT et Mr HAZOTTE d'avoir accepté d'être mes rapporteurs et de m'avoir apporté des remarques constructives afin d'améliorer mon travail. Je remercie aussi Mme GOURGUES-LORENZON, Mme HABRAKEN de m'avoir fait l'honneur d'être membre de mon jury. Je souhaite particulièrement remercier les deux autres membres de mon jury qui ont été présent lors de ma soutenance mais aussi tout au long de la thèse et même avant... Merci à Clément KELLER de m'avoir donné goût à la métallurgie et à la recherche. Merci à Mayerling MARTINEZ qui m'a permis d'avoir de belles images au MET malgré nos overdoses de lattes bainitiques et qui m'a aussi redonné le moral avec sa joie de vivre tout au long de la thèse.

Je tiens à remercier Éric HUG, mon directeur de thèse, de m'avoir choisie pour ce sujet. Son encadrement et son esprit perfectionniste m'ont permis de me dépasser. Grâce à cela, cette thèse a été pour moi formatrice et j'espère m'ouvrira des portes dans le monde de la R&D en entreprise. Je remercie aussi Jérôme CHOTTIN mon responsable Faurecia en France qui m'a soutenu et a été passionné par le projet jusqu'à son départ. Je remercie aussi Klaus UNRUH mon responsable Faurecia en Allemagne qui malgré la distance à toujours pu s'organiser pour suivre le projet et me donner des conseils avisés sur ce projet.

Un grand merci à toute l'équipe métallurgie du CRISMAT avec Cendrine FOLTON avec qui j'ai pu avoir des discussions très enrichissantes pendant les pauses café, à Sophie EVE qui m'a permis d'en apprendre plus sur les chevaux et qui m'a permis d'effectuer les TP matériaux à l'ENSI. A Antoine GUEYDAN qui a toujours été disponible pour nous donner un coup de main et pour aller boire un verre et à Gaël MARNIER à qui je souhaite une jolie vie de famille avec la petiote qui vient de naître, à Brice POMMIER ça a été un plaisir de t'avoir dans notre bureau cette dernière année et à Florent MOISY qui

j'espère trouvera un jour sa place en tant que maître de conférence. Je remercie aussi mes co-thésards dont certains ont partagé mon bureau et même mes vacances. Je suis reconnaissante envers Lucia GARCIA-DE-LA-CRUZ avec qui j'ai partagé trois ans de thèse et à qui je dois de très bons souvenirs et l'apprentissage de quelques mots en espagnol. Merci aussi à Florent PICOT et Guillaume RIQUET j'espère que l'on repartagera ensemble un pichet de tinto de verano mais cette fois-ci en faisant attention à l'endroit où l'on gare la voiture. Merci à Julie DORENLOR pour sa gentillesse sans faille, bon, même si tu ne crois pas en ma reconversion professionnelle dans le tricot. Je souhaite enfin bon courage à Maxime LELIEVRE pour la suite. Je tiens aussi à remercier le personnel du CRISMAT et du CRNT pour tous leurs conseils techniques et aides informatiques et administratives. Gratien CHERRIER, Christelle HARNOIS, Christophe CIBERT, Jérôme LECOURT, Xavier LAROSE, Richard RETOUX, Stéphanie GASCOIN, Jean-Pierre BURNOUF, Éric LECOURT, Gratien CHERRIER, Marion JORE et Solange.

Durant ces trois dernières années j'ai reçu aussi beaucoup de soutien de la part de mes collègues Faurecia, je tiens donc à remercier Aurélie ACHILLE pour sa bienveillance, Margaux MARNIER pour son aide précieuse d'ancienne doctorante et pour son soutien technique sur la Gleeble, Bénédicte NICOLAS qui est devenue ma binôme de randonnée, Eymard HOUARA KOMBA pour avoir apporté du soleil à Flers, Olivier MASSON-LEHERICY pour son énorme soutien et son amitié, Stéphane BLANCHETIERE notre irréductible Indiana Jones, Laurent BOUQUET qui m'a « presque » toujours accueilli avec un mot gentil, Pascal BALZAC qui nous manque à tous énormément, Catherine CHABOT pour sa gentillesse et sa clairvoyance sans faille. Je souhaite aussi bon courage à Thomas CHIAVAZZA qui entame bientôt sa première année de thèse. Je remercie aussi toute mon équipe à Stadtagen et Brières Ilya PESHEKHODOV, Annett FINDEKLEE, Muhannad ASSAD, Nicolas GOZDECKI, Valerie WOIMBEE. Autour de l'équipe matériaux étaient aussi présents de nombreuses personnes qui ont pu m'apporter leurs connaissances ou bien leur amitié, je remercie donc Clément TARDIFF, Kévin BEUVELOT, Maxime BERNIER, Corentin et les nombreux stagiaires qui ont permis de donner un petit coup de jeune à l'équipe : le p'tit fileux, Bastien, Theo, Amal... Je remercie aussi David EVEN, Guillaume DELATTRE, Maxime LECOQ, Claude COLASSE, Erwan COMBEMOREL de vous être intéressés à mon sujet de thèse et d'être venus le jour de ma soutenance.

Un grand merci à toute l'équipe de l'ENSICAEN de Caligny : Florian Landiger qui m'a aidé à dompter de nombreuses machines du hall technique de Caligny et pour sa tarte aux fraises, à Catherine ROCQUE pour son accueil chaleureux, Oleksandr KAPIKRANYAN à qui je souhaite bon courage pour les travaux de sa nouvelle maison, Gislaïne MARIE pour sa bonne humeur, à David BLOND pour qui j'ai un dicton qui pourra t'être utile si on se rencontre de nouveau sur un terrain : « Le coup du cobra tu maîtriseras, au badminton tu me battras »

Je souhaite pour finir, remercier mes coéquipiers et amis de badminton qui ont répondu présent pendant 3 ans, mes amies de Rouen, mon compagnon et ma famille pour leur soutien qui a commencé bien avant la thèse et qui continuera bien après.

Table of Contents

| | |
|---|-----------|
| Nomenclature and Acronyms | 1 |
| Introduction..... | 7 |
| | |
| Chapter I. Literature survey: Introduction to the properties of complex phase steel | 11 |
| 1. Complex phase steels in their industrial context..... | 11 |
| 1.1. Position of CP on AHSSs..... | 11 |
| 1.2. Thermal process of CP steels | 12 |
| 2. Metallurgical constituents of CP steels..... | 13 |
| 2.1. General characteristics of the bainitic matrix..... | 13 |
| 2.2. Other properties of the microstructure | 19 |
| 2.3. Impact of tempering on microstructure..... | 20 |
| 3. Mechanical properties of CP steels with bainitic matrix..... | 22 |
| 3.1. Impact of microstructure on mechanical properties | 22 |
| 3.2. Influence of carbides on strengthening..... | 25 |
| 3.3. Impact of the nature of phases on hardening properties | 26 |
| 3.4. Evolution of hardness after tempering | 27 |
| 4. Study of the damage evolution of multiphase steels | 28 |
| 4.1. Methods to quantify damage | 28 |
| 4.2. Impact of differences in phase hardness on damage | 30 |
| 4.3. Impact of the presence of austenite and cementite on damage evolution | 33 |
| 4.4. Impact of the temperature and the stress triaxiality on the damage mechanisms.. | |
| | 34 |
| 5. Conclusion and goals of the PhD | 36 |
| | |
| Chapter II. General metallurgical and mechanical characteristics of CP steels | 37 |
| 1. Quantification of chemical composition using glow-discharge optical emission spectroscopy..... | 38 |

| | | |
|------|--|-----------|
| 2. | Metallurgical characterisation..... | 40 |
| 2.1. | Phase identification and quantification | 40 |
| a. | Phase identification by XRD..... | 40 |
| b. | Phase identification and quantification by optical microscopy and SEM | 41 |
| c. | Phase quantification by EBSD analysis | 43 |
| d. | Differentiation of bainites | 45 |
| e. | Orientation relationship between bainitic ferrite and RA..... | 46 |
| f. | Measurement of bainitic lath size by EBSD and linear intercept method..... | 48 |
| g. | Complementary observation by TEM..... | 49 |
| 2.2. | Impact of temperature on the microstructure | 50 |
| 3. | General mechanical properties | 55 |
| 4. | Synthesis of results and conclusions..... | 57 |
| | | |
| | Chapter III. Cyclic plasticity mechanisms of CP1200 steels and impact of thermomechanical loading | 59 |
| 1. | Cyclic plasticity mechanisms of CP1200 steels: bibliography..... | 59 |
| 1.1. | Internal stress and dislocation behaviour | 60 |
| 1.2. | Cyclic stress softening and hardening of bainitic steels..... | 62 |
| 1.3. | Presentation of the Masing behaviour..... | 63 |
| 2. | Experimental technique: Presentation of the anti-buckling device | 66 |
| 3. | Investigation of cyclic softening of CP1200 steels..... | 68 |
| 4. | Masing behaviour | 71 |
| 5. | Isotropic and kinematic components of hardening..... | 74 |
| 6. | Impact of temperature on mechanical properties in tension | 79 |
| 6.1. | Presentation of experimental devices..... | 79 |
| 6.2. | Influence of temperature and holding time on mechanical properties..... | 84 |
| 6.3. | Summary of the thermomechanical analyses | 88 |

| | |
|--|------------|
| Chapter IV. Description and quantification of damage mechanisms in CP1200 steels..... | 91 |
| 1. Metallurgical and mechanical definitions of damage..... | 91 |
| 1.1. Void evolution and definition of the damage variable..... | 91 |
| 1.2. Sensitivity of damage evolution to stress triaxiality | 94 |
| 2. Quantification of damage at room temperature..... | 95 |
| 2.1. Preliminary quantification of damage using loading and unloading tests | 96 |
| 2.2. Quantification of voids with the impact of stress triaxiality..... | 98 |
| a. Presentation of the experimental procedure | 98 |
| b. Influence of stress triaxiality on the strain at fracture | 103 |
| c. Fractography of smooth and notched specimens | 105 |
| d. Damage evolution depending on stress triaxiality and plastic strain | 107 |
| e. Damage localisation in CP1200 steels | 111 |
| 3. Influence of temperature on damage evolution | 112 |
| a. Fractography of tensile specimens performed at high temperatures [400°C–600°C] | 112 |
| b. Influence of high-temperature mechanical stresses on damage evolution | 114 |
| c. Observations of void localisation and microstructure transformation | 117 |
| 4. Synthesis of the results with regard to damage evolution | 121 |
| | |
| Conclusion | 125 |
| References | 129 |
| Appendix | 137 |
| List of figures | 147 |
| List of Tables | 155 |

Nomenclature and Acronyms

| Symbol | Definition | Symbol | Definition |
|-------------|--|-----------------------|--|
| α | ferrite | B_s | Bainite start |
| α_1 | Material constant | C_{Lc} | Lemaitre and Chaboche parameter (kinematic hardening) |
| α_2 | Material constant (Rice and Tracey model) | c_i | Stress per percent provided by chemical element (i) |
| α' | Martensite | $\Delta\varepsilon$ | Strain range |
| α_b | Bainite | $\Delta\varepsilon_p$ | Plastic strain range |
| α_d | Thermal expansion coefficient | Δg_k | Average misorientation |
| a | Percentage of austenite obtained by dilatometry | ΔG^* | Thermal energy |
| a_l | Lattice parameter | ΔL | Length variation |
| Ac_1 | Beginning of austenite transformation | $\Delta\sigma$ | Stress amplitude |
| Ac_3 | End of austenite transformation | $\Delta\sigma_b$ | Strengthening of bainite |
| Aus_{dec} | Decomposition of austenite | $\Delta\sigma_d$ | Dislocation strengthening |
| b_{Lc} | Lemaitre and Chaboche parameter (rate of stability for isotropic components of hardening) | $\Delta\sigma_{Fe}$ | Fe strengthening |
| b_v | Burgers vector | $\Delta\sigma_{GS}$ | Boundaries strengthening |

| | | | |
|---------------------|---------------------------------------|-----------------|--|
| $\Delta\sigma_p$ | Precipitation strengthening | ϵ_v | True strain |
| $\Delta\sigma_{ss}$ | Solid solution strengthening | ϵ_{vD} | Strain damage criterion |
| ΔT | Variation of temperature | ϵ_{vr} | Strain at fracture |
| ΔV | Volume variation | e | Thickness of specimen |
| d | Equivalent grain size diameter | E | Young modulus |
| D | Damage | E_{eff} | Effective Young modulus |
| D_D | Distance between diffraction spots | f | Yield surface |
| D_c | Critical damage value | F_c | Critical buckling force |
| d_{hkl} | Interplanar spacing | f_f | Void fraction at the macroscopic failure |
| ϵ | strain | f_v | Void volume fraction |
| $\dot{\epsilon}$ | Strain rate | γ | Austenite |
| ϵ_e | Elastic strain | γ_{lc} | Lemaitre and Chaboche parameter (kinematic hardening) |
| $\dot{\epsilon}_e$ | Elastic strain rate | η | Stress triaxiality |
| ϵ_{eq} | Equivalent strain | H_p | Hollomon Jaffe parameter |
| ϵ_f | Fracture strain | \bar{I} | Identity tensor |
| ϵ_p | Plastic strain | I_{GZ} | Moment of area of a rectangular section |
| $\dot{\epsilon}_p$ | Plastic strain rate | k_b | Boltzmann constant |
| ϵ_{UTS} | Strain at the ultimate tensile stress | K_c | Plastic resistance coefficient |
| ϵ_r | Strain at rupture | k_y | Constant in the equation of Langford and Cohen |
| ϵ_t | Total strain | L | Width of specimen |

| | | | |
|------------------|--|------------------|--|
| L_0 | Initial width of the specimen | $\sigma_{0,2\%}$ | 0,2% proof stress |
| l | Length of specimen | $\bar{\sigma}$ | Stress tensor |
| M_c | Hardening exponent | σ_b | Maximal principal stress |
| M_s | Martensite start | $\bar{\sigma}_D$ | Deviatoric tensor |
| MS | Martensitic steel | σ_{eq} | Equivalent stress |
| ν | Poisson ratio | σ_M | Maximum stress |
| \dot{N} | Voids nucleation rate | σ_Y | Yield stress |
| p | Cumulative plastic strain | S | Section of the specimen |
| Q | Lemaitre and Chaboche parameter (asymptotic value for isotropic components of hardening) | S_0 | Initial section of the specimen |
| R | Isotropic component of hardening | S_D | Damaged section |
| R_c | Initial radius of cavity | SD | Standard deviation |
| \dot{R}_c | Rate of radius of cavity growth | S_f | Final section |
| r | Regression coefficient | S_N | Standard deviation |
| σ | Stress | τ | Shear stress applied to a dislocation |
| $\tilde{\sigma}$ | Mechanical effective stress (Rabotnov) | τ_{eff} | Effective shear stress applied to a dislocation |
| σ^* | Damaged stress equivalent criterion | τ_x | Internal shear stress applied on a dislocation |
| σ_r^* | Relaxation stress | τ^* | Effective stress |
| σ_0 | Initial yield stress | τ_G | Internal stress |

| | | | |
|-----------------------------|---|-------------------------|--|
| T | Temperature | x_c | Mean Carbide particle size |
| T_{tr} | Transformation temperature | x_i | Weight percentage of chemical element (i) |
| T_c | Critical temperature (viscoplasticity) | Z | Necking coefficient |
| X | Kinematic component of hardening | A, B, C, D | Fitting parameters |
| \bar{X} | Kinematic hardening (tensor) | | |

| Abbreviation | Definition | Abbreviation | Definition |
|--------------|---|------------------|--|
| AHSS | Advanced High Strength Steel | IQ | Image Quality |
| BCC | Body Centred Cubic | IF steels | Interstitial-Free steels |
| FCC | Faces Centred Cubic | KAM | Kernel Average Misorientation |
| CE | Carbon Equivalent | KS | Kurdjumov-Sachs |
| CP | Complex Phase | LB | Lower Bainite |
| CSSC | Cyclic Strain Stress Curve | LD | Longitudinal Direction |
| DIC | Digital Image Correlation | M/A | Martensite/Austenite |
| DP | Dual Phase | NW | Nishiyama and Wassermann |
| DSC | Differential Scanning Calorimetry | OIM | Orientation Imaging Microscopy |
| EBSD | Electron Backscatter Diffraction | OM | Optical Microscopy |
| GAM | Grain Average Misorientation | RA | Retained Austenite |
| GDOES | Glow Discharge - Optical Emission Spectroscopy | SEM | Scanning Electron Microscopy |
| GOS | Grain Orientation Spread | SMB | Sodium Metabisulfite |
| GPM | Group of Physics of Materials | RT | Room temperature |
| GS | Grain Size | TD | Transverse Direction |
| HT | High temperature | TEM | Transmission Electron Microscope |
| HV | Hardness Vickers | TMF | Tensile machine equipped with a furnace |

| | | | |
|-------------|--------------------------------------|--------------|-----------------------------------|
| TRIP | Transformation Induced Plasticity | ULSAB | Ultra Lightweight Steel Auto Body |
| TTT | Time-Temperature- Transformation | UTS | Ultimate Tensile Strength |
| UB | Upper Bainite | XRD | X-Ray Diffraction |

Introduction

Over the recent decades, the desire to protect the environment has influenced the design of products in automotive industries. Since the beginning of the 21st century, a variety of stringent laws requiring the reduction of CO₂ emissions have been implemented. With contemporary legislation many countries request values below 120 g/km, as shown in Figure 0-1 [1].

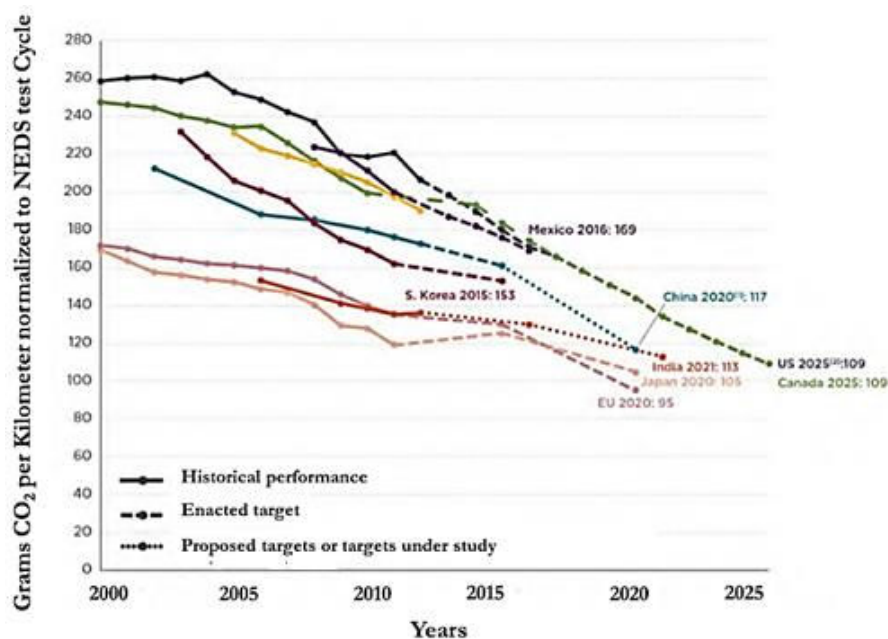


Figure 0-1. CO₂ emission of cars measured and requested from 2000 to 2025 during NECD tests (NECD: New European Driving Cycle) [1].

However, this ecological constraint has to be implemented alongside general automotive guidelines such as safety, the need to ensure the comfort of passengers, and product aesthetics. The need to satisfy these various requirements gives rise to challenges for the company Faurecia Automotive Seating. For instance, seats are defined as safety and regulation parts because, in the event of a collision, passengers are only kept in a car by seat mechanisms. This implies that a reduction in the weight of car seats must not influence mechanical properties. To overcome this issue, two modifications can be adopted. First, lighter materials such as aluminium (2700 kg/m³), magnesium (1750 kg/m³), or composites can be used [2]. However, aluminium and magnesium alloys exhibit lower mechanical properties than steels and thus cannot be used in parts where complex mechanical loadings are required. In such case, a large sheet thickness should be employed, which could lead to a cumbersome design. Another method of remedying this problem is to develop steels that exhibit

superior performance properties, namely advanced high-strength steels (AHSSs). With this aim in mind, three generations of AHSS were developed to achieve forming and strength properties not previously obtained with other materials. To develop these new generations of steels, steelmakers modified the chemical composition of these steels and adapted the heating and cooling processes to obtain complex microstructures which are usually characterised by a combination of phases. Given the superior mechanical properties of such steels, the seats in the above example could be redesigned to require less steel.

Complex phase 1200 (CP1200) steels belonging to the first generation of AHSSs are currently of interest to Faurecia due to their high energy absorption, high residual deformation capacity, and good hole expansion. The superior forming properties of these types of steels enable seat designs to be modified to reduce the volume of material required. However, the increased design complexity leads to more severe curvature radii. Thus, steels with even higher formability are required. It can therefore be necessary to deform the steel used to a degree that comes close to its deformation limit in complex loading. This project was financed to obtain a better understanding of the behaviour of CP1200 steels close to these formability limits.

A previous doctoral dissertation was undertaken in collaboration between Faurecia and the Crystallographic and Materials Science Laboratory (CRISMAT) in 2011. This previous thesis concerned damage evolution on dual-phase (DP1000) steels, with a particular focus on the impact of the stress state [3–6]. These steels also belong to the first generation of AHSSs and exhibit two phases microstructure composed of ferrite and martensite islands. The results showed that the localisation of voids, which is characteristic of damage, occurs at the interfaces between phases or by martensite cracks. Indeed, the high phase contrast between ferrite and martensite caused internal stresses that lead to the separation of interfaces. The impact of temperature was also investigated in this study. It was found that an increase in temperature from 20 °C to 600 °C yielded an increase in void growth, leading to the tempering the martensite.

In this thesis, the same methodology was used to investigate the damage mechanisms of CP1200 steels. The focus was on the similarities between these two steels in order to understand the impact of microstructure on damage and plasticity mechanisms. Complex phase 1200 steel is defined by a bainitic microstructure and the presence of retained austenite, cementite and martensite. One may wonder how this microstructure resists damage, and how it evolves after its initiation. Moreover, the bainitic microstructure of these steels is less sensitive to temperature modification than martensite. Thus, a secondary focus of this research is on how temperature influences damage mechanisms in CP1200 steels.

In order to answer these problematics identified above, this thesis is divided into four parts.

First, the complex phase (CP) steels were positioned within the AHSS generations, followed by an explanation of their elaboration processes. After this general presentation of CP steels, the characteristics and influence of the phases on the mechanical properties of such steels were highlighted. The influence of the various phases was then related to the mechanical properties of the material, with a focus on cyclic hardening. Thereafter, the literature concerning the development of damage in multiphase steels is presented. Throughout these investigations, the impact of temperature on mechanical and damage properties was investigated. The first chapter closes by identifying the research context and objectives.

In the second section, the microstructural and general mechanical features of various grades of CP1200 steel from different suppliers were investigated. To do so, the results of phase identification and quantification under optical microscopy (OM), scanning electron microscopy (SEM), electron backscattered diffraction (EBSD), and transmission electron microscopy (TEM) are presented. Based on the collected data, it is possible to acquire knowledge concerning the relative percentages of each phase as well as the degrees of misorientation among them. Finally, the thermal stability of CP1200 steels was investigated using differential scanning calorimetry and dilatometry to determine the phase transition temperatures. In the final section of this chapter, the tensile properties of the specimens was characterised in order to relate the microstructure of CP1200 to their mechanical properties.

To obtain additional information on the impact of the microstructure on cyclic hardening, tensile-compression experiments were performed. The results obtained highlight the obstacles to the motion of dislocations and enable the measurement of internal stresses. Subsequently, the influence of temperature on tensile properties is studied. Particular attention was given to the impact of the temperature [200 °C–600 °C] combining with tempering time.

The final concerns the evolution of damage mechanisms at both ambient and higher temperatures. The quantification of the voids formed was studied as a function of the plastic deformation. The influence of the loading path on void fraction was examined for different geometries of notched specimens in order to vary the stress triaxiality. The localisation of voids was then investigated by microstructural analysis at room temperature, 400 °C, 500 °C, and 600 °C.

Finally, a conclusion describing the results is provided. This section links all of the observations and discusses relationships among the microstructure, the mechanical properties, and the damage that occurs at room and high temperature.

Chapter I. Literature survey: Introduction to the properties of complex phase steel

The main characteristic of CP steels is the coaction of phases with various mechanical properties. This combination of phases offers a large range of mechanical properties, which is provided by complex mechanisms. Parameters such as the shape and the amount of phases play key roles in determining mechanical properties and damage.

This chapter begins by introducing CP steels in their industrial context. Complex phase steels belong to new generations of steels developed to respond to restrictive ecological legislation: namely, the AHSSs. In the second section, bainite, austenite, and cementite are presented, along with their microstructural specificities. A willingness to link the bainitic microstructure and the mechanical properties of the steel is established in this dissertation. The crystallographic orientation relationships that may exist between phases are presented to improve understanding of mechanical and damage behaviours. The third section examines the impact of each phase on the tensile properties of the steels. Bainite strengthening elements are presented, and the properties provided by the impact of austenite and cementite are studied. Damage mechanisms are investigated in the last section with a particular focus on phase heterogeneity, which is key to understanding those mechanisms.

1. Complex phase steels in their industrial context

1.1. Position of CP on AHSSs

Since the creation of the Ultralight Steel Auto Body (ULSAB) programme in 1994, there has been great willingness to create lightweight steels that exhibit a wide range of mechanical performances [1]. The aim of this program is to develop a better compromise between safety and fuel economy. Two different solutions emerged: the first is the development of new steels with higher resistance, while the second is the improvement of existing low-density metals. In pursuit of these goals, steel industries have developed new grades namely the AHSSs. A distinctive characteristic of these new generations is their improvement in terms of formability when compared to conventional grade steels. The challenge however, is to continuously develop grades in response to restrictive legislation. Currently, three different generations of AHSS steels have been developed to offer a large

range of mechanical properties [7–10]. Figure I-1 presents the total deformation as a function of ultimate tensile strength (UTS) of these grades.

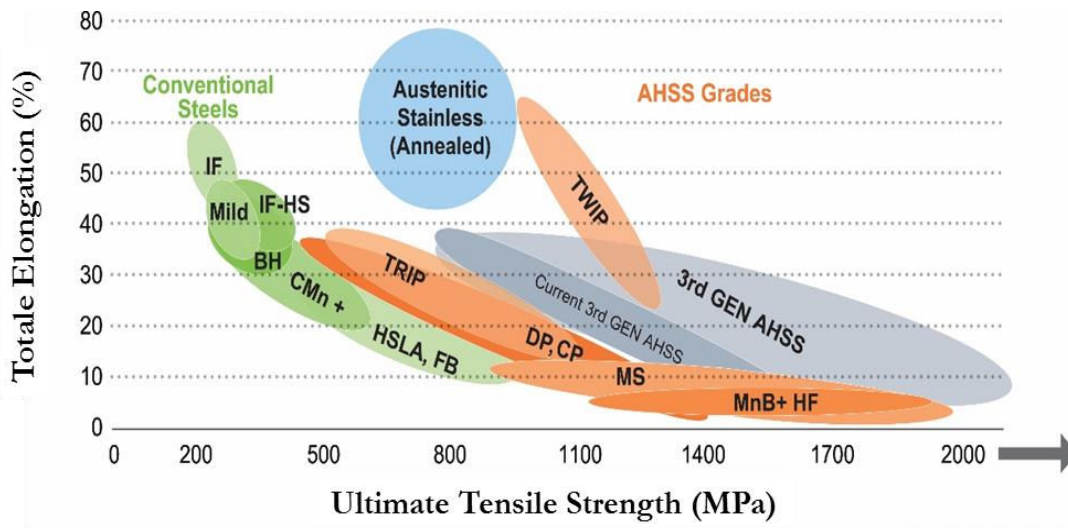


Figure I-1. Steel ductile diagram of various AHSS grades [1].

This report focuses on the first generation of AHSSs. The grade of steel studied is CP steel. Complex phase steels are defined as having a yield stress of up to 800 MPa and exhibit high energy absorption, high residual deformation capacity, and good hole expansion [8,9]. Over time, the microstructure of steels that fall under the CP category has evolved. Initially, CP steels were thin ferrite grains with a high volume of hard phase such as martensite and bainite, but they did not have austenite. This definition of the microstructure was similar to that of DP steels. The new generation of CP steels was inspired by the third generation of AHSSs with the addition of Mn and Si as additive elements. Currently, CP steels are developed with a bainitic matrix containing austenite, which leads to superior formability due to the low difference between phase hardness [11].

1.2. Thermal process of CP steels

The transformation of CP steels must be represented in a time-transformation-temperature (TTT) diagram [12], because bainite is transformed under para-equilibrium conditions that cannot be represented in a Fe-C equilibrium diagram. The TTT diagram (Figure I-2) for steels is characterized by two C curves: the first represents the reconstructive transformation with the formation of ferrite and pearlite, and the second represents the formation of bainite, Widmanstätten ferrite and martensite.

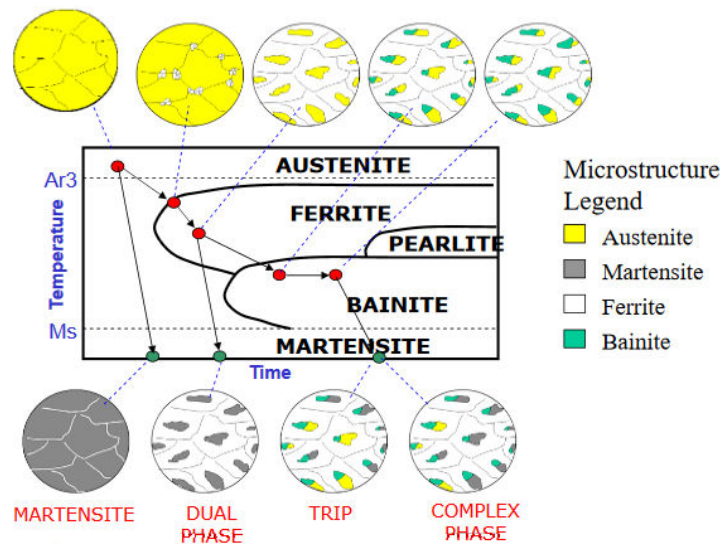


Figure I-2. Time-transformation-temperature diagram of AHSSs transformation [13].

The schematic heat treatments of CP, DP, transformed induced plasticity (TRIP), and martensitic steels are represented in Figure I-2. The cooling path is one element that can be used to explain the difference among these steels. For CP steels, the heat treatment process is divided into three different steps: first, the steel is heated up to an austenitisation temperature and cooled down to a temperature that falls between bainitic start (B_s) and martensitic start (M_s). Following this cooling, isothermal transformation is performed to allow bainite development. Quenching is the final step of the transformation and enables the transformation of the second phase (cementite, austenite, or martensite). Several studies were carried out to investigate the impact of holding time, temperature and quenching on the bainitic structures of steels [12,14–16]. The findings indicate the existence of a wide range of microstructures, which are discussed in Section 2.1 of this thesis.

2. Metallurgical constituents of CP steels

2.1. General characteristics of the bainitic matrix

Bainite was discovered by E. S. Davenport and E. C. Bain in 1930 [12]. In initial studies, bainite was described as an acicular dark etching aggregate called ‘martensite-troostite’ [17]. The denomination ‘bainite’ was established in 1934 in honour of Edgar C. Bain. This component is defined as aggregates of plates of ferrite separated by retained austenite (RA), martensite, or cementite. These clusters of plates are called sheaves and the plates are referred to as sub-units [13, 14]. All sub-units

in a sheaf are connected by a similar crystallographic orientation. A representation of this microstructure is shown in Figure I-3.

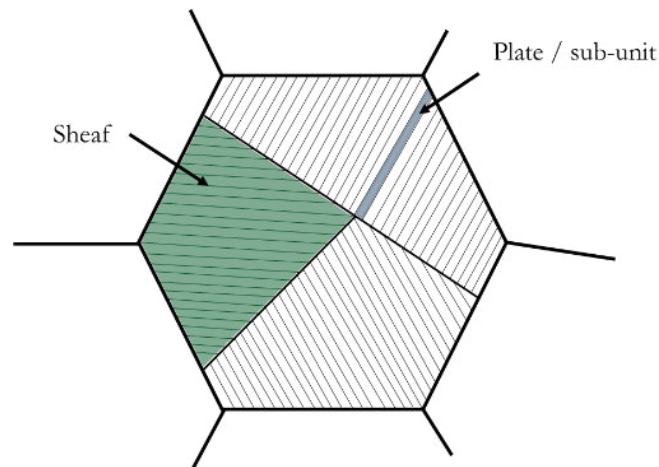


Figure I-3 Pattern of bainitic structure.

The transformation mechanism of bainite was debated for a considerable period of time. Two approaches were proposed to solve the issue of bainite transformation, namely: the displacive and the diffusive hypotheses. Displacive transformation, as in martensite transformation, is based on the shear movement of atoms. A cooperative movement of atoms can be observed. On the other hand, diffusive transformation, also called reconstructive transformation, includes the diffusion of atoms (as with ferrite and perlite). In this case, rearrangements of atoms are involved. Figure I-4 provides a schematic representation of displacive and reconstructive transformations.

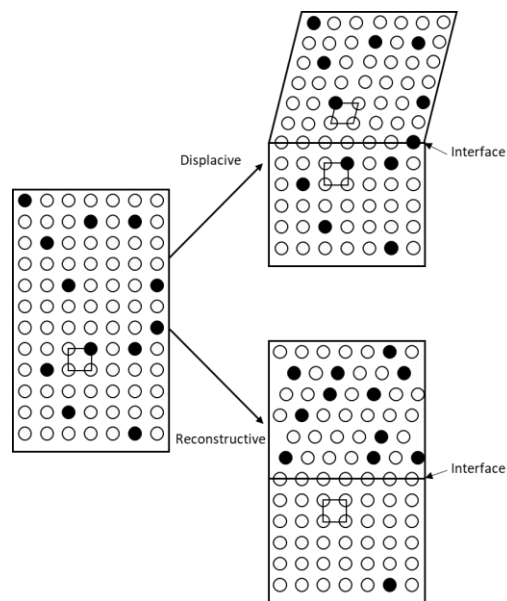


Figure I-4. Schematic representation of displacive and reconstructive transformations [20].

Recent studies support the displacive transformation based on analyses of surface relief, which is a characteristic of shear transformation. Since bainite transformation is quite similar to the martensite, both mechanisms have been compared in the literature. The main difference that stands out is the partitioning of carbon from supersaturated carbon to austenite, as presented in Table I-1[20].

Table I-1. Transformation mechanisms present in martensite (α') and bainite (α_b) [9].

| | α' | α_b | | α' | α_b |
|--|-----------|------------|--|-----------|------------|
| Nucleation and growth reaction | v | v | Large strain | v | v |
| Plate shape | v | v | Invariant plane strain shape deformation | v | v |
| Diffusionless nucleation | v | x | Diffusionless growth | v | v |
| Carbon diffusion during nucleation | x | v | Carbon diffusion during growth | x | x |
| Substitutional diffusion during nucleation | x | x | Substitutional diffusion during growth | x | x |
| Confined to austenite grain | v | v | Glissile interface | v | v |

The diffusion of carbon can occur after the growth of bainitic ferrite, as shown in Figure I-5, which is adapted from the PhD thesis of Boucard [21]. Bainite sub-units are formed from the grain boundaries of austenite by displacive transformation. Subsequently, the excess of carbon contained inside the ferrite diffuses at the interfaces from ferrite to austenite. However, the hypothesis concerning the carbon diffusion mechanism has been strongly contradicted and experimental validations are complicated because the kinetic of the reaction occurs too rapidly to be observed.

After bainitic transformation, a high density of dislocations has been observed. Swallow and Bhadeshia [22] have explained this with reference to the plastic relaxation created in austenite. This relaxation creates defects that resist the advancement of bainite/austenite interfaces. The size of bainite platelets is then also controlled by plastic relaxation. At the end of the transformation, the microstructure is composed of bainitic ferrite with a high amount of dislocations and RA with carbon.

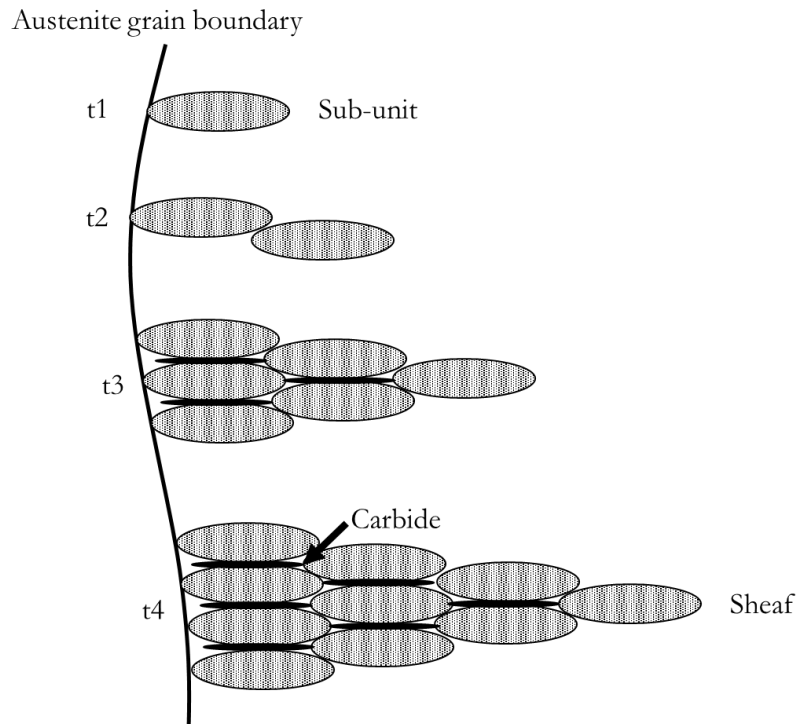


Figure I-5 Displacive transformation of bainite with diffusion of carbon after sub-unit growth [17,21].

The literature [12, 19] identifies two major types of bainite obtained by isothermal transformation: lower bainite (LB) and upper bainite (UB). The main difference between them is carbide localisation, which is controlled by the heat treatment process (see Figure I-6) [24]. Upper bainite is formed at high temperatures. It is defined by sheaves of ferrite plates with cementite between them. During this transformation, the excess of carbon has time to partition into austenite before precipitation within the ferrite. Compared to UB, LB has thin cementite particles within the bainitic ferrite in addition to those between plates. This transformation occurs at lower temperature, which results in slower diffusion. Complete partitioning of carbon does not occur, which enables the precipitation in the supersaturated ferrite. A sharp overlap of temperature transition exists between both transformations, allowing bainite shapes to co-exist in the same steels.

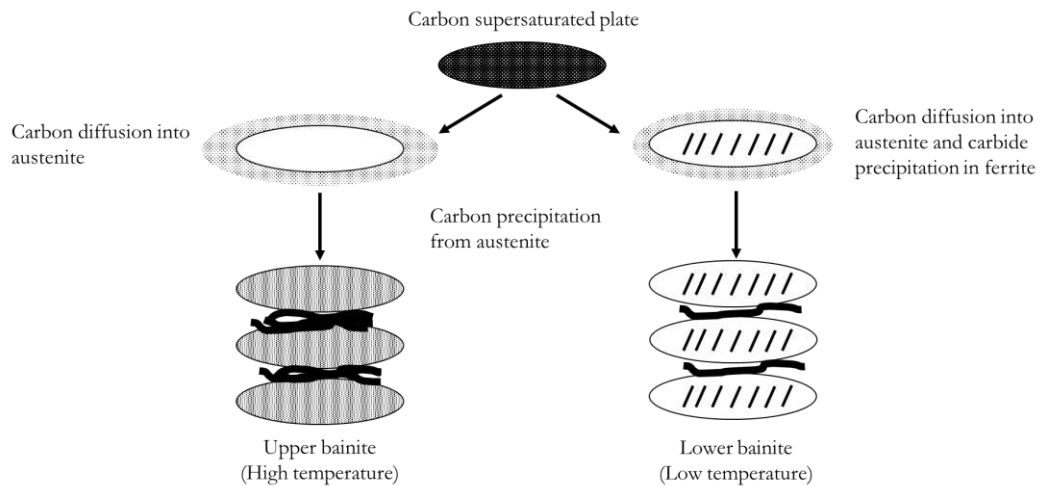


Figure I-6. Diffusion of carbon during UP and LB transformations [24].

For many years, new classifications of bainite [19,25] have appeared due to the wide range of possibilities offered by heat treatment and chemical compositions. For instance, the Zajac classification added three other morphologies to UB and LB [21, 22]:

- **Granular bainite** was discovered in the 1950s. It is created through the continuous cooling of low-carbon steels. Granular bainite is composed of coarse plates of bainitic ferrite with granular aspect and austenitic-martensitic islands at the ferrite boundaries.
- **Degenerated UB**, in which austenite or austenite with martensite is localised at the boundaries of bainitic ferrite laths.
- **Degenerated LB**, which contains interlath austenite or austenite with martensite instead of cementite.

All these microstructures are exhibited in Figure I-7:

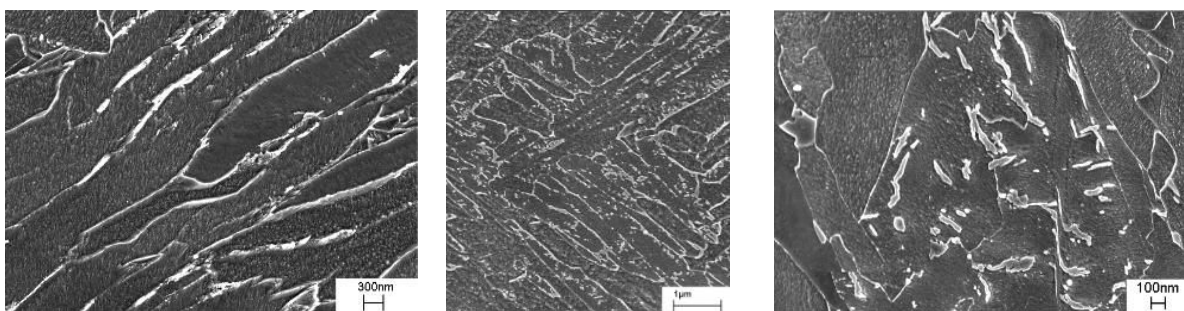


Figure I-7. SEM pictures of (a) upper bainite, (b) lower bainite and (c) granular bainite [25]

However, bainite classification is constantly evolving. Bhadeshia identifies other structures of bainite, such as inverse bainite, columnar bainite, and grain boundaries bainite [17].

All of these structures complicate phase identification by means of optical microscopy. These microstructures are differentiated using microstructural observation under SEM and also by means of EBSD analysis [25,27,28]. A high proportion of misorientation between 50° and 60° characterises LB. For UB, the amount of high misorientation angles is lower, but many low misorientation angles are observed. For UB and LB, no misorientation is measured between 15° and 50° (see Figure I-8). These misorientation angles are characteristic of granular bainite, which presents random angles [25]. Misorientation of austenite is also detected in this range at 45° . This misorientation derives from the orientation relation between the initial austenite grains and bainite.

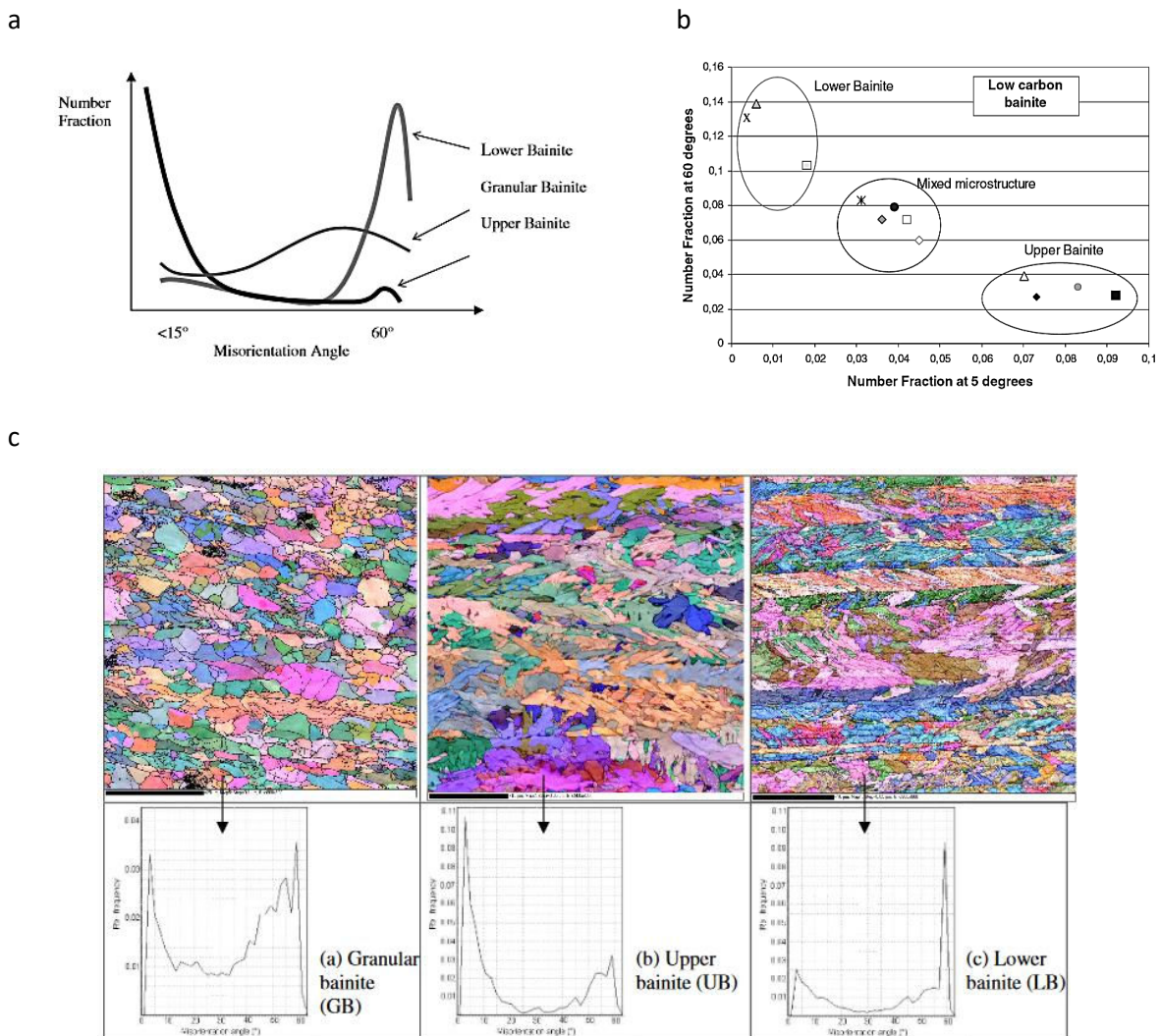


Figure I-8. (a) Misorientation angle relations between upper, lower, and granular bainite, (b) Determination of bainite structure as function of angle misorientation at 60° and 5° , (c) Example of bainite identification with granular, upper and lower bainites [25].

2.2. Other properties of the microstructure

Lath-shaped RA can be observed at the interfaces between sub-units and as islands at grain boundaries. Retained austenite is due to the incomplete transformation of bainite. Indeed, throughout the transformation of bainitic ferrite sub-units, the excess carbon is partitioning into austenite [17,29]. Up to a certain amount of carbon, the energy required to keep austenite is lower than that required to transform it into bainitic ferrite. If no alloying elements are added to promote the formation of retained austenite, carbides are formed. In new grades, the presence of retained austenite is required, which is achieved by the addition of silicon. This element enhances the formation of retained austenite due to its low solubility in cementite [30]. The RA is then supersaturated in carbon, and carbides can be found in this phase.

Carbides can be also present in microstructures at the grain boundaries and/or inside bainitic ferrite. Many types of carbides can be found in bainitic structures. However, cementite or ϵ -carbide are the most common ones [17]. In UB, carbides are located at the interfaces between laths of bainitic ferrite. Bainitic laths are formed following the partitioning of carbon into austenite during isothermal heat treatment and have a habit plane parallel to lath development. In LB, the temperature is not sufficient to permit the total diffusion of carbon. Carbides precipitate in bainitic ferrite in a single crystallographic orientation with their habit plane oriented at 60° to the plate axes. The structure of LB and UB can be identified using TEM, as it is only possible to observe the orientation of different carbides at this scale (see Figure I-9).

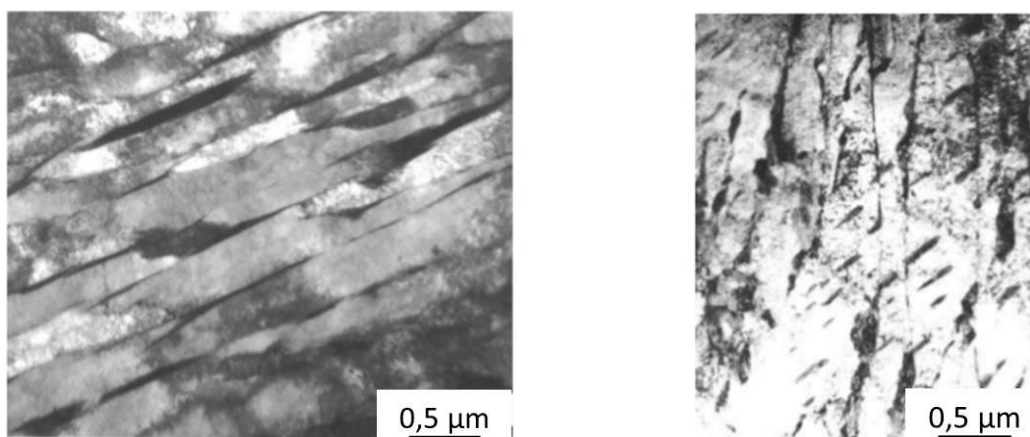


Figure I-9. TEM microstructures of UB (a) and LB (b) [23].

During the generation of bainitic steels, cementite is suppressed by the addition of silicon, which postpones its precipitation in austenite under para-equilibrium conditions [31]. Cementite is trapped by silicon during bainite transformation, which reduces the kinetics of precipitation. Above a percentage of 1.5 wt%Si, cementite is mostly replaced by RA, which offers better mechanical properties. However, the addition of silicon is ineffective during the equilibrium transition and also if initial austenite is too highly supersaturated in carbon.

As all the phases are obtained under a para-equilibrium transformation, an energy contribution could modify the entire structure. Microstructure modifications must thus be investigated.

2.3. Impact of tempering on microstructure

Tempering is a process that is more commonly used for martensitic steels than for bainitic steels. The initial aim of tempering is to increase the ductility of the material undergoing this process. Bainite is known to be less sensitive to tempering than martensite because the heat treatment process already involves austempering. Nevertheless, industrial processes such as those applied during galvanising treatment require the tempering of bainitic steels [32]. Garcia-Mateo has widely investigated the evolution of the microstructure of hard bainite (650 HV30) after tempering [33]. Different diffusion steps can be identified:

- First, at 450°C, an increase in hardness is observed. This evolution leads to the decomposition of austenite. The large regions are transformed into pearlite, while the smallest regions create carbide and ferrite.
- Below 600°C, RA is decomposed. An increase in grain microstructure size is observed.

Figure I-10, which is adapted from publication of Bhadeshia [17], presents a summary of the evolutions that occur in bainitic steels during tempering. These steps depend on the bainite transformation. For instance, in UB, diffusion of carbon from bainitic ferrite to austenite occurs during austempering. The major tempering evolutions that affect the properties of material are the decomposition of austenite, the coarsening of cementite, and the recrystallization of bainitic ferrite.

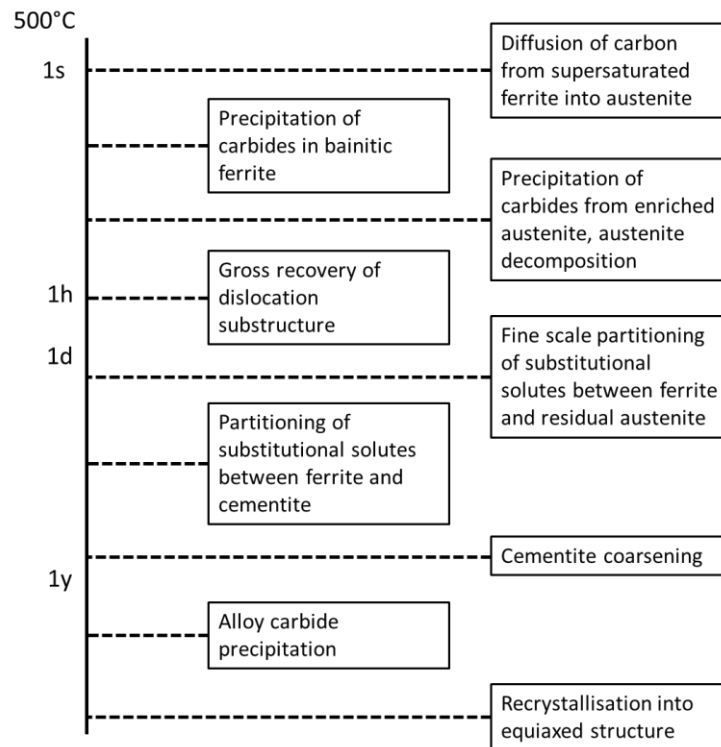


Figure I-10. Microstructure evolution of bainite depending on the time of tempering at 500°C [17].

The kinetics of austenite decomposition are temperature- and time-dependent, as demonstrated in the PhD thesis of A. S. Podder (see Figure I-11) [34]. A small increase in temperature leads to a significant increase in the decomposition of austenite.

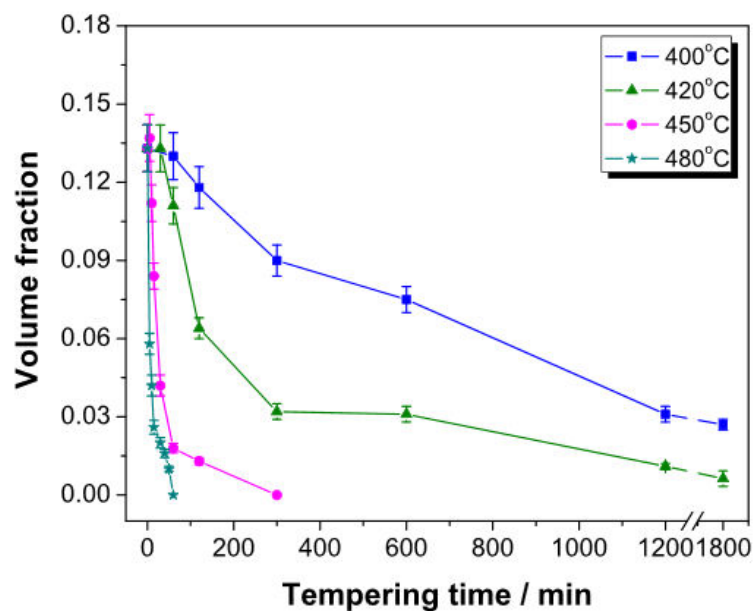


Figure I-11. Evolution of austenite fraction after tempering at various temperatures in a carbide-free bainitic steel [32,34].

3. Mechanical properties of CP steels with bainitic matrix

The previous section presented the wide variety of microstructures that can exist in CP steels. These microstructures have a significant influence on mechanical properties of CP steels. Using existing knowledge of bainitic structures, researchers have been able to identify the properties of CP structure. This section presents an overview of previous studies that have linked microstructure and their mechanical properties.

3.1. Impact of microstructure on mechanical properties

- **Strengthening of bainite**

The strengthening of bainite can be expressed by five factors: the intrinsic strength of iron ($\Delta\sigma_{Fe}$), solid solution strengthening ($\Delta\sigma_{SS}$), precipitation ($\Delta\sigma_p$), dislocations ($\Delta\sigma_d$), and boundaries linked to the grain size ($\Delta\sigma_{GS}$) [22, 29]. The strengthening can be estimated by adding up the values of these factors:

$$\Delta\sigma_b = \Delta\sigma_{Fe} + \Delta\sigma_d + \Delta\sigma_{GS} + \Delta\sigma_{SS} + \Delta\sigma_p \quad (1)$$

Figure I-12 presents an example of the contributions made by these factors.

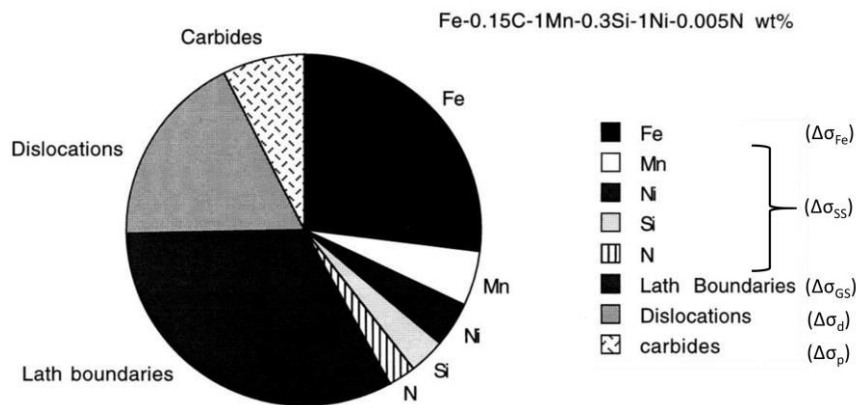


Figure I-12. Impact of different elements on strengthening [17].

The results indicate that the main factor that determines strength in bainite is the thinness of laths, which are usually 10 μm in length and 0.2 μm in thickness. However, considering the high complexity of microstructures, determining the relationship between the mechanical properties and the microstructure of a bainitic steel is not straightforward. The Hall-Petch relationship, which links

grain size measurement to yield stress (σ_y), can be applied for bainitic steels. However, for bainite structure with laths lower than 1 μm , this relationship does not exactly correspond. Indeed, the presence of low and high misorientation modifies dislocation structures. A more effective estimation of the yield stress can be obtained by using the inverse of an effective grain size [28]:

$$\sigma_y = \sigma_0 + k_y d^{-1} \quad (2)$$

Where σ_0 is the internal stress of the crystal, k_y is constant, and the parameter d represents the equivalent grain size diameter of bainite. Bhadeshia has defined the effective grain size (GS) as twice the plate thickness. In an EU report [28], d is measured by EBSD by identifying the grain boundaries between 8° and 60° . This study demonstrates that high misorientation boundaries (55° – 60°) provide more effective barriers for dislocations and thus have a greater impact on the properties of CP steels. However, for UB, the high presence of lower grain boundaries also influences mechanical properties.

The impact of iron on strength ($\Delta\sigma_{Fe}$) is also significant. It is determined in literature as a constant for low-carbon bainite steels. It is estimated at 88 MPa [17].

A high density of dislocations (ρ_d) contained inside sub-units is the third factor that can have a strengthening effect. Indeed, thin laths reduce the mean free path of dislocation. The density of dislocation is also related to the transformation temperature (T_{tr}) by Equation (3) [12, 20, 30]:

$$\log_{10}\rho_d = 10,292 + \frac{5770}{T_{tr}} - \frac{10^6}{T_{tr}^2} \quad (3)$$

The physical relationship that links strengthening due to dislocation to the density of dislocation is shown in Equation (4) below, in which α_1 is a constant material parameter, μ the shear modulus, and b_v the Burger vector:

$$\Delta\sigma_d = \alpha_1 \mu b_v \rho_d^{1/2} \quad (4)$$

For solid solution strengthening, four different elements are considered: Si, Mn, Mo, and N. Equation (5) enables estimation of the impact of the concentrations of these elements on strengthening:

$$\Delta\sigma_{SS} = \Sigma(c_i x_i) \quad (5)$$

Where x_i is the weight percentage of the element, and c_i is the stress provided by the addition of the element i . The strengthening impact of certain chemical elements is outlined in Table I-2.

Table I-2 Strengthening impact of chemical elements on solid solution [28].

| Element | c_i (MPa/%) |
|---------|---------------|
| Si | 83 |
| Mn | 37 |
| Mo | 11 |
| N | 2,920 |

- **Influence of austenite on ductility**

The presence of austenite is researched to avoid the formation of cementite and to enhance the ductility of steels [31, 32]. However, austenite's impact on the strength of bainitic steels is marginal. The main parameter modified by austenite is ductility. As noted previously, in CP steels, RA (retained austenite) is found between laths or in the form of islands. The literature offers contradictory findings as to the respective impact of the shape and localisation of RA (retained austenite) on mechanical properties. In a study conducted by Miihkinen and Edmonds [39], RA films were found to improve deformation, and the impact of the island was negligible. In the research conducted by Hell [40], a significant increase in ductility was observed when austenite islands were present due to phase transformation. This finding can be explained by the fact that both total and uniform deformation seems to reach an optimum with the variation of RA percentage, as shown in Figure I-13, which comes from the publication of Sandvik et al. [41].

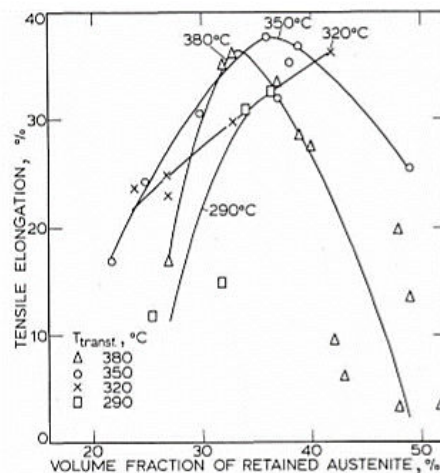


Figure I-13 Evolution of tensile deformation with various percentages of RA and with various transformation temperatures [41].

In some cases, the presence of RA prompted the TRIP effect. This phenomenon refers to the capacity of austenite to be transformed into martensite at room temperature. As Figure I-14 indicates, the presence of the TRIP effect significantly increases the uniform deformation. However, the effect also results in increased damage due to decohesion between martensite interfaces and initial austenite grain boundaries.

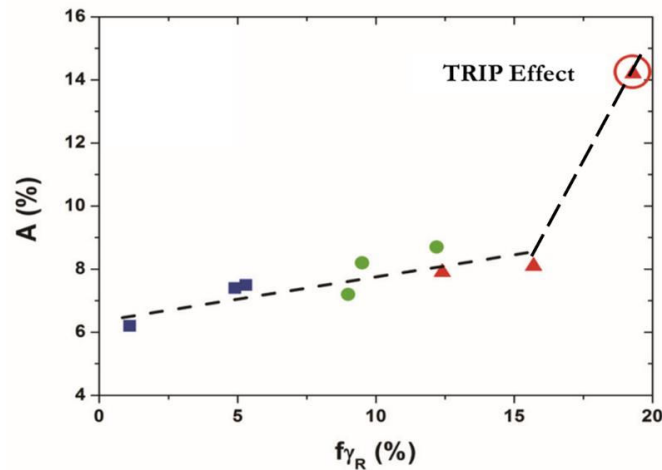


Figure I-14. Evolution of ductility obtained by varying the austenite percentage in the presence of the TRIP effect [40].

3.2. Influence of carbides on strengthening

Carbon can contribute to strengthening both in the form of a solid solution or by carbide precipitation. Bhadeshia and co-workers [17] have estimated that the impact of a carbon in solid solution is low, as they found that it is limited to approximately 400 MPa per carbon weight percentage. Only carbide precipitation leads to strengthening as a result of the creation of Orowan loops, which are the circumvention of precipitates by a dislocation. A dislocation loop is then formed around the precipitate. The impact of precipitation strengthening depends on the size of precipitates and the volume fraction of carbides ($f_{carbides}$). An estimation of the strength increment can be given by Equation (6), which uses the carbide mean size particles (x_c):

$$\Delta\sigma_p(MPa) = 5.9f_{carbides}^{\frac{1}{2}}\ln(2000x_c) \quad (6)$$

3.3. Impact of the nature of phases on hardening properties

The previous paragraphs outlined the impact of each phase on mechanical properties of multiphase steels. However, combinations of phases with different hardness can also influence hardening behaviour. This dissertation studies the impact of isotropic and kinematic components of hardening [42]. Isotropic hardening (R) corresponds to the decrease of the yield surface (see Figure I-15). Isotropic hardening is associated with the short-range interaction of dislocation movements. Kinematic hardening (X) represents the shift of the yield surface. It is influenced by the long-range interactions such as those that occur between a dislocation and grain boundaries, incoherent precipitates, and dislocation structures [43].

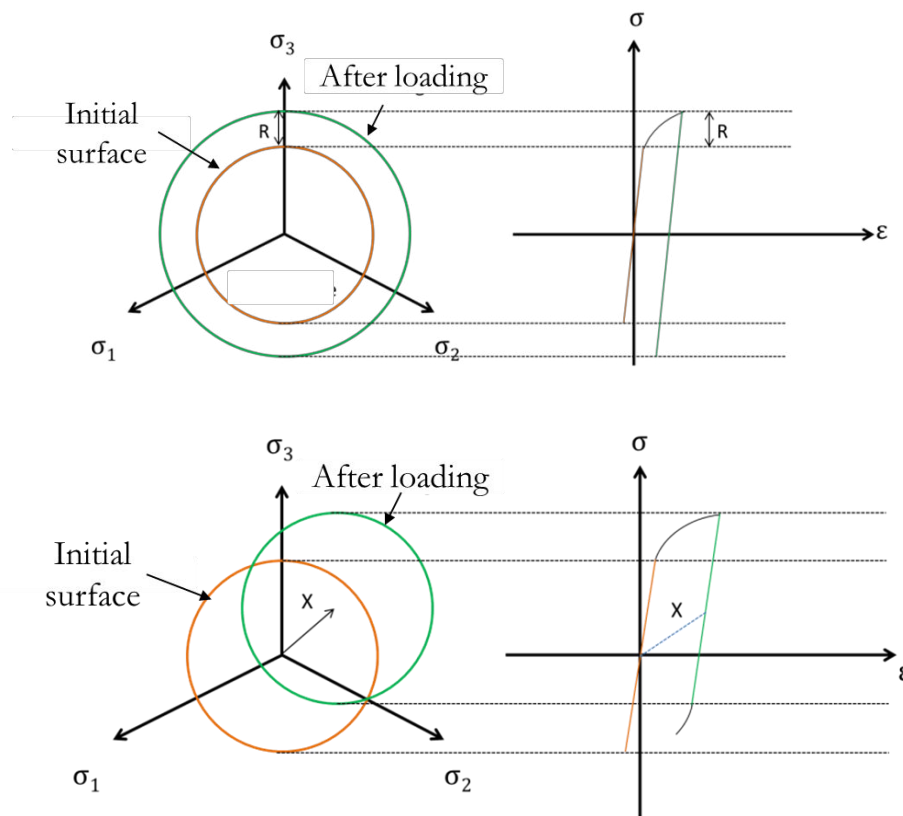


Figure I-15 Representation of X (kinematic) and R (isotropic) components of hardening (σ_1 , σ_2 and σ_3 the principal stresses)

In her PhD thesis [44,45] Silvestre demonstrated that these components evolve depending on their microstructures. Figure I-16, which is adapted from her thesis, demonstrates that AHSS steels such as DP and TRIP and martensitic steels (MSs) present negative isotropic hardening and, importantly, kinematic hardening. The results of her thesis indicate that kinematic hardening is

extremely pronounced in multiphase steels. These parameters have to be taken into account for the modelling of plasticity.

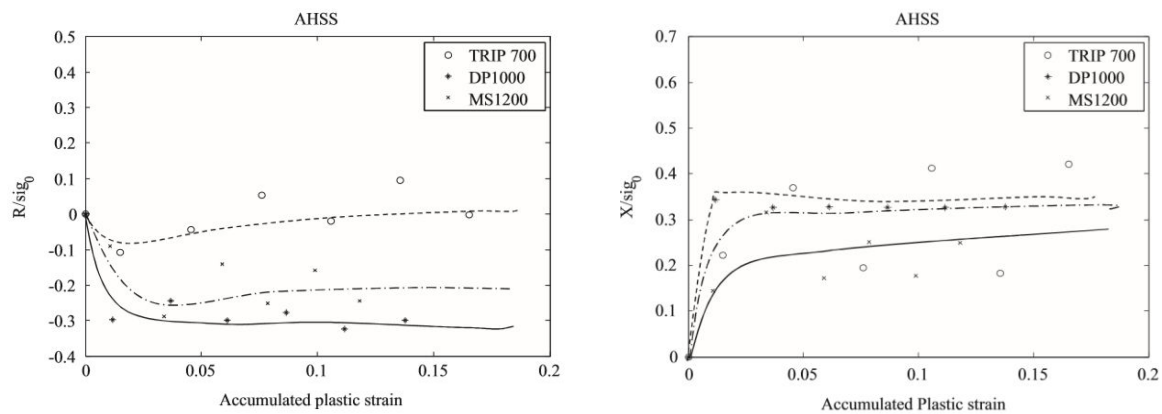


Figure I-16 Evolution of isotropic (R) and kinematic (X) hardening normalised by the yield stress [44].

Furthermore, a study by Zhonghua [46] has demonstrated that the evolution of kinematic hardening can be induced by the presence of phases with different properties. The authors investigated the differences in hardening between MSs and DP steels with various amounts of martensite. The results indicate that kinematic hardening is more pronounced in DPs than in single-phase steels such as ferrite and martensite.

3.4. Evolution of hardness after tempering

The variation of mechanical properties due to tempering is less important in bainitic steels than in martensitic ones. Figure I-17 indicates that, for low temperature, mechanical properties remain constant. For tempering temperatures higher than 650 K, a rapid decrease of hardness is observed. In the research conducted by M. J. Peet and F. G. Caballero [47], X-ray diffraction analysis demonstrated that the decomposition of austenite does not lead to a significant reduction of hardness. Their results confirm that the coarsening of bainitic grains determines the extent to which hardness is reduced.

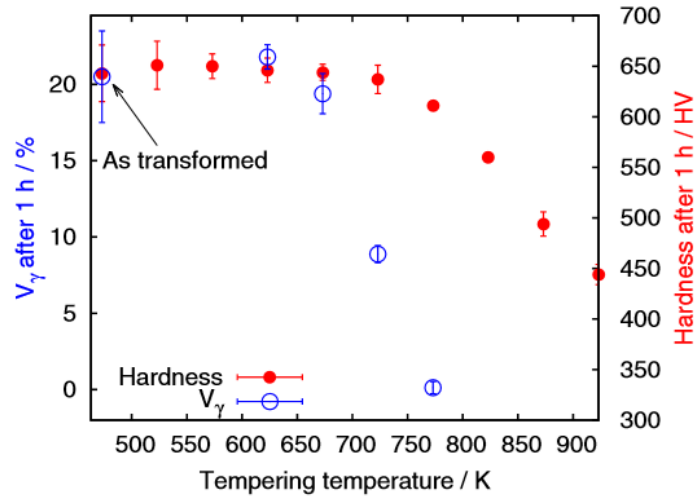


Figure I-17 Modification of hardness and volume fraction of austenite (V_γ) as a function of tempering temperature (holding time of 1 h) [47].

4. Study of the damage evolution of multiphase steels

4.1. Methods to quantify damage

Lemaitre et al. compared in their publication different methods to quantify brittle, ductile and fatigue damage. They classified them depending on their efficiency as follows: *** very good, **good and *not the most appropriate. (see Figure I-18)

| Damage | | Brittle | Ductile | Creep | Low cycle fatigue | High cycle fatigue |
|-------------------------|--|---------|---------|-------|-------------------|--------------------|
| Micrography | $D = \frac{\partial S_D}{\partial S}$ | * | ** | ** | * | * |
| Density | $D = 1 - \frac{\bar{\rho}}{\rho}^{2/3}$ | | ** | * | * | |
| Elasticity modulus | $D = 1 - \frac{\bar{E}}{E}$ | ** | *** | *** | *** | |
| Ultrasonic waves | $D = 1 - \frac{\bar{V}_L^2}{V_L^2}$ | *** | ** | ** | * | * |
| Cyclic stress amplitude | $D = 1 - \frac{\Delta\sigma}{\Delta\sigma^*}$ | | * | * | ** | * |
| Tertiary creep | $D = 1 - \left(\frac{\dot{\epsilon}_p}{\dot{\epsilon}_p^*}\right)^{1/N}$ | | * | *** | * | |
| Micro-hardness | $D = 1 - \frac{H}{H^*}$ | ** | *** | ** | *** | * |
| Electrical resistance | $D = 1 - \frac{V}{V^*}$ | * | ** | ** | * | * |

Figure I-18. Comparison of damage measurement methods for brittle, ductile and fatigue damage [48].

Ductile fracture is observed in CP steel during tensile testing, therefore quantification of damage by void measurement with X-ray tomography and metallographic techniques are presented in this report. The quantification of damage by the variation of steel properties such as hardness modification and Young modulus reduction are also introduced. This list is however not exhaustive. For all these methods, the properties of the virgin material are compared to the values obtained for the damaged material.

- **X-Ray tomography** is a non-destructive method based on radiography. The energy of X-rays can be used to observe voids inside metallic pieces by detecting thickness or density variations. A 3D image which provides a spatial distribution of damage can be then obtained. This method of damage identification was found in literature, an example is the work of Maire and al. which quantifies the damage of DP steels [49–51]. A representation of a 3D reconstruction displayed in a publication by Maire et al. is exhibited in Figure I-19. The location of damage at the centre of the specimen is clearly visible and quantification is accurate.

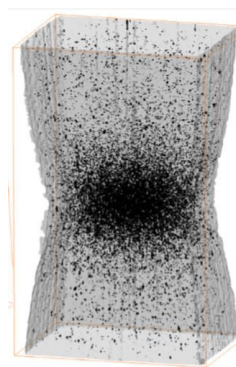


Figure I-19. Localisation of damage using X-ray tomography [49].

- **Metallographic technique** is a destructive method, which consist on fine polishing of a specimen to observe and quantify voids by microscopy after deformation. This method is more time consuming as it needs to collect a high amount of data to obtain good statistics that implies a high number of tests. However, it does not require a complex device and gives a good idea of damage evolution. Patak et al. and Heibel used this method to quantify damage on different grade of AHSS used in the automotive field (DP, CP, ...) [4,52,53]

- **Hardness** variation is a non-destructive method that enables the quantification of damage. During deformation the hardness of the metal increases due to strain hardening. A standard plasticity law can model this variation. With the development of damage, the plastic

law is modified as the creation of voids reduces the analysed surface. Thus, the difference between the hardness estimated with the plastic law and the measured one enables the quantification of damage as shown in Figure I-20.

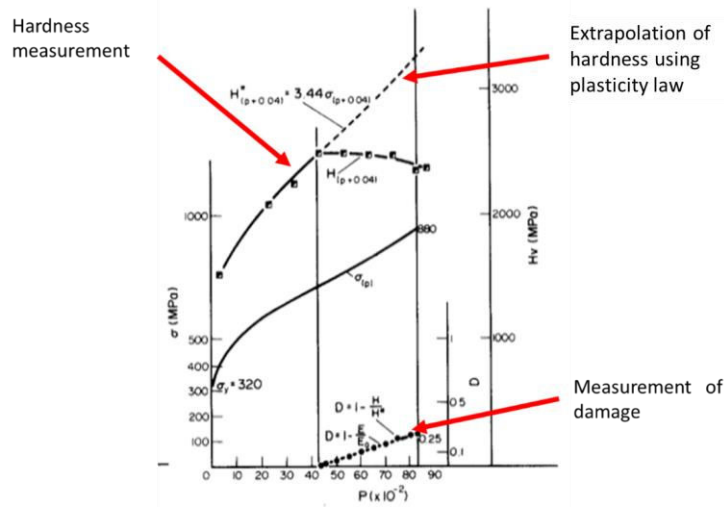


Figure I-20. Measurement of damage by hardness measurements [54].

- The last method presented in this thesis is the quantification by the **degradation of the Young modulus** [48,55]. This method can be used for metals that experience isotropic ductile damage. The initial Young modulus (E) is compared with the effective Young modulus measured on damaged material to determine damage using the following equation (more details are given in section IV.2.1):

$$D = 1 - \frac{\tilde{E}}{E} \quad (7)$$

4.2. Impact of differences in phase hardness on damage

Studies that focus on damage to multiphase steels are based on the differences between the hardnesses of different phases. To observe the evolution of damage, the results of damage to CP steels are usually compared to those of DP steels and MSs. Dual-phase steels with a mixture of ferrite and martensite present a high phase contrast. These grades of steels are currently widely used in the automotive field.

In edge stretching tests, N. Pathak et al. have demonstrated that more damage develops in DP than in CP800 at the same equivalent strain [53]. Figure I-21 presents the measured damage in these two grades. The results obtained by Pathak et al. reveal that the number of voids and the void fraction

area are more important in DP steel than in CP steel when subject to the same equivalent strain. It is also possible to observe in this publication that the average void diameter increases in CP steel when compared to DP steel, in which it decreases with strain. The authors of the publication explain this difference as a consequence of the nucleation of voids, which is more frequent in DP steel. Therefore, the nucleation of new small voids in competition with coalescence reduces the value of the average diameter of voids.

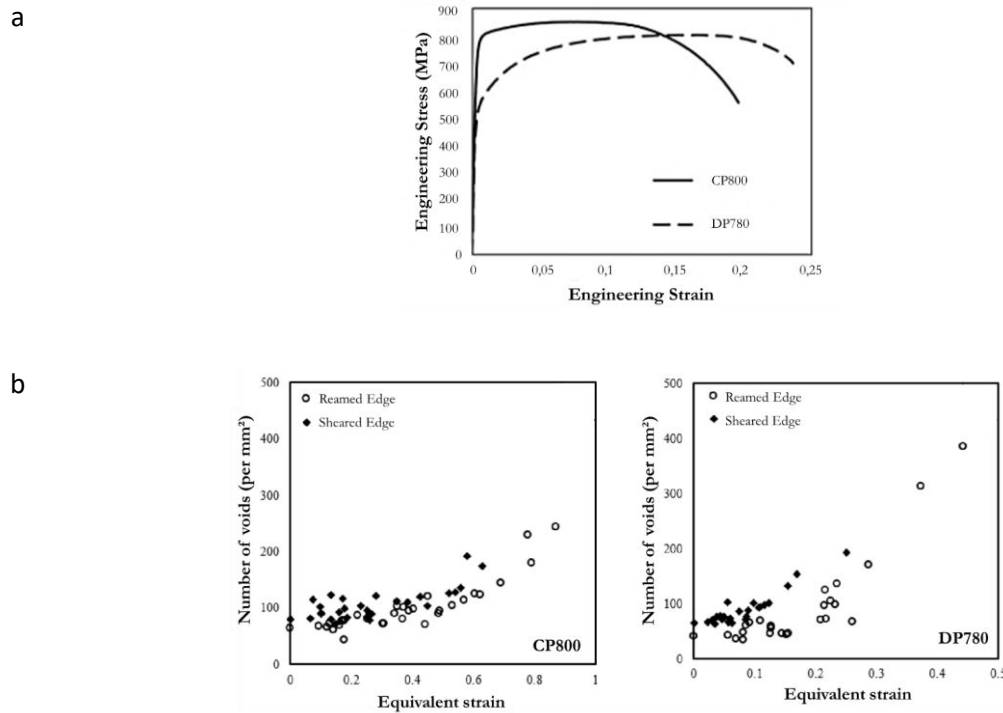


Figure I-21. Tensile curves of CP800 and DP780 (a), void fraction area of CP800 and DP780 as a function of equivalent strain (b) [53].

In the work of Heibel et al. [52], damage on various grades of DP and CP steels are studied Figure I-22. Their results shown damage evolution dependence on strength and ductility capacities of steels. Steels with lower strength capacity as DP800 and CP800 steels developed a higher amount of damage than DP1000 or CP1000 steels. However if steels with same capacities are compared DP steel exhibits a higher amount of damage than CP as it is found on the publication of Pathak. Heibel et al. explained this difference by the heterogeneity of microstructure of DP steels that made it less tolerant to damage.

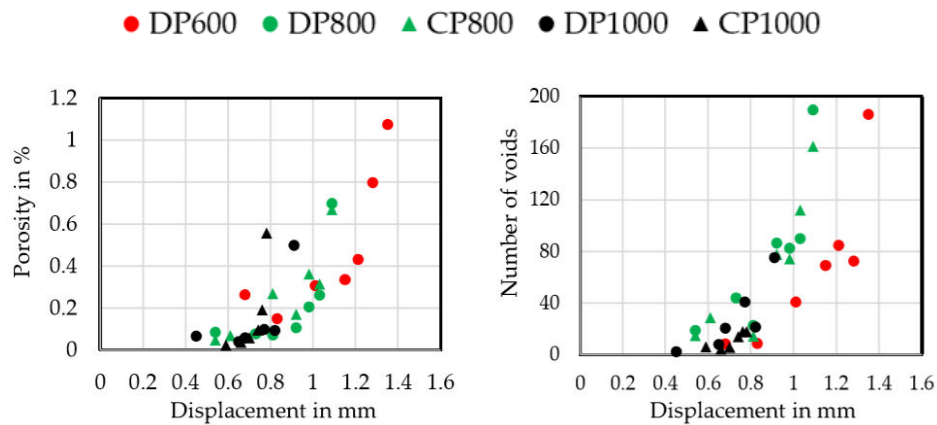


Figure I-22. Fraction of porosity and number of voids measured for various grades of AHSS (DP600, DP800, CP800, DP1000 and CP1000) [52]

The damage results presented above are linked to phase contrast, which exists in different steels. The trends created by these contrasts are summarized in Figure I-23, which is adapted from a European report [56]. Three different cases are summarized:

- For single phase-steels such as MSs, damage begins to occur fairly rapidly.
- For multiphase steels with contrast of phases hardness such as martensitic and ferritic steel (DP steels), damage appears at a higher strain but evolves quickly.
- For multiphase steels with limited contrast in terms of hardness, such as ferrite and bainite, the first voids appear at a higher level of strain. However, these voids exhibit the most rapid development. Damage in these steels is largely controlled by the nucleation, rather than the growth, of new voids however growth of voids can also be observed at inclusions.

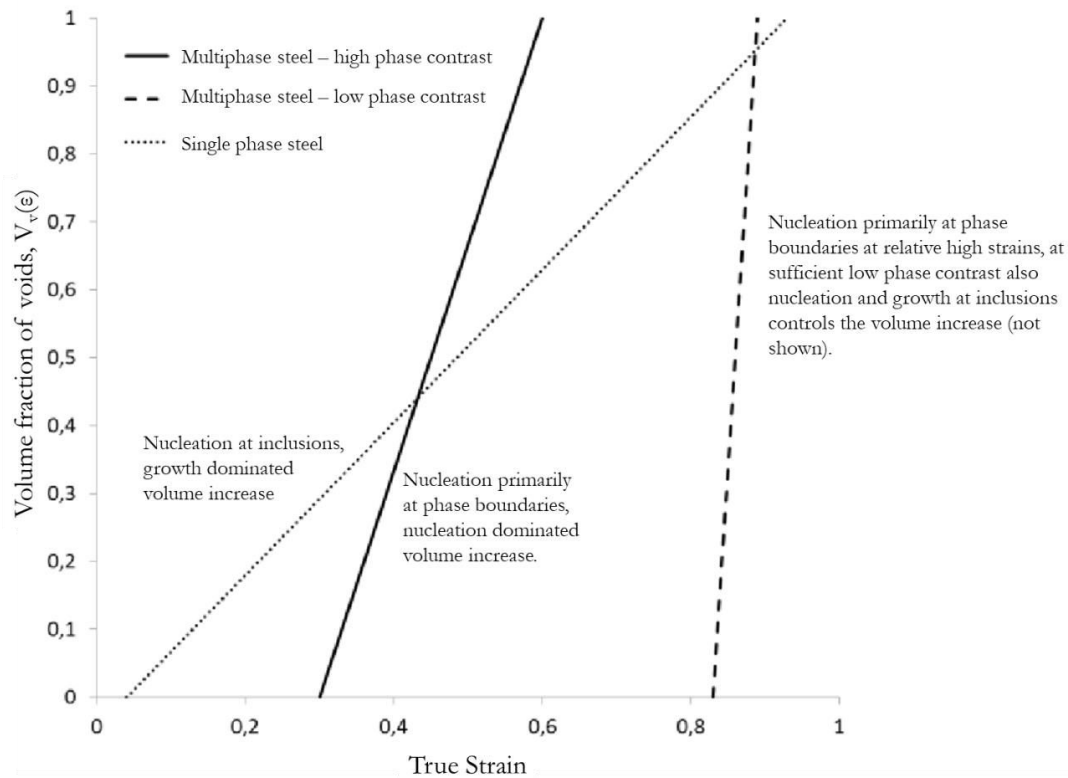


Figure I-23. Schematic trend of volume fraction of void evolution as a function of contrast in hardness phases obtained during hole expansion tests, tensile tests and bending tests [56].

4.3. Impact of the presence of austenite and cementite on damage evolution

With regard to the influence of austenite on damage mechanisms, the literature emphasises, the importance of shape and localisation. Thin laths of RA offer good damage resistance, as they allow a steel to withstand high internal stress [40]. However, the literature provides contradictory findings with regard to the impact of martensite and austenite (M/A) islands. In Hell's PhD thesis, austenite islands were found to have a negative impact on damage (see Figure I-24). The explanation is that voids are created at the boundaries between austenite and bainitic ferrite. Therefore, increasing the austenite percentage increases the probability of void nucleation. This result, however is contradicted by the findings published in a European report [56]. If the RA is transformed during deformation, the expansion of martensite (volume expansion of 3%) fills the voids created.

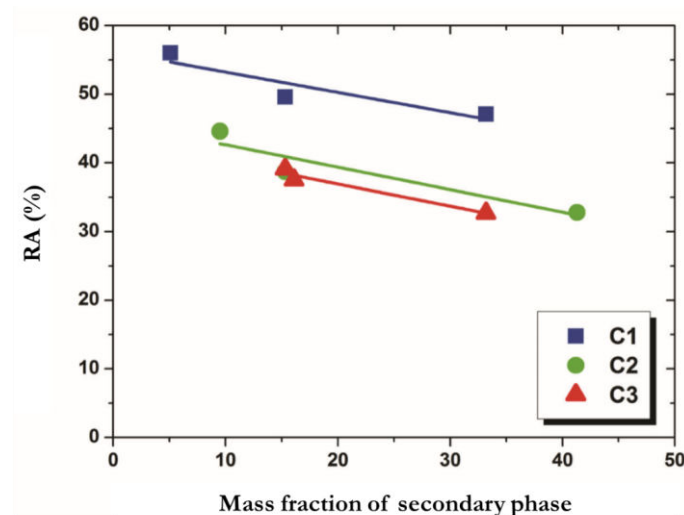


Figure I-24. Evolution of fracture section reduction as a function of austenite percentage [40].

Carbides also have a negative impact on damage. They are responsible for the nucleation of voids. In the absence of carbide particles, which is a goal of research into new generations of steels, the number of voids nucleated is small.

During tempering, the decomposition of austenite leads to the creation of carbides, which increase the number of void nucleation sites. The subsequent modification of the microstructure of a steel leads to increased damage sensitivity by tempering. However, few studies investigated the evolution of damage on CP steels as a result of tempering.

4.4. Impact of the temperature and the stress triaxiality on the damage mechanisms

A study similar to the present work was performed 10 years ago in collaboration with Faurecia, this study focused on DP1000 steels [3]. This previous work investigated the impact of a thermomechanical loading path on damage evolution. It found that voids were initiated at the interfaces between ferrite and martensite or by the cracking of martensite during tests performed at room temperature. The plastic incompatibilities between these phases created the internal stresses responsible for the void nucleation. Taking the findings of this previous study further, Figure I-25 presents the impact of temperature and stress state on damage.

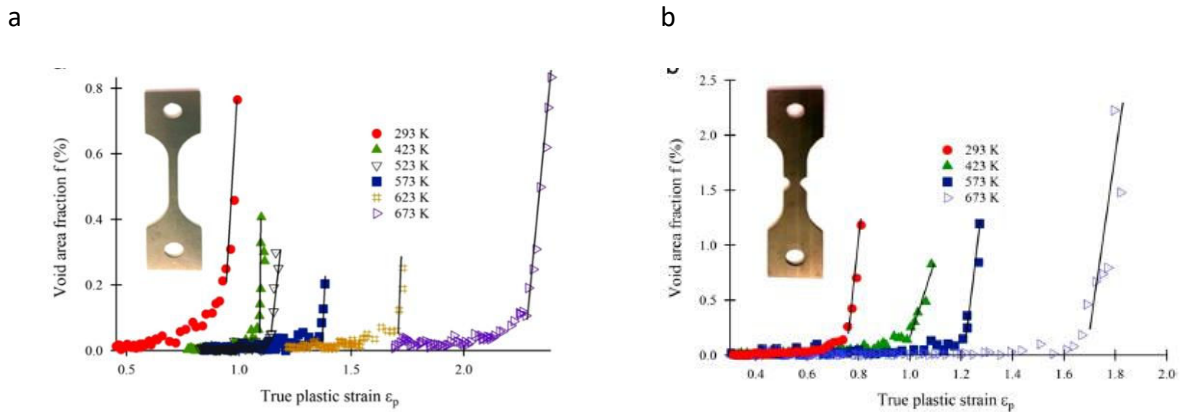


Figure I-25. Evolution of the void area fraction at various temperatures in DP1000 steel during tensile tests on (a) smooth and (b) notched specimens ($\eta = 0,5$)[4].

For DP1000 steels, the critical plastic strain, where the damage begins, increases with temperature. Moreover, a decrease of the void area fraction and the number of voids is observed between 293 K and 573 K. Above these temperatures, an increase in these two parameters can be highlighted. These modifications to the damage mechanisms may be coupled with microstructure and mechanical modifications. Therefore, as indicated in Figure I-26, a significant reduction of ultimate tensile strength was observed after 550 K. This reduction is caused by a decrease and a softening of the martensite percentage within the microstructure above 450 K due to carbon diffusion.

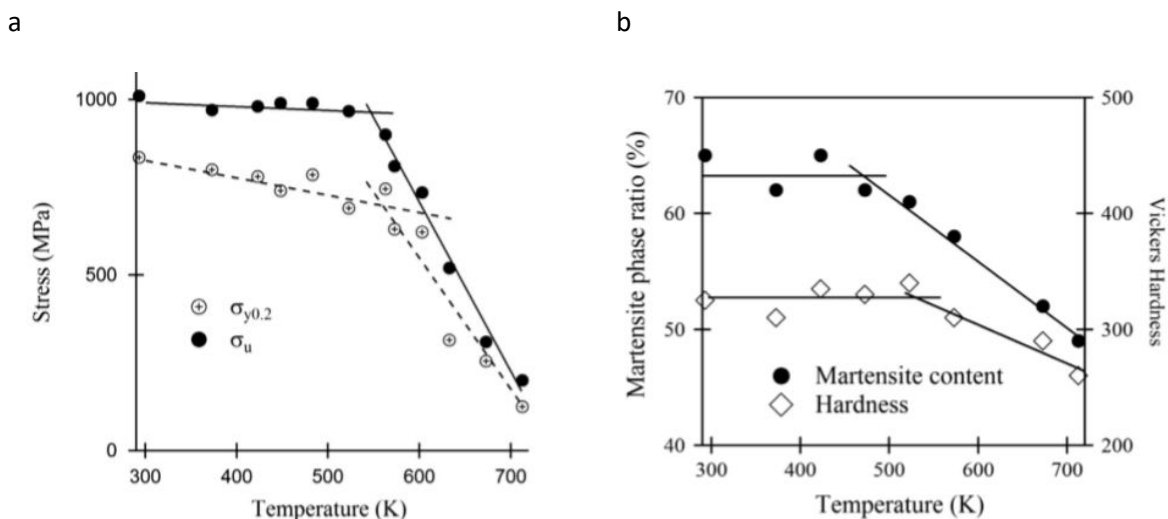


Figure I-26. Evolution of tensile properties (a) and modification of phases (b) at various temperatures [4].

To complement these observations, a microstructural investigation was conducted using TEM. These experiments led to the following conclusions: At temperatures of above 423 K, an increase in the plastic straining of ferrite is observed, without any changes to martensite deformation. At this stage, localisation of voids is identified at the interfaces and in ferrite. Above 673K, a significant increase in martensite strain can be noted. This softening of the martensite leads to an increase of void growth and a reduction of the number of voids.

5. Conclusion and goals of the PhD

Complex phase 1200 steels are a new generation of steels that are currently being studied and used by Faurecia because they exhibit good forming properties. Therefore, one may wonder if these steels could replace the DP1000 steels in some applications. Indeed, as has been shown in this section, many publications have reported on the benefits of a bainitic matrix of limiting damage evolution. However, because each of these steels presents a complex microstructure that requires a precise heating process, considerable variation in terms of microstructures and mechanical properties may be observed among the steels provided by different suppliers. Hence, a precise investigation of the grades used by Faurecia was conducted to acquire data for numerical simulation and to better understand the role of a steel's microstructure in terms of determining its mechanical and damage properties, which are important in specifying steel requirements.

In addition, the impact of temperature on this grade of steel has not been extensively investigated. In contrast to DP1000 steels, the critical temperature for CP1200 steels should be increased, as the bainitic microstructures of such steels are more stable at high temperatures. It would then be interesting to investigate whether CP1200 steels exhibit the same damage mechanisms as does DP1000 steels at room and high temperatures.

Chapter II. General metallurgical and mechanical characteristics of CP steels

The aim of this chapter is to present the metallurgical and mechanical characteristics of CP1200 steels. To do so, many grades provided from different suppliers were initially studied. However, in this report, only three of grades are presented. To simplify their identification, the samples are labelled CP1, CP2, and CP3, and their general properties as specified in supplier data sheets are presented in Table II-1.

Table II-1. General properties of the studied CP1200 steels

| | σ_M (MPa) | $\sigma_{0.2}$ (MPa) | A_{80} | %C | Sheet Thickness (mm) |
|------------|------------------|----------------------|-----------|-------------|----------------------|
| CP1 | 1180–1330 | ≥ 850 | ≥ 11 | ≤ 0.23 | 1.6 |
| CP2 | 1180–1350 | 900–1100 | ≥ 7 | ≤ 0.23 | 1.6 |
| CP3 | 980–1140 | 710–950 | ≥ 10 | ≤ 0.23 | 1.7 |

In the first section of this chapter, the standard metallurgical features of CP1200 steels are investigated. XRD, SEM coupled with an electron backscattered diffraction (EBSD) detector, TEM, and spectroscopic chemical methods were used to analyse the chemical compositions, microstructures, and phases of these grades.

The second section presents an analysis of the thermal stability of CP steels. The forming process may include tempering treatments such as electrogalvanising (around 200°C), which makes it easier to paint steels. The transition temperatures were determined by differential scanning calorimetry (DSC) and dilatometry analyses. Moreover, since mechanical properties are highly linked to the microstructure of the steel, general mechanical analyses through hardness and tensile tests were performed. The results thereof are presented in the last section of this chapter.

1. Quantification of chemical composition using glow-discharge optical emission spectroscopy

Alloying elements and carbon content have an important effect on the stabilisation or suppression of certain phases in steels and can also affect the physical properties of microstructural components. The effects of some of these elements are summarised in Table II-2.

Table II-2. Impact of the main chemical elements present in CP steels [17].

| Alloying elements | Effects |
|-------------------|--|
| C | Increases the hardness of bainite. |
| Si | Suppresses the formation of cementite during bainitic transformation. |
| Mn | Improves strength as a solid-solution element. |
| Al | Enhances the C content in RA. |
| Cr + Mo | Cr improves the quench hardenability and the strength while Mo delays the decomposition of austenite and extends the range of cooling rates for bainitic transformation. |

In order to quantify alloying elements, the samples were analysed using a spectroscopy method involving a GD Profiler Horiba Scientific glow-discharge optical emission spectrometer (GDOES)¹. This device extracts elements at the surface of a bulk specimen and projects them in plasma created between the specimen and its anode. Each element emits a radiation signature. The emission is then analysed by spectroscopy, which determines its chemical nature. In order to verify the repeatability of the experiments, the tests were performed three times on polished specimens. Table II-3 compares the data for the three CP alloys. The detection limits are also displayed.

¹ All tests were performed by Margaux Marnier (a doctor-Engineer at Faurecia) and Olivier MASSON-LEHERICY (an assistant technician at Faurecia)

Table II-3. Chemical composition (weight percentage + Standard Deviation (SD)) of CP grades.

| | | C | Si | Al | Mn | Cr | Mo | CE (%) |
|-------------------------|-----|--------|--------|--------|-------|--------|--------|--------|
| Detection limits | | < 5 | < 5 | < 1 | < 1 | < 1 | < 1 | |
| (ppm) | | | | | | | | |
| CP1 | %wt | 0.11 | 1.7 | 0.033 | 1.91 | 0.31 | 0.0049 | 0.61 |
| | SD | 0.04 | 0.03 | 0.001 | 0.02 | 0.004 | 0.0008 | |
| CP2 | %wt | 0.12 | 0.91 | 0.021 | 2.6 | 0.19 | 0.0034 | 0.65 |
| | SD | 0.0004 | 0.0009 | 0.0001 | 0.01 | 0.0005 | 0.0001 | |
| CP3 | %wt | 0.11 | 0.84 | 0.023 | 2.6 | 0.24 | 0.0045 | 0.65 |
| | SD | 0.0002 | 0.0007 | 0.0001 | 0.009 | 0.0008 | 0.0001 | |

The results exhibit significant differences among grades. Particular attention was given to the amounts of Si, C, and Mn. As noted in the literature, Si is used in CP1200 to avoid the formation of cementite, which is a brittle phase that can lead to fracture [31]. This element delays the formation of cementite and promotes the presence of RA. The results show that CP1 had the highest amount of silicon. Therefore, based on the literature, it was expected that CP1 would exhibit austenite islands, which would result in this sample having superior ductility properties [31, 46]. Since the Si content is the lowest in CP3, this grade was expected to present less austenite and worse ductility when compared to CP1. Like silicon, carbon also has an impact on mechanical properties when included as a strengthening element. However, the current trend is to produce bainitic steels with low amounts of carbon to reduce the precipitation of cementite [30]. With a carbon percentage of approximately 0.10 wt%, all grades are considered as being low carbon steels.

In order to estimate the impact of chemical elements on hardenability, the carbon equivalent was assessed using Equation (8). This equation is usually used to obtain information concerning weldability. However, it can also be linked to hardness. When used as alloying elements, Mn, Cr, Mo, V, Si, Cu and Ni tend to increase hardness.

$$CE = \%C + \frac{\%Mn}{6} + \frac{\%Cr + \%Mo + \%V}{5} + \frac{\%Si + \%Cu + \%Ni}{15} \quad (8)$$

The expression of CE denotes the influence of the strengthening element Mn, which is present in CP2 and CP3 in high amounts.

In the next section, phase quantification is performed to confirm the links that exist among the chemical composition, phases, and mechanical properties of CP1200 steels.

2. Metallurgical characterisation

To characterise and differentiate the steel grades presented in this report, microstructural analyses were conducted. To provide a wide range of observations, various methods were applied at different observation scales. First, phases were identified using XRD analysis. Second, to obtain data on phase quantification and repartition, microstructural observations were performed using optical and electron microscopy. Thereafter, to obtain more information about microstructural characteristics, the crystal orientation relationship was investigated using EBSD and TEM analyses to draw final conclusions concerning the thermal stability of these microstructures.

2.1. Phase identification and quantification

a. Phase identification by XRD

In order to identify phases, XRD analysis was performed using a Panalytical X'Pert diffractometer² using Cu K α radiation ($\lambda = 0.1541$ nm). For each specimen, two two-hour scans with a variation of 2θ from 20° to 120° were performed. The peaks were identified as belonging to two phases: austenite, which crystallises in a face-centred cubic (FCC) system, and bainitic ferrite, which has a body-centred cubic (BCC) structure (see Table II-4). However, bainitic ferrite and martensite cannot be separated using this method because their structures are quite similar.

Table II-4. X-ray diffraction angles references for austenite and ferrite.

| | | | | | |
|--|-------|-------|-------|-------|--------|
| Ferrite (α) | {110} | {200} | {211} | {220} | {222} |
| | 44.7° | 65.1° | 82.3° | 99.3° | 130.2° |
| Austenite (γ) | {111} | {200} | {220} | {311} | {222} |
| | 43.5° | 50.6° | 74.6° | 91.0° | 95.5° |

² All tests were performed by Stephanie Gascoin (a research engineer at the CRISMAT)

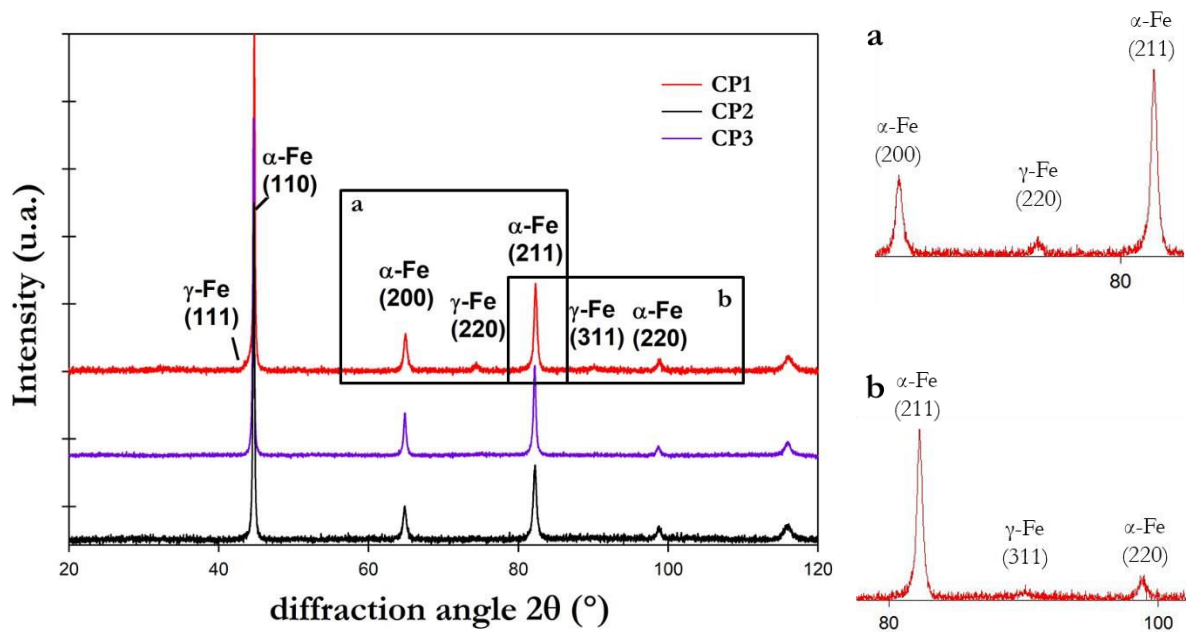


Figure II-1. X-ray diffraction diagram of CP1200 grades, with (a) and (b) presenting magnified austenite peaks.

According to the results (see Figure II-1), peaks corresponding to austenite were only observable in CP1, whereas the percentages of austenite among the other grades were too low to be detected. This analysis confirms the presence of RA in CP1 steel that is observed by chemical etching and microstructural observation of the specimen in the following section.

b. Phase identification and quantification by optical microscopy and SEM

The challenge of multiphase steel etching was to identify a chemical solution that would reveal each phase. Sodium metabisulfite (SMB) concentrated at 15% enables the identification of bainitic ferrite, martensite, and RA [21, 47, 48]. Under optical microscopy (OM), bainite is coloured light brown, martensite brown, and RA islands white. The SEM pictures obtained with a secondary electron detector (SE2) depict austenite as the light grey phase, martensite as slightly etched, and bainite as dark grey areas. A comparison of the results of these two methods of phase identification when applied to CP1 is displayed in Figure II-2-a-b. The microstructures of the other grades visualised with SEM – CP2 and CP3 – are shown in Figure II-2-c-d.

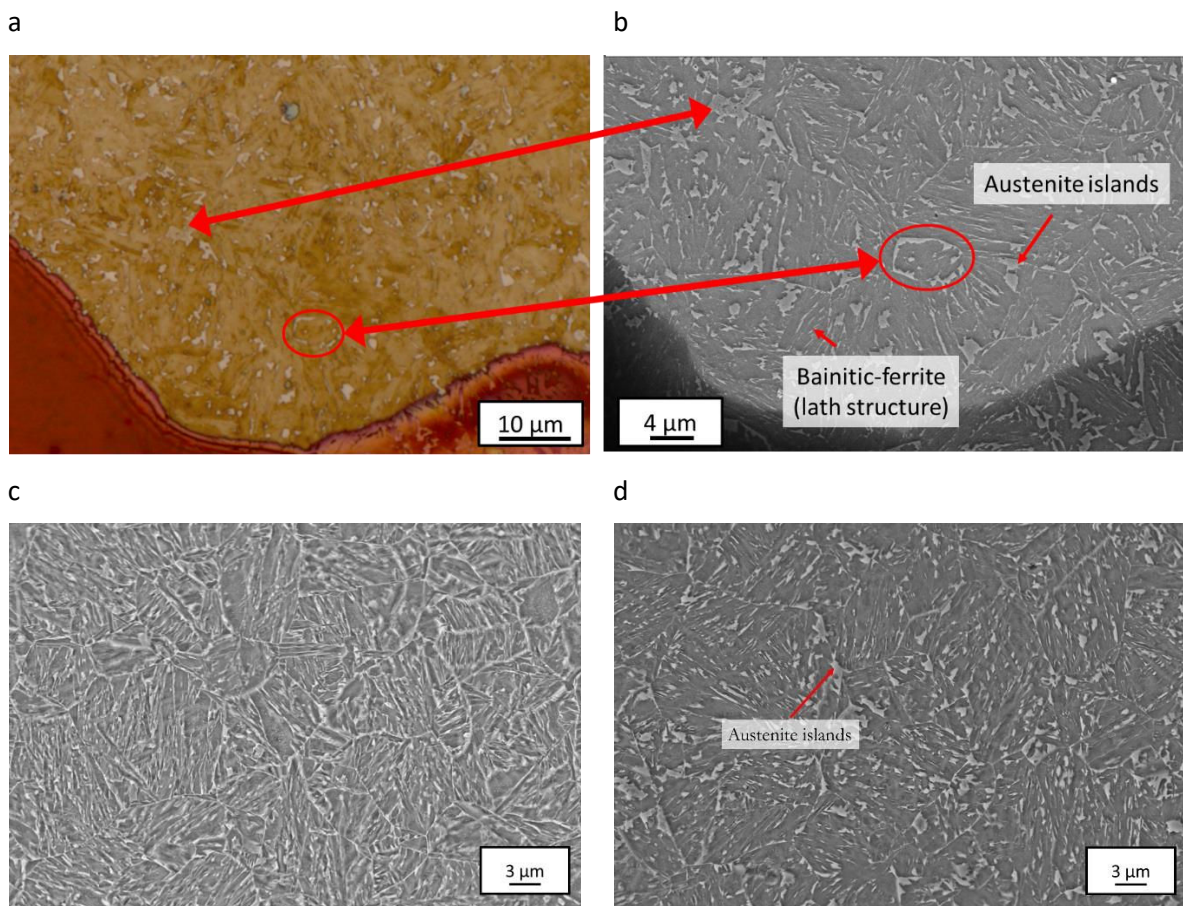


Figure II-2. Comparison of microstructure under (a) optical microscope (OM) and (b) SEM with SMB etching on CP1. The microstructures of CP 2 (c) and CP3 (d) were also visualised using SEM and the same etching solution.

The images reveal that the lath structures and RA islands are more present in CP1. After chemical etching, the colour contrast made it possible to quantify phase by picture analysis using the IGOR Pro software. The quantification was performed on 10 pictures of each grade and the average austenite percentage is presented in Table II-5.

Table II-5. Retained austenite percentage obtained by image analysis on OM and SEM pictures.

| | CP1 | CP2 | CP3 |
|--|-----|-----|-----|
| OM | | | |
| (At this scale, only the austenite islands were detected) | 9% | - | 2% |
| SEM | | | |
| (SEM was used to detect austenite islands and laths) | 18% | 15% | 11% |

This analysis revealed the presence of RA in all grades, regardless of their chemical composition. However, two morphologies of austenite can be noted in Figure II-2 (islands and lath), which leads to the need to measure the differences between the SEM and OM results. Due to the thinness of lath structures, RA interlaths can only be detected by SEM, as this microscope allows for the highest degree of magnification. With regard to the differences between the grades, it can be noted that CP1 and CP2 exhibit the highest amounts of austenite, which may be due to their percentages of silicon. Moreover, unlike CP2, CP1 and CP3 exhibit austenite islands. (This finding is correlated to mechanical properties of the steels in Section 3). The presence of islands should increase the ductility of a material due to the TRIP effect that may occur during deformation. This effect is more pronounced for islands that are less stable [35, 49]. However, uncertainty concerning the phase nature of lath between bainitic platelets remains. Indeed, since the analysis performed did not attain a sufficiently high resolution, it was not possible to distinguish between austenite and carbides.

c. Phase quantification by EBSD analysis

Previous analyses allowed differentiation of bainite from austenite, although the bainitic structures could not be distinguished. In addition, the carbides that characterise LB were not identified during the previous analyses. Electron backscattered diffraction analyses were then performed to obtain further information concerning the following:

- Phase quantification
- Differentiation of bainite
- Crystal orientation relationships

Electron backscattered diffraction tests were performed on a SEM Zeiss Ultra55 operating at 20 kV, with a tilt angle of 70° and a step size of 80 nm. To obtain a clear surface, specimens were carefully polished with the diamond paste of 1µm and electropolished with a solution consisting of 78 mL of perchloric acid, 90 mL of water, 730 mL of ethanol, and 100 mL of 2-butoxyethanol. The results were then analysed using orientation imaging microscopy (OIM) software to obtain inverse pole figure (IPF) and phase quantification maps (see Figure II-3). This technique enables the differentiation of bainitic ferrite and austenite, as they have different crystallographic structures. However, the indexing of martensite was more challenging when using EBSD due to the low image quality (IQ) measured on this phase.

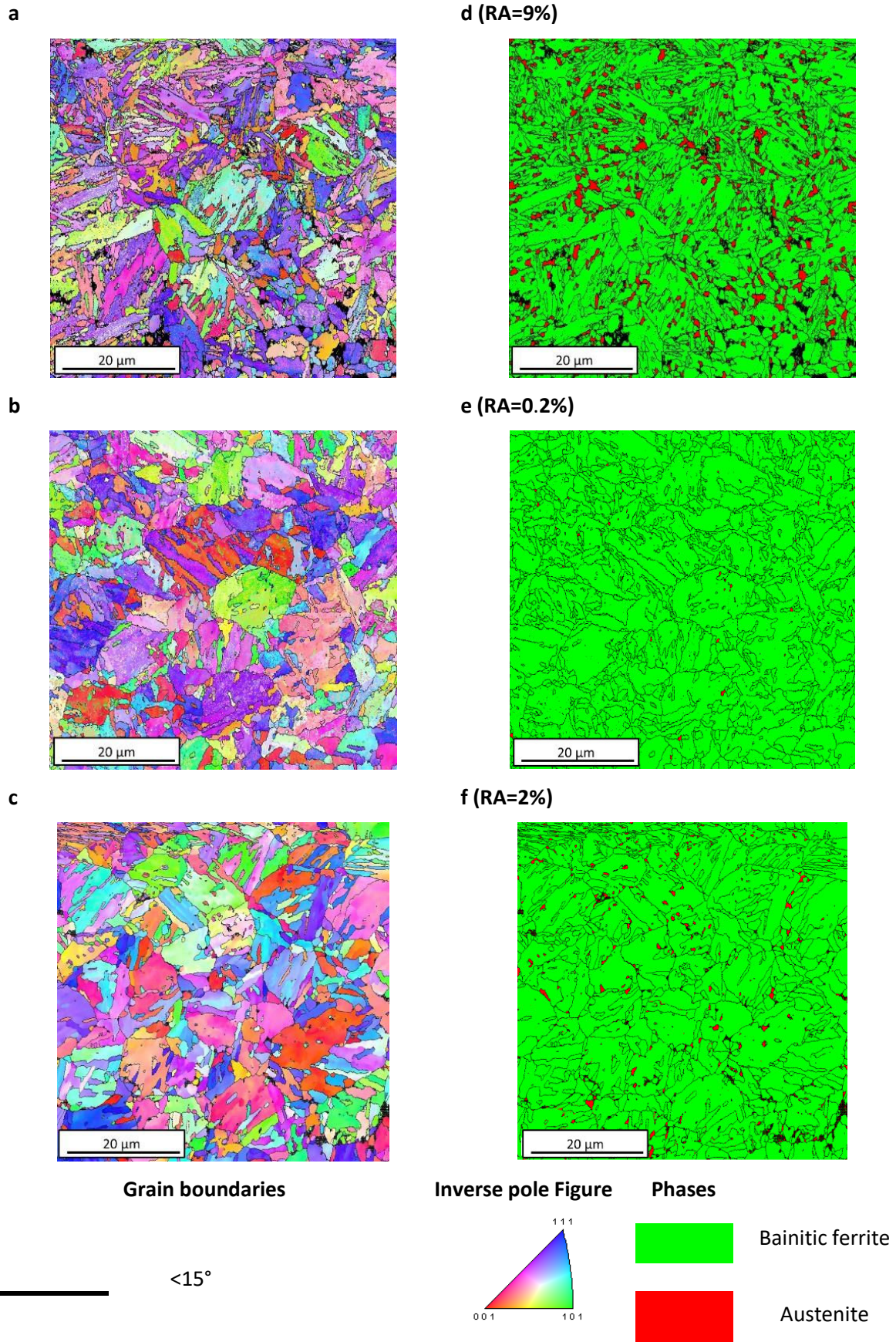


Figure II-3. Electron backscattered diffraction orientation maps (a, b, c) and phase distribution (d, e, f) on CP1, CP2, and CP3.

Based on the IPF maps of the normal direction presented in Figure II-3, bainitic sheaves can be observed in all samples, whereas lath structures cannot be directly identified, as they share fairly similar orientations. Nevertheless, the EBSD analysis confirms the percentages of RA for CP1, CP2, and CP3 obtained with OM measurements. Indeed, in Figure II-3 (e, f, g) a significant amount of austenite islands can be observed in CP1 (9%), with less in CP3 (2%) and an extremely small percentage in CP2 (0.2%). In contrast, the SEM results are more suitable for verifying the presence of RA laths, as such features are too thin to be indexed or identified with the other two methods.

d. Differentiation of bainites

Lower, granular, and upper bainites were identified using the method proposed by Zajac et al. [25], which is based on grain boundaries misorientation angles. Lower bainite is characterised by a significant amount of high misorientation angles (47–65°), upper bainite is defined by a higher amount of low misorientation angles (< 15°), and granular bainite exhibits a random orientation. Therefore, in Figure II-4, the number fraction of boundaries is represented as a function of their misorientation angles for CP1, CP2, and CP3. The results reveal four distinct peaks:

- Between 2° and 15°, which corresponds to the low misorientation angles characteristic of upper bainite.
- Approximately 45°, caused by the presence of RA.
- From 50° to 55°, which according to the EU report [28], is predominantly located at the prior austenite grain boundaries.
- Between 55° and 65°, which reflects LB.

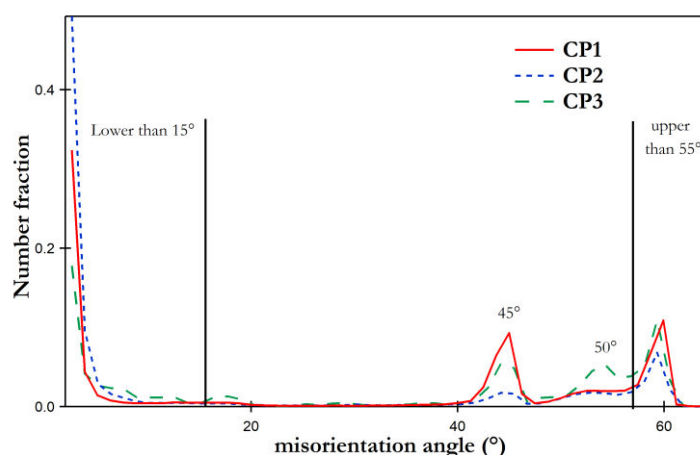


Figure II-4. Grain boundary misorientation angles measured by EBSD for CP1, CP2, and CP3.

The results reveal that CP1200 steels exhibit a combined microstructure composed of UB and LB due to the peaks detected below 15° and above 55°. However, the analysis does not allow for their

quantification, which requires microstructural observation. Moreover, the peak at 45° represents the interface between RA and bainitic ferrite. The evolution of the number fraction of this misorientation is in agreement with phase quantification previously obtained using OM images. In terms of RA CP1 presents the highest value and CP2 the lowest.

In the following section, the correlation between the amount of RA islands and misorientation angles is highlighted, as interfaces could be involved in the initiation of damage [5, 50, 51].

e. Orientation relationship between bainitic ferrite and RA

An increasing number of studies have noticed crystallographic orientation relationships during the transformation from prior austenite to bainite. The more commonly used models were developed by Bain, Nishiyama-Wassermann (NW), and Kurdjumov-Sachs (KS) [12, 35, 52, 53]. The crystallographic transformations of these models are displayed in Figure II-5.

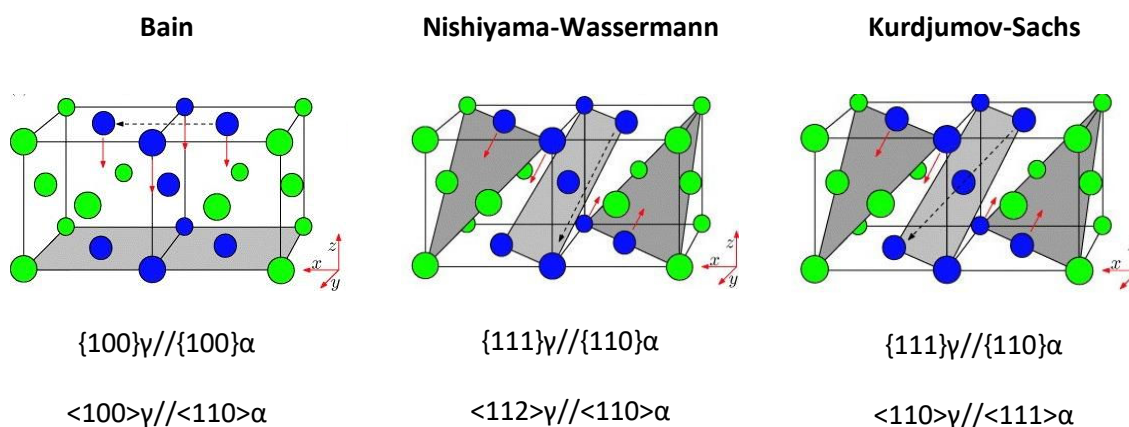


Figure II-5. Orientation relationship between prior austenite (FCC) and bainite (BCC) according to Bain (a), NW (b), and KS (c) models. Blue atoms represent BCC structure, whereas green atoms represent FCC structure [18].

The differences among these models are based on weak angle rotations and parallel plane variations between ferrite and austenite after transformation. These models are not applied in this thesis due to the complexity of determining their parameters with sufficient precision. However, a verification of the constant misorientation angle between bainite and RA due to the transformation of prior austenite into bainite was performed.

To assess misorientation relationship, the analysis was performed on CP1, as this sample presented the highest amount of austenite islands. Figure II-6 displays IPF maps of bainitic ferrite and

austenite in the same area. It can be observed that the austenitic islands contained in the same sheaves exhibit similar orientations (blue and green circles).

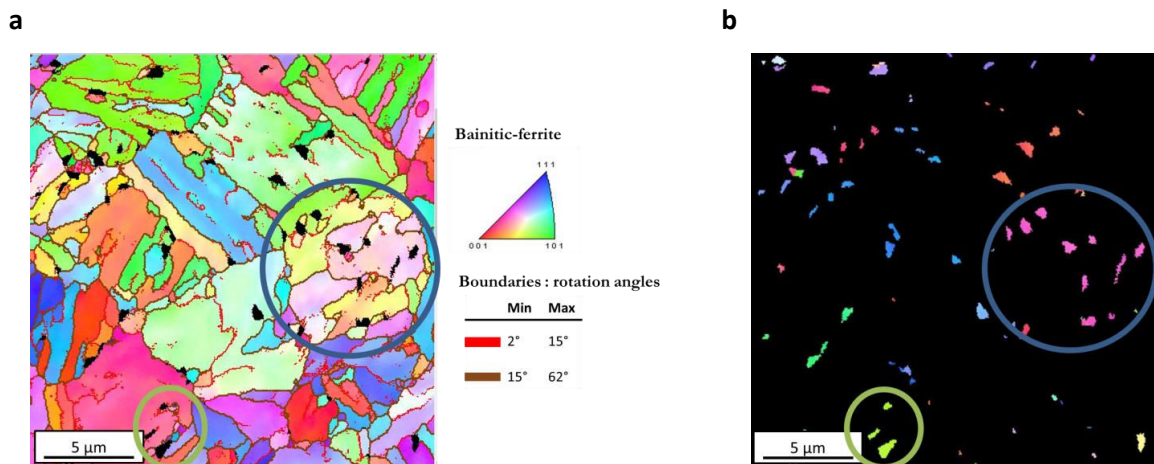


Figure II-6. Crystal orientation of bainitic ferrite (a) – two clusters of laths are highlighted (blue and green circles), crystal orientation of austenite (b) in the same area.

To estimate the misorientation angles between phases, orientation line profiles were presented in Figure II-7. The results denote a similar misorientation of approximately 45°, which that is in agreement with the previous results presented in Figure II-4.

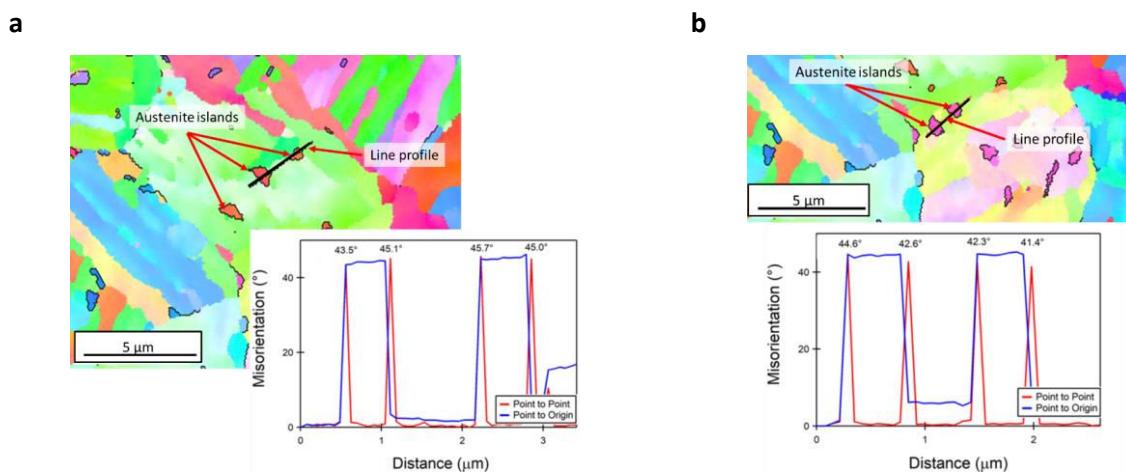


Figure II-7. Misorientation angle relationship between bainitic ferrite and austenite islands. Local misorientation angle on CP1 with the line profiles representation and misorientation.

For this section of this dissertation, the phases were characterised and quantified, and an orientation of 45° was observed between them. As seen in the first chapter, an increase in the strength of CP steel as a result of the reduction of the lath dimension, so, in order to complete microstructural characterisation, the bainitic lath size was estimated using two methods.

f. Measurement of bainitic lath size by EBSD and linear intercept method

An equation formulated by Langford and Cohen (9) was used to determine the impact of lath dimensions on mechanical properties [12, 54, 55]. The equation of the yield stress (σ_y) as a function of the effective grain size diameter (d) is as follows:

$$\sigma_y = \sigma_0 + k_y d^{-1} \quad (9)$$

Where σ_0 is the friction stress in the absence of grain boundaries and k_y is a constant.

However, since bainitic plates exhibit an anisotropic morphology, determining the grain diameter was not straightforward. In the work of Bhadeshia [17], d represents twice the thickness determined by the linear intercept method. The analysis was performed by measuring average thickness on random lines normal to the direction of the long edge of the plate. However, according to the EU report N°21245 [25], the equivalent grain size can also be measured by EBSD. This study found that only grain boundaries of up to 8° can influence mechanical properties. When estimating grain size, the low grain boundaries limit starts at 8° . Therefore, in this dissertation the lath sizes were estimated using the two methods discussed above. The methods were applied to CP1, CP2, and CP3, and the resulting lath diameter measurements are presented in Figure II-8.

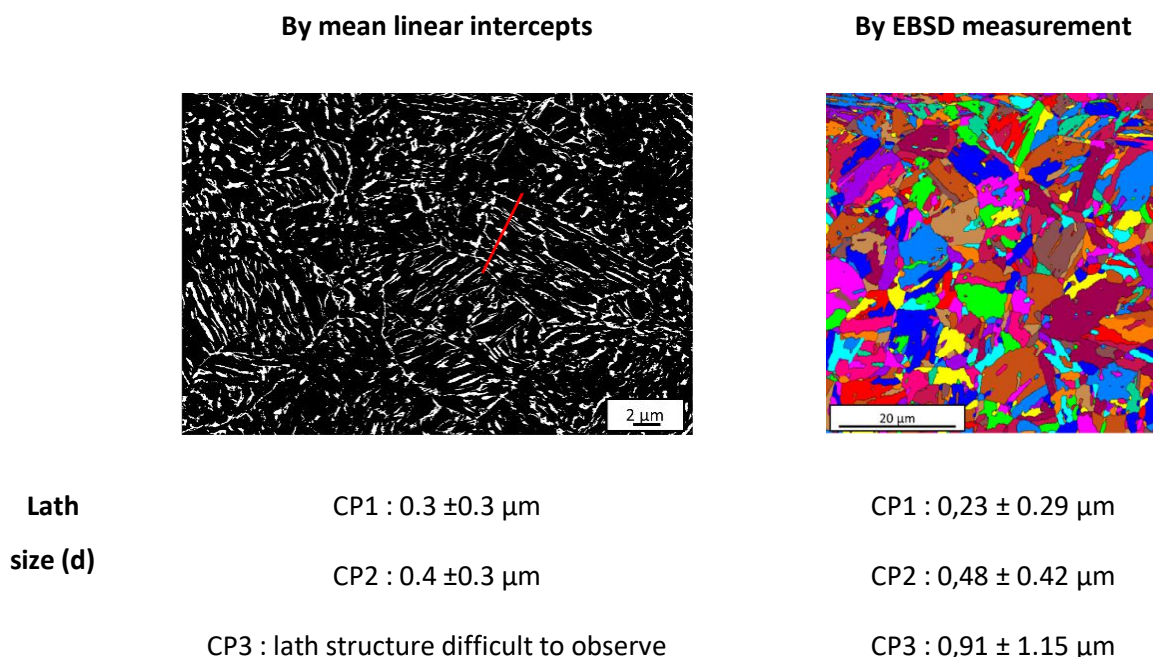


Figure II-8. Comparison of lath sizes between mean linear intercepts using SEM images and unique grain colour map obtained by EBSD measurement with grain boundaries $< 8^\circ$.

Similar values were obtained when applying these two methods, although there was a wide range of dispersion in the results. Based on these results, the lath sizes of the samples were ranked. The results are compared with the mechanical properties in the conclusion of this dissertation.

g. Complementary observation by TEM

Having general microstructure characterisation, it was possible to perform complementary TEM analysis³ to acquire information about initial structure of dislocations. All tests were carried out on a JEOL2010 electron microscope operating at 200 kV. To prepare each specimen, its thickness was initially reduced by mechanical polishing down to 100 μm . The specimen was then electropolished using a double-jet procedure with a 10% perchloric acid solution (at a temperature of -10°C and a voltage of 20 V).

Figure II-9 and Figure II-10 display the microstructures obtained for CP2 and CP1. These two samples respectively contain the lowest and the highest amounts of RA islands. Bainitic sheaves with thin lath structures can be observed in CP2. One lath is highlighted in red on the first picture of the Figure II-9. Moreover, a high amount of dislocations can be identified within the laths, which is the result of the plastic relaxation of austenite that occurs during the bainitic transformation (red circle in the second picture of the Figure II-9).

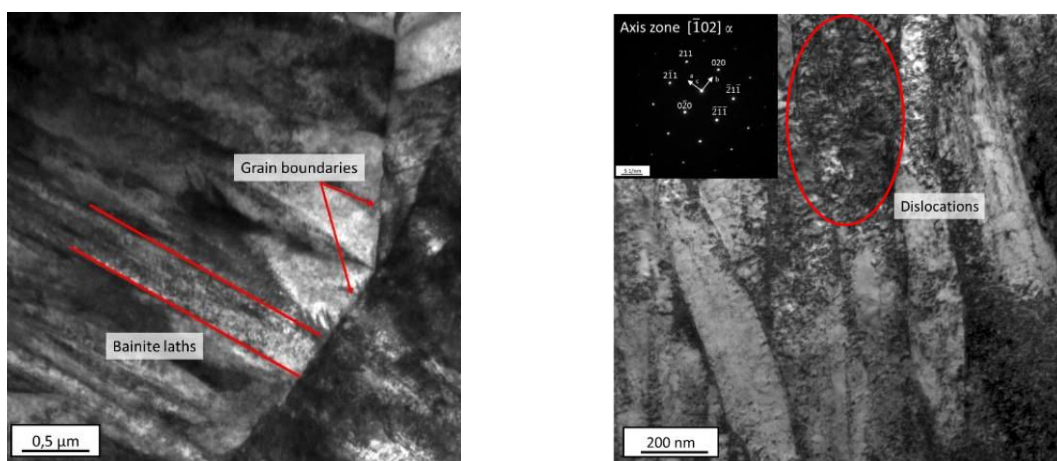


Figure II-9. Transmission electron microscopy images of CP2 showing the lath structure and a high dislocation density.

³ All tests were performed by Mayerling Martinez (An assistant professor at the University of Caen)

In CP1, a significant difference was observed with CP2 in terms of the presence of austenite islands, which were identified by electron diffraction (see Figure II-10). Further analysis of the diffraction pattern using the procedure described in Appendix A confirmed the similar crystallographic orientation of austenite islands within a bainitic sheaf (see Figure II-10).

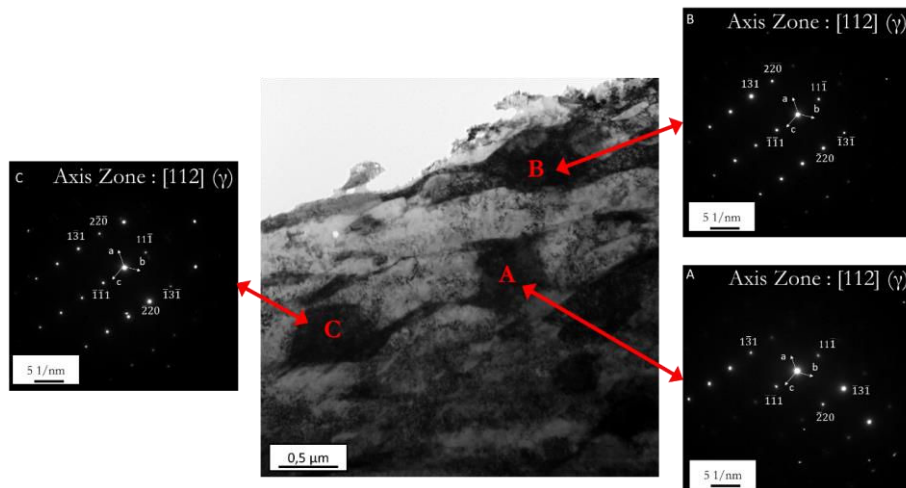


Figure II-10. Transmission electron microscopy observation of the initial microstructure of CP1. Austenite islands are labelled with the letters A, B, and C.

An initial microstructure characterisations for the three grades of CP1200 was performed. The results indicate a bainite lath structure with various dimensions and the presence of RA with different morphologies (both laths and islands). However, the chapter on the literature revealed that the microstructures of this type of steels are temperature sensitive. Therefore, the next section investigates the thermal stability of CP1200 microstructures.

2.2. Impact of temperature on the microstructure

DSC experiments were performed to acquire phase transformation temperatures. Thereafter, dilatometry analyses were conducted to confirm these temperatures.

A DSC analysis is a thermo-analytical method that measures the heat flow necessary to keep a specimen and the reference at the same temperature during a thermal programme. The DSC results displayed in Figure II-11 were obtained after continuous heating from room temperature up to 900°C at a rate of 10°C/min. The corresponding transition temperatures are presented in Table II-6.

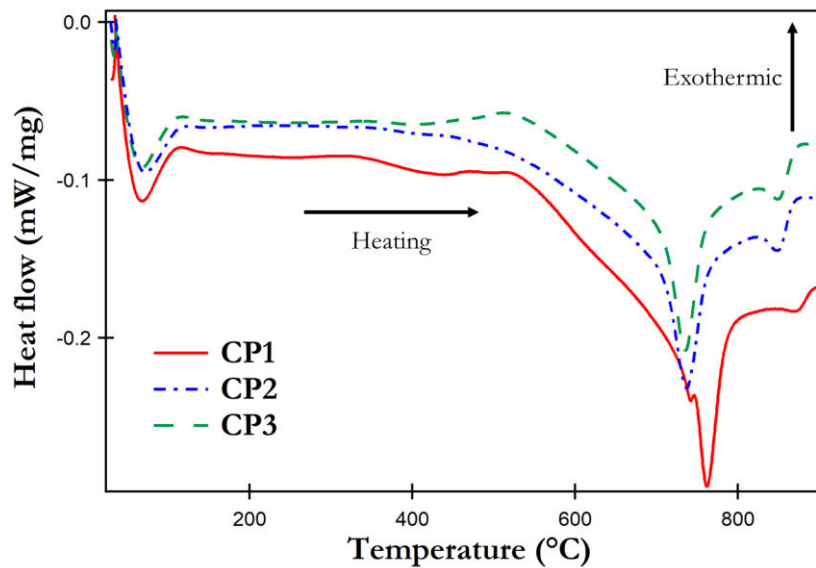


Figure II-11. Differential scanning calorimetry results during heating for CP1, CP2, and CP3.

Three different evolutions can be observed during heating. The first is a slight deviation from the baseline between 340°C and 580°C ($A_{S_{dec}}$). According to the literature [66–68], the decomposition of austenite (γ) into ferrite (α) and cementite (Fe_3C) occurs at these temperatures. This explains the more pronounced deviation in CP1, which had the highest amount of RA. The second peak starts between 680°C and 728°C achieving a maximum around 750°C (A_{C_1}). This transformation corresponds to the eutectoid temperature where the transformation of bainite (α_b) into austenite begins. The last peak, which occurs between 870°C and 895°C, represents the A_{C_3} transition, where the complete transformation of bainite into austenite occurs.

Table II-6. Temperature transitions measured by DSC (°C).

| | $A_{S_{dec}}$ | A_{C_1} | Peak ₁ | Peak ₂ | A_{C_3} |
|-----|---------------|-----------|-------------------|-------------------|-----------|
| CP1 | 338 | 728 | 761 | 870 | 895 |
| CP2 | 365 | 680 | 734 | 846 | 870 |
| CP3 | 364 | 690 | 735 | 845 | 872 |

$A_{S_{dec}}: \alpha_b + Fe_3C + \gamma \rightarrow \alpha_b + Fe_3C$
 $A_{C_1}: \alpha_b + Fe_3C \rightarrow \gamma + \alpha$
 $A_{C_3}: \gamma + \alpha \rightarrow \gamma$

In order to complete the phase transformation analysis and confirm its results during the heating process, dilatometry tests were performed. Only sample CP2 was chosen for this analysis, as

it is the grade currently used by Faurecia. In literature dilatometry experiments in bainitic steels can be found to determine the temperatures of phase transformations during cooling [66]. In this PhD it is phase transformation temperatures during heating which were reached.

Dilatometry tests measure the shrinkage or the expansion (see Equation (10)) of a material with the variations in temperature. Using this information, it is possible to identify phase transformation temperatures. A relationship between the volume variation change ($\Delta V = 3x\Delta L$) on the one hand and the initial width (L_0), the variation of temperature (ΔT), and the thermal expansion coefficient (α_d) in the other hand can be obtained:

$$\frac{\Delta L}{L_0} = \alpha_d \Delta T \quad (10)$$

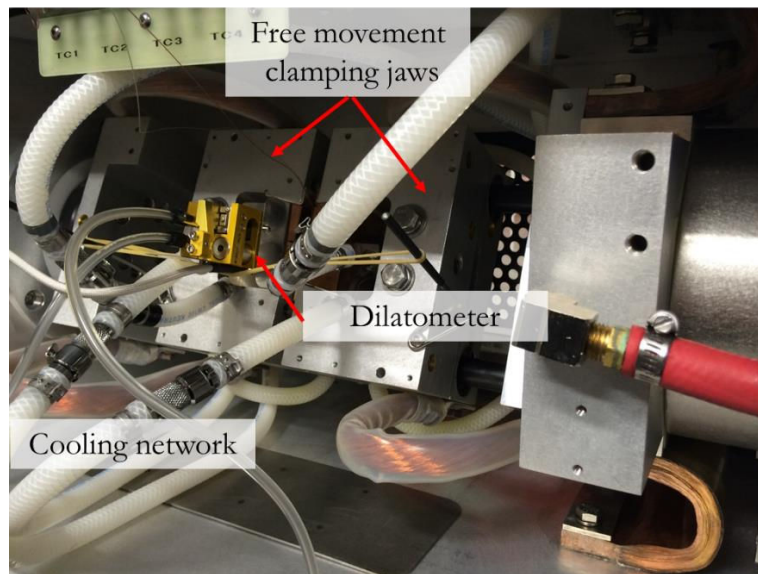
The thermal expansion coefficient depends on phases and can be added for multiphase metals following a cumulative law (11):

$$\alpha_d = \sum_1^i X_i \alpha_{di} \quad (11)$$

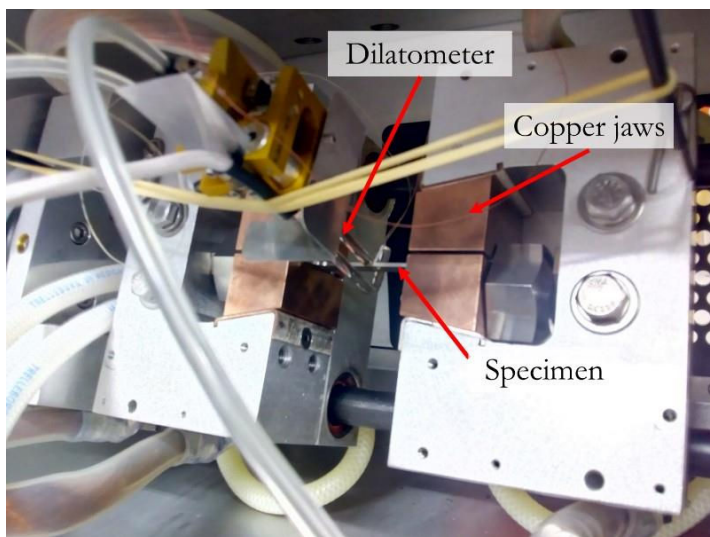
where X_i is the amount of the phase i and α_i is its thermal dilatation coefficient.

A Gleeble 3500-GTC thermal-mechanical physical simulation system was used to complete a dilatometry analysis (see Figure II-12-a and b). (Further information concerning the Gleeble device is provided in Appendix B.) This device provides the heat power by means of the Joule effect, which enables a precise control over the temperature used. Strain was measured using a C-gauge (see Figure II-12-c), which detects the width variation of the specimen with a precision of $0,4\mu\text{m}$. To control the temperature, a thermocouple K (Alumel-Chromel) was welded to the surface of a specimen. This thermocouple provided a standard error between 2.2% and 0.75% with a control of temperature at $\pm 1\%$. Specimens were heated at a rate of 10°C/s and cooled down by air quenching. Tests were performed on flat specimen with a thickness of 1.56 mm and a width of 10 mm.

a



b



c

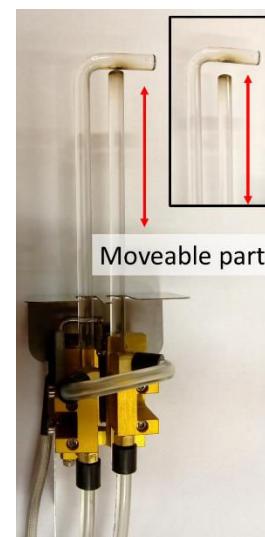


Figure II-12. Dilatometer installation in the Gleeble device: (a) setup of free moving clamping jaws on the furnace with the cooling system, (b) focus on the dilatometer installations on the specimen, and (c) dilatometer.

This method provides additional evidence supporting the impact of temperature on a steel's microstructure. Figure II-13 presents the dilatometry results, while Table II-7 presents related the acronyms related to transformation.

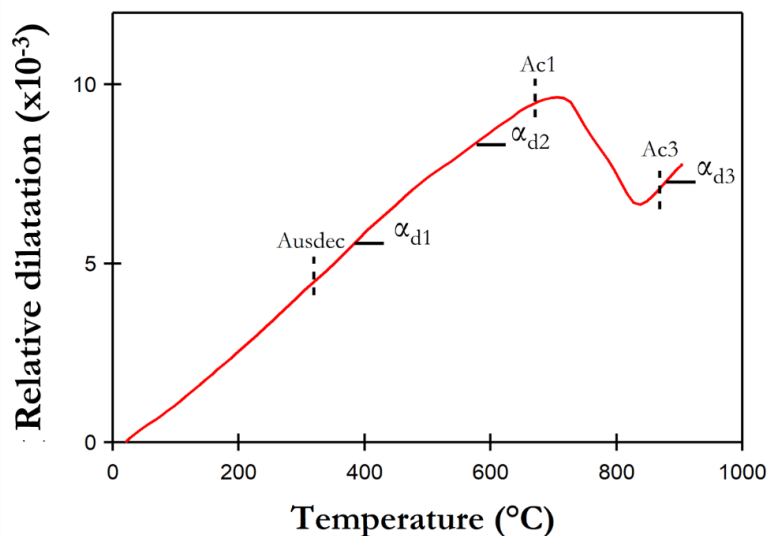


Figure II-13. Dilatometry curve of the heating of CP2 from room temperature to 900°C performed on CP2.

Table II-7. Temperature transitions obtained by dilatometry and DSC (°C).

| | Aus _{dec} | Ac ₁ | Ac ₃ |
|------------------------|--------------------|-----------------|-----------------|
| Transition temperature | 357 | 635 | 860 |
| Comparison with DSC | 365 | 690 | 872 |

Aus_{dec}: $\alpha_b + \text{Fe}_3\text{C} + \gamma \rightarrow \alpha_b + \text{Fe}_3\text{C}$
 Ac₁: $\alpha_b + \text{Fe}_3\text{C} \rightarrow \gamma + \alpha$
 Ac₃: $\gamma + \alpha \rightarrow \gamma$

Variations in temperature transitions can be noted between the DSC and dilatometry analyses. These variations can be explained by the differences between these devices in terms of the heating process and rate. These phase transformation temperatures were also determinate in the publications of De Moor et al. [69] on quench & Partitioning steels and Yang et al. [70] on bainitic steels by dilatometry and DSC methods. As for the results presented in this thesis, the decomposition of austenite is measured around 350°C/500°C in function of the steel grade. These publications highlighted different steps: the carbon segregation, the precipitation of carbides, the precipitation of retained austenite and the formation of cementite. However the results of these publications put forward the variation of transformation temperature with the heating rate and the initial heat treatment.

3. General mechanical properties

Initially quantifying mechanical properties with Vickers hardness (HV) measurements is straightforward. Tests were performed using a Clemex micro-hardness device, and the applied load was fixed at 1 kgf to go through hardening surface issued of the specimen preparation. Ten measurements were taken at a quarter of the thickness of the specimen set to 1.6 mm, to obtain the dispersion (see Table II-8).

Table II-8. Results of measuring the hardness of CP1200 steels.

| | CP1 | CP2 | CP3 |
|------------------------------|---------|---------|---------|
| Vickers hardness (HV) | 416 ± 9 | 402 ± 6 | 360 ± 7 |

These results indicate a difference in hardness that is higher between CP1 and CP3. Considering chemical elements, CP3 contains more Manganese than CP1 for the similar amount of carbon. Therefore higher hardness is expected. However it is possible to observe in CP1 a high amount of silicon. Silicon enhances the formation of austenite which in a certain amount leads to TRIP effect. This phase transformation during plasticity deformation could explain the higher hardness of CP1. To complete this discussion of the mechanical properties, the tensile properties of CP1200 steels at room temperature are displayed in Figure II-14. Ten tests (five in the transverse direction [TD] and five in the longitudinal direction [LD]) were carried out under a quasi-static regime at a constant strain rate of 10^{-3} s^{-1} . The strain was measured with an extensometer of 50 mm using digital image correlation (DIC). To perform this measurement, a black pattern on a white background was painted on the specimen. Then, using the Aramis software, the measurement of the relative movement between points in the pattern enabled the acquisition of local strain.

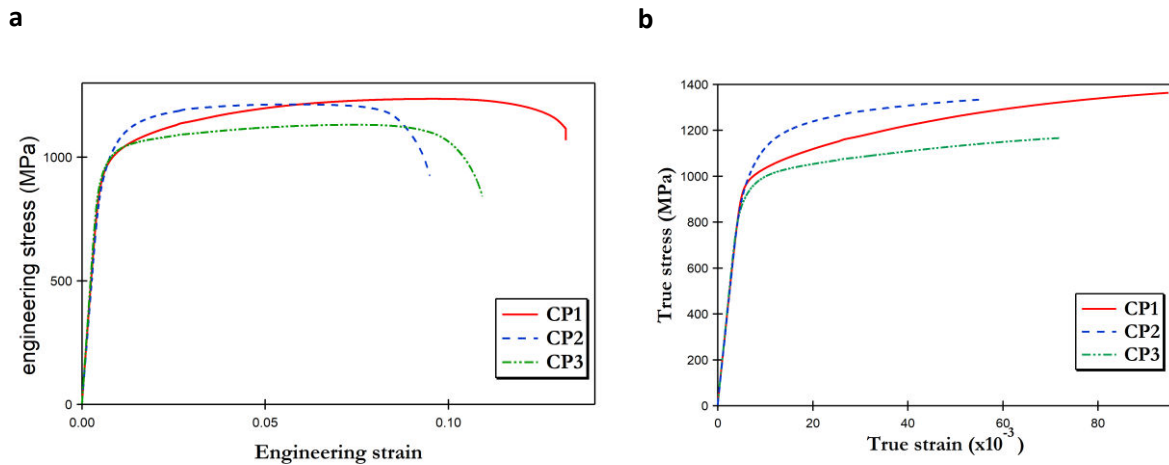


Figure II-14. Stress-strain curves obtained during tensile tests for three grades of CP provided by various suppliers: (a) engineering tensile curves, (b) true tensile curves.

Table II-9 presents results of the Young modulus (E), UTS, the yield stress at 0,2% of plastic strain ($\sigma_{0,2\%}$), the strain at the UTS (ϵ_{UTS}), the strain at the fracture (ϵ_f) and the necking coefficient (Z), which is expressed by Equation (12) with S_0 and S_f : the initial section and the final section:

$$Z = \left(\frac{S_0 - S_f}{S_0} \right) \times 100 \quad (12)$$

Table II-9. Tensile properties of CP1200 grades (all measurements were performed on a true curve, with the exception of the strain at the fracture).

| | | E (GPa) | UTS (MPa) | $\sigma_{0,2\%}$ (MPa) | ϵ_{UTS} | ϵ_f | Z (%) |
|------------|-----------|--------------|---------------|------------------------|-------------------|-------------------|------------|
| CP1 | <i>LD</i> | 200 ± 13 | 1384 ± 22 | 962 ± 6 | $0.09 \pm 0,01$ | $0.136 \pm 0,005$ | 46 ± 6 |
| | <i>TD</i> | 219 ± 1 | 1385 ± 2 | 977 ± 3 | $0.083 \pm 0,006$ | $0.133 \pm 0,003$ | 44 ± 6 |
| CP2 | <i>LD</i> | 196 ± 8 | 1309 ± 5 | 1022 ± 13 | $0.059 \pm 0,004$ | $0.061 \pm 0,001$ | 64 ± 1 |
| | <i>TD</i> | 201 ± 2 | 1294 ± 7 | 1010 ± 13 | $0.049 \pm 0,006$ | $0.060 \pm 0,003$ | 65 ± 2 |
| CP3 | <i>LD</i> | 196 ± 4 | 1161 ± 11 | 927 ± 12 | $0.075 \pm 0,009$ | $0.110 \pm 0,001$ | 62 ± 3 |
| | <i>TD</i> | 210 ± 4 | 1158 ± 8 | 921 ± 16 | $0.064 \pm 0,004$ | $0.08 \pm 0,01$ | 55 ± 4 |

The specimens can be classified as a function of the maximum strength and the strain at rupture: $CP1 > CP2 > CP3$, and $CP1 > CP3 > CP2$. Interestingly, Z does not follow the same evolution as

deformation, as CP1 presents the highest deformation but the lowest Z. Conversely, CP2 and CP3 present a high necking coefficient but the lowest deformation. This difference indicates a high reduction of the thickness during necking that is not detectable by the extensometer. Moreover, low differences were measured between the LD and TD.

Initial microstructural and mechanical characterisations of CP steels were completed. The important relationships existing between both features are discussed in the next section.

4. Synthesis of results and conclusions

In the previous chapter, the importance of metallurgical characterisation of CP steels was highlighted to explain mechanical properties of CP steels. To facilitate further discussion of these findings, key results presented in this chapter are summarised, some results of this chapter are summarised in Table II-10.

Table II-10. Synthesis of phase percentages measured for the three grades of CP1200.

| | UTS (MPa) | ϵ_f | RA (%) | | | Si (wt%) | Lath size (μm) |
|------------|--------------|---------------|-----------------|----------------------|------|----------|--------------------------------|
| | | | OM | SEM (morphology) | EBSD | | |
| CP1 | 1385 ± 14 | 0.131 ± 0,005 | 9 | 18 (laths + islands) | 9.1 | 1.4 | 0.2 ± 0.3 |
| CP2 | 1301 ± 10 | 0.083 ± 0,006 | Small amount | 15 (laths) | 0.2 | 0.91 | 0.5 ± 0.4 |
| CP3 | 1161 ± 8 | 0.105 ± 0,001 | 2 | 11 (laths + islands) | 2 | 0.84 | 1 ± 1 |

These results make it possible to draw the following conclusions:

- A wide range of mechanical properties can be observed under the designation CP1200. In the three grades studied, 200 MPa on the UTS and a variation of 0.05 on the total deformation were measured between extremum values. These differences can be explained with reference to differences among microstructures.

- All grades revealed the presence of austenite presented in two different morphologies: islands and laths. This austenite is developed thanks to the presence of silicon, which delays the formation of cementite. However, the presence of austenite does not ensure the ductility of the material. Indeed, it has been argued that island structures are more beneficial in terms of ductility, and this observation is confirmed by our experiments.
- Analysis of misorientation angles using EBSD reveals two types of bainite (upper and lower). The methods used in this research made it possible to identify, but not quantify, the bainite found. However, based on the angle misorientation investigation, it is possible to note the existence of an angle of 45° between bainitic ferrite and austenite, these angles could serve as barriers to dislocation and could be the initiation of damage.
- Finally, measuring lath sizes confirmed their strengthening effect. Indeed, the UTS rankings (CP1 < CP2 < CP3) are inverted when considering lath sizes (CP3 < CP2 < CP1).

Aspects of the thermal stability of CP1200 were studied by DSC and dilatometry analyses. Three different microstructural modifications during heating from room temperature to 900°C can be noted. First, the decomposition of RA into ferrite and cementite is measured. Thereafter, the phase transformation of bainitic ferrite and cementite into austenite occurs, and the microstructure becomes then fully austenitic (see Figure II-15). These results are in accordance with the publications on bainitic steels tempering. [29, 43, 59, 60]

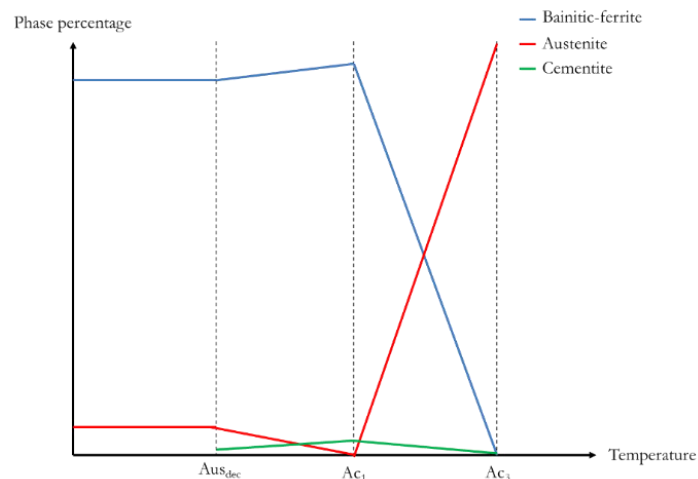


Figure II-15. Schematic representation of phase transformation during heating.

A complete characterisation of the initial microstructure was performed in this chapter. The motivation for the following chapter was to obtain more details concerning the impact of this thin and multiphase microstructure on plasticity mechanisms.

Chapter III. Cyclic plasticity mechanisms of CP1200 steels and impact of thermomechanical loading

In Chapter II, three different grades of CP were studied to investigate differences in the microstructural features and mechanical properties of the steels provided by different suppliers. This chapter focuses on the results obtained for CP2 steel, which is the grade currently used by Faurecia. Therefore, a summary of the characteristics of CP2 steel, as determined at room temperature in Chapter II, is presented in Table III-1.

Table III-1. Summary of the mechanical properties and microstructural characteristics of CP2 characterised at room temperature.

| UTS (MPa) | $\sigma_{0.2\%}$ (MPa) | ϵ_f | Medium lath size (μm) | RA island percentage (%) |
|---------------|------------------------|-------------------|------------------------------------|--------------------------|
| 1301 \pm 10 | 1016 \pm 13 | 0.083 \pm 0,006 | 0.48 \pm 0,42 | 0.2 |

In order to investigate plasticity mechanisms, cyclic tension-compression experiments were performed. These tests provided further information concerning the impact of the initial microstructure, which exhibits a high density of dislocations during the evolution of cyclic softening as a result of the presence of obstacles to dislocation motion. The quantification of the isotropic and kinematic hardening components was performed, as the investigation of Masing behaviour, which results from the formation of dislocation arrangements. In the second section of this chapter, the impact of temperature on mechanical properties is investigated and the relation between microstructural evolution and strength properties is discussed.

1. Cyclic plasticity mechanisms of CP1200 steels: bibliography

To support the results presented in this chapter, theories on cyclic plasticity mechanisms are first investigated. To begin with, an overview of dislocation motion in BCC crystals is presented.

Thereafter, cyclic softening and hardening are analysed, with relevant findings from the literature concerning bainitic steels being presented. Finally, isotropic and kinematic hardening components are investigated, and this chapter concludes with a discussion of the Masing behaviour.

1.1. Internal stress and dislocation behaviour

At room temperature, plasticity is driven by the dislocation glide. Dislocations are linear defects characterised by a Burgers vector (defined by the magnitude and slip direction of the vector) that move in slip planes [71]. With regard to slip systems in BCC crystal, three planes from $\{110\}$ and $\{112\}$ and six from $\{123\}$ contain the $\langle 111 \rangle$ close-packed direction. These connections enable the dislocations to easily slip in different planes as a function of the applied stress. Therefore, the increase in movement possibilities multiplies the probability of dislocation interactions and promotes plasticity. However, various obstacles can disturb dislocation glide. Such obstacles include incoherent precipitates, grain boundaries, and dense dislocation structures (cells, walls), which are characteristic of long-range interactions. Short-range interactions can also influence dislocation motion through coherent precipitates, Peierls valleys – a force due to the friction of the crystal network in opposition to the slip of dislocations – and forests of dislocations, which represent the tangles of non-parallel dislocations. All of these interactions directly contribute to the increase of shear stress (τ) as highlighted in Figure III-1. Long-range interactions generate microscopic internal stresses (τ_x) and short-range interactions produce effective stresses (τ_{eff}). In order to measure these interactions at the macroscopic scale, cyclic solicitations can be performed. In this case, the internal stress is represented in the kinematic component of hardening (X) and the effective stress in the isotropic part (R) [43].

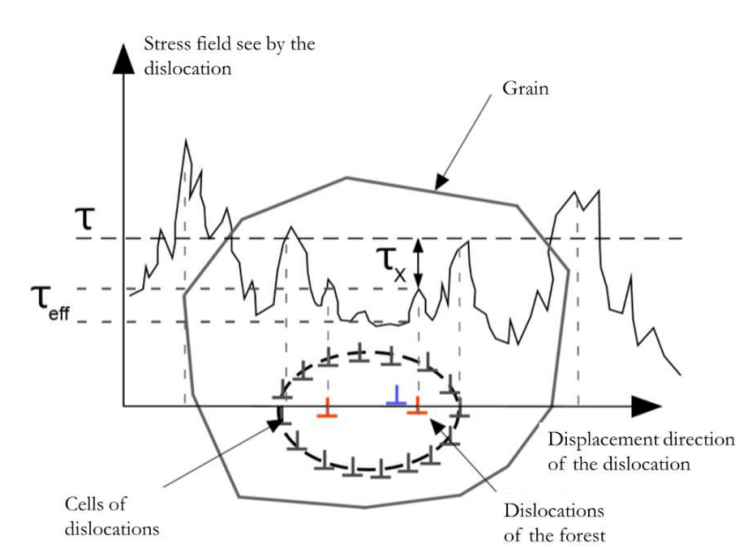


Figure III-1. Schematic representation of interactions between dislocation and obstacles related to effective and internal stresses [72].

From a mechanical point of view, the kinematic and isotropic components of hardening influence the stress transition between elastoplasticity and plasticity mechanisms in all loading directions and are represented by the yield surface (f). The presence of isotropic hardening with the scalar R modifies the radius of the surface (see Figure I-15-a). For kinematic hardening, the tensor \bar{X} , which is indicative of kinematic hardening, shifts the elastic domain (see Figure I-15-b).

For CP steels, the hypothesis of isotropic material with an anisotropic hardening is adopted due to the significant presence of a kinematic component of hardening, as reported in literature on multiphase steels [39, 41]. Thus, in this dissertation, the combined hardening with the non-linear kinematic and isotropic components of hardening is considered using the model developed by Lemaitre and Chaboche. Following this model, the yield stress can be expressed by R and X in Equation (13), which respectively verify Equations (14) and (15). In these expressions, Q represents the stress saturation and b_{LC} the rate of saturation of isotropic hardening, p is the cumulative plastic strain, C_{LC} and γ_{LC} are two constants of the kinematic hardening.

$$f = f(\bar{\sigma}, \bar{X}, R) = F(\bar{\sigma} - \bar{X}) - R = 0 \quad (13)$$

$$dR = b_{LC}(Q - R)dp \quad (14)$$

$$d\bar{X} = \frac{2}{3}C_{LC}d\bar{\varepsilon}_p - \gamma_{LC}\bar{X}dp \quad (15)$$

These components of hardening can be measured by alternating mechanical tests such as tensile tests, shear tests, or bending-unbending tests [40, 61–63]. In the literature, DP or TRIP steels have been frequently investigated under tension-compression loading [39, 64] by quantifying of the Bauschinger effect. This effect is characterised by the stress softening observed during compression, which results from kinematic hardening. Bauschinger effect is a consequence of the elastic micro-stresses present inside a polycrystal after unloading [42]. This phenomenon has been explored in DP steels in the work of Zhonghua and Haicheng [46]. Using experimental and numerical experiments, they estimated the variation in internal stresses between the soft phase (ferrite) and the hard phase (martensite) [41, 65, 66]. The authors concluded that a significant difference in hardness creates different internal stresses within phases, which lead to premature plasticity in compression. For CP steels, the phase contrast is less present due to the presence of a significant amount of bainite, which has a medium hardness compared to ferrite and martensite. However, the thin lath structure induces

high barriers to dislocation glide and a high amount of interfaces, which could lead to the development of internal stresses.

1.2. Cyclic stress softening and hardening of bainitic steels

Based on alternating tensile tests, complementary results regarding dislocation motion can be obtained when studying cyclic softening and hardening. Softening and hardening are respectively defined as the reduction and the increase of stress during cyclic loading (see Figure III-2).

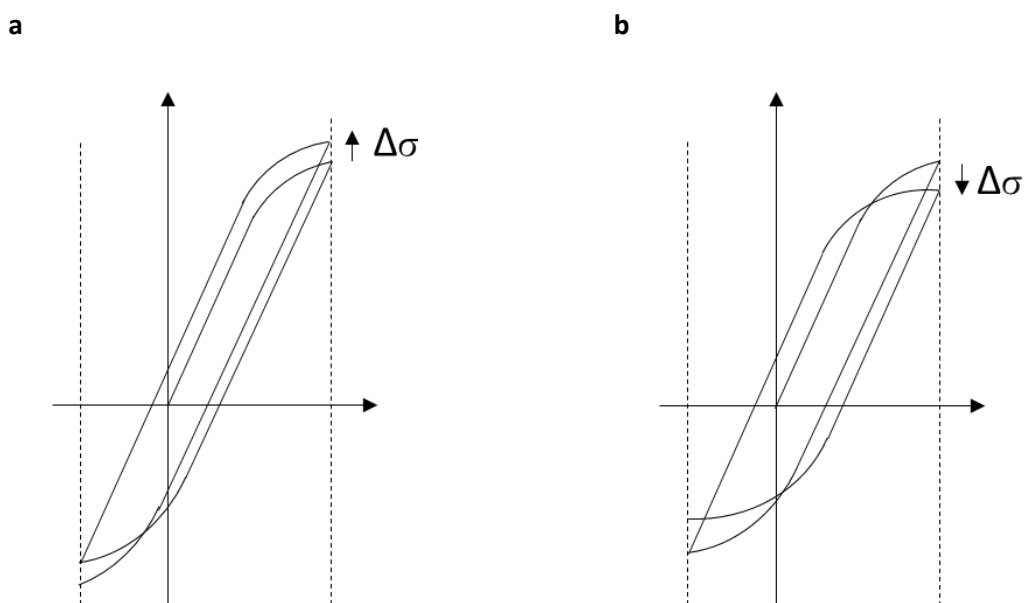


Figure III-2. Schematic representation of cyclic (a) hardening and (b) softening.

Q. Zhou et al. [79] and T. B. Hilditch et al. [80] proposed an explanation of cyclic hardening and softening in DP steels and TRIP steels that is based on dislocation motion. For these steels, at a low number of cycles, dislocations become entangled and immobile, which contributes to cyclic hardening. Hence, cyclic saturation is measured first, followed by cyclic softening. This stress decrease results from the annihilation of dislocations and the formation of low-energy structures such as dislocation cells. For bainitic steels, a fine microstructure with a high amount of dislocations is initially exhibited. This microstructure limits the mean free path, meaning the average distance between a dislocation and a particle, which in turn promotes multiple and/or cross-slipping of dislocations. Therefore, the slip systems that enhance dislocation annihilation can be observed even at a low number of cycles. These features produce softening. Figure III-3 extracted from the publication of Long et al. exhibits the cyclic stress softening of bainitic steels during low-cycle fatigue tests. A variation of cyclic saturation is

observable as a function of the strain amplitude. At 1% of strain amplitude, the cyclic softening is observable at a low number of cycles while at 0.6% the saturation is present until the break of the specimen.

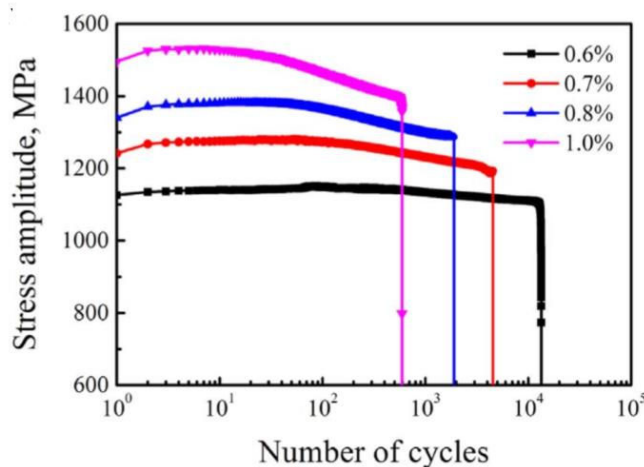


Figure III-3. Evolution of stress amplitude as function of the number of cycles during low-cycle fatigue experiments at various strain amplitude [81].

1.3. Presentation of the Masing behaviour

Masing behaviour enables the identification of relations between dislocation arrangements and the stress applied during cyclic loading. In fact, if a metal satisfies the Masing law, this implies that the same dislocation arrangement is conserved during the entire test. This behaviour can be estimated with an incremental cyclic test that consists of applying cycles of various strain amplitudes to a single specimen. Hence, stabilised cyclic curves are shifted such that the minimum of all curves coincides to 0MPa. If there is a superposition of the loading parts of the cyclic curves as observed in Figure III-4, the material obeys the Masing law. The Masing behaviour can be linked to dislocation structures: if the Masing behaviour is obeyed similar dislocation arrangements are present for the strain amplitudes concerned, if the Masing behaviour is not obeyed different dislocation structures are formed.

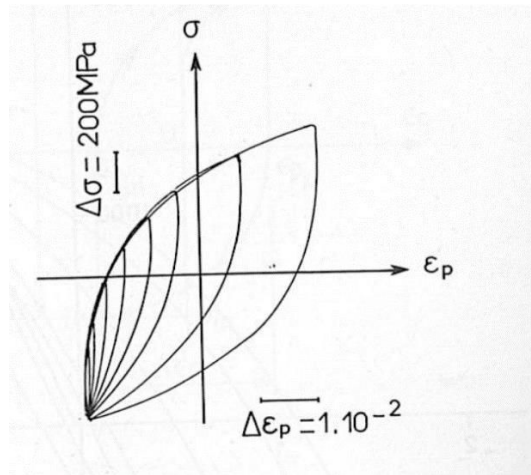


Figure III-4. Validation of Masing behaviour observed in TA6V [42].

Watanabe et al. [82] investigated the non-respect of the Masing behaviour of various materials, including bainitic steels. This study identified different dislocation structures as a function of plastic strain amplitude: no dislocation arrangement, dislocation structures consisting of loop patches and cells. The cyclic stress-strain curves under stress control obtained of this publication are exhibited in Figure III-5. According to the Masing behaviour, these results reveal different stages on dislocation arrangement. Between 202 MPa and 226 MPa and then between 251 MPa and 260 MPa the Masing law is obeyed.

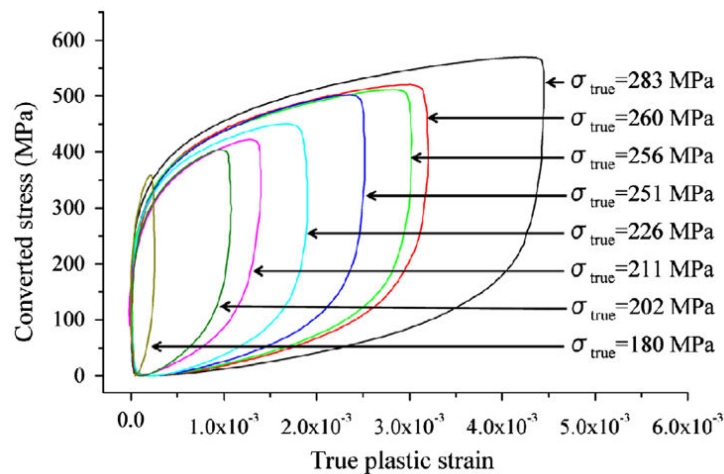


Figure III-5. Stress-strain cyclic curves under stress ratio of R=-1 [82].

TEM pictures were extracted from the work of Watanabe et al. and revealed loop-patch dislocation structures from 180 MPa to 251 MPa of stress amplitudes. Between 251 MPa and 260 MPa

the formation of dislocation structure occurred from 0% to 100% cell structure as it is observable in Figure III-6. The respect of the Masing law was then led to the formation of dislocation cells.

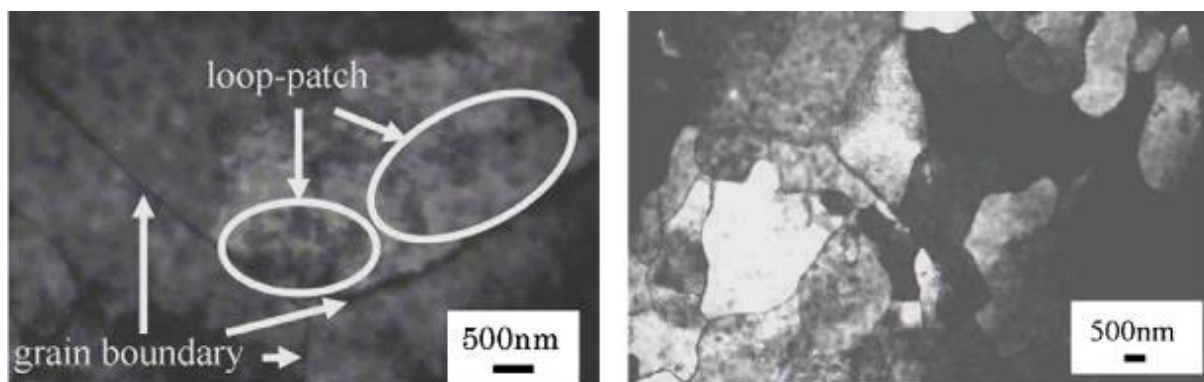


Figure III-6. TEM images showing dislocation arrangements of cyclic test under stress ratio $R=-1$ (a) at a stress amplitude of 251 MPa and (b) 260 MPa [82].

Shih and al. [83] also observed the same evolution of dislocation arrangements on interstitial-free (IF) steel. This grade of steel is ferritic, which enables an easier identification of dislocation structures (see Figure III-7). This work revealed a modification of dislocation structure as a function of strain amplitude. At low strain no dislocation structure is observable, then the formation of loop-patches occurs and at higher strain the formation of cells can be noticed.

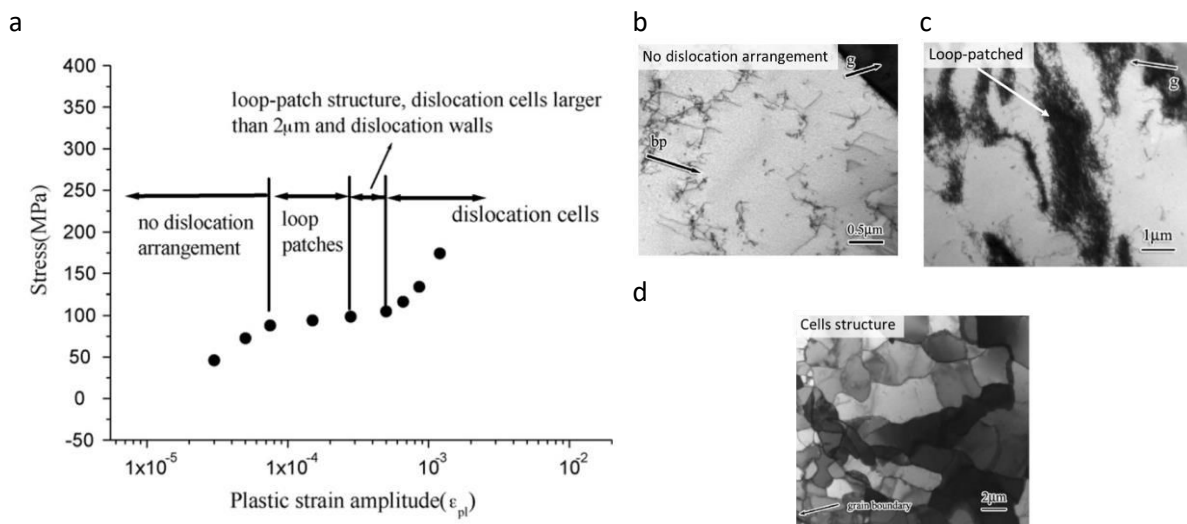


Figure III-7. (a) Evolution of dislocation structures as a function of plastic strain amplitude during alternated tensile tests on IF steels, (b) image without dislocation arrangement, (c) picture of loop patch structures, and (d) picture of dislocation cells [83].

The present dissertation investigates the evolution of the cyclic softening, hardening components and Masing behaviour as functions of strain amplitude and relate them to dislocation arrangements of CP2.

2. Experimental technique: Presentation of the anti-buckling device

Tension/compression tests were performed⁴ on flat specimens using MTS servo-hydraulic fatigue machine with a cyclic strain ratio of -1. Unfortunately, for flat specimens, it was not possible to reach sufficient compression stress without encountering the problem of buckling. Thus, an estimation of the theoretical limit compression stress for our specimen geometry was determined using the Euler equation was applied to a particular configuration where the maintaining borders of the specimen were embedded (see Equation (16)). This critical force is dependent on the Young modulus (E), the moment of area for a rectangular section ($I_{Gz} = \frac{e \cdot L}{12} (e^2 + L^2)$), the length of buckling (l), the thickness (e), and the width (L) of the specimen. According to this equation, the buckling starts at a stress of -58 MPa:

$$F_c = \frac{\pi^2 E I_{Gz}}{0.5l^2} \quad (16)$$

To increase the compression capacity in this experiment, two solutions can be considered. First, the specimen geometry can be modified. However, in this case, the range of possibilities was constrained by the thickness of the metal sheet. The second solution, which was adopted in this project is to physically prevent the buckling using an external device (see Figure III-9). Therefore, measurements were taken using custom-built anti-buckling devices inspired by the work of Yoshida et al., Silvestre et al., Schayes and Härtel [44,74,84–89]. This setup was constituted of four parts (two top and two bottom parts). The right-hand and left-hand parts were held together with screws. A vertical guide rod that allowed the clamping device to slide joined the bottom and top parts. In the front of the device, an aperture was included to measure strain using a ceramic extensometer, which was fixed in place by two indents made at the surface of the specimen. The machining of these indents inevitably led to a premature failure, which hindered drawing conclusions regarding cyclic fractures. Another disadvantage of the presence of such a device was the friction created on the lateral faces of the specimen even with the lubrication of the device with grease. In order to evaluate the friction created

⁴ All cyclic experiments were performed in collaboration with Dr Clément Keller (Group of Physics of Materials of Rouen (GPM))

by the anti-buckling device, cyclic tests were carried out on a fractured specimen. A constant force of 0.2 kN was found (see Figure III-8), which means that the friction is negligible compared to the load measured during the cyclic tests (maximum load 24kN).

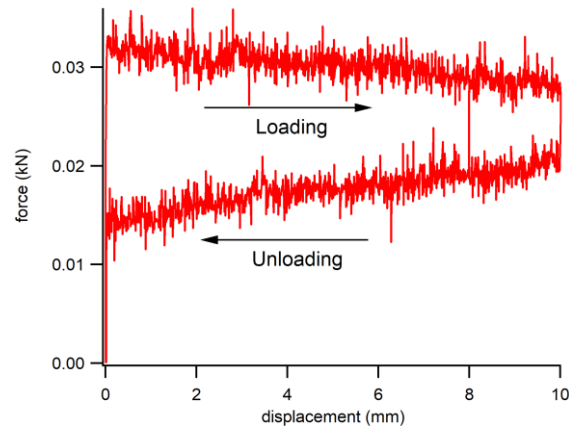


Figure III-8. Friction force measured during cyclic tests on a broken specimen.

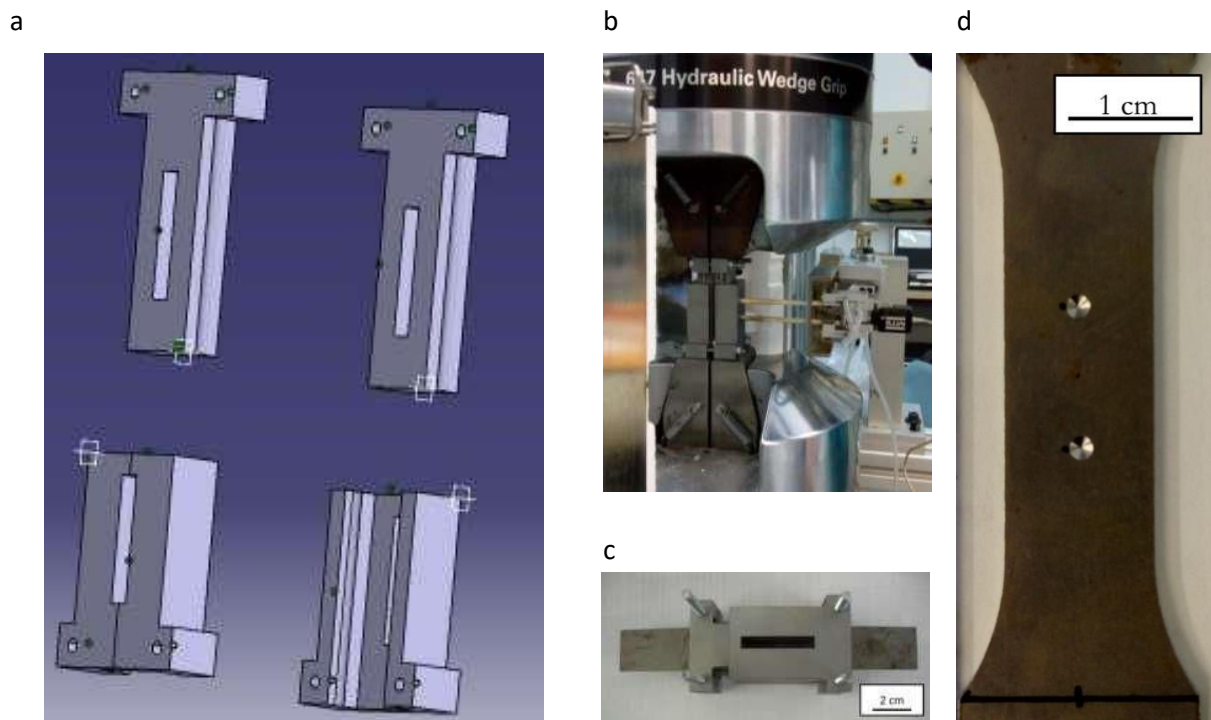


Figure III-9. Presentation of the clamping device: (a) three-dimensional (3D) representation drawn using the computer-aided design (CAD) software Catia v5, (b) positioning of the device on the tensile machine, (c) setup of the device on a specimen, and (d) indents at the surface of the specimen.

Unfortunately, buckling was not completely avoided by the clamping device and its occurrence was not always repeatable. However, the results seem relevant as no significant are observed on cyclic

curves as it is possible to see in cyclic strain-stress curves represented in Figure III-10. Some limits and improvements could be made, such as the implementation of the control of screws tightening. Moreover, even if the clamping device slipped with deformation of the specimen, some parts of the specimen were not clamped at high deformation. Thus, the clamping device had to cover the entirety of the specimen during the test, as was the case in the study conducted by Härtel et al. [74].

3. Investigation of cyclic softening of CP1200 steels

With the help of the clamping device, the alternated cyclic curves were obtained by the method of incremental tests. As is shown in Figure III-10, cycles with an increasing level of strain amplitude were applied to a single specimen. The results were acquired with three specimens (t1, t2 and t3), where sufficient cycles were reached without a sensitive buckling. The first and second tests were performed with a similar strain amplitude programme to verify the repeatability of measurements, whereas the third was performed with higher levels of strain amplitudes. More details on the programme characteristics can be found in Appendix C.

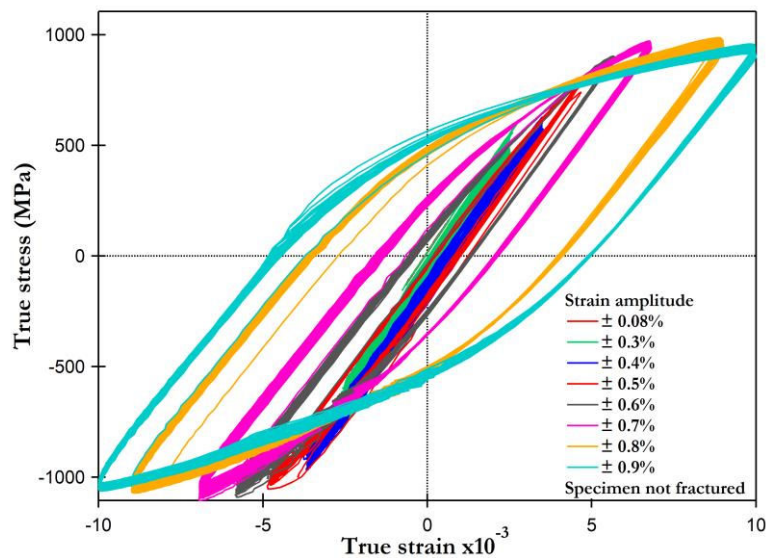


Figure III-10. Cyclic tensile and compression curves obtained with the incremental test method performed on CP2 at strain amplitudes of $\pm 0.08\%$, $\pm 0.3\%$, $\pm 0.4\%$, $\pm 0.5\%$, $\pm 0.6\%$, $\pm 0.7\%$, $\pm 0.8\%$ and $\pm 0.9\%$.

In order to observe cyclic hardening or softening, the cyclic stress-strain curve (CSSC) is displayed in Figure III-11. To evaluate these results, the stress amplitude of saturated cycles for each

level has to be represented as a function of the strain amplitude. However, for these experiments, even after 100 cycles per level, cyclic saturation was not observed after $\pm 0.4\%$. Therefore, the values of the last cycle for each strain amplitude were taken into consideration. The number of cycles was fixed at 100 cycles to not damage the specimen already weakened by the indents. Figure III-11 presents a comparison of the CSSC with the monotonous tensile curves.

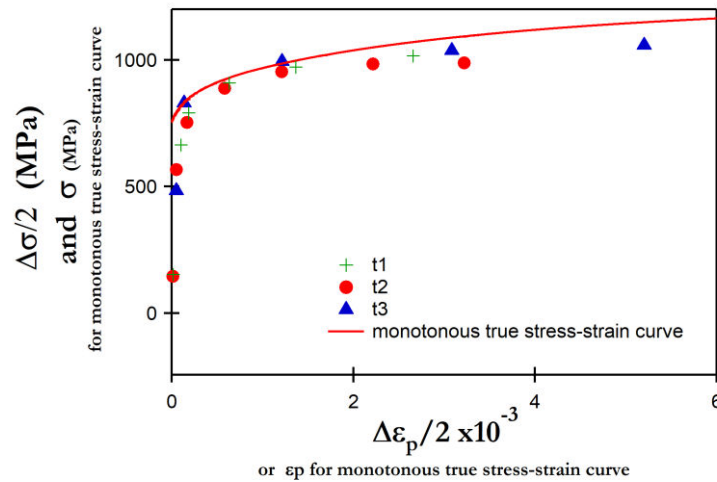


Figure III-11. Representation of the CSSC after alternating tests.

The CSSC values reveal lower stresses than the tensile curves (see Figure III-11). Therefore, the CP2 steel exhibits cyclic softening. To interpolate the CSSC curve the following equation was used according to the work of Lemaitre and Chaboche [42]:

$$\Delta \epsilon_p = \left(\frac{\Delta \sigma}{K_c} \right)^{M_c} \quad (17)$$

Where K_c represents the plastic resistance coefficient, M_c the hardening exponent, $\Delta \sigma$ the cyclic stress amplitude and $\Delta \epsilon_p$ the plastic strain amplitude. To determine the coefficients, the logarithm function is applied to transform the equation into its linear form (see Equation (18) and Figure III-12):

$$\Delta \epsilon_p = \left(\frac{\Delta \sigma}{K_c} \right)^{M_c} \rightarrow \ln(\Delta \epsilon_p) = M_c \ln(\Delta \sigma) - M_c \ln(K_c) \quad (18)$$

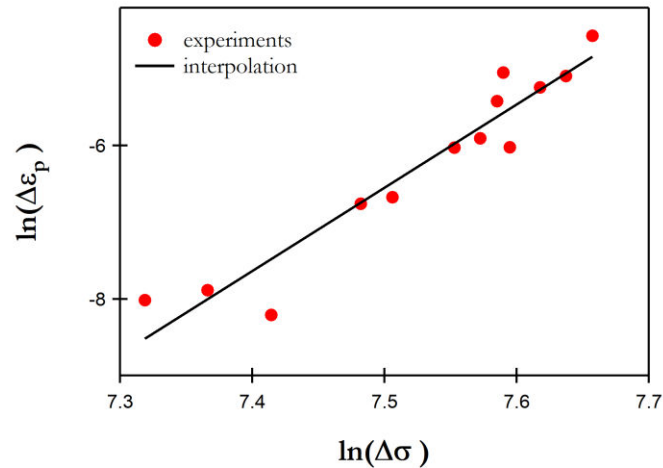


Figure III-12. Linear interpolation of logarithmic equation of CSSC.

The results obtained from interpolating the CSSC are $M_c = 10.9$ and $K_c = 3207$ MPa. To complete the analysis, the evolution of cyclic stress amplitude is displayed as a function of the number of cycles for all cycles (see Figure III-13).

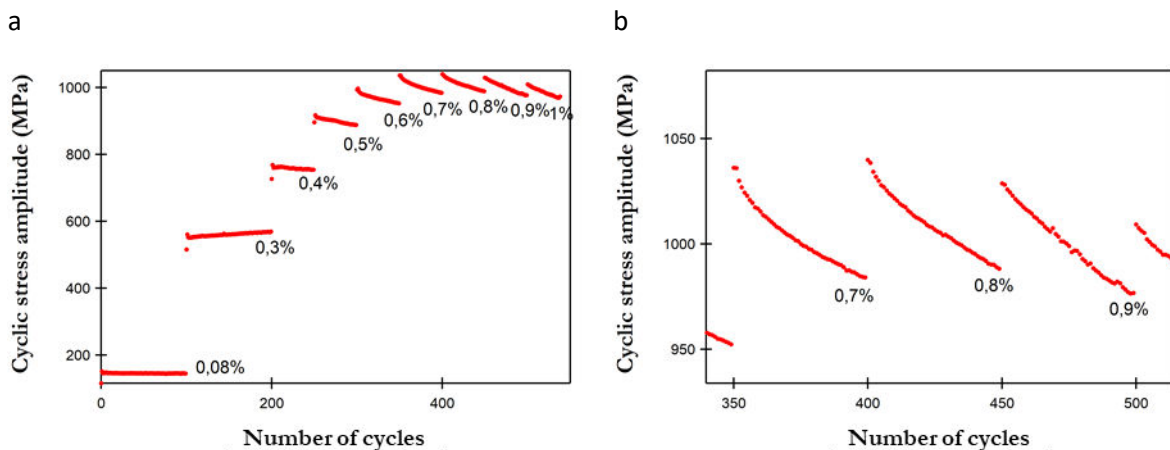


Figure III-13. Determination and observation of cyclic softening: (a) evolution of the cyclic stress amplitude during incremental tests and (b) magnification of the reduction of stress to observe cyclic softening (test t2).

For cyclic strain amplitudes between $\pm 0.08\%$ and $\pm 0.3\%$, a slight increase in cyclic stress amplitude is noticeable. However, after $\pm 0.4\%$, cyclic softening occurs during the first cycles. These results correlate favourably with those of the work of Yoshida et al. [84] described in Section III.1.1.c. At a low number of cycles, dislocations are tangled and immobile, leading to the hardening of the material. Nevertheless, in bainitic steel, a high amount of dislocations was observed. Thus, their interactions rapidly enhance their annihilation and the formation of dislocation arrangements, which promotes the

softening of the steel. However, the literature indicates a dependence of cyclic hardening and softening on strain amplitude [67, 68] thus, more conditions have to be tested to verify these results.

4. Masing behaviour

The investigation into cyclic softening reveals the impact of the high density of dislocations and arrangement with cyclic strain amplitude. In order to confirm this finding, the Masing behaviour was investigated using incremental tests. To perform the analysis, true plastic strain and stress were calculated, and the loading elastic domains were aligned for all cycles. All minimum curve values were then coincided to normalise the cyclic curves (see Figure III-14).

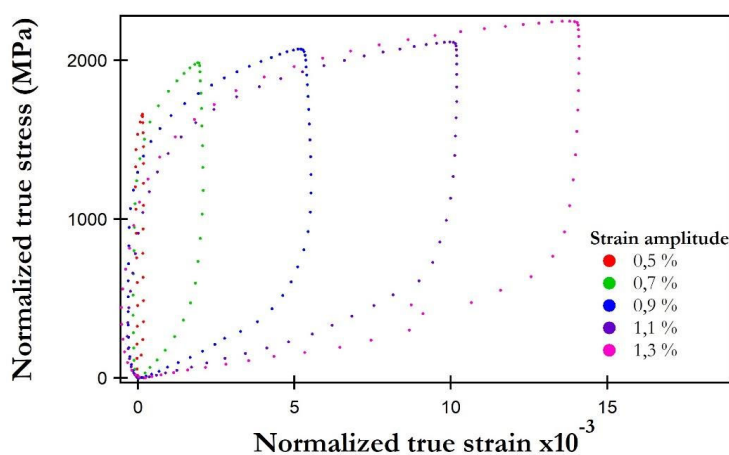


Figure III-14. Verification of the Masing law by normalisation of the cyclic curves obtained in the incremental tests of CP2 (test t3).

Before $\Delta\epsilon/2 = 0.9\%$, the superposition of loading true stress is not noticeable. Between $\Delta\epsilon/2 = 1.1\%$ and $\Delta\epsilon/2 = 1.3\%$, an overlap of the tensile parts of the curves can be observed. Based on the literature [82,83,90,91], the non-superposition of loading true stress highlights a modification of dislocation arrangements and the overlap of loading part reveals similar dislocation arrangement for these strain amplitudes. To confirm this theory, microstructural characterisation was performed. Cyclic tests consisting of 50 cycles were carried out at an amplitude strain of $\pm 0.5\%$ and $\pm 1\%$ with a cyclic ratio of -1. Microstructural observations were then conducted by EBSD and TEM at the centre of these samples.

Electron backscatter diffraction experiments were first performed to observe microstructure modifications after cyclic tests. To this end, the OIM software offers various tools for analysing local deformation. These methods are based on the local misorientations created during deformation.

However, the results are highly dependent on the specimen preparation method. Therefore, in this dissertation the results obtained enable a comparison between the specimens.

Figure III-15 presents the results of comparisons of GAM, GOS, and KAM intended to determine the local deformation between the initial state of the specimen, the specimen after cyclic deformation at $\pm 0.5\%$ and $\pm 1\%$ during 50 cycles (with respectively a cumulated plastic strain of 0.12 and 0.75). The EBSD maps and explanations of the OIM tools (GAM, GOS and KAM) used can be found in Appendix D.

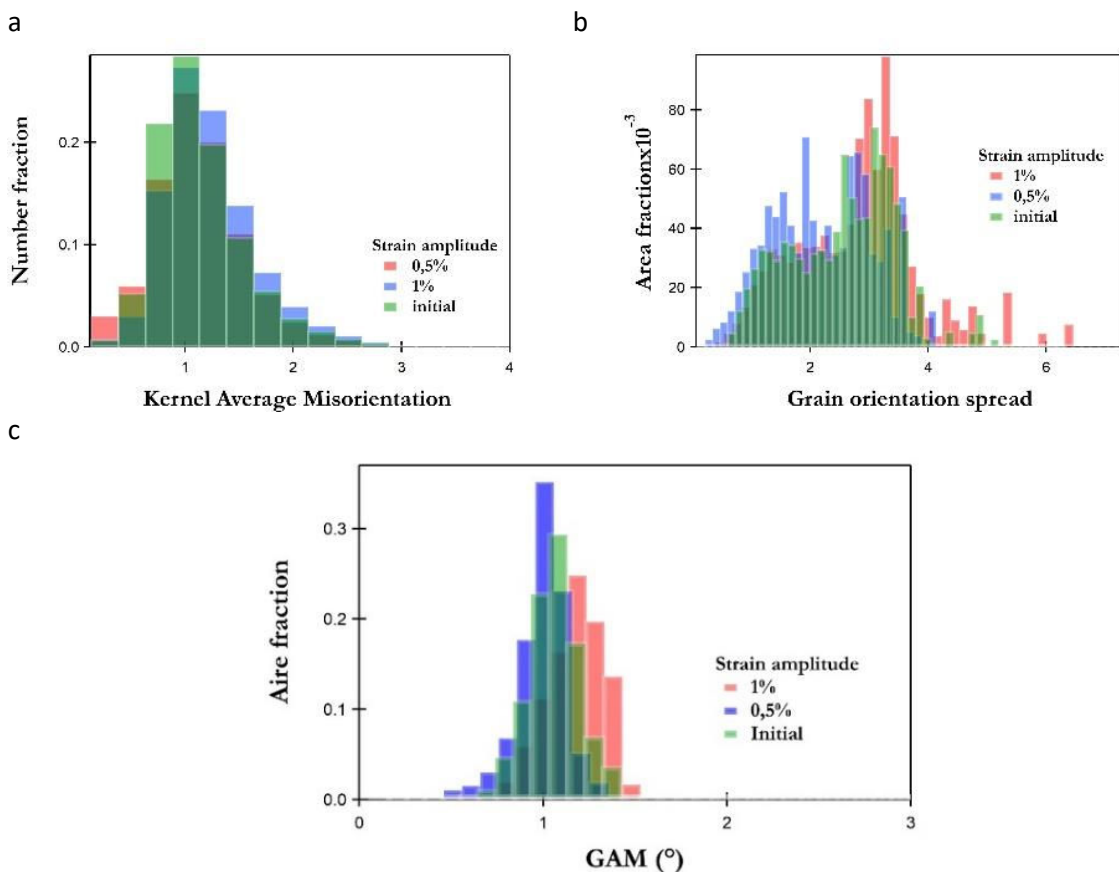


Figure III-15. (a) KAM, (b) GOS, and (c) GAM measurements for initial and cyclic specimens (50 cycles).

The results obtained by EBSD do not reveal many differences between the initial specimen and the specimens that had been subjected to cyclic deformation. Even should the specimens have been slightly deformed, the initial amount of misorientations in bainite would be too high for any differences to be noticeable. Therefore, at this scale, any modification of microstructural structures is not noticeable.

To take the analysis further, TEM analyses were performed to observe the dislocation arrangement modifications predicted from the non-compliance with the Masing law (see Figure III-16).

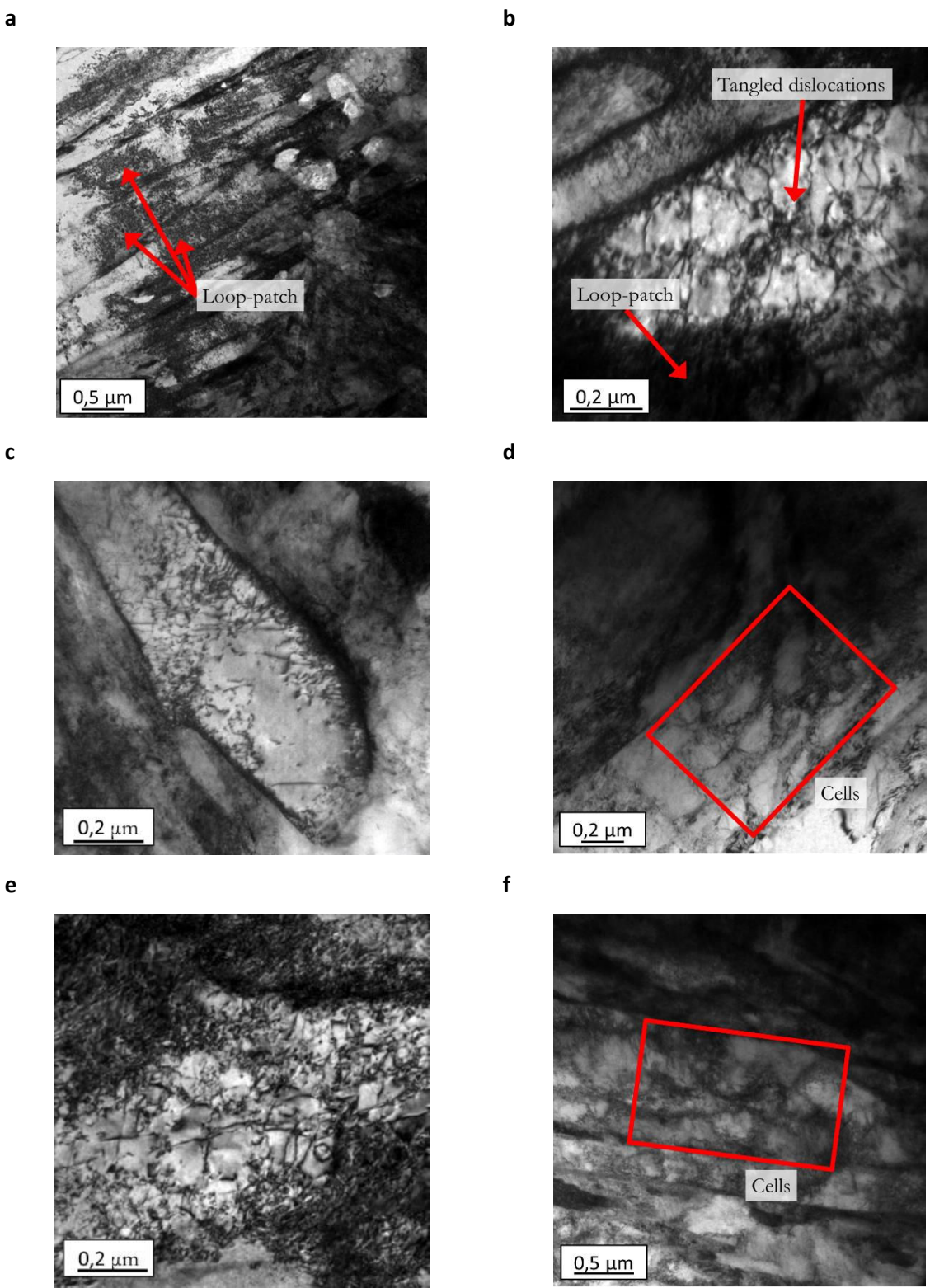


Figure III-16. Transmission electron microscopy images after 50 cycles at an amplitude of 0.5%, showing tangled dislocations (a, b, and c), and after 50 cycles at an amplitude of 1% (d, e, and f) displaying the presence of cells.

Tangled dislocations and a high number of loop patches could be observed in the microstructures of the deformed state after cyclic deformation ($\pm 0.5\%$), these features were similarly present in the specimen in its initial stage. For the specimen deformed at a strain amplitude of 1%, the formation of cells is noticeable. These results are in agreement with the work of Shih et al. presented in Section III.1.1.d [83].

5. Isotropic and kinematic components of hardening

To complete the analysis of the cyclic experiments, the evolution of the isotropic and kinematic components of hardening was investigated. Both the expansion of the yield stress surface (R) and the shift of the middle stress (X) of the elastic domain were determined, and they are presented in Figure III-17.

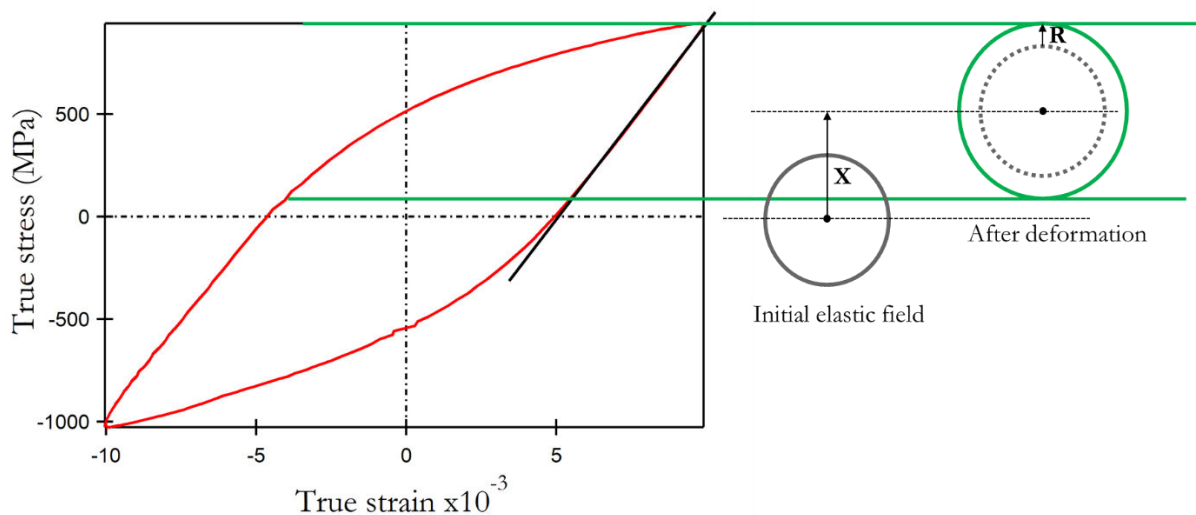


Figure III-17. Example of the measurement of isotropic and kinematic hardening.

To define the limit of the elastic domain, an offset of 0.1% of the plastic strain was applied. In this thesis, the model developed by Lemaitre and Chaboche was used to determine isotropic and kinematic hardening. According to this model, hardening is dependent on cumulative plastic strain (p). To obtain its expression, the cumulative plastic strain rate (\dot{p}) related to the plastic strain rate ($\dot{\epsilon}_p$) is used⁵:

⁵ The results were analysed using an IGOR Pro program initially developed by Gael Marnier and modified for this work.

$$\dot{p} = \left(\frac{2}{3} \overline{\dot{\varepsilon}}_p \overline{\dot{\varepsilon}}_p \right)^{1/2} \quad (19)$$

In tension-compression loading, the accumulated plastic strain can then be simplified as follows:

$$p = \sum |\varepsilon_p| \quad (20)$$

To quantify the isotropic hardening, the parameter R had to be determined. This parameter represents the expansion of the yield surface during plasticity and the integration of its expression (14) for tension-compression tests leads to the following equation:

$$R = Q(1 - e^{-pb_{LC}}) \quad (21)$$

where Q is the saturation of isotropic hardening, and b_{LC} the rate of saturation. Therefore the parameter R is represented in Figure III-18 as a function of the cumulated plastic strain.

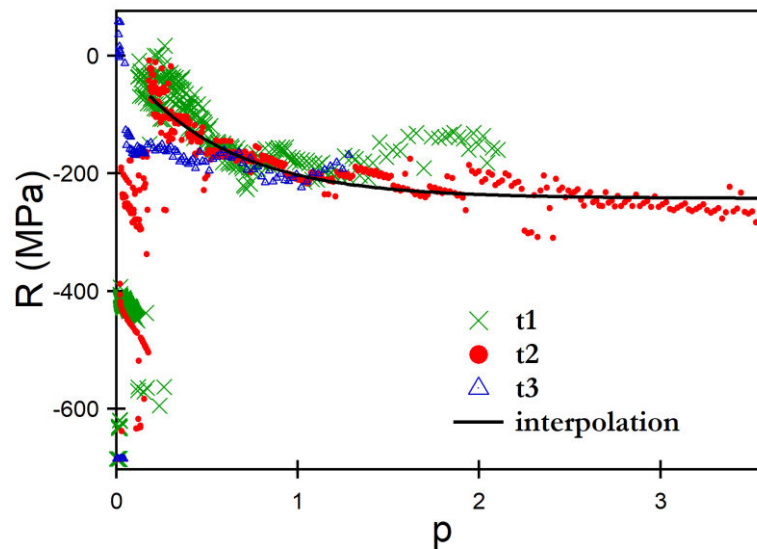


Figure III-18. Evolution of isotropic hardening as functions of the cumulated plastic strain (three tests: t1, t2 and t3).

The interpolation of R as a function cumulated plastic strain with Lemaitre and Chaboche model gives as parameters: $b_{LC} = 1.82$ and $Q = -242$ MPa.

To determine the kinematic hardening, the parameter X was needed. It represents the shift of the yield surface which is expressed in a monotonous tensile test by Equation (22). When considering only one backstress, Equation (15) can be simplified as follows:

$$f = \sigma_{11} - X_{11} - R(p) = \sigma_0 \quad (22)$$

$$X_{11} = \sigma_{11} - R(p) - \sigma_0 \quad (23)$$

Then, if Equation (23) is integrated on the tensile direction, with $p = \epsilon_p$ the equation can be modified as follows:

$$X = \frac{C_{LC}}{\gamma_{LC}} (1 - e^{-\gamma_{LC} \epsilon_p}) \quad (24)$$

The representation of X as a function of cumulated plastic strain is exhibited in Figure III-19.

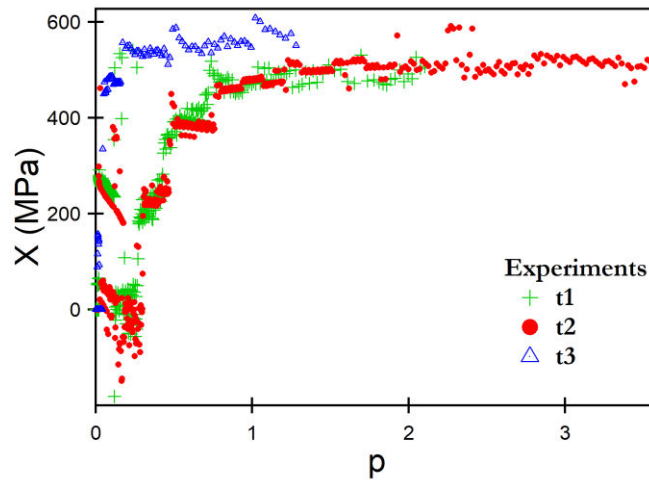


Figure III-19. Evolution of kinematic hardening as functions of the cumulated plastic strain (three tests: t1, t2 and t3).

However, to interpolate the kinematic hardening, one backstress is not sufficient, as can be observed in Figure III-20. The kinematic hardening can be represented at high plastic strain but not at the beginning of deformation. This observation is explained in the work of Lemaitre and Chaboche [42,92] by the non-linearity of the kinematic hardening at high strain.

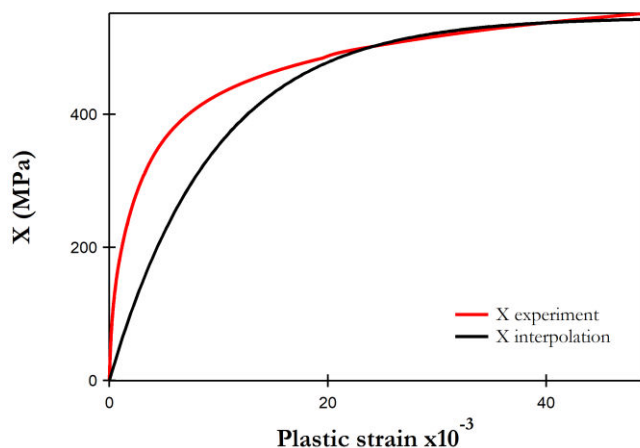


Figure III-20. Lemaitre and Chaboche interpolation with one back stress with interpolation parameters: $C = 56985 \text{ MPa}$ and $\gamma = 104.3 \text{ MPa}$.

Therefore, it was necessary to determine multiple backstresses. As noted in the work of Silvestre et al. [45,92] and Lemaitre and Chaboche [42], the addition of three backstresses is sufficient to obtain a better representation of hardening (see Figure III-21 and Equation (25)):

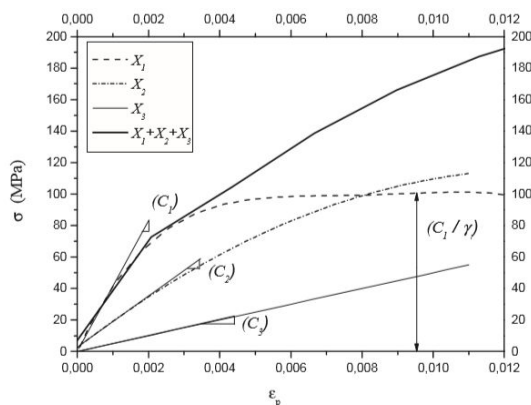


Figure III-21. Evolution of stress response using three backstresses (X_1, X_2 and X_3)[92]

The model proposed by Lemaitre and Chaboche is the addition of a linear term as proposed by Prager and two nonlinear components (see Equation (26)). The superposition of these three components enables the representation of the linear increase at low strain and the linear saturation at higher strain.

$$X = \sum_i X_i \tag{ 25 }$$

$$X = X_1 + X_2 + X_3 = C_1 \varepsilon_p + \frac{C_2}{\gamma_2} (1 - \exp(-\gamma_2 \varepsilon_p)) + \frac{C_3}{\gamma_3} (1 - \exp(-\gamma_3 \varepsilon_p)) \quad (26)$$

The same interpolation was performed on CP2 and the kinematic hardening was measured and presented on Table III-2. The representation of X_1 , X_2 and X_3 as functions of plastic strain are displayed in Figure III-22-b. Moreover, the Figure III-22-b exhibits the addition of all backstresses and its comparison to the monotonous stress-strain tensile curve.

Table III-2. Kinematic parameters using three backstresses.

| | X_1 | X_2 | X_3 |
|-------------|-------|-------|--------|
| C_i (MPa) | 2689 | 75196 | 386480 |
| γ_i | | 251 | 2919 |

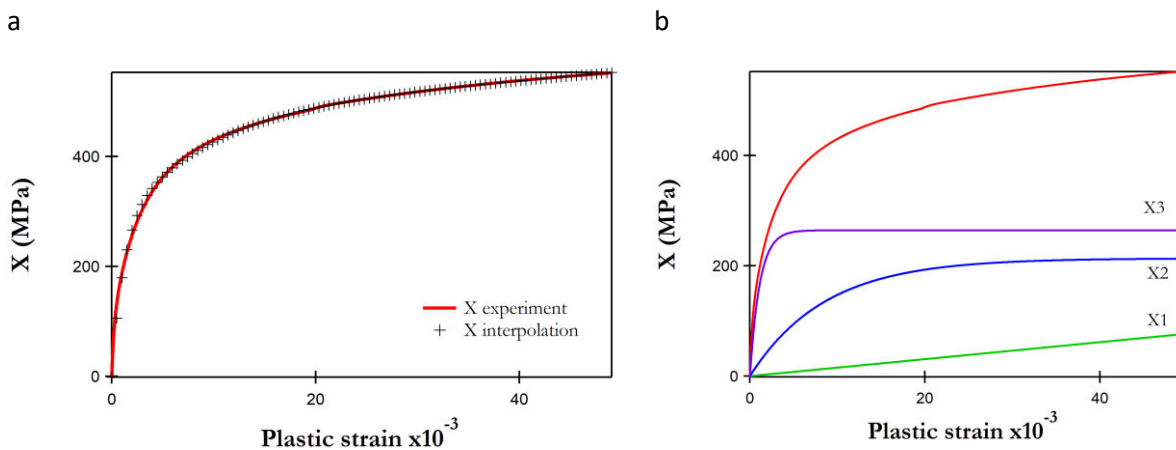


Figure III-22. Lemaitre and Chaboche interpolation with three back stresses (a) and representation of back stress curves (b).

With three backstresses, a better interpolation of kinematic hardening can be observed (Figure III-22). However, a variation at very low strain is observed, thus, the interpolation can be improved. To validate these parameters, the model developed by Lemaitre and Chaboche with the previous findings have to be compared to the cyclic curves. This validation has not been performed in this work.

After the determination of the parameters of the hardening rules the evolution of kinematic and isotropic components of hardening as functions of plastic strain were analysed (see Figure III-18 and Figure III-19). At a low cumulative plastic strain, a reduction in isotropic hardening and an

increase of kinematic hardening can be noted. However, when the plastic strain amplitude reaches 0.2%, a stabilisation of both components of hardening is observed. As noted in Section III.1.1.b, the reduction in isotropic hardening and the increase in kinematic hardening indicate the significant influence of long-range interactions on the mechanical properties of CP2. In accordance with the microstructural characterisation performed on the Chapter II of this thesis, the long-range interactions which impact the kinematic hardening could be induced by the high amount of dislocation in the initial microstructure and the high presence of grain boundaries due to the thin laths microstructure. To verify these hypothesis similar tests could be performed on bainitic steels with a different lath size.



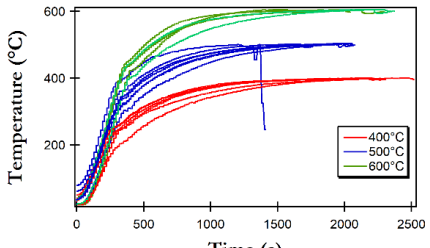
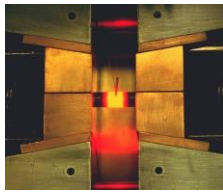
6. Impact of temperature on mechanical properties in tension

In this section, the thermal stability of mechanical properties of CP1200 steel is investigated over a temperature range from 200°C to 600°C. Since the maximal temperature did not exceed Ac1, austenitisation did not occur during the tests. Thus, all conclusions concern the bainitic microstructure.

6.1. Presentation of experimental devices

In order to analyse the thermomechanical behaviour of CP1200 steel, two devices were used: a tensile machine equipped with a furnace (TMF) and a thermomechanical simulator (Gleeble). The use of both of these devices made it possible to investigate a broad range of parameters, including heating rate and heating processes. However, the most significant differences identified between the output of these two devices have to be taken into account when the comparing the results. Therefore, the peculiarities of each machine are presented in Table III-3. Thereafter, the tensile properties of CP1200 steels at 400°C, 500°C, and 600°C are investigated in both devices and compared.

Table III-3. Comparison between the Gleeble and tensile machine.

| Tensile machine with furnace | Gleeble |
|---|---|
|  |  |
| <p>Figure III-23. Tensile machine equipped with a furnace.</p> | <p>Figure III-24. Gleeble chamber in tensile configuration.</p> |
| Temperature control and limit | |
| <ul style="list-style-type: none"> • Temperature measurements by thermocouple placed on the surface of the specimen • Thermocouples at the top, middle, and bottom of the furnace | <ul style="list-style-type: none"> • Temperature measured by thermocouple welded at the centre of the specimen <ul style="list-style-type: none"> • (Type K – Alumel Chromel) |
| Supplementary notes | |
| <ul style="list-style-type: none"> • Extensometer placed on the specimen (20 mm) | <ul style="list-style-type: none"> • Fixation of extensometer on the jaws of the device (50 mm) |
| Complementary remarks | |
| <ul style="list-style-type: none"> • No control of heating rate | <ul style="list-style-type: none"> • Heating and strain were localised in the middle of the specimen used |
|  |  |
| <p>Figure III-25. Evolution of temperature during tensile tests performed on the TMF.</p> <ul style="list-style-type: none"> • Minimum furnace temperature: 400°C | <p>Figure III-26. Heating of the round specimen on Gleeble⁶.</p> <ul style="list-style-type: none"> • Impact of electric current on diffusion mechanisms not well understood |

⁶ Image taken from the help notice of Gleeble

Before studying the differences in the tensile results obtained at different temperatures, the impact of the heating rate and the localisation of temperature observed with the Gleeble must be noted. Three heating rates were tested: 1000°C/s, which is approximately the heating rate reached during laser welding, 10°C/s and 25°C/min for two temperatures: 400°C and 600°C. All tests were performed with the Gleeble due to the lack of heating rate control in the furnace. The results displayed in Figure III-27 do not indicate a significant impact of heating rate on strength, as similar UTSs can be observed. These tests show that a difference in heating rate has no significant impact on mechanical properties.

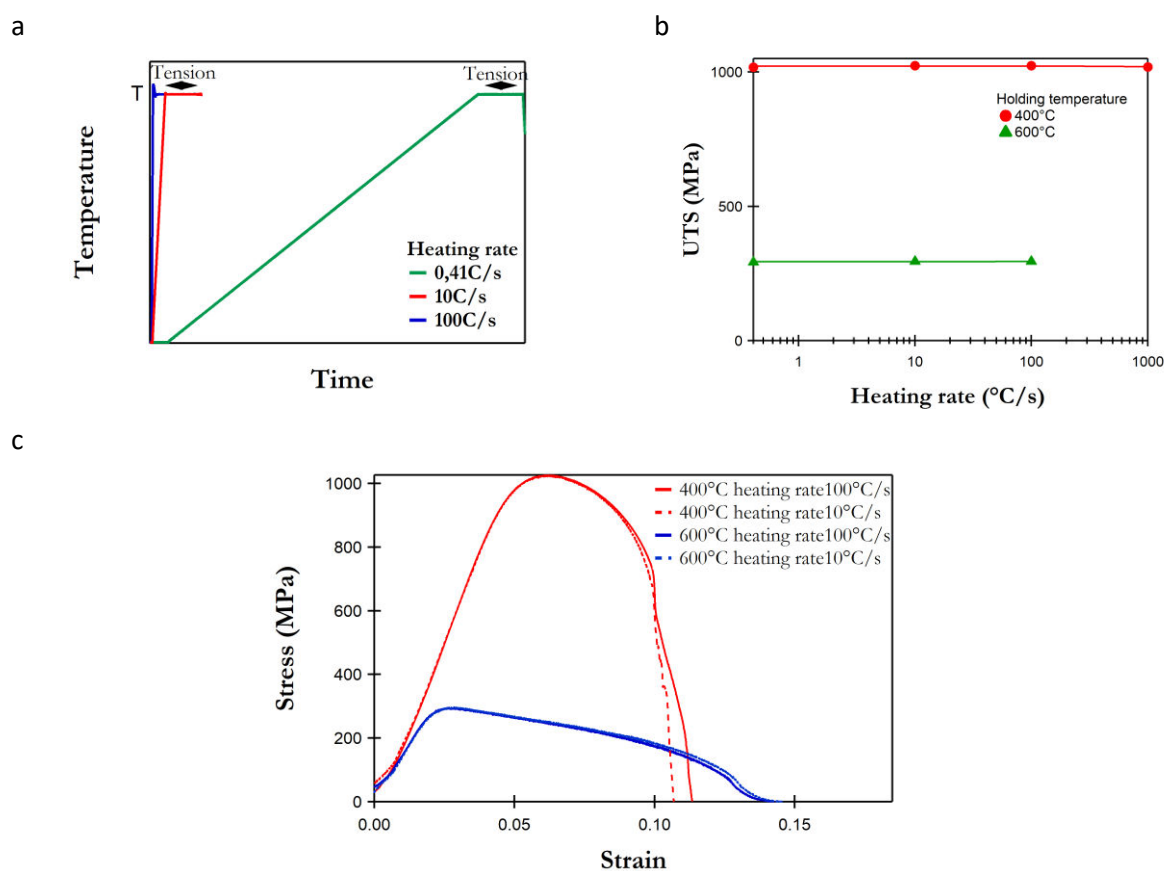


Figure III-27. Evolution of UTS as a function of the heating rate: (a) heating instructions, (b) results, and (c) monotonous tensile curves.

In order to explore the heterogeneous heating noted when using the Gleeble device, an experiment with two thermocouples - one welded to the middle of the specimen used as the control and another 1 cm away - was performed.

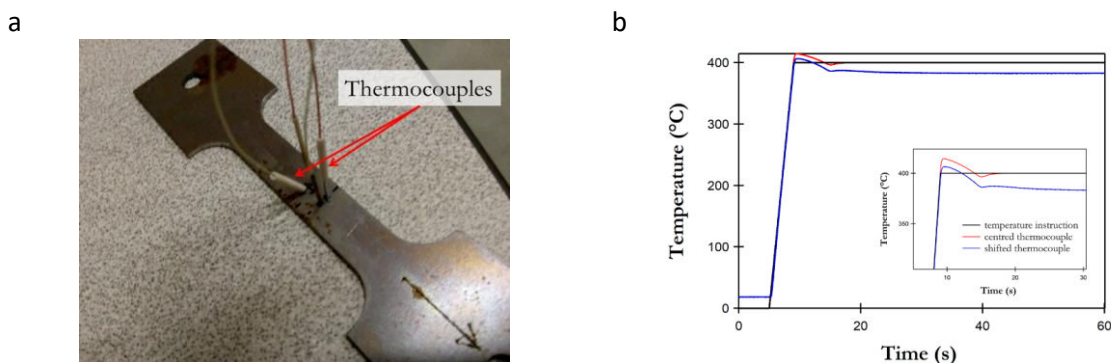


Figure III-28. Difference in temperature between a thermocouple placed at middle of the specimen and a thermocouple placed 1 cm away from the middle: (a) picture of welded thermocouple and (b) temperature evolution.

For a temperature of 400°C, a difference of 17°C was observed (see Figure III-28). Thus, a difference in temperature is present throughout the specimen during heating. This inhomogeneity of heating leads to a localisation of maximum strain in the middle of the specimen.

To further investigate the differences between the Gleeble machine and the TMF, monotonous tensile tests were conducted at a heating rate of $100^{\circ}\text{C}\cdot\text{s}^{-1}$, a tensile rate of 10^{-3} s^{-1} , and at four different temperatures: 200°C, 400°C, 500°C, and 600°C. The tensile curves obtained with the Gleeble device and TMF are displayed in Figure III-29.

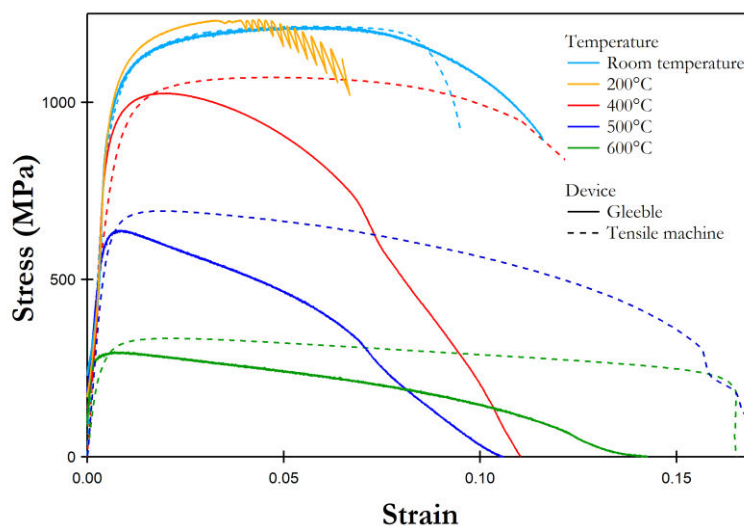


Figure III-29. Tensile stress-strain curves at different temperatures (room temperature, 200°C, 400°C, 500°C, and 600°C) performed on the Gleeble and the TMF.

A complication that arises is that great differences are noted between the results obtained using the Gleeble and TMF devices with regard to hardening evolution and ductility. These differences can be explained with the reference to the setting of the extensometer on the jaws of the Gleeble. In this case, the deformation measured includes not only the strain of the entire specimen but also one of the jaws. Moreover, the localisation of temperature at the centre of the specimen induces the strain localisation that reduces the total strain measurements compared to the results obtained with the TMF. Regardless of these differences, the evolution of UTS as a function of temperature is shown in Figure III-30. The figure indicates that the two devices produced similar strength results.

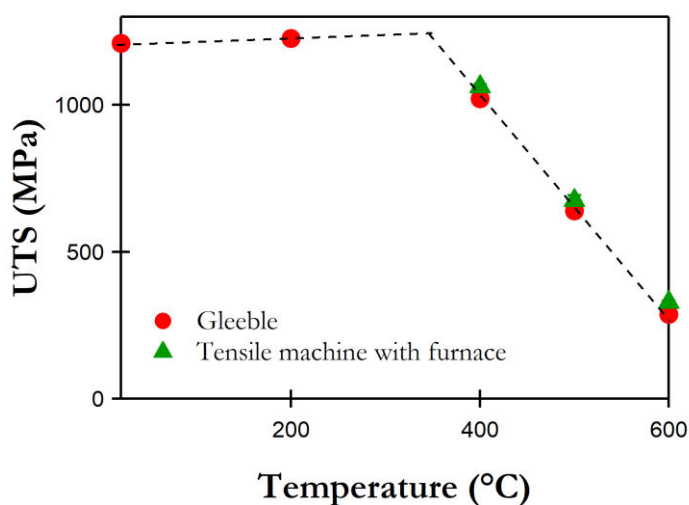


Figure III-30. Evolution of the UTS as a function of temperature determined with the Gleeble and the TMF (standard deviation ± 5 MPa).

The main difference between the Gleeble device and the TMF devices used in this research is the fact that the latter measures strain using an extensometer set in the specimen. To obtain an evolution of the strain at fracture independent of the device used, the localised strain with section reduction was determined by the Bridgman equation (27) where S and S_0 are the sections after and before deformation, respectively.

$$\varepsilon_p = \ln \left(\frac{S_0}{S} \right) \quad (27)$$

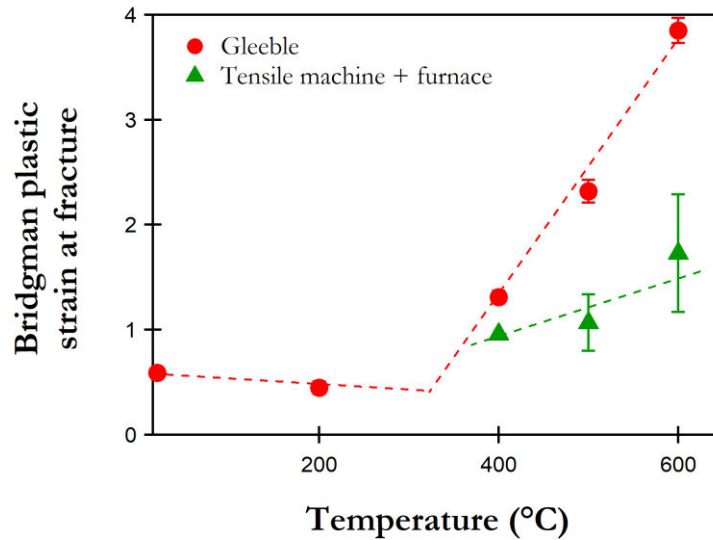


Figure III-31. Evolution of plastic strain at fracture as a function of temperature.

Despite the fact that the specimen geometries were different, the evolutions of plastic strain obtained by the two methods present similar trends. Indeed, the equivalent plastic strain increases significantly with temperature after 400°C. However, a more significant increase is measured with the Gleeble device. This difference could be due to the local heating presents with Gleeble device, as explained in Table III-3, which leads to a rapid localisation of strain at the middle of the specimen. This strain localisation is not measurable with longitudinal extensometer as it was observed in Figure III-29 but it have a significant influence on the results of Bridgman equation.

6.2. Influence of temperature and holding time on mechanical properties

To investigate the thermomechanical behaviour of CP2, tensile tests were performed on Gleeble device at temperatures between 200°C and 600°C, and at various holding times inferior to 1 hour. In order to simplify the designation of tensile tests performed at high temperatures, the acronym HT is used. All the tensile results are exhibited in Figure III-32.

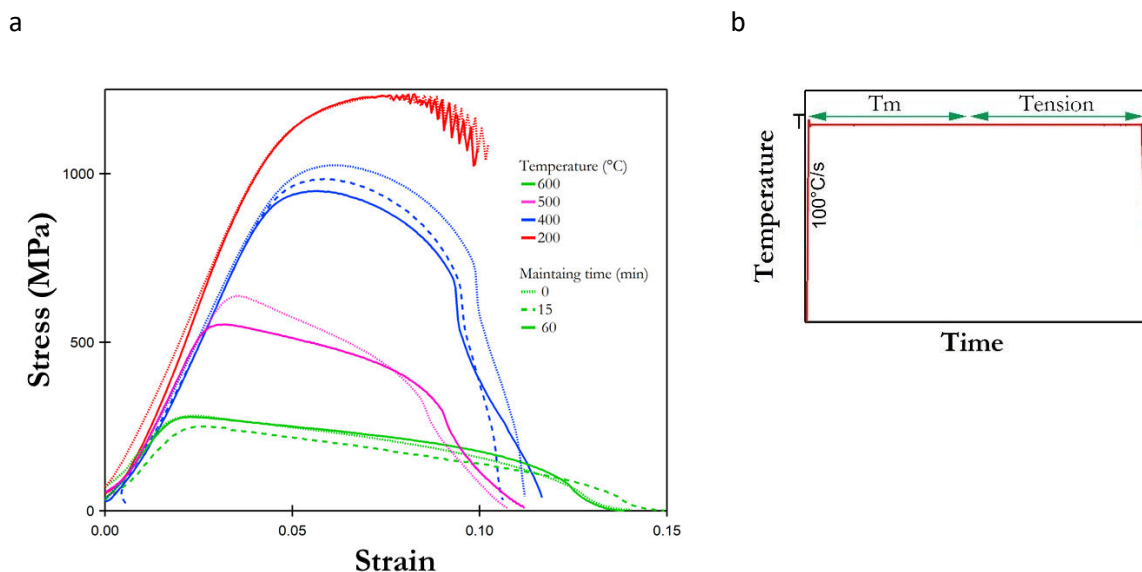


Figure III-32. (a) Tensile tests performed on Gleeble device at different temperatures [200°C–600°C], (b) thermal programmes corresponding to these tests.

The most striking results that emerge from the data are the serrated tensile curves at 200°C. This observation is characteristic of the Portevin-Le Chatelier effect. In steels, this effect can be explained by a diffusion of carbon that stops the displacement of dislocations [17,93]. The liberation of dislocations leads to a significant decrease in stress, which creates fluctuations on the tensile curves. Since this phenomenon is complex and dependent on strain rate and temperature, it was not investigated further during this project. At temperatures up to 400°C, a decrease in stress is highlighted with an increase in temperature and holding time (see Figure III-34). Viscoplasticity effects and microstructure modification can explain this reduction. To decorrelate these two parameters, tensile tests were performed at room temperature after a similar tempering at HTs (see Figure III-33). These tests are referred to as RTs in this chapter.

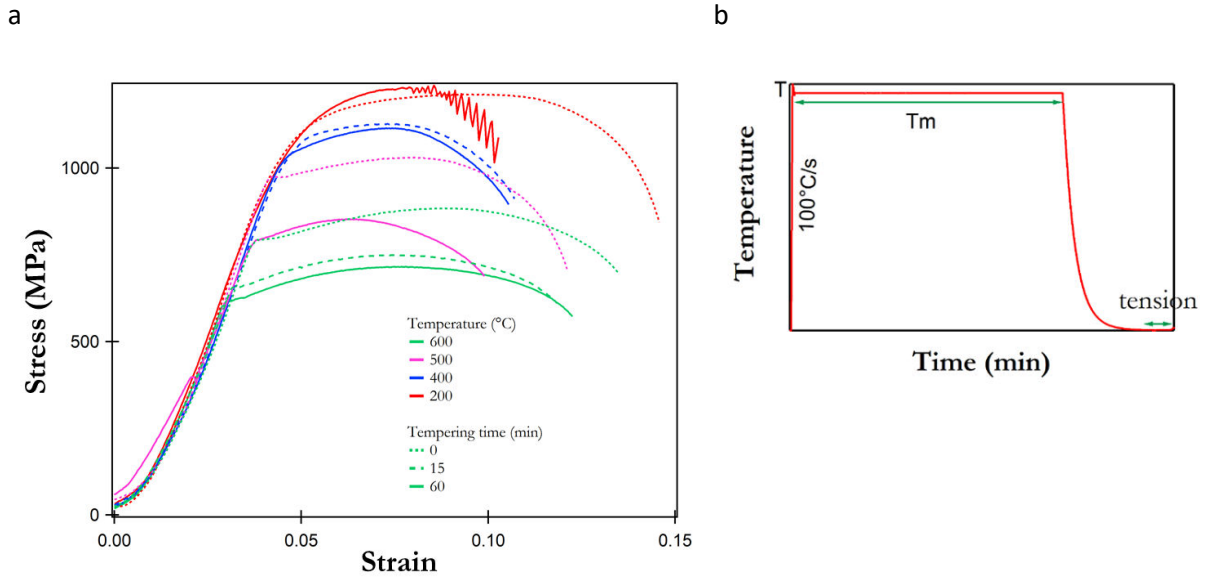


Figure III-33. (a) Tensile tests performed with Gleeble device at room temperature after tempering at various temperatures [200°C–600°C], (b) thermal programmes corresponding to these tests.

The RT tests after tempering at various temperatures made it possible to identify stress loss resulting from a modification of the microstructure of the samples. At HT a reduction of strength can be identified as a result of the increase in temperature. To compare the results of the HT and RT tests, the UTS are displayed as functions of the temperature and time of tempering (see Figure III-34).

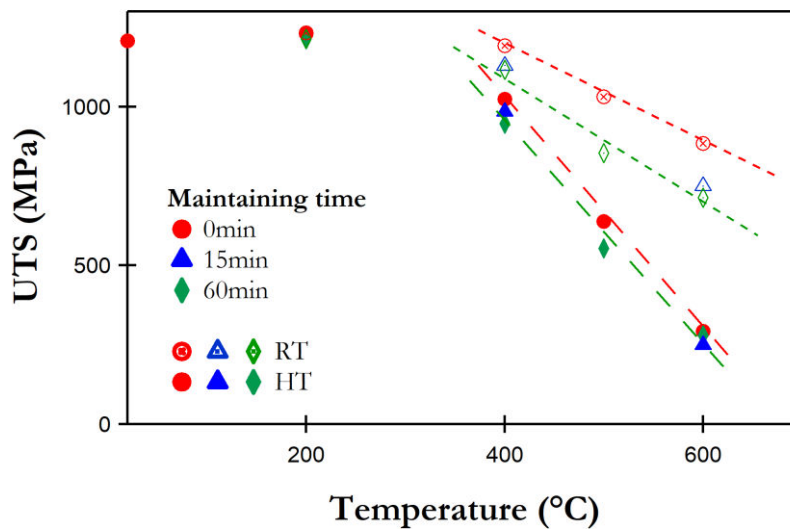


Figure III-34. Evolution of UTS as a function of holding time during tensile tests performed at room and high temperatures.

For all tests, a slight increase in strength is observed between specimens tested at room temperature and at 200°C. Hence, up to 400°C, a significant decrease of UTS is detected. However, the decrease in strength is less significant in the tests performed at RT. At 600°C without tempering time, a difference of 600 MPa in UTS is measured in Figure III-34. Such differences represent the impact of viscoplasticity on the investigated properties, which is more significant. Another noteworthy point is that no modification of the UTS is observed at HTs with an increase in holding time, whereas, for RT, a significant reduction is observed.

Many publications have investigated the impact of tempering on the mechanical properties of steels. A linear relation between time and temperature of tempering exists and is expressed in Equation (28) by the relation of Hollomon-Jaffe [94–96].

$$Hp = T(20 + \log(t)) \quad (28)$$

where H_p is the Hollomon-Jaffe parameter, T the temperature (°C), and t the tempering time (h). This relation is usually used with hardness tests but can be applied to tensile tests due to the relation between UTS and hardness. The results obtained are presented in Figure III-35.

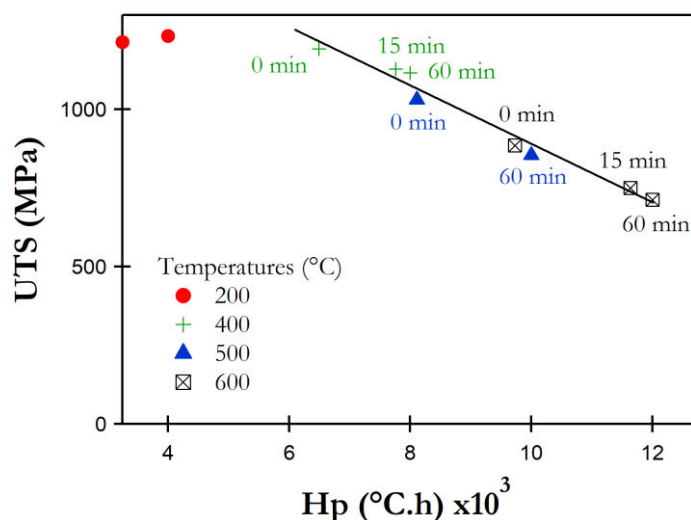


Figure III-35. Representation of UTS as a function of the H_p coefficient.

The results indicate that the tests followed the relation of Hollomon and Jaffe after 400°C. Indeed, the following linear relation is exhibited with a linear coefficient of $r^2 = 0.98$:

$$UTS(H_p) = 1807.8 - 0.092 \times H_p \quad (29)$$

It is then possible to highlight an equivalence between tempering and time-temperature that controls UTS. However, this linear relation does not reveal information on microstructure modifications but only provides an estimation of maximum strength.

6.3. Summary of the thermomechanical analyses

The thermomechanical results of this study reveal a decrease of strength above 400°C. This reduction of mechanical properties can be explained with reference to two phenomena: viscoplasticity mechanisms and the modification of the steel's microstructure. At room temperature, plasticity is governed by the glide of dislocations, whereas diffusion mechanisms can be activated as a result of an increase in temperature. According to D. Hull and D. J. Bacon [71], the force (ΔF^*) needed for a dislocation to overcome an obstacle can be divided into a mechanical energy (τ^*V^*) and thermal energy (ΔG^*) (see Equation (30)):

$$\Delta F^* = \tau^*V^* + \Delta G^* \quad (30)$$

Hull and Bacon's work presents the evolution of the shear stress needed to overcome obstacles as a function of temperature (see Figure III-36). An observation that can be made on this graph is the separation of the shear stress into internal stress (τ_G) that is not or only slightly affected by temperature and effective stress (τ^*) which is totally suppressed after a critical temperature (T_c). Effective stress is induced by short-range interactions, which can be overcome by thermal activation. The long-range interactions that characterise internal stress are barriers that are too large to be affected by the thermal activation.

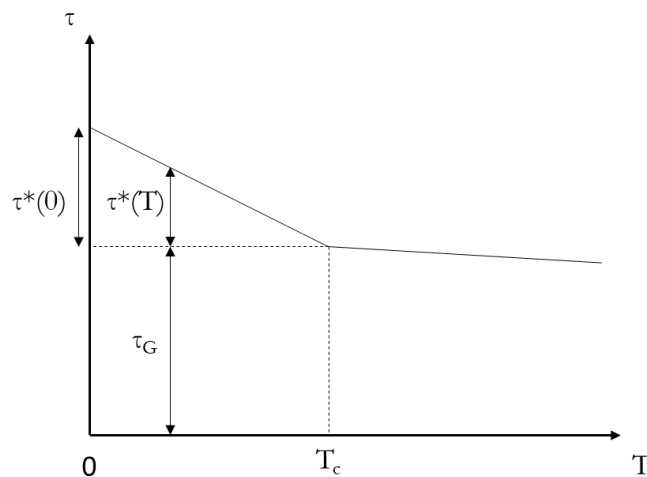


Figure III-36. Evolution of shear stress as a function of temperature [71].

Before T_c , a reduction is observed from $\tau^*(0)$, which is the stress needed to overcome obstacles at 0 K. This parameter includes the Peierls-Nabarro stress, which is defined as atoms' resistance to dislocation motion at 0 K. At temperature T , the shear stress is reduced to $\tau^*(T)$, which implies an increase in thermal energy, which can be explained by the vibration of atoms promoted by

temperature. Moreover, this increased atomic vibration facilitates the climbing of edge dislocations. Dislocation climb is characterised by the movement of a dislocation into another slip plane due to the creation or the annihilation of vacancies [71]. This mechanism is then encouraged by the diffusion of vacancies or the diffusion of interstitial atoms, which are both promoted by temperature. The activation of climbing facilitates the movement of dislocations, thus reducing the strength of and increasing ductility in CP2.

A second phenomenon that occurred in tests performed at HTs is the modification of microstructure as presented in Figure III-37. According to the literature [26, 36, 58, 77], different stages can be observed during the tempering process: first, the decomposition of austenite into carbide, which induces a reduction of mechanical stress, second, the relaxation of internal stresses and finally, the recrystallisation of bainite into an equiaxed structure over a long tempering time. All these microstructural modifications reduce the mechanical properties of CP2. The microstructural characterisation in Figure III-37 reinforces this hypothesis by depicting carbides on the microstructure after tempering at 400°C for one hour.

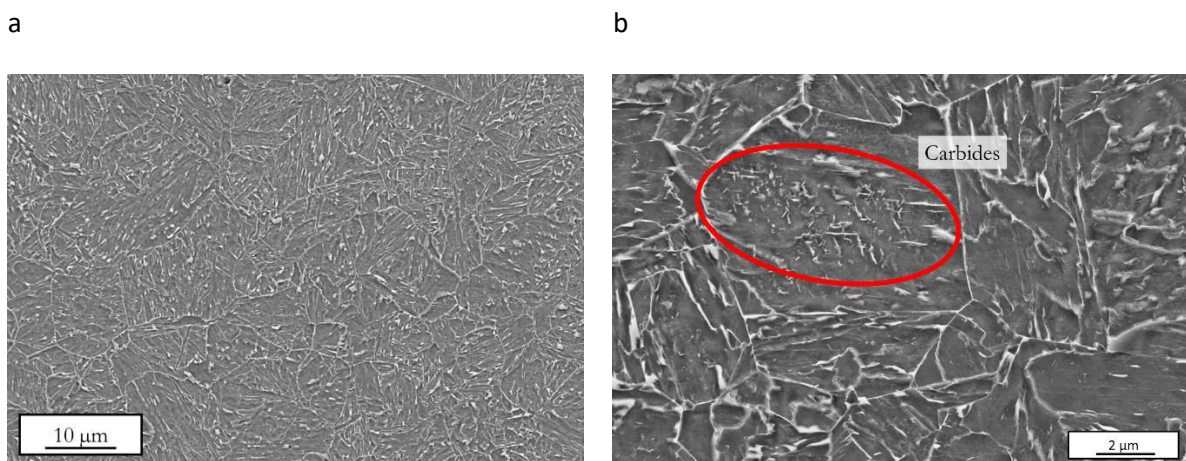


Figure III-37. Microstructure of CP2 after annealing at 400°C for 60 min (a, b).

Higher temperatures increase the diffusion and the vibration of atoms, which enhance the formation of carbides and promote the activation of viscoplastic mechanisms.

In the next chapter, damage in CP1200 after tensile solicitations on notched specimens is investigated by means of void quantification. It is observed that the presence of the internal stresses measured previously and the changes in the microstructure that occur due to temperature influence damage mechanisms.

Chapter IV. Description and quantification of damage mechanisms in CP1200 steels

This chapter presents results of investigations into the impact of mechanical damage on CP1200 steels. Damage was quantified using two different methods. First, the sensitivity of mechanical properties to damage was investigated, taking into consideration the concept of effective stress introduced by Rabotnov [54]. In a second experiment, microstructural observation of voids was performed, and void evolution was studied as a function of plastic strain at various temperatures and stress triaxialities. Finally, void localisation inside the microstructure was investigated to understand the weaknesses and strengths of the material.

1. Metallurgical and mechanical definitions of damage

1.1. Void evolution and definition of the damage variable

Damage is a physical process that leads to the creation of microsurfaces, which in turn cause discontinuities [97], as a result of the breaking of atomic bonds and plastic enlargement. These discontinuities lead to a softening of the mechanical properties and then to the fracture of the specimen [42]. As functions of the material and the loading conditions, different fracture mechanisms can be reported such as brittle, ductile, creep, and fatigue fractures. This report focuses on the ductile fractures, which occur following the formation of the voids characterised in Figure IV-1:

- **Nucleation**, which is the initiation of void formation. Nucleation usually occurs at the discontinuities of a material, such as inclusions, grains boundaries, and precipitates.
- **Growth**, which is characterised by the expansion and shape modification of voids as a function of the stress state.
- **Void coalescence**, which is the clustering of voids due to the distance reduction between them. The necking or fracture at the interfaces between two voids promotes coalescence mechanisms.

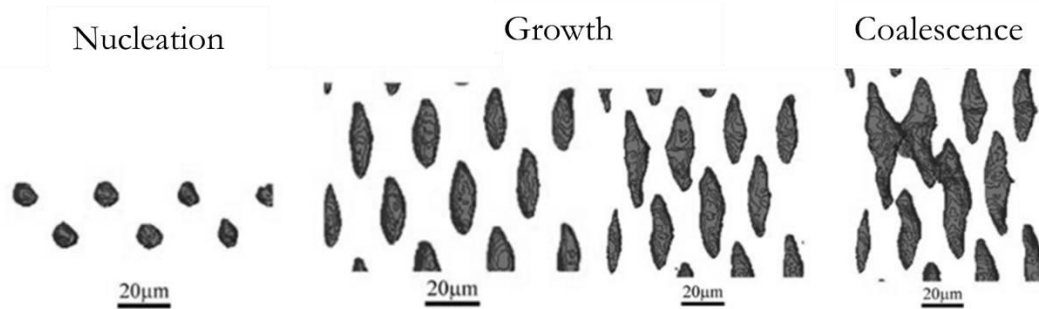


Figure IV-1. Representations of the nucleation, growth, and coalescence of voids [50].

Many publications have investigated the link between damage evolution and plasticity. Such studies state that strain localisation and damage can occur either simultaneously or separately. As functions of the material, different cases can be considered [98,99] (see Figure IV-2):

- The localisation of strain without the development of damage, which can be observed in pure metals (see Figure IV-2-a).
- The emergence of damage after the localisation of plasticity into shear bands (see Figure IV-2-b).
- The nucleation of voids before the localisation of strain (see Figure IV-2-c).
- The simultaneous development of void coalescence and macroscopic strain localisation (see Figure IV-2-d).

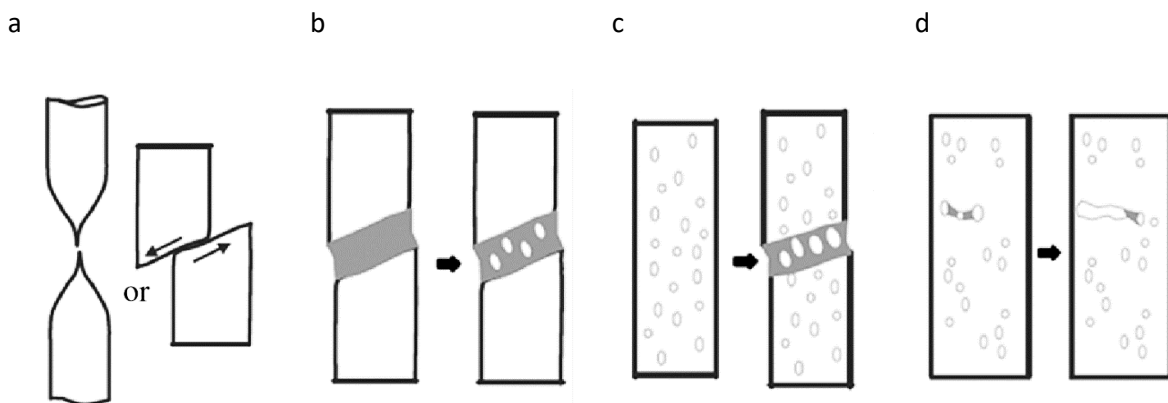


Figure IV-2. Failure as the result of (a) localised plastic flow, (b) localised plastic flow prior to damage, (c) damage softening simultaneously due to localised plastic flow, and (d) void coalescence [99].

To quantify the impact of damage, the variable D is established. This variable is defined by Lemaitre [54] as the surface density of discontinuities in a particular plane. If a representation volume

element (RVE) is considered inside a damaged material with micro-cracks, voids, and stress concentrations, it is possible to position a point M at a plane with the normal direction \vec{n} and the width as abscissa x along the direction \vec{n} (see Figure IV-3). To estimate the parameter D, the damaged section is considered to belong to the intersection between the plane and the RVE (δS_{Dx}). The section is then normalised by the area of the entire material (both the damaged and virgin material) (δS) (see Equation (31)). Consequently, if $D = 0$, the material does not exhibit damage and if $D = 1$, the structure is fully fractured:

$$D_{(M,x)} = \frac{\delta S_{Dx}}{\delta S} \quad (31)$$

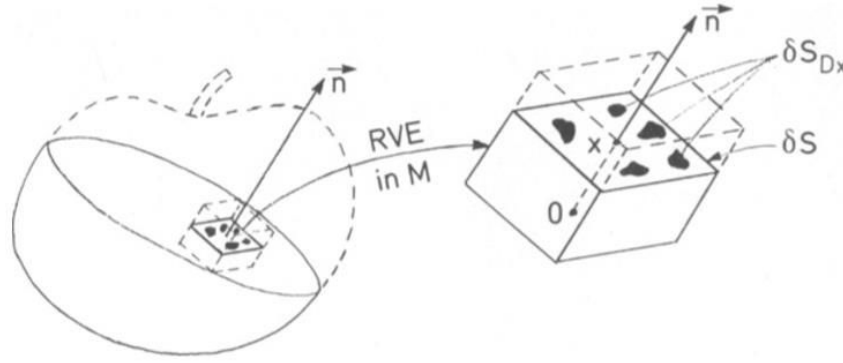


Figure IV-3. Representation of the initial surface (S) and damaged surface (\tilde{S}) [54].

Considering one dimension of homogeneous damage at the failure plane (suppressing the dependence of x), the parameter D can be rewritten as follows:

$$D = \frac{S_D}{S} \quad (32)$$

According to the literature, for metals, this representative equivalent volume is estimated at 0.1 mm^3 [54]. Moreover, in continuum damage mechanics (CDM), it is worth noting that the material itself does not exhibit particular modifications. Indeed, the loss loading capacity is caused by the section variation generated by void formation. To modify the elastoplastic response without affecting the proper plasticity of the material, Rabotnov introduced the concept of the effective stress ($\tilde{\sigma}$) [42].

$$\tilde{\sigma} = \frac{\sigma}{S - S_D} = \frac{\sigma}{1 - D} \quad (33)$$

This notion of effective stress was then inserted into the models defined for the virgin materials (see Equation (34)):

$$\varepsilon = f(\sigma, \dots) \rightarrow \varepsilon = f\left(\frac{\sigma}{1-D}, \dots\right) \quad (34)$$

1.2. Sensitivity of damage evolution to stress triaxiality

As for plasticity with the von Mises criterion, a damage criterion can be established using an equivalent stress (σ^*). For the plastic yield stress criterion, the Von Mises relation is defined by the shear energy. This energy depends on the slipping mechanisms responsible for plastic strain. For the damage criterion, the shear energy is also needed. However, the influence of the volume deformation energy is required, which is a consequence of the dependency between void growth and hydrostatic stress. Therefore, the damage equivalent criterion can be expressed as follows:

$$\sigma^* = \sigma_{eq} \left[\frac{2}{3}(1+\nu) + 3(1-2\nu) \left(\frac{\sigma_H}{\sigma_{eq}} \right)^2 \right]^{1/2} \quad (35)$$

This equation highlights the impact of stress triaxiality (η), which is the ratio between the hydrostatic stress (σ_H) and the von Mises equivalent stress (σ_{eq}):

$$\eta = \frac{\sigma_H}{\sigma_{eq}} \quad (36)$$

$$\sigma_H = \frac{1}{3} \text{tr } \bar{\sigma} \quad (37)$$

$$\sigma_{eq} = \sqrt{\frac{3}{2} \bar{\sigma}^D : \bar{\sigma}^D} \quad (38)$$

where $\bar{\sigma}^D$ is the deviatoric tensor, $\bar{\sigma}^D = \bar{\sigma} - \sigma_H \bar{I}$ (39)

and \bar{I} is the identity tensor.

As damage is highly influenced by stress triaxiality, damage laws used this parameter to describe damage evolution in multiphase steels [100–104]. The most famous model of void growth is the Rice and Tracey expressed by the Equation (40). This equation models the evolution of spherical voids growing in an infinite, rigid, and perfectly plastic material. In addition, this equation indicates that an exponential increase in void growth will occur in the presence of stress triaxiality:

$$\frac{\dot{R}_c}{R_c} = \alpha_2 \exp\left(\frac{3}{2} \frac{\sigma_H}{\sigma_{eq}}\right) \dot{\varepsilon}_p \quad (40)$$

where R_c is the initial radius of the cavity, σ_{eq} is the von Mises equivalent stress, σ_H is the hydrostatic stress $\dot{\varepsilon}_p$ is the equivalent plastic strain rate, and α_2 is a material constant.

However, the determination of damage with plasticity is not constant. Indeed, the stress triaxiality is dependent on the specimen geometry, which is modified during the deformation. In literature, numerical simulation results were obtained to represent the evolution of stress triaxiality with plastic strain. For instance in the PhD thesis of J.Chottin [3] numerical simulation on DP1000 steels was performed for various specimen geometries as it is shown in Figure IV-4.

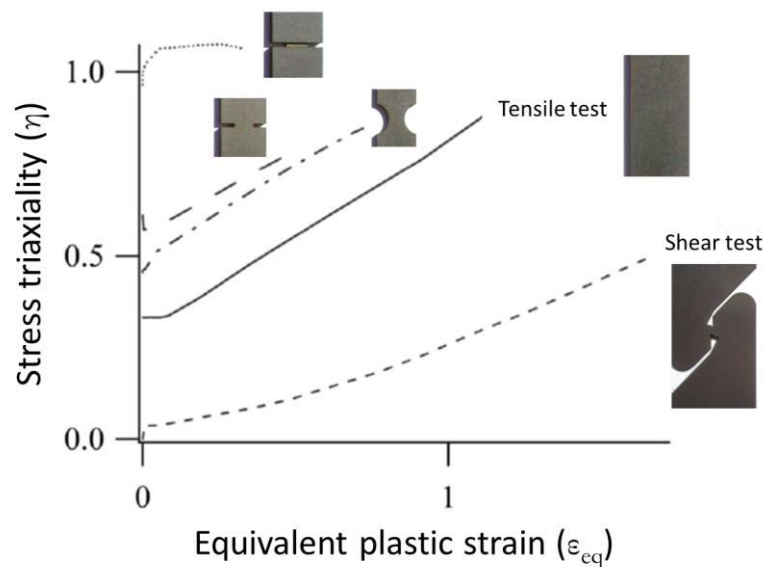


Figure IV-4. Evolution of stress triaxiality as functions of equivalent plastic strain for various specimen geometries [3].

These results exhibit an increase of stress triaxiality with the plastic strain for all geometries. In this thesis, numerical simulation was not performed, therefore the initial stress triaxialities were used to analyse results.

2. Quantification of damage at room temperature

Two different methods were chosen to quantify the damage. First, the impact of damage on mechanical properties was studied by the reduction of the Young modulus. Second, damage at the microstructure scale was analysed by measuring the characteristics of voids as a function of the plastic strain. To take this analysis further, the impact of the stress state on damage was determined by tests performed at various stress triaxialities.

2.1. Preliminary quantification of damage using loading and unloading tests

Using the concept of mechanical effective stress, the evolution of damage can be expressed as the reduction of the Young modulus during loading/unloading tensile tests [48]. This method is easy to set up and provides a first estimation of damage evolution. However, this technique entails the development of a homogeneous and isotropic damage, which is not the case for CP steels. Therefore, in the work of Lemaitre and Chaboche, an uncertainty of $\pm 5\%$. This uncertainty is estimated when considering measurement errors [78, 83]. For an isotropic material, the damage variable is expressed by Equation (41):

$$D = 1 - \frac{S_{eff}}{S} = 1 - \frac{E_{eff}}{E} \quad (41)$$

Loading and unloading tests were performed on a 50 kN tensile machine featuring the clamping device described in Chapter III. The stress strain curves are displayed in Figure IV-5-a, while the reduction of the Young modulus as a function of the true plastic strain (ϵ_{pl} defined in Equation (42)) is presented in Figure IV-5-b.

$$\epsilon_{pl} = \epsilon - \epsilon_e \quad (42)$$

With ϵ the true strain and ϵ_e the elastic strain.

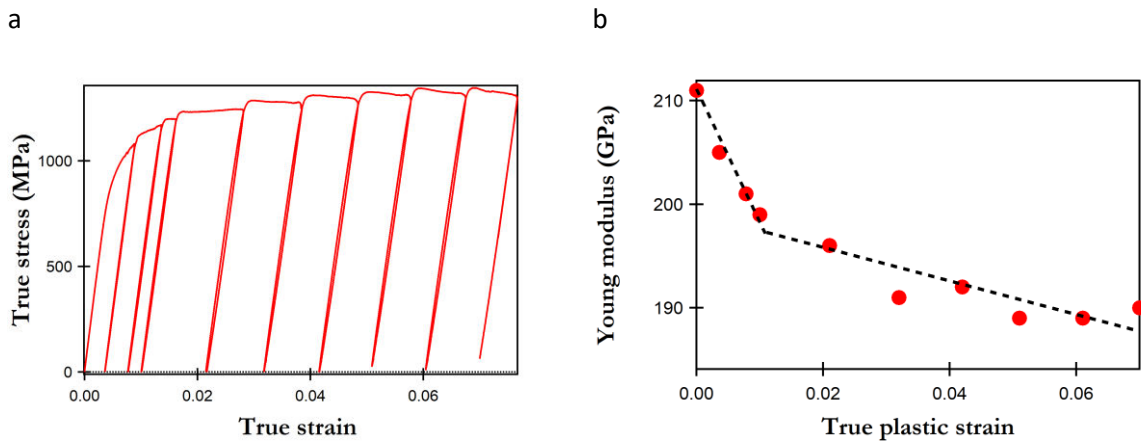


Figure IV-5 (a) Stress-strain loading and unloading curves, (b) evolution of Young modulus with plastic strain during the loading and unloading tests.

The results demonstrate a significant decrease in the Young modulus at a plastic strain below 0.02, which stabilises thereafter. This initial reduction of the Young modulus at low plastic strain is not caused by damage mechanisms, it is due to the bending of dislocations and carbon diffusion [42]. To

represent the damage, a linear law (43) formulated by Lemaitre and Chaboche was applied to the results. This law was initially developed to represent the growth and coalescence of voids at high plastic strain. This equation features a critical damage value (D_c) and a fracture true strain criteria (ϵ_{vR}) which refers to when the material is totally fractured. The other main parameter is the critical true plastic strain range in which, no damage is measured ($\epsilon_{vR} < \epsilon_{vD}$). This law is applied to the evolution of the damage measured by Equation (43) and the results of its application are displayed in Figure IV-6.

$$D = D_c \left\langle \frac{\epsilon_v - \epsilon_{vD}}{\epsilon_{vR} - \epsilon_{vD}} \right\rangle \quad (43)$$

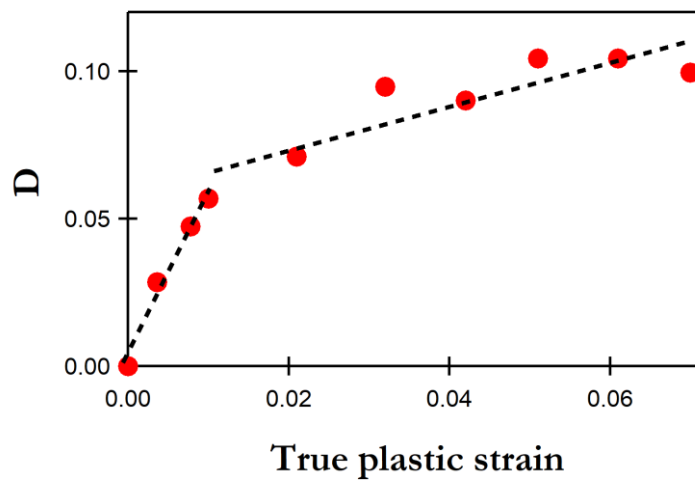


Figure IV-6. Damage parameter evolution as a function of plastic strain measured by loading and unloading tests.

Table IV-1. Numerical results of the critical damage value (D_c) and a true strain criteria (ϵ_{vR})

| | ϵ_{vR} | D_c |
|-----|-----------------|-------|
| CP2 | 0.066 | 0.075 |

Similarly to the evolution of the Young modulus, the damage trend can be divided into two parts. The first is a rapid increase in the value of the parameter D , which, as explained previously is caused by dislocation dynamics. Then, a slight increase is observed after achieving a true plastic strain of above 0.02. The linear model was applied to this last part and the results reveal a critical damage amount of 7.5% at a fracture strain of 0,066 (see Table IV-1). However, this law cannot explain the impact of critical strain, as the first increase is not caused by damage mechanisms. This experiment is usually used to estimate a first approximation of damage. However, the efficiency of this experiment means that is better suited for metals that exhibit high damage evolution and high ductility [55].

Therefore, to confirm these results and determine why the tensile properties of CP1200 steels have low sensitivity to damage at room temperature, a microstructural characterisation of damage was conducted.

2.2. Quantification of voids with the impact of stress triaxiality

a. Presentation of the experimental procedure

Microstructural characterisation of damage was performed using conventional metallurgical analysis [3, 4, 43]. To investigate the evolution of voids as a function of plastic strain, tensile tests on both smooth and notched specimens were initially carried out at room temperature. Figure IV-7 presents the global experimental procedure. Four steps should be described: First, the tensile experiments were performed on smooth and notched geometries. Longitudinal strain was measured by DIC to validate the axially of the tests. Thereafter, local strain was measured by reducing the area of the necking section using the Bridgman equation. Simultaneously, void quantification was performed by image analysis using the IGOR Pro. Thereafter, pictures were taken at the mid-thickness of all specimen surfaces to investigate the repartition of damage in the specimen. Finally, the combination of void localisation and strain measurement was considered to investigate the development of voids as a function of plastic strain.

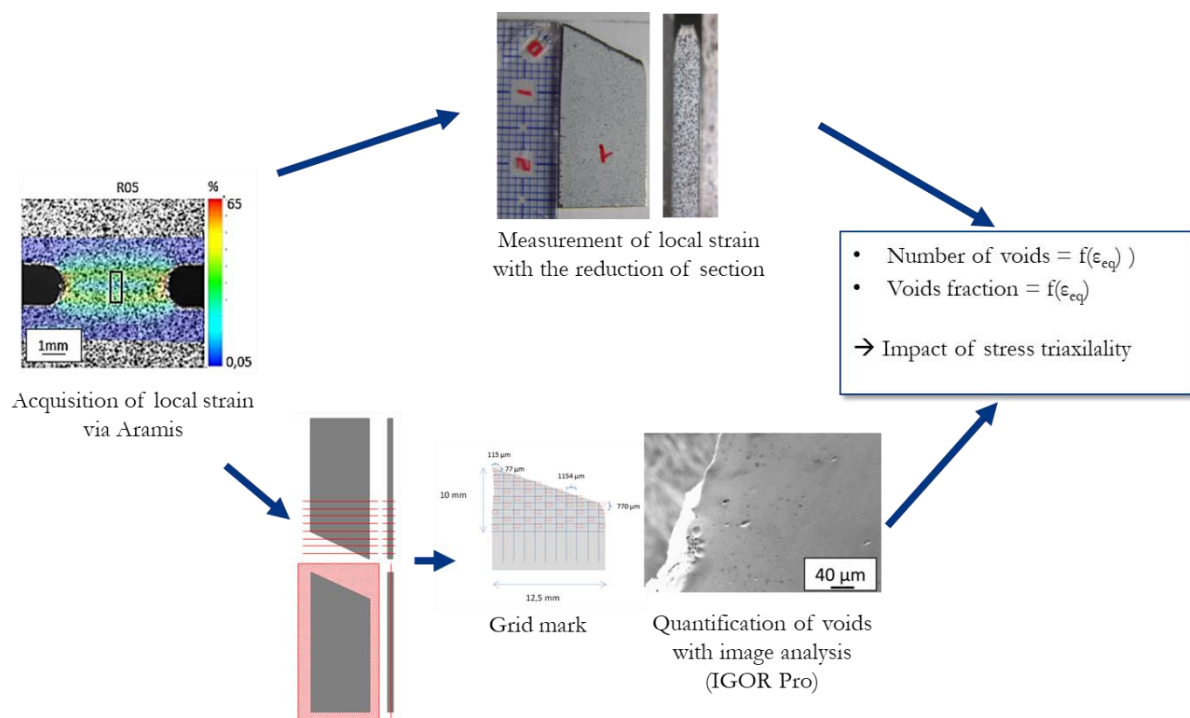


Figure IV-7. Experimental void quantification procedure involving metallurgical methods.

Further details concerning the experimental procedures are provided below:

- **Microstructural quantification by SEM measurements**

To map the damage, specimens were polished until mid-thickness with SiC discs ranging from grain 80 to grain 4000. Then, diamond polishing from 3 μm to 1 μm was carried out to obtain a mirror surface. Thereafter, electropolishing was performed using a solution consisting of 78 mL of perchloric acid, 90 mL of water, 730 mL of ethanol, and 100 mL of 2-butoxyethanol. The electropolishing was conducted under a tension of 40 V for 10 s. The aim of this polishing was to eliminate the particles and to suppress surface residual stresses inserted during the preparation. However, a drawback of this method was the enlargement of voids that could occur during the chemical etching process. Following the preparations for mapping of images covering the entire surface were taken with SEM (Figure IV-8). Approximately 150 pictures per specimen were necessary for each analysis.

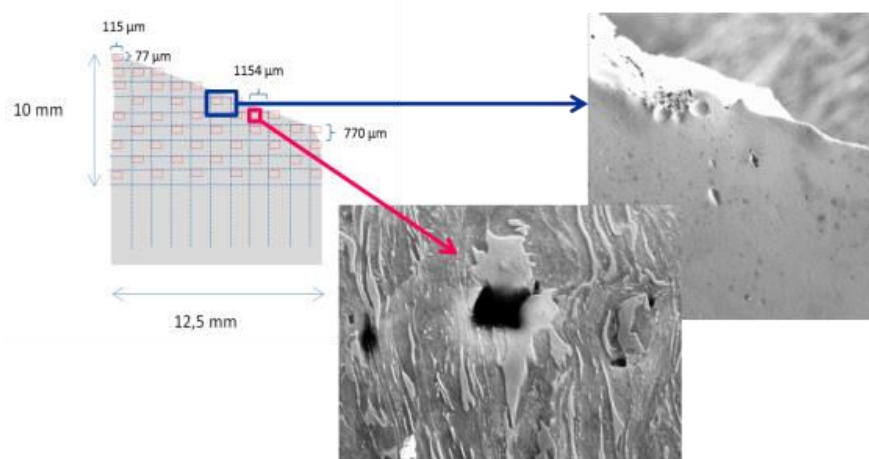


Figure IV-8. Schematic representation of the void measurement procedure.

To choose the best magnification of pictures, a compromise between void size and time of analysis was considered. For tensile specimens tested at room temperature, a high amount of large voids was observed for a specimen width of 12.5 mm. Thus, the magnification chosen was x100, which gave a minimum void size of 6.4 μm^2 using a minimum surface of 5 pixels. In case of notch tests, smaller voids were observed, and the width of the specimen was reduced to 5 mm. Therefore, a higher magnification of x750 was used to obtain a minimum void measurement of 0.11 μm^2 . Then, for the high-temperature tests, the width was fixed at 5 mm for both the smooth and notched specimens. Thus, all measurements were carried out with a magnification of x750, with the exception of those specimens without notches that were measured at room temperature.

Using the approach described above, there are several sources of potential errors that can be discussed. Indeed, since the tests were performed on the surfaces of the specimens, it was only possible to represent volume defects by means of two-dimensional measurements. Therefore, a great deal of void dimension information was lost. Moreover, the low amount of damage present on CP steel does not provide sufficient data to obtain good statistics. Hence, with regard to the number of uncertainties, only qualitative damage evolution was considered.

- **Measurement of local plastic strain**

The Bridgman equation (44) was used to link the plastic strain to void evolution. The logarithm of the ratio between the initial section (S_0) and the deformed section (S) was calculated using this equation:

$$\varepsilon_p = \ln\left(\frac{S_0}{S}\right) \quad (44)$$

To obtain the plastic strain, the thickness and width of the specimens were measured as a function of the distance to the fracture, as shown in Figure IV-9.

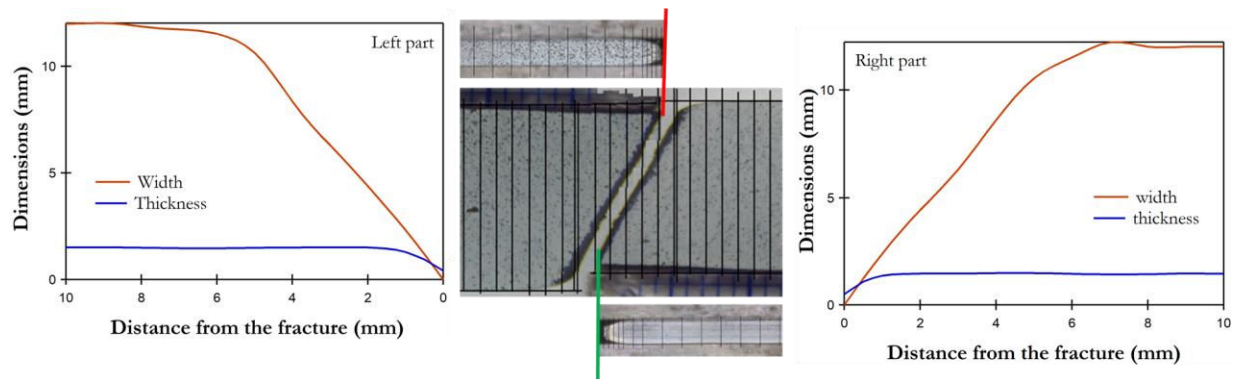


Figure IV-9. Thickness and width measurement as a function of the distance to the fracture.

However, the acquired measurements are not fully representative of the local strain. Indeed, the formation of shear bands with the highest level of plastic strain could be observed during strain localisation. Figure IV-10 represents a schematic representation of this phenomenon. The red and blue areas represent the two parts of the specimen obtained after fracture, while the yellow part is the superposition of the both parts where the necking appears. In this area, the shear bands create an inhomogeneity of strain along the width of the specimen that reduces the value of the plastic strain estimated by the Bridgman equation.

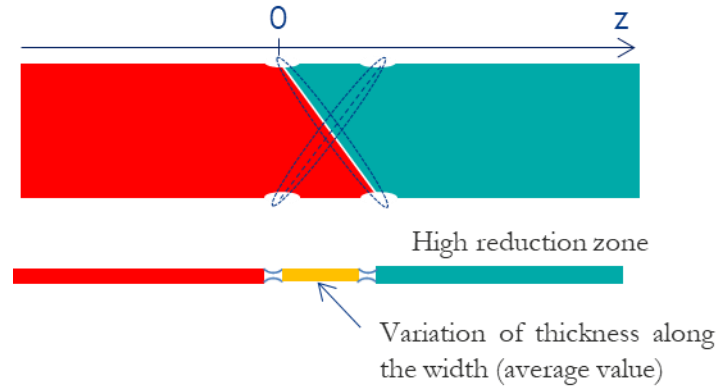


Figure IV-10. Schematic representation of shear band localisation during tensile tests.

During the mechanical tests, additional strain measurements were performed using DIC using the Aramis software. This experiment enabled the identification of the von Mises equivalent strain at the surface of the specimen. With the Von Mises strain, an estimation of plastic deformation during complex solicitations of an isotropic material can be obtained. The von Mises criterion is frequently used in the literature because it provides a good estimation of strain for ductile material. This strain is expressed by Equation (45) corresponding to a general strain tensor defined in Equation (46):

$$\varepsilon_{vM} = \frac{2}{3} \left(\frac{1}{2} [(\varepsilon_{11} - \varepsilon_{21})^2 + (\varepsilon_{22} - \varepsilon_{33})^2 + (\varepsilon_{33} - \varepsilon_{11})^2 + 6\varepsilon_{12}^2 + 6\varepsilon_{23}^2 + 6\varepsilon_{13}^2] \right)^{1/2} \quad (45)$$

$$\bar{\varepsilon} = \begin{pmatrix} \varepsilon_{11} & \varepsilon_{12} & \varepsilon_{13} \\ \varepsilon_{21} & \varepsilon_{22} & \varepsilon_{23} \\ \varepsilon_{31} & \varepsilon_{32} & \varepsilon_{33} \end{pmatrix} \quad (46)$$

To measure the von Mises equivalent strain, a speckle pattern of black points on a white surface was painted on the surface of the specimen. The software then acquired pictures of the specimen throughout the test and calculated the deformation of the pattern. When taking DIC measurements, the size of the mesh, which enables the calculation, has a significant influence on the results. All along the tensile test, pictures of the specimen were taken which enable the measurement of strain. Therefore, the calculated strain is exhibited as the function of the picture numbers for various mesh parameters (Figure IV-11-b). As, displayed in Figure IV-11-c, the mesh size was changed from 15 to 8 pixels with a recovery fixed at 2 pixels.

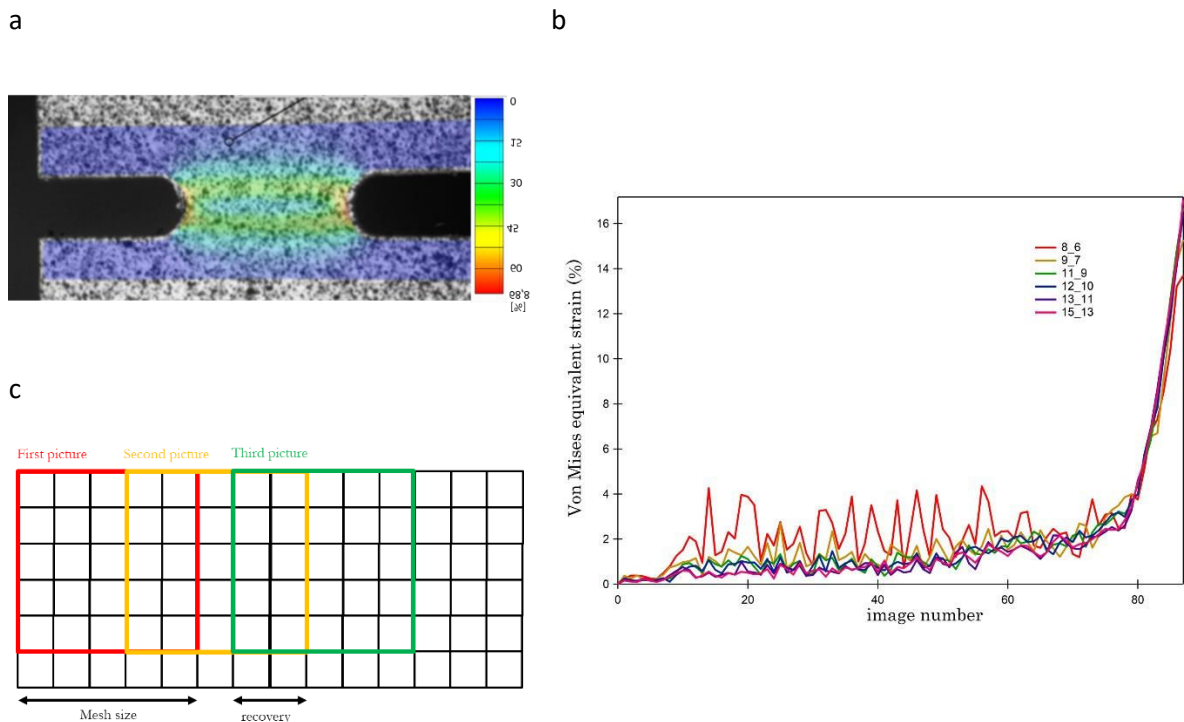


Figure IV-11. (a) Strain measurement obtained by DIC on η_{05} specimen, (b) influence of mesh on this measurement (notation: mesh size in pixel_ number of pixel recovered), and (c) schematic representation of mesh size and shift for the 5 x 5-pixel mesh size.

For the largest mesh (15_13), a smoother curve is obtained. Thus, a loss of data concerning the fracture strain is observed. For the smallest mesh (8_6), a noisy curve is obtained, which also leads to a loss of information. To acquire the best compromise, a mesh of 13 pixels² with 11 shifted pixels was used. Inevitably, inaccuracies remain, as only a 2D measurements were obtained. Therefore, no information on any thickness reduction could be collected.

- **Evolution of stress triaxiality**

Finally, to perform experiments with various stress triaxialities, tensile tests were performed on the notched specimens. The geometries displayed in Table IV-2 enabled the coverage of a range of stress triaxiality range of 0.33 during tensile tests to 1. To simplify the notation, the notched specimens with radii of 5 mm and 0.5 mm and the grooved specimen on the thickness and the width are called $\eta_{0.5}$, $\eta_{0.6}$, and η_1 , respectively.

Table IV-2. Specimen geometries and corresponding stress triaxiality.

| Thickness (mm) | 1.6 | 1.6 | 1.6 |
|--------------------------|-----------------------|--------------|--|
| Smooth | R = 5 mm | R = 0.5 mm | R = 0.5 mm (with grooves in the thickness and the width) |
| $\eta = 0.3$ | $\eta = 0.5$ | $\eta = 0.6$ | $\eta = 1$ |
| Monotonous tensile tests | Biaxial tensile tests | | |

Despite the stress triaxiality evolves with the deformation of the specimen section, the initial theoretical values was used in this thesis calculated by the Equation (47) with R_0 the radius of the notch and a the initial width of the specimen [101,105]. For the specimen with the grooves ($\eta=1$) previous estimation of the stress triaxiality performed on the thesis of J.Chottin was used [3]. To obtain the variation of stress triaxiality with deformation, a coupling with numerical simulation should be performed as it was developed in section IV.1.2.

$$\eta = \frac{1 + 2A}{3\sqrt{A^2 + A + 1}} \quad (47)$$

$$A = \ln[1 + a/(2R_0)] \quad (48)$$

b. Influence of stress triaxiality on the strain at fracture

The evolution of fracture plastic strain was highly investigated in literature to understand fracture mechanisms. The publication of Bao et al. [106] highlighted an increase of plastic fracture strain between 0 and 0.4 of stress triaxiality and a decrease after 0.4. The results of this publication revealed a fracture transition between shear and void formation fracture as it is shown in Figure IV-12.

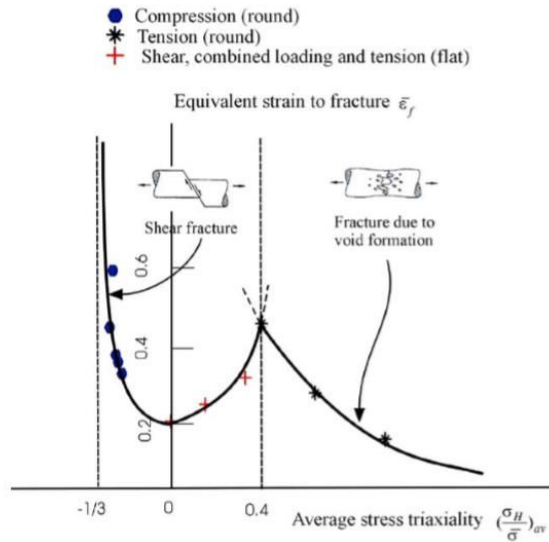


Figure IV-12. Evolution of strain to fracture as a function of average stress triaxiality [106]

To acquire the fracture criterion of CP1200 steel as a function of the stress triaxiality, mechanical properties of the notched specimens were investigated. The results with regard to the tensile curves are displayed in Figure IV-13.

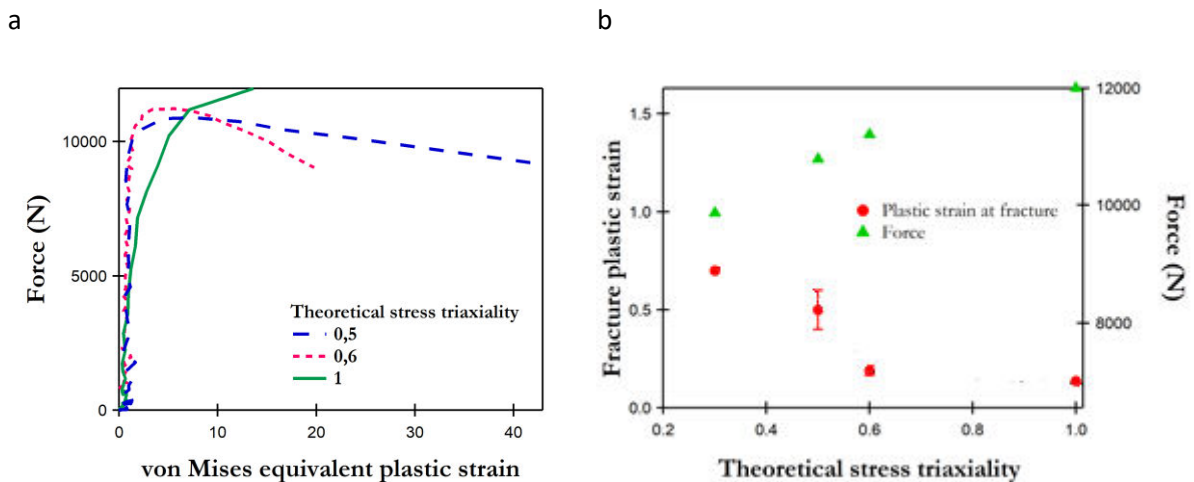


Figure IV-13. (a) Tensile curves obtained on notched and grooved specimens, (b) maximum force and fracture strain as a function of the theoretical stress triaxiality.

The results indicate an increase in mechanical strength with stress triaxiality and a decrease of plastic strain at fracture. The transition between complete ductile fracture and a mixture between ductile and shear fracture is represented in Figure IV-13-b. However this transition was not precisely defined as specimen geometry at 0.4 is missing to complete data. As was noted in the procedure

section, strain was measured using DIC and the Bridgman equation. Table IV-3 presents a comparison of the results of these methods.

Table IV-3. Strain fracture measurements using the Aramis software and the Bridgman equation.

| | Von Mises equivalent strain (%) (measured by Aramis software) | Bridgman fracture strain (%) |
|--------------|--|------------------------------|
| $\eta_{0,6}$ | 19.7 | 66 |
| η_1 | 13.6 | 13.3 |
| $\eta_{0,5}$ | 42 | 62 |

A high difference of strain at fracture for notched specimens with stress triaxialities of 0.5 and 0.6 can be observed. A reduction in thickness, which would not be visible through DIC, might account for these differences. For η_1 , this reduction of thickness is negligible, as this specimen did not present ductility for tensile loading.

c. Fractography of smooth and notched specimens

To obtain further information on fracture mechanisms, fractography analyses were performed using SEM. The pictures obtained for the smooth specimens are presented in Figure IV-14.

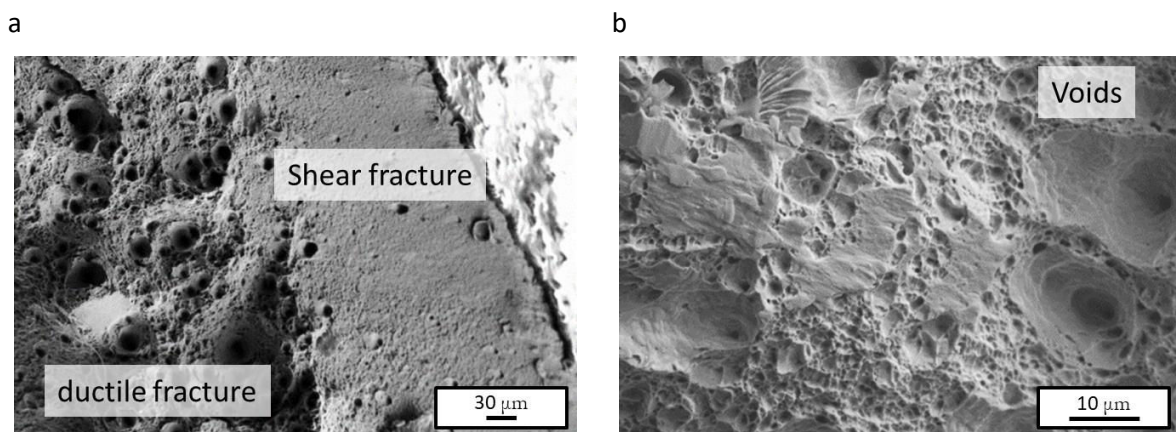


Figure IV-14. Fractography of tensile specimen performed at room temperature ($\eta = 0.33$).

In these fractography, a ductile fracture characterised by dimples and a shear fracture on the edge can be observed. This surface is characteristic of a cup and cone fracture, in which the localisation of plastic deformation occurs first, followed by the creation of a fibrous fracture. Then, the coalescence

of voids begins, which continues until the formation of cracks at the centre of the specimen. Subsequently, a rapid fracture appears as the result of shear fracture development (see Figure IV-15).

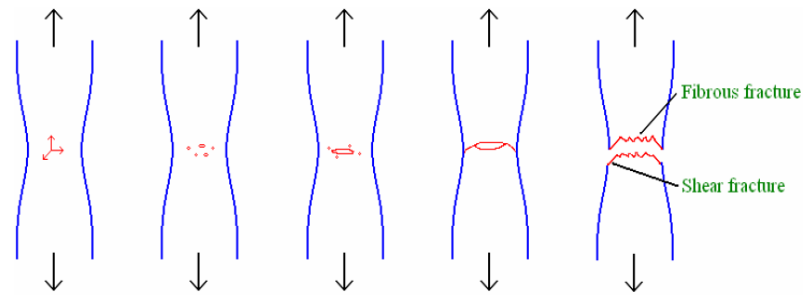


Figure IV-15. Schematic representation of a cup and cone fracture [107].

Fractography was then performed on the notched specimens, the results of which are displayed in Figure IV-16. A global view of the fractures is presented in the first row of images, followed by magnified images of the centre in the second row and of the border in the third.

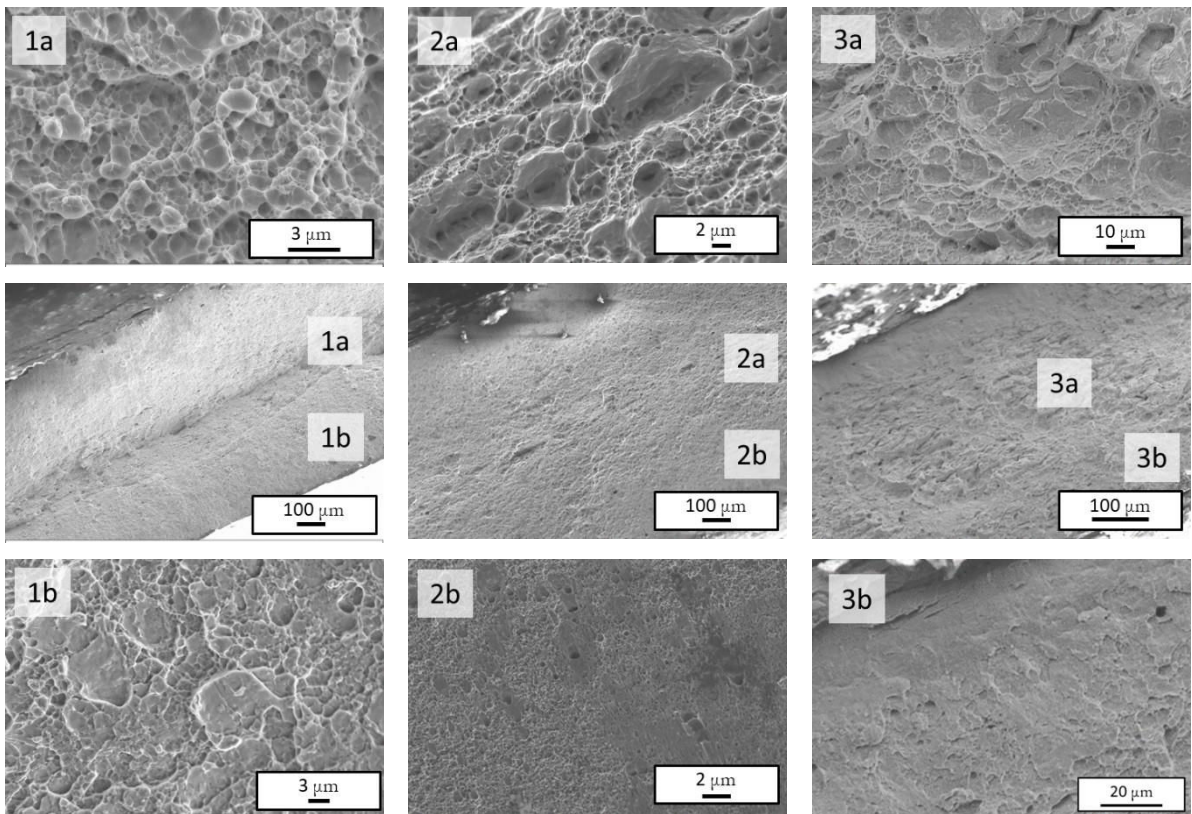


Figure IV-16. Fractography of notched specimens (1) $\eta = 0.5$, (2) $\eta = 0.6$, and (3) $\eta = 1$ at the centres (a) and at the border of each specimen (b).

For $\eta_{0.5}$ and $\eta_{0.6}$, dimples can be observed at the centres of the specimens and shear fractures at the edges. For the smooth tensile tests, cleavage fractures can also be observed, but in lower

amounts. For η_1 , the fracture surface presents a high amount of cleavage areas. The presence of brittle fractures is in accordance with the lack of plasticity observed during tensile loading.

d. Damage evolution depending on stress triaxiality and plastic strain

Before analysing the void evolution of the specimens as functions of plastic strain, the dependence of the maximum void area fraction on stress triaxiality is presented in Figure IV-17.

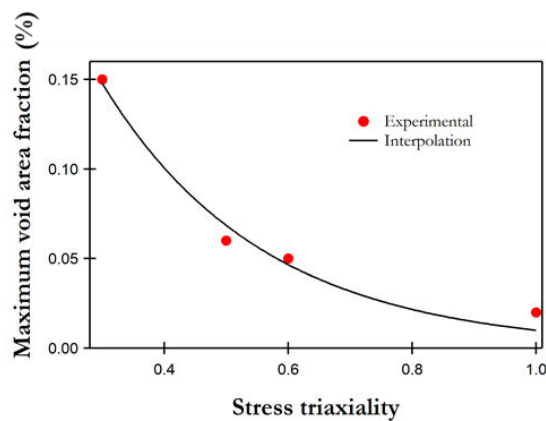


Figure IV-17. Void area fraction as a function of stress triaxiality.

The results show a significant reduction of the maximum void area fraction with an increase in the stress triaxiality. This evolution can be explained by the decrease in plastic strain with the increase of stress triaxiality, as reported by Figure IV-13. In Figure IV-18, the maximum void area fractions are displayed as a function of plastic strain at fracture.

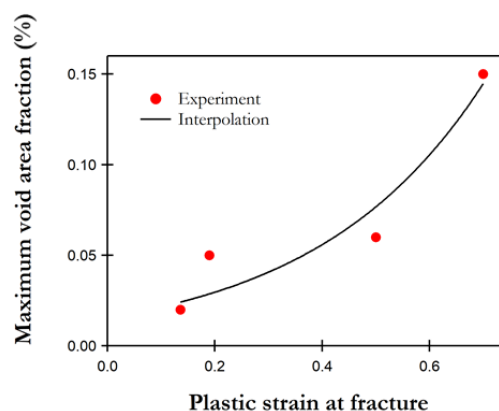


Figure IV-18 Void area fraction as a function of plastic strain at fracture.

Results exhibit an important increase of the maximum void area fraction with the increase of plastic strain at fracture. The formation of voids is then promoted by the ductility of the specimen. To obtain further information on damage, the evolution void area fraction, number of voids and average area of voids as functions of plastic strain were investigated for each specimen. First, analyses were carried out on tensile specimens (see Figure IV-19-b). The void area fraction is displayed as a function of plastic strain (Figure IV-19-b) and the repartition of void area fraction on the surface of the material is presented in Figure IV-19-a. The number and average area of voids were then plotted as functions of plastic strain (see Figure IV-19-c-d). These parameters provide information on nucleation and void growth, respectively.

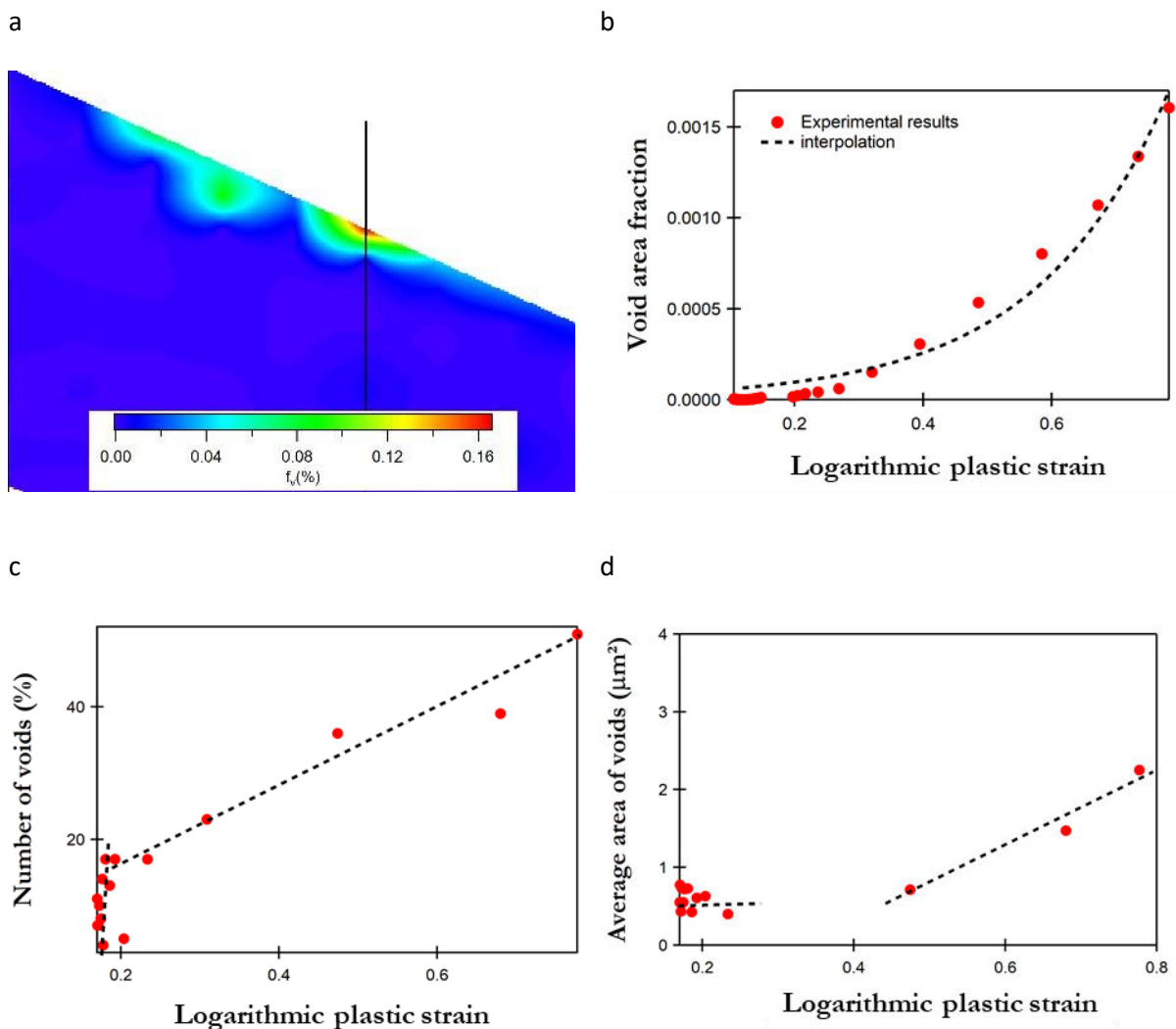


Figure IV-19. (a) Mapping of the void area fraction at the mid-thickness of the specimen after fracture, (b) evolution of area fraction, (c) number, and (d) average diameter of voids as a function of plastic strain.

The mapping of damage reveals the localisation of voids at the crossing of the shear bands created during necking. Moreover, with regard to the evolution of the void parameters, two stages can be considered: At a plastic strain of 0.2, which seems to be the critical value for the initiation of damage, a low number of voids with small dimensions (below $1 \mu\text{m}^2$) are measured. Then, above this level of plasticity strain, an increase in the number of voids, as well as larger areas can be observed. However, the amount of damage stays low even at fracture (0.15%). It is therefore possible to conclude that the fracture of the specimen is rapid and occurs at the first appearance of damage.

According to previous studies on DP1000 steel [4], an exponential law deduced from the model developed by the Rice and Tracey model can be used to represent the evolution of the void area fraction as a function of plastic strain:

$$f_v = A \exp(B \varepsilon_p) \quad (49)$$

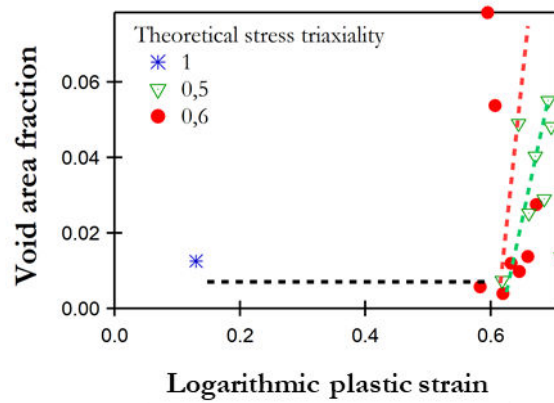
where A is defined as the estimation of the initial void fraction before the beginning of void growth and B depends on the stress triaxiality. The results of the parameters A and B can be compared to these measured on DP1000 steel on the publication of Hug et al.

Table IV-4. Numerical values of parameters A and B of the equation (49) for DP1000 [4] and CP1200 steels.

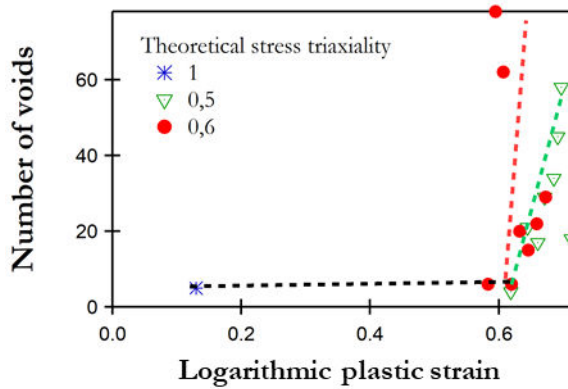
| | A | B | $f_{v\max}$ (%) |
|---------------|----------------------|------|-----------------|
| CP1200 | $4.6 \cdot 10^{-5}$ | 4.59 | 0.16 |
| DP1000 | $1.46 \cdot 10^{-6}$ | 12.7 | 0.8 |

Results reveal that few amount void are quantified before the void growth in CP1200 as in DP1000 steels. The variation between these two steels is observable on the parameter B which is higher for DP1000 steel. Therefore, large voids in DP1000 steel are formed more rapidly on this specimen. However the maximum void area fraction is noticed on Table IV-4 and exhibits a significant reduction of void area in CP1200 steel compared to DP1000 steel. In CP1200 steel, the fracture of specimen occurs then rapidly after the beginning of void growth. Void growth, number, and fraction were also plotted for notched specimens in Figure IV-20. For η_1 , the measured plastic strain was too low to be measured as a function of the distance of the fracture. Hence, the void area fraction, number of voids and average void area are only represented at the maximum plastic strain value in Figure IV-20.

a



b



c

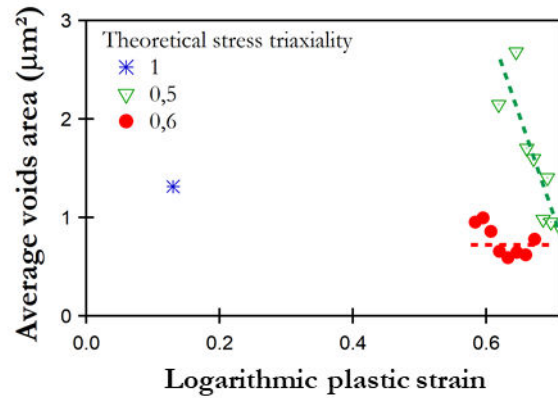


Figure IV-20. (a) Void area fraction, (b) number of voids, and (c) average void area as functions of plastic strain.

The results obtained for each specimen exhibit increases in fraction, growth, and number of voids with plastic strain. With regard to the evolution of the void area fraction, $\eta_{0.5}$ and $\eta_{0.6}$ exhibit a similar critical strain (0.6), after which a rapid development of voids can be observed. For η_1 , the void area fraction is lower, which is consistent with the low ductility observed during the tensile tests. This lack of ductility reduces the development of voids. It is therefore possible to suppose that a transition between ductile and brittle fracture occurs at a stress triaxiality between 1 and 0.6. Further experiments with an intermediate stress triaxiality should be performed to confirm this hypothesis.

Moreover, the number of voids is quite similar for $\eta_{0.5}$ and $\eta_{0.6}$, and a lower amount of voids was measured for η_1 . However, for $\eta_{0.6}$ and η_1 , the average void area is approximately $1.5 \mu\text{m}^2$. Slightly high values of average void area are measured in $\eta_{0.5}$. Therefore, the growth of voids accelerated with stress triaxiality, as η_1 presented similar void areas at a lower plastic strain than $\eta_{0.5}$ and $\eta_{0.6}$. This

observation is in accordance with the Rice and Tracey model, which predicts an increase in void growth with stress triaxiality. Nevertheless, it is possible to conclude that the microstructures of CP1200 steels do not permit a high development of damage, as they exhibit low values for the area fraction, growth, and number of voids.

e. Damage localisation in CP1200 steels

To explore the impact of the microstructures of CP1200 steels on void nucleation, void localisation was performed. Figure IV-21 presents images depicting the smallest voids present in the microstructure. These images were taken to determine their localisation.

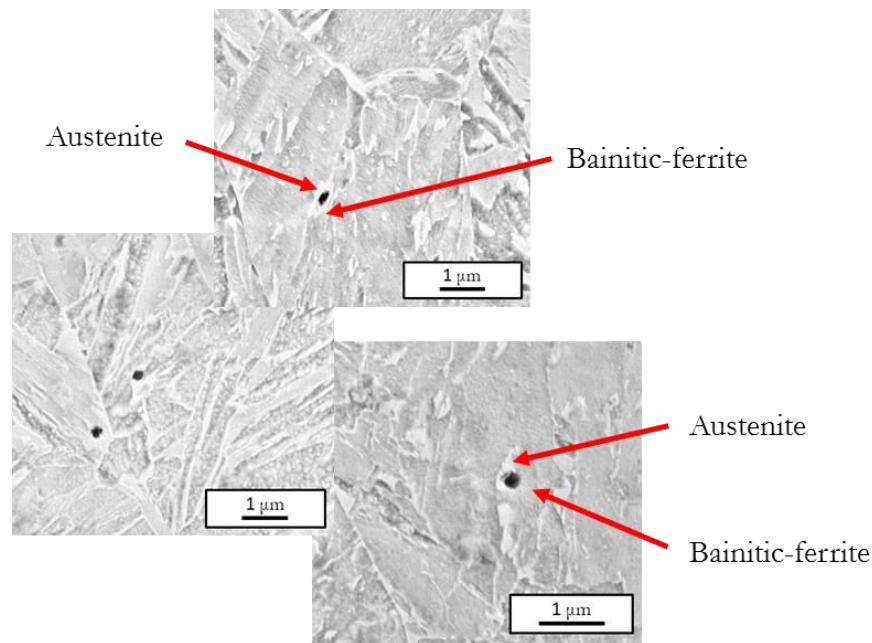


Figure IV-21. SEM pictures of CP1200 microstructure after tensile tests to observe void localisation ($\eta=0.3$).

In the tensile test specimens, voids were mostly found to be located at the interfaces between laths or between austenite and bainitic ferrite. This observation can be extended to the specimens subjected to higher stress triaxialities. Figure IV-22 presents an example of the images obtained for $\eta_{0.5}$. Based on these findings, it can be concluded that modifying the stress state does not influence the localisation of voids.

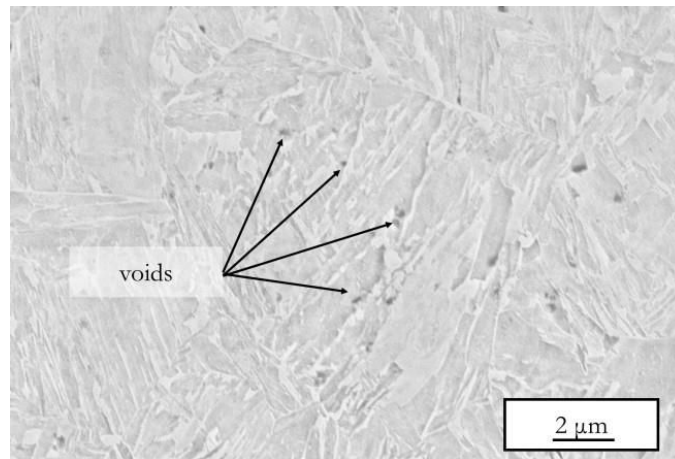


Figure IV-22. SEM picture of $\eta_{0.5}$ to observe the void localisation in the microstructure.

3. Influence of temperature on damage evolution

As shown in Chapter III, the mechanical properties of CP1200 are highly modified by an increase in temperature. Consequently, strain at fractures and damage mechanisms could also be influenced by a change in temperature.

a. Fractography of tensile specimens performed at high temperatures [400°C–600°C]

The fracture surfaces of the tensile specimens tested on the TMF were analysed. Figure IV-23 presents the fractographies observed during the tests conducted at the temperatures of 400°C, 500°C, and 600°C.

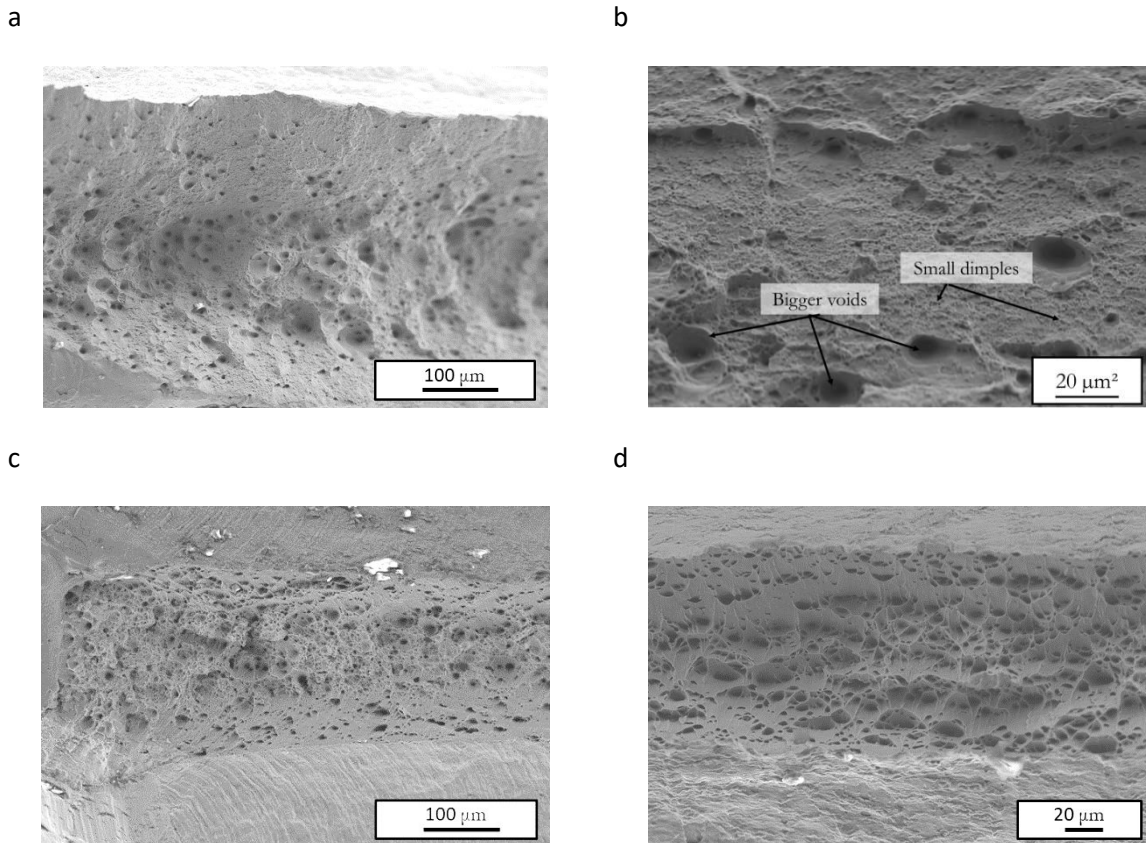


Figure IV-23. Impact of temperature on fractography of tensile specimens at (a,b) 400°C, (c) 500°C, and (d) 600°C.

From room temperature to 500°C, two different populations of dimples can be observed. For example, at 400°C, larger voids surrounded by smaller dimples are exhibited (see Figure IV-23-a and b). At 600°C, a single population of voids of the same magnitude can be observed. Moreover the measurements of voids on fracture surfaces (see Table IV-5) indicate a reduction in void size with temperature.

Table IV-5. Average void area on fracture surface (μm^2).

| 400°C | 500°C | 600°C |
|-------|-------|-------|
| 26 | 11.7 | 3.7 |

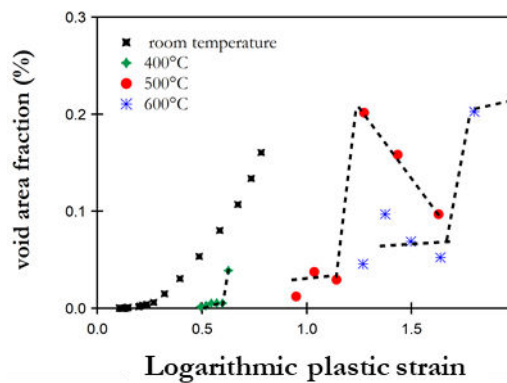
Two mechanisms of fracture surface creation are suggested by these observations: Below 500°C, a first nucleation of voids occur. These voids are responsible for the shear band formation. Thereafter, the creation of localised plasticity accelerates voids growth and nucleation [108]. This

fracture mechanism is not observed at 600°C, however, where only one population of voids can be observed.

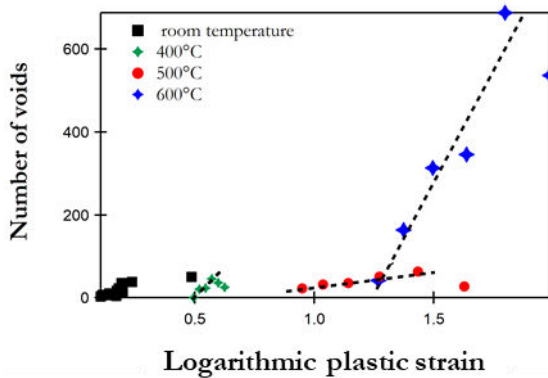
b. Influence of high-temperature mechanical stresses on damage evolution

According to the previous results, damage evolution is modified by an increase in temperature. Having obtained this result, as before, the void area fraction, number, and growth of voids were investigated (see Figure IV-24).

a



b



c

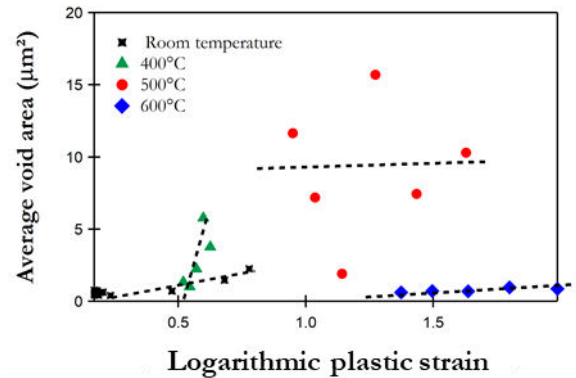


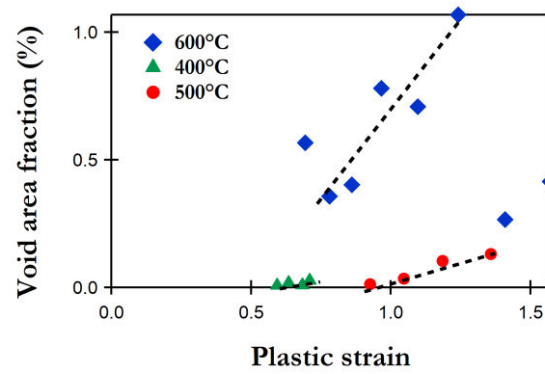
Figure IV-24. Evolution of (a) void area fraction, (b) number of voids, and (c) growth of voids as functions of the plastic strain for tensile specimens ($\eta = 0.33$).

For all temperatures, a critical strain after which the void area fractions increase significantly can be observed: At 400°C, the critical strain is measured at 0.6, at 500C 1.14 and, at 600°C 1.6. Below these plastic strains, the measured damage is stable. As shown in Figure IV-24-a, this critical strain value increases with temperature. Following this augmentation of voids characteristics, a reduction or stabilisation of void formation is observed near the fracture. With regard to the number of voids, an

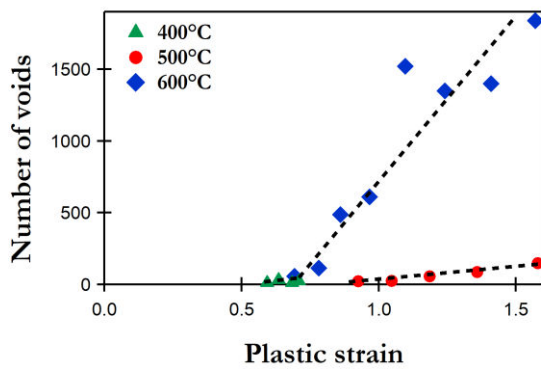
increasing trend, which is dependent on the plastic strain, is found for all temperatures. However, it should be noted that a small amount of voids developed below 500°C and that a significant increase in void formation occurred at 600°C. Finally, the growth of voids was measured. In Figure IV-24-c, to keep the graphic readable, only the average values are represented. Indeed, for all temperatures, a standard deviation twice above the average was calculated. The results indicate that, at 400°C, an increase in void size occurred as a result of greater plastic strain, whereas, at 500°C, a medium value of approximately 10 μm^2 , with a high dispersion of results, can be identified. Finally, at 600°C, a higher number of voids is observed, with the average size being approximately 1 μm^2 . Based on these results, two different stages can be identified: Below 500°C, the number of voids increases slightly with temperature, and a high increase in average void area was measured. The growth mechanism seems to be responsible for the damage. At 600°C, a significant increase in the number of voids can be observed. Moreover, a high reduction of the void area is measured. Then, at 600°C, nucleation appears to become the main damage mechanism. These results suggest that a transition between damage mechanisms occurs between 500°C and 600°C.

To further explore the impact of the stress state, the same analysis was performed on the notched specimens (see Figure IV-25).

a



b



c

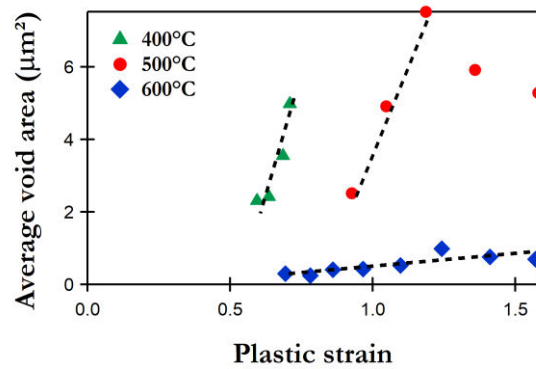


Figure IV-25. Evolution of (a) void fraction area, (b) number of voids, and (c) growth of voids as a function of the plastic strain for the notched specimens ($\eta = 0.5$).

As for the smooth tensile tests, below 500°C, an increase in the void fraction area and growth of voids can be observed. However, at 600°C, a significant increase in the number of voids can be observed. Furthermore, the reduction in void size should also be noted.

To sum up the results, the evolution of the number of voids, the maximum average void area and the critical strain after which the void area fractions increase were represented as functions of temperature and stress triaxiality in Figure IV-26.

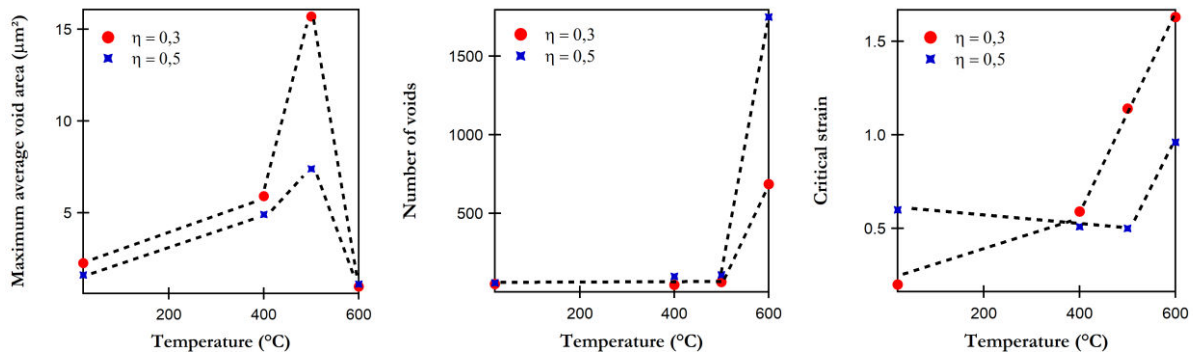


Figure IV-26. Evolution of (a) the maximum average void area , (b) the number of voids and (c) the critical strain where after which the void area fraction increase as functions of temperature and stress triaxiality ($\eta=0.3$ and $\eta=0.5$).

Both the smooth and notched specimens exhibit similar behaviour in temperature. In order to understand the transition between void localisation and the metallurgical characterisation of the specimens after tempering were then studied.

c. Observations of void localisation and microstructure transformation

Figure IV-27 presents the evolution of void localisation with temperature and stress triaxiality.

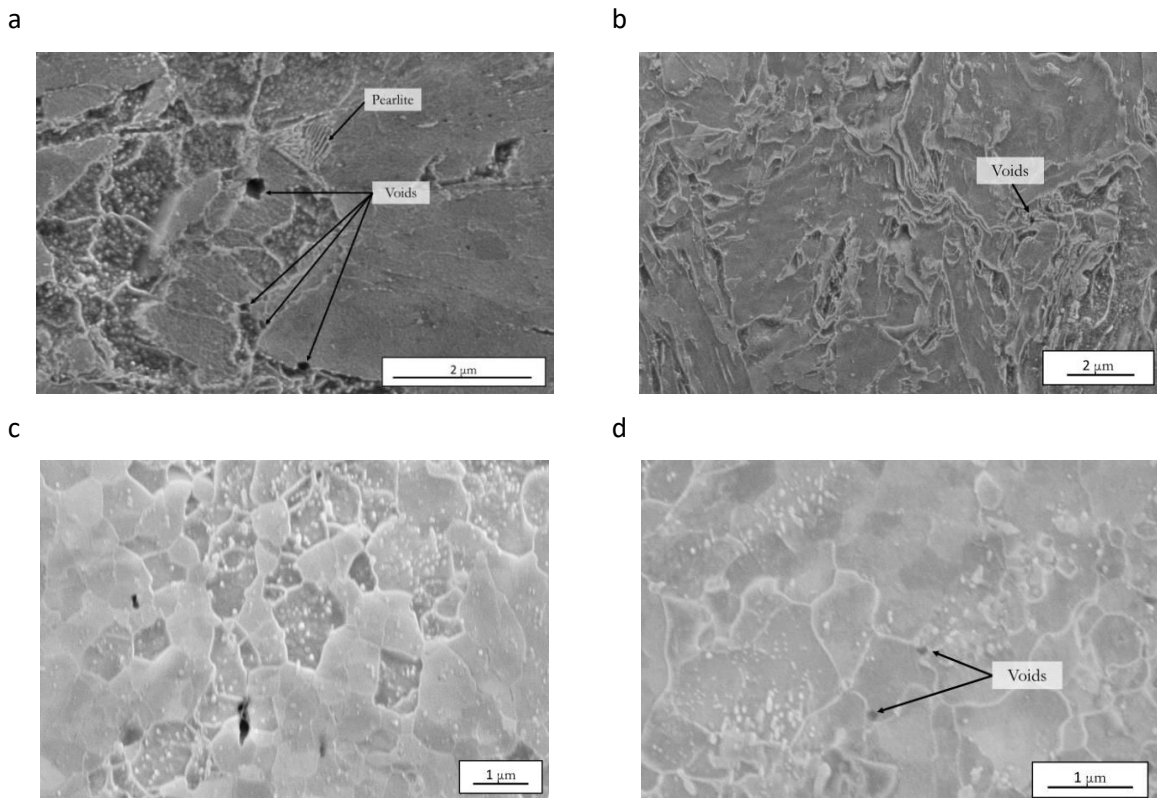


Figure IV-27. Example of void localisation with the temperature and stress triaxiality: 400°C (a) smooth specimen and (b) $\eta = 0.5$, 600°C (c) smooth specimen and (d) $\eta = 0.5$.

For all specimens, void nucleation occurred at the interfaces between bainitic-ferrite and austenite. Disturbed microstructures similar to those observed after the tensile tests at room temperature become observable at 400°C and 500°C. However, the modifications that occur to the microstructures of the samples at 600°C are remarkable. Therefore, to obtain further information on this modification, EBSD analyses of the specimens deformed at 600°C were performed. In addition, IPF cartographies are displayed in Figure IV-28.

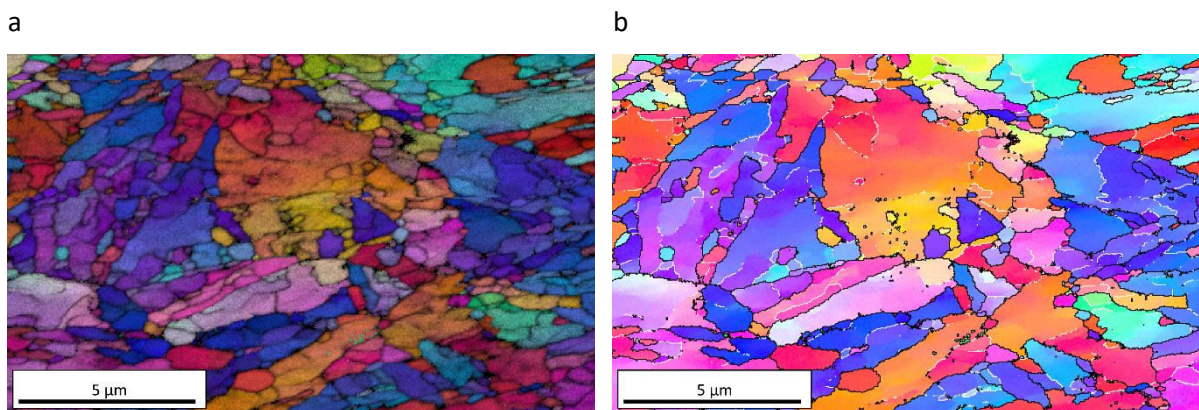


Figure IV-28. (a) Inverse pole figure and IQ mapping, (b) IPF mapping with low angle (white: 2°–15°) and high angle (black: < 15°) boundaries of tensile specimens deformed at 600°C.

In the image depicting the superposition of the IQ and IPF maps, a similar microstructure to that portrayed in the SEM pictures can be observed. However, the IPF mapping reveals that no modification of crystallographic orientation is observable between these structures. These observations can be explained by the recrystallisation of the microstructure during the tensile test performed at 600°C. Two factors may have influenced this recrystallisation: the temperature and the applied stress. Therefore, in order to explore the impact of stress on this microstructure, a metallurgical characterisation of the head of the tensile specimen was performed. In this localisation, the microstructure was tempered but not deformed (see Figure IV-29).

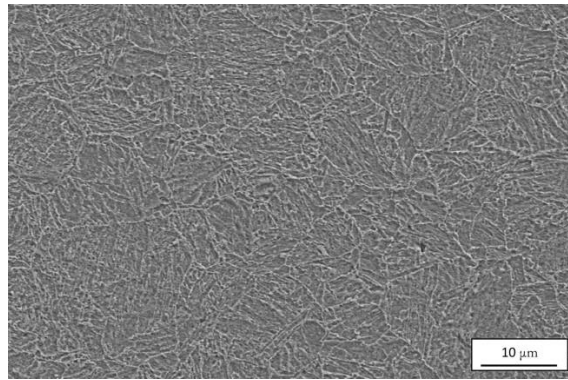


Figure IV-29. Scanning electron microscopy image of the head of a specimen tempered at 600°C ($\eta = 0.33$).

The above image does not reveal the presence of the equiaxed structure observed previously. It is therefore possible to suppose that the applied stress had an influence on the recrystallisation. Therefore, at 600°C, a dynamic recrystallisation can be observed in CP1200.

Microstructures similar to those depicted in Figure IV-27 were observed by TEM in the work conducted by Garcia Mateo et al. [33], as is shown in Figure IV-30. These images were obtained after subjecting a bainitic steel sample to different temperatures and various tempering times. As was found to be the case for the steels investigated in this dissertation, RA was found to be present in both island and films in the samples considered by Garcia-Mateo et al.

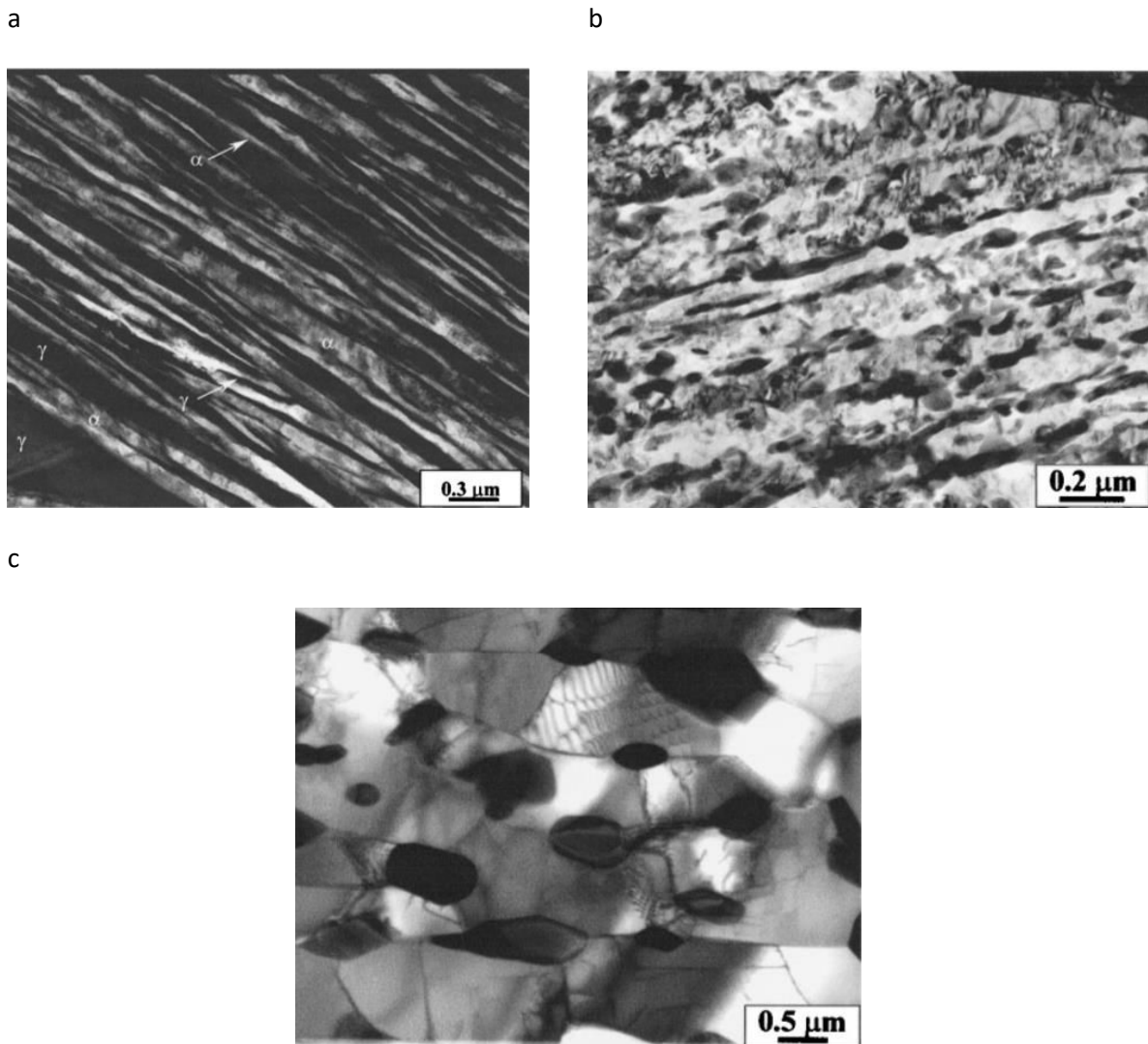


Figure IV-30. TEM images of the microstructure of the samples in the work of Garcia-Mateo et al: (a) the initial microstructure, (b) the microstructure at 600°C after 1 h of tempering, and (c) the microstructure at 730°C after 42 days [33].

The different microstructures observed by Garcia-Mateo et al. suggest that the precipitation of carbides occurs due to the diffusion of carbon promoted by the temperature. After 42 days, the sample tempered at 730°C exhibits the recrystallisation of ferrite and the formation of large carbides. The experiments conducted for this thesis used lower tempering times. However, the formation of ferrite grains was also observed in the present study. Therefore, it is possible to suggest the hypothesis that a diffusion of carbon occurs during the tensile test and that this carbon leads to the modification. It was noted in the literature review that carbides are brittle phase and lead to a premature fracture of bainitic steels. Therefore, an increase in the number of voids could be explained by the formation of carbides. To confirm this hypothesis, carbides should be identified by diffraction analysis performed by TEM.

4. Synthesis of the results with regard to damage evolution

Four main results can be extracted from this chapter:

- The first investigation of damage using loading and unloading tests highlighted the low impact of damage on tensile properties of CP2. However, this method was only used to obtain a first approximation as is usually used for metals exhibiting greater ductility and damage than CP2. Therefore, this method is not the most efficient means of quantifying damage.
- The evolution of damage was also studied with the void evolution as a function of plastic strain. The results indicated a high dependence of the void area fraction on stress triaxiality and plastic strain. A reduction in the number of voids without significant modification of the average diameter was observed with an increase of stress triaxiality. However, a specimen geometry featuring an intermediate stress triaxiality would be required to draw more complete conclusions.
- Following the quantification of voids, their localisation within the microstructure was investigated. The majority of voids were found to be located at the intersection between RA and bainitic ferrite. These results are in accordance with previous studies on multiphase steels that have highlighted the nucleation of voids at the interfaces of bainitic-ferrite and austenite [4,56].
- Next, the influence of temperature on damage was studied. An intriguing transition of damage mechanisms was observed after 600°C. Indeed, below this temperature, the main modification related to the rise of temperature was the increase in the critical strain, at which point the nucleation of damage became measurable. At these temperatures, no significant impact on the number and growth of voids was observed. However, at 600°C, an important increase in the number of voids, along with a reduction in void growth, was noted. This modification can be linked to the dynamic recrystallisation of the microstructure.

One problematic aspect of this subject was comparing the results obtained for DP1000 and CP1200 steels. To this end, a summary of the general mechanical, metallurgical, and damage characteristics of these steels is presented in Table IV-6.

Table IV-6. Comparison of damage properties between DP1000 and CP1200 steels.

| | DP1000 | CP1200 |
|--|--|--|
| General metallurgical and mechanical properties | | |
| UTS (MPa) | 1040 | 1301 |
| Deformation | 0.8 | 0.8 |
| Critical temperature of mechanical properties reduction | 290°C | 400°C |
| Microstructure | Martensite and ferrite | Bainite and RA |
| Impact of temperature on microstructure | Tempered martensite with carbides and soft ferrite | Bainitic structure with carbides until 500°C; above 600°C, dynamic recrystallisation |
| Damage properties | | |
| Void quantification | + | - |
| Void localisation | At the interfaces by martensite cracking and debonding at the inclusions | At the interfaces between bainite and austenite and between bainite sheaves |
| Void localisation under mechanical solicitations at high temperatures | By ferrite cracking | At the interfaces between bainite sheaves |

To understand the difference in damage mechanisms between DP1000 and CP1200 steels, the conclusions regarding the damage evolution observed in DP steels are presented first [4]. Damage in DP steels depends on the nucleation and growth of voids due to decohesion of the interfaces between ferrite and martensite, by the cracking of martensite, and by debonding around the inclusions. These mechanisms result from micro-strain heterogeneities between the hard and soft phases. During this study, the impact of temperature (ranging between 20°C and 480°C) on this microstructure was investigated. At low temperature (130°C), voids were observed at the interfaces and inside the ferrite. These observations can be explained by the higher deformation of ferrite and the low plastic straining of the martensite. When the temperature increases (380°C), both phases are highly deformed, which produces both an increase in void size and a decrease in the number of voids. Moreover, at high

temperatures, the formation of carbides within the martensite was detected. This diffusion leads to the austempering of martensite, which generates high number of mobile dislocations. This causes a softening of the ferrite, which increases its capacity to nucleate voids and promotes void growth.

Complex phase steels present lower damage than DP steels. The results presented in Chapter III initially indicated that a high amount of internal stress leads to kinematic hardening. Thus, this thin microstructure of CP2, which is characterised by a high density of dislocations, hinders void growth. However, with an increase in strain, multiple slip systems are activated, which promotes the softening of the material. In spite of this, the first appearance of damage leads to the formation of shear bands, which accelerate the growth and the formation of voids.

With an increase in temperature, certain mechanisms of damage evolution in CP steels become similar to those exhibited by DP steels. Indeed, below 500°C, the decomposition of austenite discussed in Chapter II occurred in CP2. The creation of carbides was then observed, which led to the softening of bainite. After 600°C, dynamic recrystallisation was observed. It was observed that an increase in void nucleation was achieved without an enlargement of void size.

Conclusion

The objectives of this thesis were to acquire information on the plasticity and damage mechanisms of the CP1200 multiphase steels. The company Faurecia Automotive Seating, which seeks such information to improve the requirements with regard to steels, initiated this study. At the moment, the company is confronted with the difficulty of having to choose among the various steels offered by different suppliers and the variable microstructural and mechanical properties of these steels. Thus, the first aim of this project was to define the metallurgical and mechanical properties of CP1200. The second objective of this project was to develop a better understanding of complex phase steels and obtain data concerning the plastic and damage behaviours of these steels.

The main findings with regard to the characteristics of these steels at room temperature can be summarised as follows:

- Steels depending on their suppliers exhibit a large range of mechanical properties and microstructures. Chapters I and II investigated the impact of bainitic lath size and the presence of RA on the mechanical and damage properties of CP1200. It was found that the thinness of the bainitic structures determines the strength and that the presence of RA islands leads to an increase in ductility.
- The investigation concerning the plasticity mechanisms by cyclic tension/compression experiments made it possible to explore the development of the kinematic hardening caused by the long-range interactions of dislocations. The rapid apparition of cyclic softening for low amounts of plastic strain, confirmed the presence of a high density of dislocations in the initial microstructure.
- The evolution of damage with an increase in stress triaxiality at room temperature confirm that damage amount is reduced with triaxiality. The localisation of voids at the interfaces between bainitic ferrite and austenite can also be observed. As soon as the first voids are created the fracture of the material occurs rapidly, which implies a high sensitivity of CP1200 steel to damage. Large deformation was not observable after apparition of damage.

Moreover, studying the thermal stability of CP1200 enables the acquisition of new information concerning the behaviour of these steels:

- The microstructure of bainitic steels is highly influenced by temperature. According to the DSC and dilatometry experiments, the decomposition of austenite into ferrite and cementite occurs at temperatures between 300°C and 400°C. At higher temperatures, the transformation of ferrite and cementite into austenite can be observed.
- The microstructure of bainitic steels is highly influenced by temperature, and has an important impact on the mechanical behaviour. In fact, a significant reduction in strength and an increase in strain at fracture were observed after 400°C, with the transformation of ferrite and cementite into austenite. In addition to this metallurgical transformation, viscoplastic effects caused a reduction in tensile properties.
- Investigating the impact of temperature on damage revealed a change in damage mechanisms at 600°C. Below this temperature, an increase in void growth was observed. However, after 600°C, a significant increase in the number of voids was depicted, which was accompanied by a decrease in void growth. This phenomenon can be linked to a modification of the microstructure.

The above mentioned results provide information on the plasticity and damage mechanisms of CP1200 steels. However, it would be interesting to continue the investigation conducted in this project by exploring the following areas:

- To improve the results that concern the damage investigation, the experiments should be repeated to acquire more statistical data. With enough data, the damage laws could be applied. Moreover, an additional specimen geometry between the stress triaxialities of 0.6 and 1 must be performed to complete the figure depicting the evolution of void area fraction as a function of stress triaxiality.
- The use of numerical simulation could add value to future works. For example, the stress triaxiality during tensile tests on notched specimens could be better determined using numerical tools. Moreover, the use of numerical simulations could enable the application and verification of the hardening coefficient identified during the tension-compression tests.
- The evolution of microstructures at 600°C under the conditions used for the tensile tests was observed but not deeply investigated. Complementary experiments such as in situ tensile tests under SEM at high temperature temperature could be performed to investigate the

phenomenon that leads to this microstructure modification and why this structure promotes the nucleation of voids.

- Three grades of steel, with various amounts of RA and lath sizes, were studied. However, mechanical and damage properties were only investigated for one grade of steel. The literature review indicated that the percentage of RA islands influences the plasticity and damage properties of CP. Therefore, it could be interesting to perform similar tests on the other grades of CP1200 steels to examine the impact of RA islands and lath sizes on the properties of these steels. Such new tests could make it possible to investigate the impact of the TRIP effect.

Results collected on this thesis provide supplement knowledge and data for Faurecia. A complete microstructural characterisation was performed on different steel grades coming from various suppliers. This microstructural proprieties were associated to general mechanical properties. Thereafter experiments with cyclic tensile revealed a high impact of kinematic hardening provided by dislocation long-range interactions. Finally this PhD thesis provides information on the evolution of damage at various stress triaxialities. A rapid fracture of the specimen was observed after the first apparition of damage. Therefore, it is possible to conclude that the forming of the CP1200 steel is limited as soon as the first apparition of damage, otherwise the fracture of the product could occurs suddenly. However, the damage evolution is highly modified in temperature: the growth of voids was more present in temperature and the nucleation occurred at higher strain.

References

- [1] S. Keeler, M. Kimchi, P.J. Mooney, *Advanced High-Strength Steels Application Guidelines Version 6.0*, Adv. High-Strength Steels Appl. Guidel. (2017).
- [2] *An Assessment of Mass Reduction Opportunities for a 2017-2020 Model Year Vehicle Program*, Lotus Engineering Inc., (2010).
- [3] J. Chottin, *Etude de l'endommagement des aciers Dual-Phase : Application au procédé de mise en forme par cambrage*, PhD Thesis, University of Caen, (2011).
- [4] E. Hug, M. Martinez, J. Chottin, Temperature and stress state influence on void evolution in a high-strength dual-phase steel, *Mater. Sci. Eng. A*. 626 (2015) 286–295.
- [5] J. Chottin, E. Hug, M. Rachik, Damage accumulation in DP1000 steel sheets submitted to various stress states, *Steel Res. Int.* (2011) 895–900.
- [6] J. Chottin, E. Hug, M. Rachik, Influence of stress state on mechanical properties of Dual Phase steel sheets. Experimental and finite element analysis approach., *Steel Res. Int.* 81 (2010) 809–812.
- [7] N. Fonstein, *Advanced High Strength Sheet Steels*, Edition Springer Libri, (2015).
- [8] R. Kuziak, R. Kawalla, S. Waengler, *Advanced high strength steels for automotive industry*, *Arch. Civ. Mech. Eng.* 8 (2008) 103–117.
- [9] E. Billur, Dykeman, J, T. Altan, Three generations of advanced high-strength steels for automotive applications, Part II, *Stamp J.* (2014) 12–13.
- [10] J.-H. Schmitt, T. Lung, New developments of advanced high-strength steels for automotive applications, *Comptes Rendus Phys.* 19 (2018) 641–656.
- [11] A. Grajcar, R. Kuziak, W. Zalecki, Third generation of AHSS with increased fraction of retained austenite for the automotive industry, *Arch. Civ. Mech. Eng.* 12 (2012) 334–341.
- [12] H.K.D.H. Bhadeshia, A Personal Commentary on “Transformation of Austenite at Constant Subcritical Temperatures,” *Metall. Mater. Trans. A*. 41 (2010) 1351–1390.
- [13] S.P. Bhat, *Advances in high strength steels for automotive applications*, Great designs in steel seminar (2011).
- [14] F.G. Caballero, M.J. Santofimia, C. García-Mateo, C.G. De Andres, Time-temperature-transformation diagram within the bainitic temperature range in a medium carbon steel, *Mater. Trans.* 45 (2004) 3272–3281.
- [15] S. Samanta, P. Biswas, S. Giri, S.B. Singh, S. Kundu, Formation of bainite below the MS temperature: Kinetics and crystallography, *Acta Mater.* 105 (2016) 390–403.

- [16] D. Liu, B. Bai, H. Fang, W. Zhang, J. Gu, K. Chang, Effect of tempering temperature and carbide free bainite on the mechanical characteristics of a high strength low alloy steel, *Mater. Sci. Eng. A.* 371 (2004) 40–44.
- [17] H.K.D.H. Bhadeshia, *Bainite in steels: theory and practice*, Third edition, Maney Publishing, Leeds, (2015).
- [18] H.I. Aaronson, W.T. Reynolds, G.J. Shiflet, G. Spanos, Bainite viewed three different ways, *Metall. Trans. A.* 21A (1990) 1343–1379.
- [19] B.L. Bramfitt, J.G. Speer, A perspective on the morphology of bainite, *Metall. Trans. A.* 21 (1990) 817–829.
- [20] H. Bhadeshia, Some phase transformations in steels, *Mater. Sci. Technol.* 15 (1999) 22–29.
- [21] E. Boucard, *Etude de l'influence de l'état métallurgique de l'austénite sur le microstructure de transformation de phase dans les aciers bas carbone*, PhD Thesis, University of Lorraine, 2014.
- [22] E. Swallow, H.K.D.H. Bhadeshia, High resolution observations of displacements caused by bainitic transformation, *Mater. Sci. Technol.* (1996) 121–125.
- [23] H.K.D.H. Bhadeshia, R. Honeycombe, *Steels: microstructure and properties*, Third edition, Elsevier/Butterworth-Heinemann, 2006.
- [24] M. Takahashi, H.K.D.H. Bhadeshia, Model for transition from upper to lower bainite, *Mater. Sci. Technol.* (1990) 592–603.
- [25] S. Zajac, V. Schwinn, K.H. Tacke, Characterisation and Quantification of Complex Bainitic Microstructures in High and Ultra-High Strength Linepipe Steels, *Mater. Sci. Forum.* 500–501 (2005) 387–394.
- [26] K. Radwański, Structural characterization of low-carbon multiphase steels merging advanced research methods with light optical microscopy, *Arch. Civ. Mech. Eng.* 16 (2016) 282–293.
- [27] A.-F. Gourgues, H.M. Flower, T.C. Lindley, Electron backscattering diffraction study of acicular ferrite, bainite, and martensite steel microstructures, *Mater. Sci. Technol.* 16 (2000) 26–40.
- [28] S. Zajac, J. Komenda, P. Morris, P. Dierickx, S. Matera, F. Penalba Diaz, Quantitative structure-property relationships for complex bainitic steels, European commission EU21245, (2005).
- [29] L.C. Chang, H. Bhadeshia, Austenite films in bainitic microstructures, *Mater. Sci. Technol.* 11 (1995) 874–882.
- [30] A. Varshney, S. Sangal, S. Kundu, K. Mondal, Super strong and highly ductile low alloy multiphase steels consisting of bainite, ferrite and retained austenite, *Mater. Des.* 95 (2016) 75–88.
- [31] E. Kozeschnik, H.K.D.H. Bhadeshia, Influence of silicon on cementite precipitation in steels, *Mater. Sci. Technol.* 24 (2008) 343–347.
- [32] A. Saha Podder, H.K.D.H. Bhadeshia, Thermal stability of austenite retained in bainitic steels, *Mater. Sci. Eng. A.* 527 (2010) 2121–2128.

- [33] C. Garcia-Mateo, M. Peet, F.G. Caballero, H.K.D.H. Bhadeshia, Tempering of hard mixture of bainitic ferrite and austenite, *Mater. Sci. Technol.* 20 (2004) 814–818.
- [34] A.S. Podder, Tempering of a mixture of bainite and retained austenite, PhD Thesis, University of Cambridge, (2011).
- [35] R.W.K. Honeycombe, F.B. Pickering, Ferrite and bainite in alloy steels, *Metall. Trans.* 3 (1972) 1099–1112.
- [36] C. Garcia-Mateo, F.G. Caballero, Ultra-high-strength Bainitic Steels, *ISIJ Int.* 45 (2005) 1736–1740.
- [37] B.C. De Cooman, Structure–properties relationship in TRIP steels containing carbide-free bainite, *Curr. Opin. Solid State Mater. Sci.* 8 (2004) 285–303.
- [38] P.J. Jacques, Transformation-induced plasticity for high strength formable steels, *Curr. Opin. Solid State Mater. Sci.* 8 (2004) 259–265.
- [39] V.T.T. Miihkinen, D.V. Edmonds, Fracture toughness of two experimental high-strength bainitic low-alloy steels containing silicon, *Mater. Sci. Technol.* (1987) 441–449.
- [40] J.-C. Hell, *Aciers bainitiques sans carbure : Caractérisations microstructurales multi-échelles et in situ de la transformation austénite-bainite et relations entre microstructure et comportement mécanique*, PhD Thesis, University of Paul Verlaine (Metz), 2011.
- [41] B.P.J. Sandvik, H.P. Nevaleinen, Structure-property relationships in commercial low-alloy bainitic-austenitic steel with high strength, ductility, and toughness, *Met. Technol.* (1981) 213–220.
- [42] J. Lemaitre, J.-L. Chaboche, *Mécanique des matériaux solides*, second, Edition Dunod Paris, (1988).
- [43] X. Feaugas, C. Gaudin, Different levels of plastic strain incompatibility during cyclic loading: in terms of dislocation density and distribution, *Mater. Sci. Eng. A.* 309 (2001) 382–385.
- [44] E. Silvestre, J. Mendiguren, L. Galdos, E. Sáenz de Argandoña, Comparison of the hardening behaviour of different steel families: From mild and stainless steel to advanced high strength steels, *Int. J. Mech. Sci.* 101–102 (2015) 10–20.
- [45] E. Silvestre, Sheet metal roll levelling optimization by means of advanced numerical models and development of new concepts for last generation materials, PhD Thesis, University of Arrasate-Mondragon, (2015).
- [46] L. Zhonghua, G. Haicheng, Bauschinger effect and residual phase stresses in two ductile-phase steels: Part I. The influence of phase stresses on the Bauschinger effect, *Metall. Trans. A.* 21 (1990) 717–724.
- [47] M.J. Peet, S.S. Babu, M.K. Miller, H.K.D.H. Bhadeshia, Tempering of Low-Temperature Bainite, *Metall. Mater. Trans. A.* 48 (2017) 3410–3418.

- [48] J. Lemaitre, J. Dufailly, Damage measurements, *Eng. Fract. Mech.* 28 (1987) 643–661.
- [49] E. Maire, O. Bouaziz, M. Di Michiel, C. Verdu, Initiation and growth of damage in a dual-phase steel observed by X-ray microtomography, *Acta Mater.* 56 (2008) 4954–4964.
- [50] A. Weck, D.S. Wilkinson, E. Maire, H. Toda, Visualization by X-ray tomography of void growth and coalescence leading to fracture in model materials, *Acta Mater.* 56 (2008) 2919–2928.
- [51] H. Toda, A. Takijiri, M. Azuma, S. Yabu, K. Hayashi, D. Seo, M. Kobayashi, K. Hirayama, A. Takeuchi, K. Uesugi, Damage micromechanisms in dual-phase steel investigated with combined phase- and absorption-contrast tomography, *Acta Mater.* 126 (2017) 401–412.
- [52] S. Heibel, T. Dettinger, W. Nester, T. Clausmeyer, A. Tekkaya, Damage Mechanisms and Mechanical Properties of High-Strength Multiphase Steels, *Materials*. 11 (2018) 1–34.
- [53] N. Pathak, C. Butcher, M. Worswick, E. Bellhouse, J. Gao, Damage Evolution in Complex-Phase and Dual-Phase Steels during Edge Stretching, *Materials*. 10 (2017) 1–34.
- [54] J. Lemaitre, A course on damage mechanics, second Edition, Edition Springer, 1996.
- [55] N. Bonora, A. Ruggiero, D. Gentile, S. De Meo, Practical Applicability and Limitations of the Elastic Modulus Degradation Technique for Damage Measurements in Ductile Metals, *Strain*. 47 (2011) 241–254.
- [56] L. Ryde, D. Lindell, A. Pichler, J. Garcia Ferreno, Y. Vilander Granbom, E. Werner, A. Fillafer, R. Wesenjak, P. Tsiouridis, A. Nitschke, Micro-scale damage tolerance of AHSS steels as function of microstructure and stress-strain state, European Commission EUR 25863, (2013).
- [57] P.J. Jacques, F. Delannay, J. Ladrière, On the influence of interactions between phases on the mechanical stability of retained austenite in transformation-induced plasticity multiphase steels, *Metall. Mater. Trans. A*. 32 (2001) 2759–2768.
- [58] B.L. Bramfitt, Metals Handbook - Structure/property Relationships in Irons and Steels, in: *Struct. Relatsh. Irons Steels*, Desk Edition, Edition J.R. Davis, (1998), pp. 153–173.
- [59] G. F. Vander Voort, Etching isothermally treated steels, *Heat Treat. Prog.* APRIL/MAY 2001 (2001).
- [60] F.G. Caballero, C. García-Mateo, J. Chao, M.J. Santofimia, C. Capdevila, C.G. De Andres, Effects of morphology and stability of retained austenite on the ductility of TRIP-aided bainitic steels, *ISIJ Int.* 48 (2008) 1256–1262.
- [61] C. Landron, O. Bouaziz, E. Maire, J. Adrien, Characterization and modelling of void nucleation by interface decohesion in dual phase steels, *Scr. Mater.* 63 (2010) 973–976.
- [62] C. Cabus, H. Réglé, B. Bacroix, Orientation relationship between austenite and bainite in a multiphased steel, *Mater. Charact.* 58 (2007) 332–338.
- [63] K. Verbeken, L. barbé, D. Raabe, Evaluation of the Crystallographic Orientation Relationships between FCC and BCC Phases in TRIP Steels, *ISIJ Int.* (2009) 1601–1609.

- [64] F.G. Caballero, C. Garcia-Mateo, M.K. Miller, Design of novel bainitic steels: moving from ultrafine to nanoscale structures, *Jom.* 66 (2014) 747–755.
- [65] J.P. Naylor, The influence of the Lath Morphology on the Yield Stress and Transition Temperature of Martensitic-Bainitic Steels, *Metall. Trans. A.* 10A (1979) 861–873.
- [66] F.G. Caballero, C. Garcia-Mateo, C.G. de Andrés, Dilatometric study of re-austenitisation of high silicon bainitic steels: Decomposition of retained austenite, *Mater. Trans.* 46 (2005) 581–586.
- [67] W. Cui, D. San-Martín, P.E.J. Rivera-Díaz-del-Castillo, Stability of retained austenite in martensitic high carbon steels. Part I: Thermal stability, *Mater. Sci. Eng. A.* 711 (2018) 683–695.
- [68] N. Luzginova, L. Zhao, J. Sietsma, Evolution and thermal stability of retained austenite in SAE 52100 bainitic steel, *Mater. Sci. Eng. A.* 448 (2007) 104–110.
- [69] E. De Moor, S. Lacroix, L. Samek, J. Penning, J.G. Speer, Dilatometric study of the quench and partitioning process, *Proceedings of the 3rd International Conference on Advanced Structural Steels*, (2006), pp. 1–6.
- [70] J.R. Yang, H. Bhadeshia, Continuous heating transformation of bainite to austenite, *Mater. Sci. Eng. A.* 131 (1991) 99–113.
- [71] D. Hull, D.J. Bacon, *Introduction to dislocations*, fifth Edition, BH, (2011).
- [72] C. Keller, *Etude expérimentale avec transitions volume/surface des propriétés mécaniques du nickel polycristallin de haute pureté*, PhD Thesis, University of Caen Basse-Normandie, (2006).
- [73] A.F.G. Pereira, P.A. Prates, N.A. Sakharova, M.C. Oliveira, J.V. Fernandes, On the identification of kinematic hardening with reverse shear test, *Eng. Comput.* 31 (2015) 681–690.
- [74] M. Härtel, C. Illgen, M.F.-X. Wagner, Experimental evaluation of Bauschinger effects during tension-compression in-plane deformation of sheet materials, *IOP Conf. Ser. Mater. Sci. Eng.*, IOP Publishing, (2016), pp. 1–10.
- [75] X. Lemoine, A. Aouafi, Bauschinger effect correspondence of experimental tests, *Int. J. Mater. Form.* 1 (2008) 241–244.
- [76] L. Zhonghua, G. Haicheng, Bauschinger effect and residual phase stresses in two ductile-phase steels: Part II. The effect of microstructure and mechanical properties of the constituent phases on Bauschinger effect and residual phase stresses, *Metall. Mater. Trans. A.* 21 (1990) 725–732.
- [77] Z. Tan, C. Magnusson, B. Persson, The Bauschinger effect in compression-tension of sheet metals, *Mater. Sci. Eng. A.* 183 (1994) 31–38.
- [78] R. Sowerby, D.K. Uko, Y. Tomita, A review of certain aspects of the Bauschinger effect in metals, *Mater. Sci. Eng.* 41 (1979) 43–58.
- [79] Q. Zhou, L. Qian, J. Meng, L. Zhao, F. Zhang, Low-cycle fatigue behavior and microstructural evolution in a low-carbon carbide-free bainitic steel, *Mater. Des.* 85 (2015) 487–496.

- [80] T.B. Hilditch, I.B. Timokhina, L.T. Robertson, E.V. Pereloma, P.D. Hodgson, Cyclic Deformation of Advanced High-Strength Steels: Mechanical Behavior and Microstructural Analysis, *Metall. Mater. Trans. A*. 40 (2009) 342–353.
- [81] X.Y. Long, F.C. Zhang, C.Y. Zhang, Effect of Mn content on low-cycle fatigue behaviors of low-carbon bainitic steel, *Mater. Sci. Eng. A*. 697 (2017) 111–118.
- [82] E. Watanabe, T. Asao, M. Toda, M. Yoshida, S. Horibe, Relationship between Masing behavior and dislocation structure of AISI 1025 under different stress ratios in cyclic deformation, *Mater. Sci. Eng. A*. 582 (2013) 55–62.
- [83] C.-C. Shih, N.-J. Ho, H.-L. Huang, The relationship between cyclic stress-strain curve and dislocation structures in cyclically deformed IF steel, (2009) 235–238.
- [84] F. Yoshida, T. Uemori, K. Fujiwara, Elastic–plastic behavior of steel sheets under in-plane cyclic tension–compression at large strain, *Int. J. Plast.* 18 (2002) 633–659.
- [85] G.H. Bae, H. Huh, Tension/compression test of auto-body steel sheets with the variation of the pre-strain and the strain rate, *WIT Transactions on Engineering Sciences*, (2011), pp. 213–225.
- [86] R.K. Boger, R.H. Wagoner, F. Barlat, M.G. Lee, K. Chung, Continuous, large strain, tension/compression testing of sheet material, *Int. J. Plast.* 21 (2005) 2319–2343.
- [87] S.J. Marcadet, D. Mohr, Effect of compression–tension loading reversal on the strain to fracture of dual phase steel sheets, *Int. J. Plast.* 72 (2015) 21–43.
- [88] Z.L. Kowalewski, L. Dietrich, G. Socha, Anti-buckling fixture for large deformation tension-compression cyclic loading of thin metal sheets, 8th Australas. Congr. Appl. Mech., (2014).
- [89] C. Schayes, Low cycle fatigue of the Fe-3Si steel: damage mechanisms and strain localisation by EBSD, PhD Thesis, University of Lille, (2016).
- [90] Y. Li, C. Laird, Masing behavior observed in monocrystalline copper during cyclic deformation, *Mater. Sci. Eng. A*. 161 (1993) 23–29.
- [91] T. Mayer, E. Mazza, S.R. Holdsworth, Parameter evolution in a continuous Masing approach for cyclic plasticity and its physical interpretation, *Mech. Mater.* 57 (2013) 86–96.
- [92] E. Silvestre, J. Mendiguren, E. Saenz de Argandona, L. Galdos, Influence of number of backstresses on the mixed hardening Chaboche-Lemaitre model for modelling roll levelling processes, *IDDRG*, (2013), pp. 125–131.
- [93] B. Grzegorzczak, A. Kozłowska, M. Morawiec, R. Muszyński, A. Grajcar, Effect of Deformation Temperature on the Portevin-Le Chatelier Effect in Medium-Mn Steel, *Metals*. 9 (2018) 1–13.
- [94] A. Constant, J.-C. Charbonnier, G. Henry, *Principes de base des traitements thermiques thermomécaniques et thermochimiques des aciers*, PYC Editions, 1992.
- [95] M.B.H. Slama, Étude multi-échelle et in situ des évolutions microstructurales en conditions isothermes d’aciers bainitiques en lattes, PhD Thesis, University of Lorraine, (2018).

- [96] Z. Janjusevic, Z. Gulisija, M. Mihailovic, A. Pataric, The investigation of applicability of the Hollomon-Jaffe equation on tempering the HSLA steel, *Chem. Ind. Chem. Eng. Q.* 15 (2009) 131–136.
- [97] D. François, *Endommagement et rupture des matériaux*, EDP sciences, 2004.
- [98] C. Defaisse, *Etude de la rupture ductile d'un acier à très haute résistance pour des applications aéronautiques*, PhD Thesis, PSL University (Mines Paris Tech), 2018.
- [99] C. Tekoglu, J.W. Hutchinson, T. Pardoen, On localization and void coalescence as a precursor to ductile fracture, *Philos. Trans. A.* (2015) 1–19.
- [100] G. Mirone, Role of stress triaxiality in elastoplastic characterization and ductile failure prediction, *Eng. Fract. Mech.* 74 (2007) 1203–1221.
- [101] Y. Bai, X. Teng, T. Wierzbicki, On the Application of Stress Triaxiality Formula for Plane Strain Fracture Testing, *J. Eng. Mater. Technol.* 131 (2009) 1–10.
- [102] D. Anderson, S. Winkler, A. Bardelcik, M.J. Worswick, Influence of stress triaxiality and strain rate on the failure behavior of a dual-phase DP780 steel, *Mater. Des.* 60 (2014) 198–207.
- [103] Y. Zhang, Z. Chen, On the effect of stress triaxiality on void coalescence, *Int. J. Fract.* 143 (2007) 105–112.
- [104] N. Bonora, D. Gentile, A. Pironi, G. Newaz, Ductile damage evolution under triaxial state of stress: theory and experiments, *Int. J. Plast.* 21 (2005) 981–1007.
- [105] N. Selini, M. Elmequenni, M. Benguediab, Effect of the Triaxiality in Plane Stress Conditions. Triaxiality Effect in a PVC Material, *Eng. Technol. Appl. Sci. Res.* 3 (2013) 373–380.
- [106] Y. Bao, T. Wierzbicki, On fracture locus in the equivalent strain and stress triaxiality space, *Int. J. Mech. Sci.* 46 (2004) 81–98.
- [107] H.A.F. Mohammed, *Investigation of repeated failure of movable joints in heavy vehicles*, PhD Thesis, Sudan University of Science and Technology, 2015.
- [108] D. Mohr, S.J. Marcadet, Micromechanically-motivated phenomenological Hosford-Coulomb model for predicting ductile fracture initiation at low stress triaxialities, *Int. J. Solids Struct.* 67–68 (2015) 40–55.

Appendix

Appendix A: Identification of phase using electron diffraction pattern

Appendix B: Supplementary information on Gleeble

Appendix C: Supplementary details on tension/compression tests

Appendix D: Introduction to local strain deformation by EBSD and results

Appendix A. Identification of phase using electron diffraction pattern

The use of electron diffraction in TEM enables the identification and establishment of the crystallographic orientation of the analysed phases. To identify the phase and the zone axis, the distances between diffraction spots (in mm) and the angle between them are measured. Then, the interplanar spacings (d_{hkl}) are estimated using Equation (50), where D_D is the distance in mm between the diffraction spots.

$$d_{hkl} = \frac{18.8526}{D_D} \quad (50)$$

The determination of different D_D in mm and the corresponding interplanar space in Å are displayed in the example in Fig A-1, the diffraction pattern obtained corresponds to austenite islands.

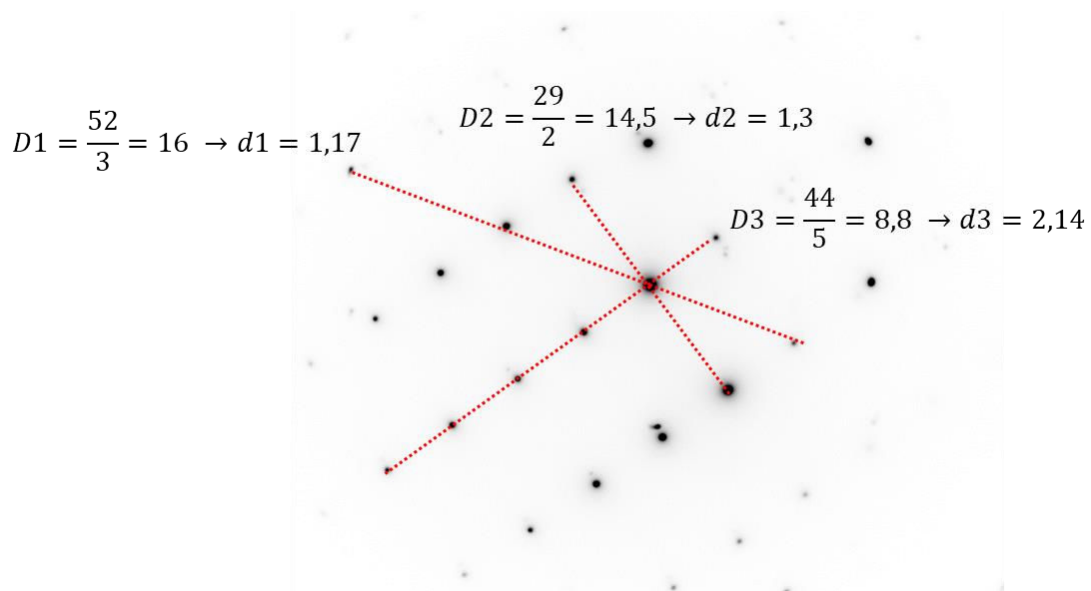


Fig A-1. Identification of interplanar spacing on TEM diffraction pattern.

First, the interplanar distances are compared to figures contained in the CaRine Crystallography software database. Once the phase is determined, the zone axis can be identified. If the correlation between theoretical and measured data is closed, the identification is confirmed. Concerning the identification of austenite islands in Fig A-2, D1 represents the diffraction of the planes {131}, D2 {220}, and D3 {111}, and the zone axis is [112]. The theoretical diffraction pattern of this zone axis is exhibited in Fig A-2, and the corresponding planes and angles are listed in Fig A-3.

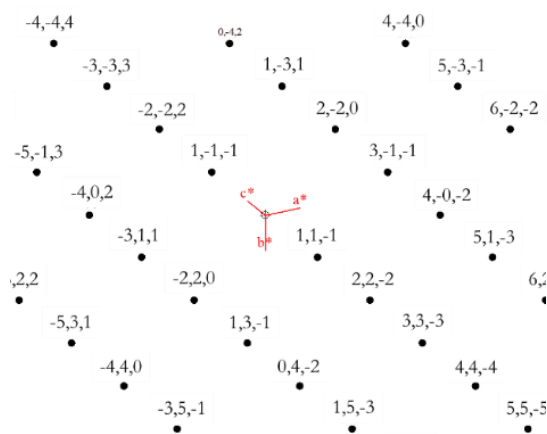


Fig A-2. Theoretical diffraction pattern for FCC structure on zone axis [112].

| d_{hkl} | (hkl) |
|-----------|--|
| 2.073 | (11-1) (111) (1-11) (-111) |
| 1.082 | (-113) (3-1-1) (-131) (311) (-13-1) (131) (13-1) (113) (31-1) (-1-13) (1-13) (3-11) |
| 1.269 | (-202) (0-22) (-220) (202) (220) (022) |

Fig A-3. Planes and angle presented on the software used to identify crystallographic structure.

Appendix B. Supplementary information on Gleeble apparatus

Gleeble device is thermo-mechanical simulators used to characterise heat-affected zones (both when welding and performing heat treatments). A coupling between temperature and mechanical load enables observation of the evolution of the mechanical properties of the specimen with temperature and allows the acquirement of the TTT and continuous cooling transformation diagram. However, it is worth noting that, in this researching, heating applied using the Joule effect. It was thus produced by a dissipation of electric energy due to the resistance of atoms to the displacement of current. The impact of this energy on diffusion mechanisms is currently not well understood. Table B-2 presents the main characteristics of this device.

Table B-1. Main characteristics of Gleeble 3500-GTC device.

| Properties | Limit |
|--|---------------------------------|
| Heating rate | 10000°C/s |
| Maximum temperature (°C) | 1250°C (K- thermocouples limit) |
| Thickness of specimens (for flat geometry) | From 1 to 2.25 mm |
| | From 4 to 5.25 mm |
| Load capacity | 100kN |

Console :
Interface between the device and
the computer



Furnace and
force cell

Hydraulic pump →

Fig B-1. Photograph of Gleeble 3500-GTC.

Only the interior of the chamber was used while preparing of tests. Fig B-2 depicts the furnace set up used for the tensile tests performed at high temperature.

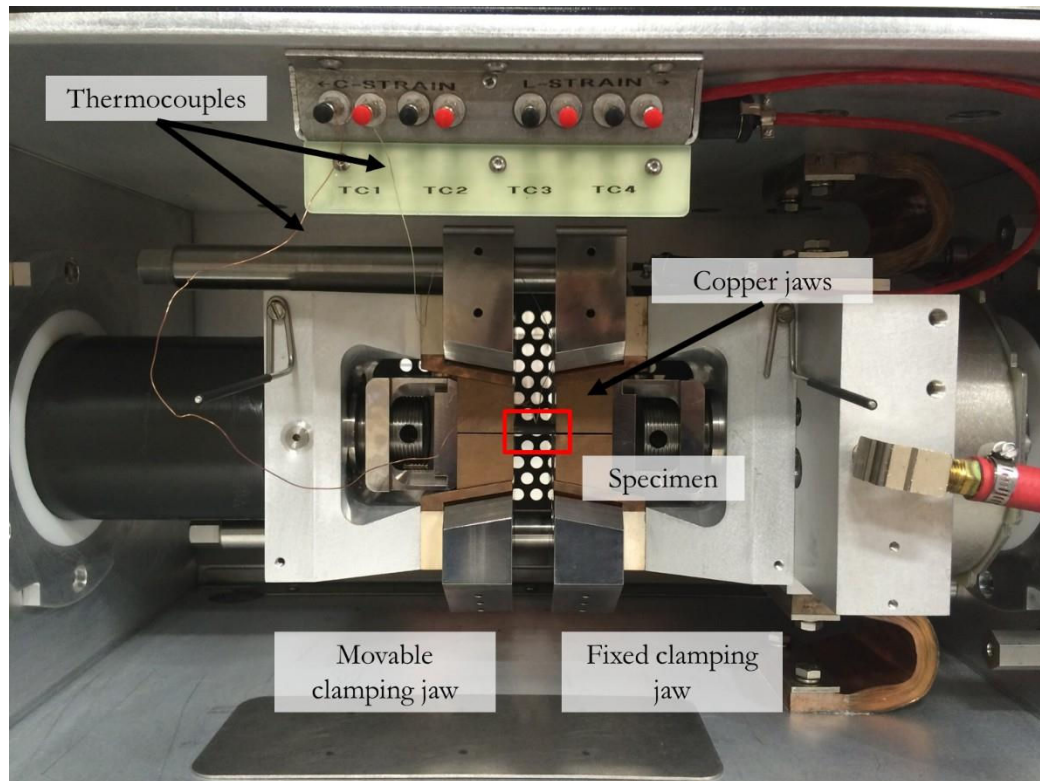


Fig B-2. Tensile configuration in the interior of the Gleeble chamber.

Appendix C. Supplementary details on tension/compression tests

Example of programme for alternated tests

Table C-1. Cyclic programme test 1.

| | Number of cycles | Max Strain (%) | Min strain (%) | Frequency (Hz) |
|---|------------------|----------------|----------------|----------------|
| 1 | 100 | 0.08 | -0.08 | 1 |
| 2 | 100 | 0.3 | -0.3 | 1 |
| 3 | 50 | 0.4 | -0.4 | 2 |
| 4 | 50 | 0.5 | -0.5 | 1,5 |
| 5 | 50 | 0.6 | -0.6 | 1 |
| 6 | 50 | 0.7 | -0.7 | 0.75 |
| 7 | 22 | 0.8 | -0.8 | 0.5 |

Table C-2. Cyclic program test 2

| | Number of cycles | Max Strain (%) | Min strain (%) | Frequency (Hz) |
|----------|------------------|----------------|----------------|----------------|
| 1 | 100 | 0.08 | -0.08 | 1 |
| 2 | 100 | 0.3 | -0.3 | 1 |
| 3 | 50 | 0.4 | -0.4 | 2 |
| 4 | 50 | 0.5 | -0.5 | 1.5 |
| 5 | 50 | 0.6 | -0.6 | 1 |
| 6 | 50 | 0.7 | -0.7 | 0.75 |
| 7 | 50 | 0.8 | -0.8 | 0.5 |
| 8 | 50 | 0.9 | -0.9 | 0.5 |
| 9 | 39 | 1 | -1 | 0.5 |

Table C-3. Cyclic program test 3

| | Number of cycles | Max Strain (%) | Min strain (%) | Frequency (Hz) |
|----------|-------------------------|-----------------------|-----------------------|-----------------------|
| 1 | 25 | 0.3 | -0.3 | 1 |
| 2 | 25 | 0.5 | -0.5 | 1.5 |
| 3 | 25 | 0.7 | -0.7 | 0.75 |
| 4 | 25 | 0.9 | -0.9 | 0.5 |
| 5 | 25 | 1.1 | -1.1 | 0.5 |
| 6 | 10 | 1.3 | -1.3 | 0.5 |

Appendix D. Introduction to local strain deformation by EBSD and results

To assist to understand the misorientation investigation within grains,⁷ kernel average misorientation (KAM), grain average misorientation (GAM), and grain orientation spread (GOS) are explained below.

- Kernel average misorientation is a local misorientation analysis. The misorientation of each pixel is compared with the misorientation of its neighbours. Misorientations are taken into account if they do not exceed a maximum value. Otherwise, values are not considered for the average. The local misorientation between a pixel and its neighbours is then represented in Fig D-1.

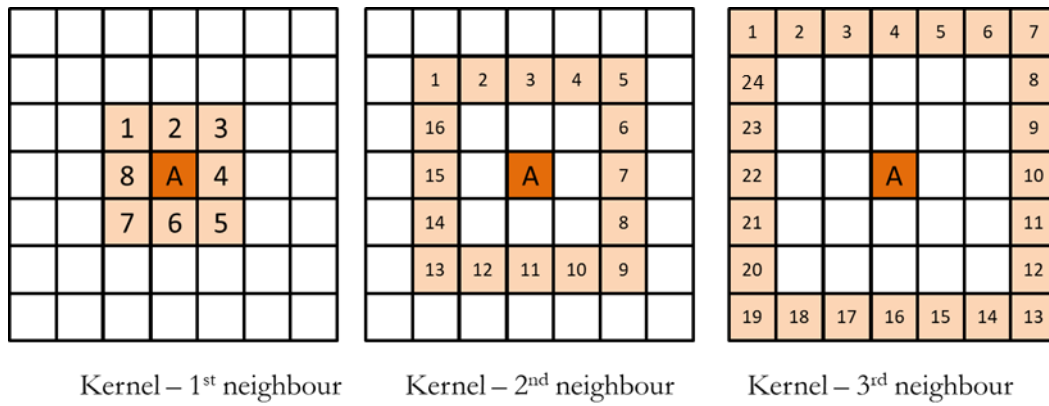


Fig D-1. Representation of KAM.

The average of misorientation is then calculated as follows (using the example of the first neighbour):

$$\Delta g_k = \frac{1}{8} (\Delta g_{A1} + \Delta g_{A2} + \Delta g_{A3} + \Delta g_{A4} + \Delta g_{A5} + \Delta g_{A6} + \Delta g_{A7} + \Delta g_{A8}) \quad (51)$$

- Grain average misorientation: the misorientation between two pixels inside a grain is measured. An average of the overall misorientations with the grain is then determined (see Fig D-2).

⁷ Help notice OIM software

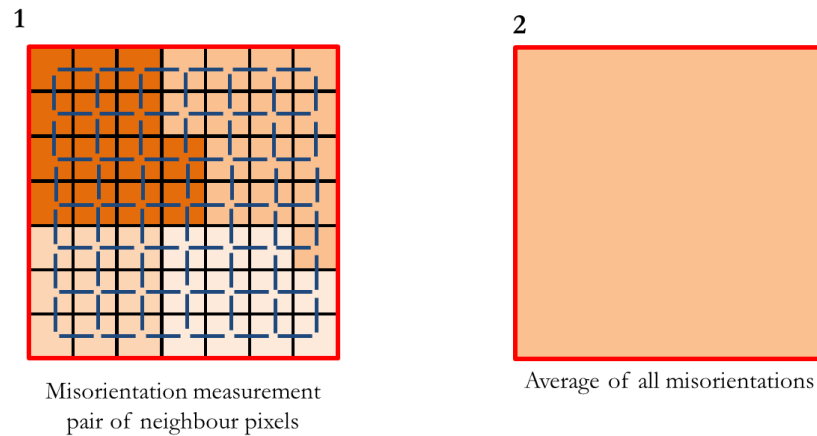


Fig D-2. Representation of grain average misorientation.

- Grain orientation spread: The average value of the misorientation within a grain is measured. The misorientation between this average and the orientation of each pixel from that grain is then calculated. Finally, the average of these measurements is performed. This analysis provides information on the scatter within the misorientation of one grain (see Fig D-3).

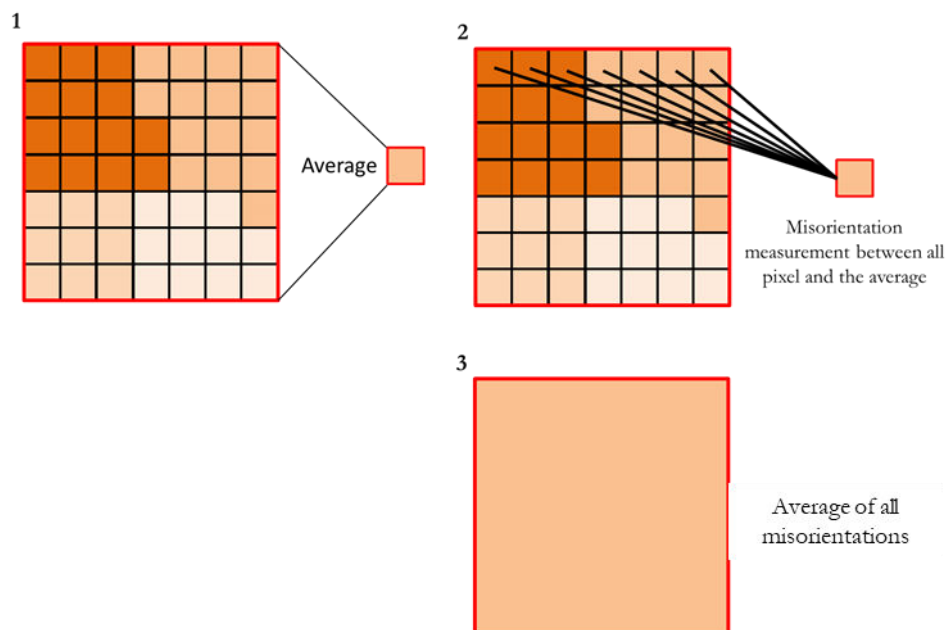


Fig D-3. Grain orientation spread representation.

The results obtained from EBSD analyses were presented in Chapter III and corresponding maps are exhibited in Fig D-4.

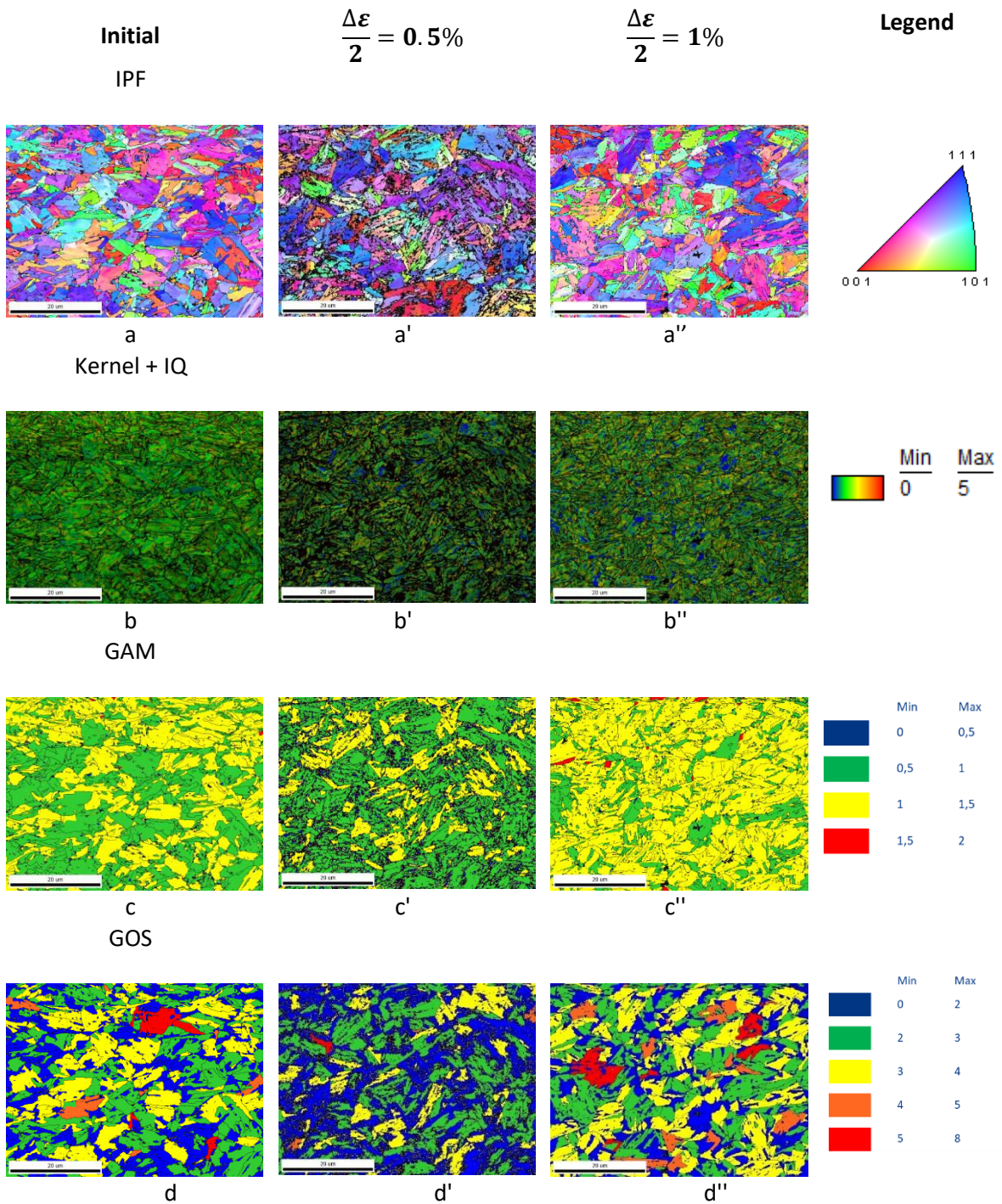


Fig D-4. Electron backscatter diffraction maps at various strain amplitudes: 0, 0.5% and 1% (a, a', a'') IPF, and (b, b', b'') Kernel + IQ, and (c, c', c'') GAM, and (d, d', d'') GOS.

List of figures

| | |
|--|----|
| Figure 0-1. CO ₂ emission of cars measured and requested from 2000 to 2025 during NECD tests (NECD: New European Driving Cycle) [1]. | 7 |
| Figure I-1. Steel ductile diagram of various AHSS grades [1]. | 12 |
| Figure I-2. Time-transformation-temperature diagram of AHSSs transformation [13]. | 13 |
| Figure I-3 Pattern of bainitic structure. | 14 |
| Figure I-4. Schematic representation of displacive and reconstructive transformations [20]. | 14 |
| Figure I-5 Displacive transformation of bainite with diffusion of carbon after sub-unit growth [17,21]. | 16 |
| Figure I-6. Diffusion of carbon during UP and LB transformations [24]. | 17 |
| Figure I-7. SEM pictures of (a) upper bainite, (b) lower bainite and (c) granular bainite [25]. | 17 |
| Figure I-8. (a) Misorientation angle relations between upper, lower, and granular bainite, (b) Determination of bainite structure as function of angle misorientation at 60° and 5°, (c) Example of bainite identification with granular, upper and lower bainites [25]. | 18 |
| Figure I-9. TEM microstructures of UB (a) and LB (b) [23]. | 19 |
| Figure I-10. Microstructure evolution of bainite depending on the time of tempering at 500°C [17]. | 21 |
| Figure I-11. Evolution of austenite fraction after tempering at various temperatures in a carbide-free bainitic steel [32,34]. | 21 |
| Figure I-12. Impact of different elements on strengthening [17]. | 22 |
| Figure I-13 Evolution of tensile deformation with various percentages of RA and with various transformation temperatures [41]. | 24 |
| Figure I-14. Evolution of ductility obtained by varying the austenite percentage in the presence of the TRIP effect [40]. | 25 |
| Figure I-15 Representation of X (kinematic) and R (isotropic) components of hardening (σ_1 , σ_2 and σ_3 the principal stresses) | 26 |
| Figure I-16 Evolution of isotropic (R) and kinematic (X) hardening normalised by the yield stress [44]. | 27 |

| | |
|--|----|
| Figure I-17 Modification of hardness and volume fraction of austenite (V_γ) as a function of tempering temperature (holding time of 1 h) [47]..... | 28 |
| Figure I-18. Comparison of damage measurement methods for brittle, ductile and fatigue damage [48]. | 28 |
| Figure I-19. Localisation of damage using X-ray tomography [49]. | 29 |
| Figure I-20. Measurement of damage by hardness measurements [54]..... | 30 |
| Figure I-21. Tensile curves of CP800 and DP780 (a), void fraction area of CP800 and DP780 as a function of equivalent strain (b) [53]..... | 31 |
| Figure I-22. Fraction of porosity and number of voids measured for various grades of AHSS (DP600, DP800, CP800, DP1000 and CP1000) [52] | 32 |
| Figure I-23. Schematic trend of volume fraction of void evolution as a function of contrast in hardness phases obtained during hole expansion tests, tensile tests and bending tests [56]. | 33 |
| Figure I-24. Evolution of fracture section reduction as a function of austenite percentage [40]. | 34 |
| Figure I-25. Evolution of the void area fraction at various temperatures in DP1000 steel during tensile tests on (a) smooth and (b) notched specimens ($\eta = 0,5$)[4]. | 35 |
| Figure I-26. Evolution of tensile properties (a) and modification of phases (b) at various temperatures [4]..... | 35 |
| Figure II-1. X-ray diffraction diagram of CP1200 grades, with (a) and (b) presenting magnified austenite peaks. | 41 |
| Figure II-2. Comparison of microstructure under (a) optical microscope (OM) and (b) SEM with SMB etching on CP1. The microstructures of CP 2 (c) and CP3 (d) were also visualised using SEM and the same etching solution. | 42 |
| Figure II-3. Electron backscattered diffraction orientation maps (a, b, c) and phase distribution (d, e, f) on CP1, CP2, and CP3. | 44 |
| Figure II-4. Grain boundary misorientation angles measured by EBSD for CP1, CP2, and CP3..... | 45 |
| Figure II-5. Orientation relationship between prior austenite (FCC) and bainite (BCC) according to Bain (a), NW (b), and KS (c) models. Blue atoms represent BCC structure, whereas green atoms represent FCC structure [18]. | 46 |
| Figure II-6. Crystal orientation of bainitic ferrite (a) – two clusters of laths are highlighted (blue and green circles), crystal orientation of austenite (b) in the same area..... | 47 |

| | |
|--|----|
| Figure II-7. Misorientation angle relationship between bainitic ferrite and austenite islands. Local misorientation angle on CP1 with the line profiles representation and misorientation. | 47 |
| Figure II-8. Comparison of lath sizes between mean linear intercepts using SEM images and unique grain colour map obtained by EBSD measurement with grain boundaries $< 8^\circ$ | 48 |
| Figure II-9. Transmission electron microscopy images of CP2 showing the lath structure and a high dislocation density. | 49 |
| Figure II-10. Transmission electron microscopy observation of the initial microstructure of CP1. Austenite islands are labelled with the letters A, B, and C. | 50 |
| Figure II-11. Differential scanning calorimetry results during heating for CP1, CP2, and CP3. | 51 |
| Figure II-12. Dilatometer installation in the Gleeble device: (a) setup of free moving clamping jaws on the furnace with the cooling system, (b) focus on the dilatometer installations on the specimen, and (c) dilatometer. | 53 |
| Figure II-13. Dilatometry curve of the heating of CP2 from room temperature to 900°C performed on CP2. | 54 |
| Figure II-14. Stress-strain curves obtained during tensile tests for three grades of CP provided by various suppliers: (a) engineering tensile curves, (b) true tensile curves. | 56 |
| Figure II-15. Schematic representation of phase transformation during heating. | 58 |
| Figure III-1. Schematic representation of interactions between dislocation and obstacles related to effective and internal stresses [72]. | 60 |
| Figure III-2. Schematic representation of cyclic (a) hardening and (b) softening. | 62 |
| Figure III-3. Evolution of stress amplitude as function of the number of cycles during low-cycle fatigue experiments at various strain amplitude [81]. | 63 |
| Figure III-4. Validation of Masing behaviour observed in TA6V [42]. | 64 |
| Figure III-5. Stress-strain cyclic curves under stress ratio of $R=-1$ [82]. | 64 |
| Figure III-6. TEM images showing dislocation arrangements of cyclic test under stress ratio $R=-1$ (a) at a stress amplitude of 251 MPa and (b) 260 MPa [82]. | 65 |
| Figure III-7. (a) Evolution of dislocation structures as a function of plastic strain amplitude during alternated tensile tests on IF steels, (b) image without dislocation arrangement, (c) picture of loop patch structures, and (d) picture of dislocation cells [83]. | 65 |
| Figure III-8. Friction force measured during cyclic tests on a broken specimen. | 67 |

| | |
|---|----|
| Figure III-9. Presentation of the clamping device: (a) three-dimensional (3D) representation drawn using the computer-aided design (CAD) software Catia v5, (b) positioning of the device on the tensile machine, (c) setup of the device on a specimen, and (d) indents at the surface of the specimen. | 67 |
| Figure III-10. Cyclic tensile and compression curves obtained with the incremental test method performed on CP2 at strain amplitudes of $\pm 0.08\%$, $\pm 0.3\%$, $\pm 0.4\%$, $\pm 0.5\%$, $\pm 0.6\%$, $\pm 0.7\%$, $\pm 0.8\%$ and $\pm 0.9\%$ | 68 |
| Figure III-11. Representation of the CSSC after alternating tests..... | 69 |
| Figure III-12. Linear interpolation of logarithmic equation of CSSC. | 70 |
| Figure III-13. Determination and observation of cyclic softening: (a) evolution of the cyclic stress amplitude during incremental tests and (b) magnification of the reduction of stress to observe cyclic softening (test t2). | 70 |
| Figure III-14. Verification of the Masing law by normalisation of the cyclic curves obtained in the incremental tests of CP2 (test t3). | 71 |
| Figure III-15. (a) KAM, (b) GOS, and (c) GAM measurements for initial and cyclic specimens (50 cycles). | 72 |
| Figure III-16. Transmission electron microscopy images after 50 cycles at an amplitude of 0.5%, showing tangled dislocations (a, b, and c), and after 50 cycles at an amplitude of 1% (d, e, and f) displaying the presence of cells..... | 73 |
| Figure III-17. Example of the measurement of isotropic and kinematic hardening..... | 74 |
| Figure III-18. Evolution of isotropic hardening as functions of the cumulated plastic strain (three tests: t1, t2 and t3)..... | 75 |
| Figure III-19. Evolution of kinematic hardening as functions of the cumulated plastic strain (three tests: t1, t2 and t3)..... | 76 |
| Figure III-20. Lemaitre and Chaboche interpolation with one back stress with interpolation parameters: $C = 56985$ MPa and $\gamma = 104.3$ MPa. | 77 |
| Figure III-21. Evolution of stress response using three backstresses (X1, X2 and X3)[92]..... | 77 |
| Figure III-22. Lemaitre and Chaboche interpolation with three back stresses (a) and representation of back stress curves (b)..... | 78 |
| Figure III-23. Tensile machine equipped with a furnace..... | 80 |
| Figure III-24. Gleeble chamber in tensile configuration..... | 80 |

| | |
|---|----|
| Figure III-25. Evolution of temperature during tensile tests performed on the TMF..... | 80 |
| Figure III-26. Heating of the round specimen on Gleeble. | 80 |
| Figure III-27. Evolution of UTS as a function of the heating rate: (a) heating instructions, (b) results, and (c) monotonous tensile curves. | 81 |
| Figure III-28. Difference in temperature between a thermocouple placed at middle of the specimen and a thermocouple placed 1 cm away from the middle: (a) picture of welded thermocouple and (b) temperature evolution..... | 82 |
| Figure III-29. Tensile stress-strain curves at different temperatures (room temperature, 200°C, 400°C, 500°C, and 600°C) performed on the Gleeble and the TMF. | 82 |
| Figure III-30. Evolution of the UTS as a function of temperature determined with the Gleeble and the TMF (standard deviation ± 5 MPa). | 83 |
| Figure III-31. Evolution of plastic strain at fracture as a function of temperature..... | 84 |
| Figure III-32. (a) Tensile tests performed on Gleeble device at different temperatures [200°C–600°C], (b) thermal programmes corresponding to these tests..... | 85 |
| Figure III-33. (a) Tensile tests performed with Gleeble device at room temperature after tempering at various temperatures [200°C–600°C], (b) thermal programmes corresponding to these tests. | 86 |
| Figure III-34. Evolution of UTS as a function of holding time during tensile tests performed at room and high temperatures. | 86 |
| Figure III-35. Representation of UTS as a function of the H_p coefficient. | 87 |
| Figure III-36. Evolution of shear stress as a function of temperature [71]. | 88 |
| Figure III-37. Microstructure of CP2 after annealing at 400°C for 60 min (a, b). | 89 |
| Figure IV-1. Representations of the nucleation, growth, and coalescence of voids [50]. | 92 |
| Figure IV-2. Failure as the result of (a) localised plastic flow, (b) localised plastic flow prior to damage, (c) damage softening simultaneously due to localised plastic flow, and (d) void coalescence [99]. | 92 |
| Figure IV-3. Representation of the initial surface (S) and damaged surface (S') [54]. | 93 |
| Figure IV-4. Evolution of stress triaxiality as functions of equivalent plastic strain for various specimen geometries [3]. | 95 |
| Figure IV-5 (a) Stress-strain loading and unloading curves, (b) evolution of Young modulus with plastic strain during the loading and unloading tests..... | 96 |

| | |
|---|-----|
| Figure IV-6. Damage parameter evolution as a function of plastic strain measured by loading and unloading tests. | 97 |
| Figure IV-7. Experimental void quantification procedure involving metallurgical methods. | 98 |
| Figure IV-8. Schematic representation of the void measurement procedure. | 99 |
| Figure IV-9. Thickness and width measurement as a function of the distance to the fracture. | 100 |
| Figure IV-10. Schematic representation of shear band localisation during tensile tests. | 101 |
| Figure IV-11. (a) Strain measurement obtained by DIC on $\eta_{0.5}$ specimen, (b) influence of mesh on this measurement (notation: mesh size in pixel_ number of pixel recovered), and (c) schematic representation of mesh size and shift for the 5 x 5-pixel mesh size. | 102 |
| Figure IV-12. Evolution of strain to fracture as a function of average stress triaxiality [106] | 104 |
| Figure IV-13. (a) Tensile curves obtained on notched and grooved specimens, (b) maximum force and fracture strain as a function of the theoretical stress triaxiality. | 104 |
| Figure IV-14. Fractography of tensile specimen performed at room temperature ($\eta = 0.33$). | 105 |
| Figure IV-15. Schematic representation of a cup and cone fracture [107]. | 106 |
| Figure IV-16. Fractography of notched specimens (1) $\eta = 0.5$, (2) $\eta = 0.6$, and (3) $\eta = 1$ at the centres (a) and at the border of each specimen (b). | 106 |
| Figure IV-17. Void area fraction as a function of stress triaxiality. | 107 |
| Figure IV-18 Void area fraction as a function of plastic strain at fracture. | 107 |
| Figure IV-19. (a) Mapping of the void area fraction at the mid-thickness of the specimen after fracture, (b) evolution of area fraction, (c) number, and (d) average diameter of voids as a function of plastic strain. | 108 |
| Figure IV-20. (a) Void area fraction, (b) number of voids, and (c) average void area as functions of plastic strain. | 110 |
| Figure IV-21. SEM pictures of CP1200 microstructure after tensile tests to observe void localisation ($\eta=0.3$). | 111 |
| Figure IV-22. SEM picture of $\eta_{0.5}$ to observe the void localisation in the microstructure. | 112 |
| Figure IV-23. Impact of temperature on fractography of tensile specimens at (a,b) 400°C, (c) 500°C, and (d) 600°C. | 113 |

| | |
|--|-----|
| Figure IV-24. Evolution of (a) void area fraction, (b) number of voids, and (c) growth of voids as functions of the plastic strain for tensile specimens ($\eta = 0.33$)..... | 114 |
| Figure IV-25. Evolution of (a) void fraction area, (b) number of voids, and (c) growth of voids as a function of the plastic strain for the notched specimens ($\eta = 0.5$). | 116 |
| Figure IV-26. Evolution of (a) the maximum average void area , (b) the number of voids and (c) the critical strain where after which the void area fraction increase as functions of temperature and stress triaxiality ($\eta=0.3$ and $\eta=0.5$). | 117 |
| Figure IV-27. Example of void localisation with the temperature and stress triaxiality: 400°C (a) smooth specimen and (b) $\eta = 0.5$, 600°C (c) smooth specimen and (d) $\eta = 0.5$ | 118 |
| Figure IV-28. (a) Inverse pole figure and IQ mapping, (b) IPF mapping with low angle (white: 2°–15°) and high angle (black: < 15°) boundaries of tensile specimens deformed at 600°C. | 118 |
| Figure IV-29. Scanning electron microscopy image of the head of a specimen tempered at 600°C ($\eta = 0.33$). | 119 |
| Figure IV-30. TEM images of the microstructure of the samples in the work of Garcia-Mateo et al: (a) the initial microstructure, (b) the microstructure at 600°C after 1 h of tempering, and (c) the microstructure at 730°C after 42 days [33]. | 120 |
| Fig A-1. Identification of interplanar spacing on TEM diffraction pattern. | 138 |
| Fig A-2. Theoretical diffraction pattern for FCC structure on zone axis [112]. | 139 |
| Fig A-3. Planes and angle presented on the software used to identify crystallographic structure. | 139 |
| Fig B-1. Photograph of Gleeble 3500-GTC..... | 140 |
| Fig B-2. Tensile configuration in the interior of the Gleeble furnace. | 141 |
| Fig D-1. Representation of KAM. | 144 |
| Fig D-2. Representation of average grain misorientation..... | 145 |
| Fig D-3. Representation of grain orientation spread representation. | 145 |
| Fig D-4. Electron backscattered diffraction cartographies at various strain amplitudes: 0, 0.5% and 1% (a, a', a'') IPF, and (b, b', b'') Kernel + IQ, and (c, c', c'') GAM, and (d, d', d'') GOS. | 146 |

List of Tables

| | |
|--|-----|
| Table I-1. Transformation mechanisms present in martensite (α') and bainite (α_b) [9]..... | 15 |
| Table I-2 Strengthening impact of chemical elements on solid solution [28]..... | 24 |
| Table II-1. General properties of the studied CP1200 steels..... | 37 |
| Table II-2. Impact of the main chemical elements present in CP steels [17]. | 38 |
| Table II-3. Chemical composition (weight percentage + Standard Deviation (SD)) of CP grades. | 39 |
| Table II-4. X-ray diffraction angles references for austenite and ferrite. | 40 |
| Table II-5. Retained austenite percentage obtained by image analysis on OM and SEM pictures. | 42 |
| Table II-6. Temperature transitions measured by DSC ($^{\circ}\text{C}$)..... | 51 |
| Table II-7. Temperature transitions obtained by dilatometry and DSC ($^{\circ}\text{C}$). | 54 |
| Table II-8. Results of measuring the hardness of CP1200 steels..... | 55 |
| Table II-9. Tensile properties of CP1200 grades (all measurements were performed on a true curve, with the exception of the strain at the fracture)..... | 56 |
| Table II-10. Synthesis of phase percentages measured for the three grades of CP1200. | 57 |
| Table III-1. Summary of the mechanical properties and microstructural characteristics of CP2 characterised at room temperature. | 59 |
| Table III-2. Kinematic parameters using three backstresses..... | 78 |
| Table III-3. Comparison between the Gleeble and tensile machine..... | 80 |
| Table IV-1. Numerical results of the critical damage value (D_c) and a true strain criteria (ϵ_{vR}) | 97 |
| Table IV-2. Specimen geometries and corresponding stress triaxiality. | 103 |
| Table IV-3. Strain fracture measurements using the Aramis software and the Bridgman equation. . | 105 |
| Table IV-4. Numerical values of parameters A and B of the equation (49) for DP1000 [4] and CP1200 steels..... | 109 |
| Table IV-5. Average void area on fracture surface (μm^2)..... | 113 |
| Table IV-6. Comparison of damage properties between DP1000 and CP1200 steels..... | 122 |

Pauline MARTIN

Directeur de thèse : Éric HUG

Synthèse en français

**ÉTUDE DES MECANISMES D'ENDOMMAGEMENT ET DE PLASTICITE D'ACIER MULTIPHASES A
MATRICE BAINITIQUE SOUS DIFFERENTS TRAJETS DE CHARGEMENT - IMPACT DE LA TEMPERATURE**

Table des matières

| | |
|---|-----------|
| Introduction..... | 1 |
| Chapter I. Caractérisation métallurgique et mécanique générale des aciers CP | 4 |
| 1. Quantification des phases par microscopie optique et électronique à balayage | 4 |
| 1.1. Différenciation des bainites par l'étude de la désorientation des joints de grains .5 | 5 |
| 1.2. Mesure de la taille des lattes bainitiques via l'utilisation de l'EBSB et la méthode des interceptions | 7 |
| 2. Impact de la température sur la microstructure | 8 |
| 2.1. Détermination des températures de transformation de phases par calorimétrie différentielle à balayage (DSC)..... | 8 |
| 3. Introduction des propriétés mécaniques en traction | 9 |
| 4. Synthèse des résultats et conclusion | 11 |
| Chapter II. Etude des mécanismes de plasticité cyclique des aciers CP1200 et impact d'un chargement thermomécanique..... | 13 |
| 1. Mécanismes de plasticité cyclique des aciers CP1200..... | 13 |
| 1.1. Effet de la densité de dislocation sur l'adoucissement cyclique dans l'acier CP1200 | 13 |
| 1.2. Analyse des structures de dislocations par l'application de la loi de Masing..... | 14 |
| 1.3. Etude des interactions des dislocations par l'analyse de l'écroutissage isotrope et cinématique | 16 |
| 2. Impact de la température sur les propriétés en traction..... | 17 |
| 2.1. Influence de la température et du temps de maintien sur les propriétés mécaniques | 17 |
| 2.2. Bilan de l'analyse thermomécanique..... | 19 |
| Chapter III. Description et quantification des mécanismes d'endommagement de l'acier CP1200 | 21 |
| 1. Quantification des vides avec l'impact du taux de triaxialité..... | 21 |
| 2. Influence de la température sur l'évolution de l'endommagement | 24 |

| | |
|--|-----------|
| 2.1. Influence des sollicitations mécaniques à haute température sur l'évolution de l'endommagement..... | 24 |
| 2.2. Observation de la localisation des vides et de la transformation de la microstructure | 26 |
| 3. Synthèse des résultats concernant l'endommagement | 27 |
| Conclusion | 29 |
| Références | 31 |

Introduction

Au cours des dernières décennies, la problématique de la protection de l'environnement a influencé la conception des produits dans l'industrie automobile. Depuis le XXI^e siècle sont mises en œuvre des lois strictes concernant la réduction des émissions de CO₂, exigeant des valeurs inférieures à 120 g/km comme le montre la Figure 0-1 [1]. Néanmoins, cette contrainte écologique doit être conciliée avec les directives générales de l'industrie automobile concernant la sécurité, le confort des passagers et l'esthétique des produits. Toutes ces exigences créent un défi pour la société Faurecia Automotive Seating. En effet, les sièges sont définis comme des éléments impactant fortement sur la sécurité du passager. Lors d'un choc, les passagers ne sont maintenus dans la voiture que par les mécanismes présents dans les sièges. Cela implique que l'allègement du siège dans les voitures ne doit pas diminuer ses propriétés mécaniques. Pour surmonter ce problème, deux méthodes peuvent être adoptées. Premièrement, des matériaux plus légers tels que l'aluminium (2700 kg/m³), le magnésium (1750 kg/m³) et les composites peuvent être utilisés [2].

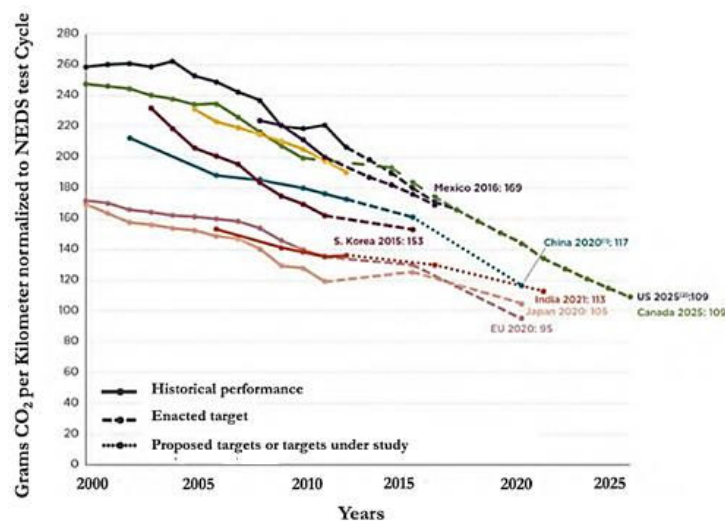


Figure 0-1. Émissions de CO₂ des voitures mesurées et requises de 2000 à 2025 lors des tests NECD (NECD: New European Driving Cycle) [1].

Cependant, les alliages d'aluminium et de magnésium présentent des propriétés mécaniques inférieures à celles des aciers et ne peuvent donc pas être utilisés dans des pièces où des sollicitations mécaniques complexes sont attendues. Une solution serait d'utiliser une importante épaisseur de tôle, mais cela conduirait à un design de pièces encombrant. Une autre méthode consiste à développer des aciers plus performants, à savoir les aciers avancés à haute résistance (AHSS). Dans cette optique, trois générations d'AHSS ont été développées afin d'atteindre des propriétés de mise en forme et de

résistance encore non obtenues avec d'autres matériaux. Pour développer ces nouvelles générations d'aciers, les sidérurgistes ont modifié la composition chimique de l'alliage et adapté les processus de mise en température et de trempe afin d'obtenir des microstructures complexes généralement composées d'une combinaison de phases. Avec une augmentation des propriétés mécaniques, la conception du siège peut être repensée pour réduire le volume d'acier utilisé.

Les aciers complexes phases 1200 (CP1200) classés dans la première génération d'AHSS sont au centre des préoccupations de Faurecia pour leur forte absorption d'énergie, leur grande capacité de déformation et leur bonne résistance lors des tests d'expansion de trous. Cette amélioration des propriétés de mise en forme permet l'utilisation d'une moindre quantité d'acier. Cependant, cela induit aussi une complexification du design qui conduit à des rayons de courbure plus sévères. Ainsi, des aciers avec une formabilité encore plus élevée sont exigés. Il pourra être nécessaire de déformer l'acier au plus près de sa limite de déformation lors de chargements complexes. C'est pour mieux comprendre le comportement des aciers CP1200 proches de ses limites de formabilité que ce projet a été financé.

L'étude des mécanismes d'endommagement a précédemment été effectuée sur les aciers CP1200 en utilisant la même méthodologie que la thèse de J.CHOTTIN [3] sur les aciers DP1000. La recherche des similitudes entre ces deux aciers a été réalisée pour comprendre l'impact de la microstructure sur les mécanismes d'endommagement et de plasticité. Les aciers complexes phases 1200 sont définis par une matrice bainitique avec la présence d'austénite résiduelle et de martensite. Il s'agit de savoir comment cette microstructure résiste à l'endommagement et la façon dont elle évolue après la nucléation des vides. De plus, la microstructure bainitique est moins sensible que la martensite à la température. Ainsi, un deuxième axe de recherche de ce projet concerne l'influence de la température sur les mécanismes d'endommagement dans les aciers CP1200.

Afin de répondre à ces questions, ce rapport est divisé en trois parties.

Le premier chapitre vise à effectuer une présentation générale des aciers CP ainsi que des caractéristiques microstructurales et mécaniques de nuances d'aciers CP1200 provenant de différents fournisseurs. Pour ce faire, les résultats de l'identification et de la quantification des phases en microscopie optique (OM), en microscopie électronique à balayage (MEB) et en diffraction d'électrons rétrodiffusés (EBSD) sont présentés. Nous avons ensuite étudié la stabilité thermique des aciers CP1200 en utilisant la calorimétrie à balayage différentiel et la dilatométrie afin de déterminer les températures de transition de phase. Enfin, la caractérisation en traction des éprouvettes est effectuée afin de faire le lien entre les propriétés mécaniques et l'aspect microstructural.

Pour obtenir des informations supplémentaires sur l'impact de la microstructure sur le durcissement cyclique, des expériences de traction-compression ont été réalisées et sont présentées dans le deuxième chapitre. Les résultats obtenus mettent en évidence les obstacles au déplacement des dislocations et permettent de mesurer les contraintes internes. L'influence de la température sur les propriétés de traction est aussi étudiée. Une attention particulière est accordée à l'impact de la température sur un intervalle de 200 °C à 600 °C, combiné au temps de revenu.

Enfin, le dernier chapitre concerne l'évolution des mécanismes d'endommagement à température ambiante et à des températures plus élevées. La quantification des vides formés est étudiée en fonction de la déformation plastique. L'influence du chemin de chargement sur la fraction de vides est examinée pour différentes géométries d'échantillons entaillés afin de faire varier la triaxialité de contraintes. La localisation des vides est ensuite étudiée par analyse microstructurale à température ambiante, à 400 °C, à 500 °C et à 600 °C.

Une conclusion des résultats est enfin incluse pour relier toutes les observations et discuter de la relation entre la microstructure, les propriétés mécaniques, l'endommagement à température ambiante et à températures élevées.

Chapter I. Caractérisation métallurgique et mécanique générale des aciers CP

L'objectif de ce chapitre est de présenter les caractéristiques métallurgiques et mécaniques des aciers CP1200. Pour ce faire, de nombreuses nuances fournies par différents fournisseurs ont été initialement étudiées. Ce rapport se concentre sur trois nuances : CP1, CP2 et CP3. Pour caractériser et différencier les nuances d'acier présentées dans ce rapport, des analyses microstructurales ont été effectuées. Afin de fournir un large éventail d'observations, diverses méthodes ont été appliquées à différentes échelles d'observation. Tout d'abord, les phases ont été identifiées à l'aide d'une analyse DRX. Des observations microstructurales ont aussi été effectuées à l'aide de la microscopie optique et électronique (MEB et MET) pour obtenir des données sur la quantification et la répartition des phases. Pour obtenir plus d'informations, la caractérisation des orientations cristallines a été réalisée à l'aide d'analyses EBSD. Cela a permis de tirer des conclusions finales concernant la stabilité thermique de ces microstructures.

1. Quantification des phases par microscopie optique et électronique à balayage

La difficulté quant à effectuer une attaque chimique sur les aciers multiphasés est d'identifier une solution chimique capable de révéler chaque phase. Le métabisulfite de sodium (SMB) concentré à 15% permet l'identification de la ferrite bainitique, de la martensite et de l'austénite résiduelle [4–6]. En microscopie optique (OM), la bainite, la martensite et les îlots d'austénite résiduelle sont respectivement colorés en brun clair, en marron et en blanc. Les images au microscope optique à balayage (MEB) obtenues avec un détecteur d'électrons secondaires (SE2) montrent l'austénite sous la forme d'une phase gris clair, la martensite est légèrement attaquée et la bainite est observée en gris foncé. La Figure I-1 montre pour la nuance CP1 une comparaison des résultats de ces deux méthodes d'identification de phases.

Les images révèlent une microstructure sous la forme de lattes avec des îlots d'austénite résiduelle. Après l'attaque chimique, le contraste de couleur a permis de quantifier la phase par analyse d'images à l'aide du logiciel IGOR Pro. La quantification a été effectuée sur dix images de chaque nuance et le pourcentage moyen d'austénite est présenté dans la Table I-1.

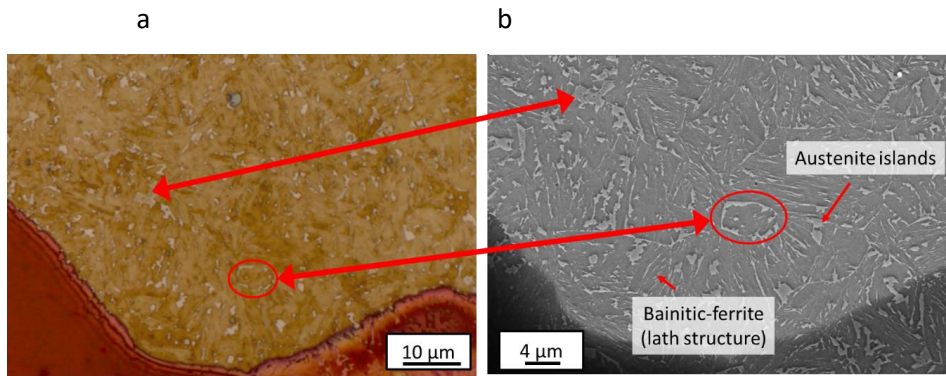


Figure I-1. Comparaison des images obtenues par OM et par MEB après une attaque chimique au SMB sur la nuance CP1.

Table I-1. Pourcentages d'austénite résiduelle obtenus par analyse d'image en MO et au MEB.

| | CP1 | CP2 | CP3 |
|--|-----|-----|-----|
| OM (Austénite résiduelle sous forme d'îlots détectée) | 9% | - | 2% |
| SEM (Lattes et îlots d'austénite résiduelle détectée) | 18% | 15% | 11% |

Cette analyse a révélé la présence d'austénite résiduelle dans toutes les nuances, quelle que soit leur composition chimique. Cependant, deux morphologies d'austénite peuvent être notées sur la Figure I-1 (îlots et lattes), ce qui conduit à des différences entre les résultats obtenus par MEB et par microscopie optique. En raison de la finesse des lattes, les inter-lattes de l'austénite ne peuvent être détectées que par MEB, ce microscope permettant un grossissement plus important.

Les nuances CP1 et CP2 présentent les quantités les plus élevées d'austénite, ce qui peut être dû à leurs pourcentages de silicium. De plus, contrairement à l'acier CP2, les aciers CP1 et CP3 présentent des îlots austénitiques. La présence d'îlots devrait augmenter la ductilité du matériau en raison de l'effet TRIP pouvant se produire lors de la déformation. Cet effet est plus prononcé quand les îlots sont moins stables [35, 49]. Cependant, des incertitudes subsistent quant à la nature de la phase entre les lattes de ferrite bainitiques. En effet, l'analyse effectuée ne permet pas d'atteindre une résolution suffisamment élevée, il n'a donc pas été possible de distinguer l'austénite des carbures.

1.1. Différenciation des bainites par l'étude de la désorientation des joints de grains

Des analyses antérieures ont permis de différencier la ferrite bainitique de l'austénite, bien que les structures bainitiques n'aient pas pu être distinguées. De plus, les carbures caractérisant la bainite inférieure n'ont pas été identifiés lors des analyses précédentes.

Les bainites inférieure, granulaire et supérieure ont été identifiées à l'aide de la méthode proposée par Zajac et al. [7], qui repose sur les angles de désorientation des joints de grains. La bainite inférieure est caractérisée par un nombre important de joints de fortes désorientations (47 à 65 °), la bainite supérieure est définie par un plus grand nombre de joints de faibles désorientations (<15 °) et la bainite granulaire présente une orientation aléatoire. La Figure I-3 présente la distribution des angles de désorientations des joints pour les trois nuances et quatre pics sont distingués :

- Entre 2 ° et 15 °, caractéristique de la bainite supérieure.
- A 45 °, causé par la présence d'austénite résiduelle.
- De 50 ° à 55 °, correspondant aussi aux joints de grains d'austénite (valeurs limites selon le rapport de l'UE [28]).
- Entre 55 ° et 65 °, reflétant la bainite inférieure.

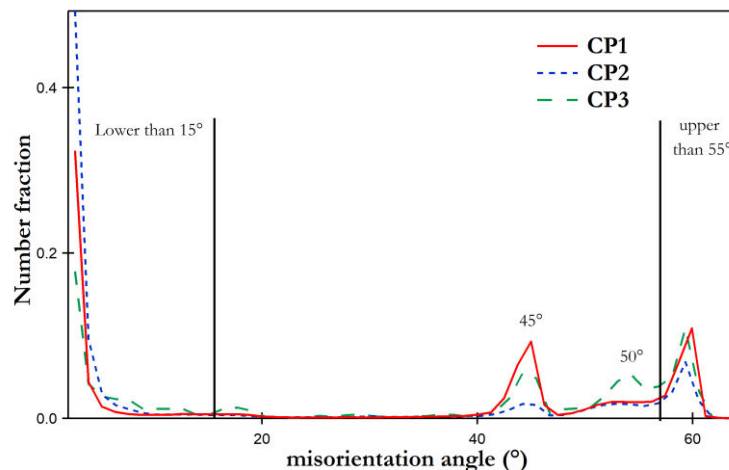


Figure I-2. Distribution des angles de désorientations obtenus par analyse EBSD sur les nuances CP1, CP2 et CP3.

Les résultats révèlent que les aciers CP1200 présentent une microstructure combinée composée de bainite supérieure et inférieure en raison des pics détectés au-dessous de 15 ° et au-dessus de 55 °, respectivement. De plus, le pic à 45 ° représente l'interface entre l'austénite résiduelle et la ferrite bainitique. L'évolution de la fraction en nombre de ces joints de grain de désorientation particulière est en accord avec la quantification de phase précédemment mesurée à l'aide d'images obtenues au microscope optique. Concernant l'austénite résiduelle, la nuance CP1 présente le pourcentage le plus élevé et la nuance CP2 possède le plus bas taux.

1.2. Mesure de la taille des lattes bainitiques via l'utilisation de l'EBSD et la méthode des interceptions

Une équation formulée par Langford et Cohen (Equation 1) a été utilisée pour déterminer l'impact des dimensions des latte sur les propriétés mécaniques [8–10]. L'équation de la limite d'élasticité (σ_y) en fonction du diamètre effectif de la taille des grains (d) est la suivante :

$$\sigma_y = \sigma_0 + k_y d^{-1} \quad (1)$$

Cependant, comme les plaques bainitiques présentent une morphologie anisotrope, la détermination du diamètre des grains n'est pas simple. Dans le travail de Bhadeshia [9], d représente deux fois l'épaisseur déterminée par la méthode de l'interception linéaire. L'analyse a été réalisée en mesurant l'épaisseur moyenne sur des lignes aléatoires perpendiculaires à la direction du bord long de la plaque. Selon le rapport de l'UE n° 21245 [11], la taille de grain équivalente peut également être mesurée par EBSD. Cette étude a révélé que seuls les joints de grains jusqu'à 8° peuvent influencer les propriétés mécaniques. Lors de l'estimation de la taille des grains, la limite basse de la désorientation des joints de grains est fixée à 8°. Dans cette thèse, les dimensions des lattes ont été estimées à l'aide des deux méthodes décrites ci-dessus. Les méthodes ont été appliquées aux nuances CP1, CP2 et CP3, et les mesures résultantes du diamètre des lattes sont présentées à la Figure II-8.

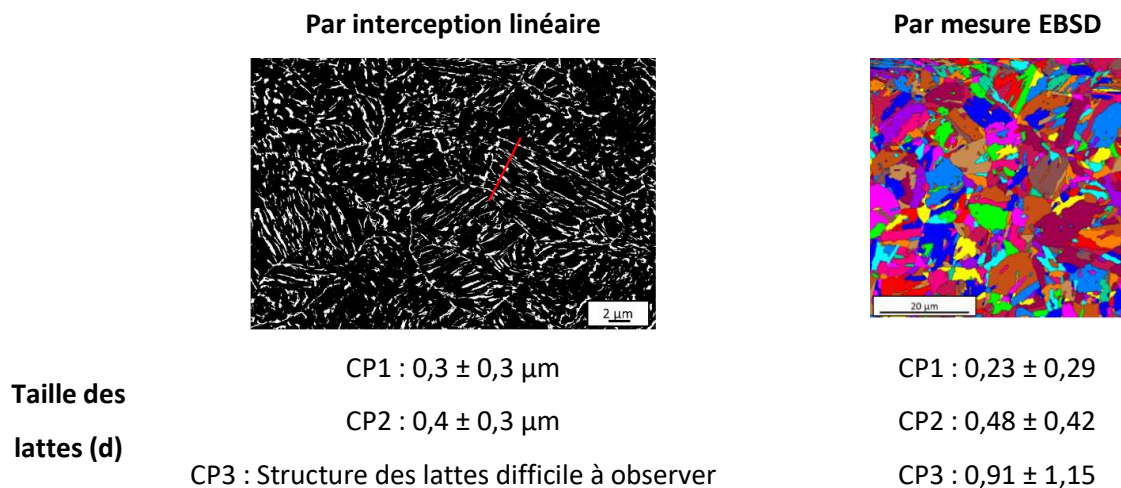


Figure I-3. Comparaison des tailles des lattes obtenues par interception linéaire sur des images MEB, et avec la cartographie des grains obtenue par EBSD (orientation minimale de joint de grain fixée à 8°).

Des valeurs similaires ont été obtenues en appliquant ces deux méthodes, bien que les résultats présentent une large dispersion. Les tailles de lattes des échantillons ont été classées et les résultats sont comparés aux propriétés mécaniques dans la conclusion de rapport de thèse.

2. Impact de la température sur la microstructure

2.1. Détermination des températures de transformation de phases par calorimétrie différentielle à balayage (DSC)

Des expériences DSC ont été effectuées pour acquérir les températures de transformation de phase. Des analyses de dilatométrie ont ensuite été effectuées pour confirmer ces températures.

Une analyse DSC est une méthode thermo-analytique qui mesure le flux de chaleur nécessaire pour maintenir un échantillon et la référence à la même température pendant un programme thermique. Les résultats DSC présentés à la Figure I-4 ont été obtenus après un chauffage continu de la température ambiante jusqu'à 900 °C à une vitesse de 10 °C/min. Les températures de transition correspondantes sont présentées dans la Table I-2.

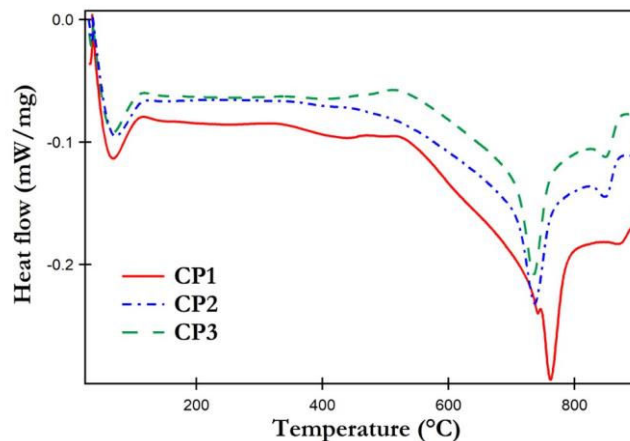


Figure I-4. Résultats des expériences DSC pour les nuances CP1, CP2, et CP3.

Trois écarts à la ligne de base sont observés pendant le chauffage. Le premier est léger et a lieu entre 340 °C et 580 °C ($A_{S_{dec}}$). Selon la littérature [12–14], la décomposition de l'austénite (γ) en ferrite (α) et en cémentite (Fe_3C) se produit dans cette gamme de températures. Ceci explique l'écart plus prononcé de CP1, qui présente la plus grande quantité d'austénite résiduelle. Le second pic commence entre 680 °C et 728 °C pour atteindre un maximum autour de 750 °C (A_{c1}). Cette transformation correspond à la température eutectoïde où commence la transformation de la bainite (α_b) en austénite. Le dernier pic, observable entre 870 °C et 895 °C, représente la transition A_{c3} où se produit la transformation complète de la bainite en austénite.

Table I-2. Températures de transition mesurées par DSC (°C).

| | Aus_{dec} | Ac₁ | Peak₁ | Peak₂ | Ac₃ |
|------------|--------------------------|-----------------------|-------------------------|-------------------------|-----------------------|
| CP1 | 338 | 728 | 761 | 870 | 895 |
| CP2 | 365 | 680 | 734 | 846 | 870 |
| CP3 | 364 | 690 | 735 | 845 | 872 |

$Aus_{dec}: \alpha_b + Fe_3C + \gamma \rightarrow \alpha_b + Fe_3C$
 $Ac_1: \alpha_b + Fe_3C \rightarrow \gamma + \alpha$
 $Ac_3: \gamma + \alpha \rightarrow \gamma$

Des variations dans les températures de transitions peuvent être notées entre les analyses DSC et les analyses dilatométriques présentées dans le manuscrit de thèse rédigé en anglais. Ces variations peuvent être expliquées par les différences entre ces appareils en termes de processus et de vitesse de montée en température. En ce qui concerne les résultats présentés dans cette thèse, la décomposition de l'austénite est mesurée autour de 350 °C / 500 °C en fonction de la nuance de l'acier. Ces températures de transformation de phases ont également été déterminées dans les publications de De Moor et al. [15] sur les aciers Q&P et de Yang et al. [69] sur les aciers bainitiques analysés par dilatométrie et DSC. Ces publications mettent en évidence différentes étapes : la ségrégation du carbone, la précipitation des carbures, la précipitation de l'austénite résiduelle et la formation de cémentite. Cependant, ces auteurs ont souligné l'importance de la variation de la température de transformation avec la vitesse de montée en température et le traitement thermique initial.

3. Introduction des propriétés mécaniques en traction

Pour compléter la caractérisation générale des aciers CP12000, l'analyse des propriétés mécaniques via des essais de traction monotone à la température ambiante a été menée. Les résultats sont présentés à la Figure I-5. Dix essais (cinq dans le sens transversal [TD] et cinq dans le sens longitudinal [LD]) ont été réalisés sous un régime quasi-statique à une vitesse de déformation constante de 10^{-3} s^{-1} . La déformation a été mesurée avec un extensomètre de 50 mm en utilisant la corrélation d'images numériques (DIC). Pour effectuer cette mesure, un motif noir sur fond blanc a été peint sur la surface de l'échantillon. Ensuite, à l'aide du logiciel Aramis, la mesure du mouvement relatif entre les points du motif a permis l'acquisition des données de déformation locale.

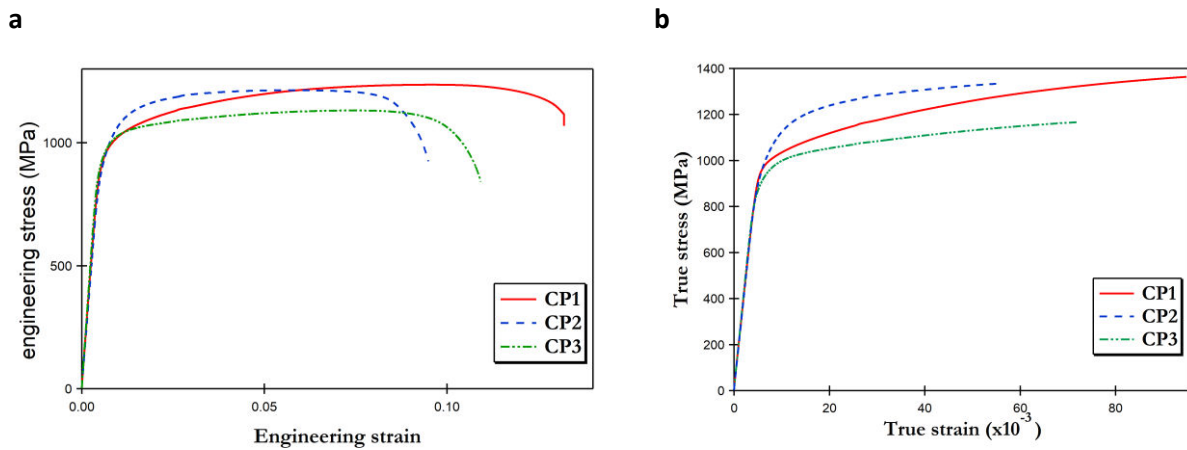


Figure I-5. Courbes de traction des trois nuances d'acier CP1200 provenant de différents fournisseurs : (a) courbes de traction conventionnelles, (b) courbes de traction rationnelles.

La Table I-3. Résultats des essais de traction de CP1, CP2 et CP3

| | | E (GPa) | UTS (MPa) | $\sigma_{0.2\%}$ (MPa) | ϵ_{UTS} | ϵ_f | Z (%) |
|-----|----|----------|-----------|------------------------|------------------|---------------|--------|
| CP1 | LD | 200 ± 13 | 1384 ± 22 | 962 ± 6 | 0,09 ± 0,01 | 0,136 ± 0,005 | 46 ± 6 |
| | TD | 219 ± 1 | 1385 ± 2 | 977 ± 3 | 0,083 ± 0,006 | 0,133 ± 0,003 | 44 ± 6 |
| CP2 | LD | 196 ± 8 | 1309 ± 5 | 1022 ± 13 | 0,059 ± 0,004 | 0,061 ± 0,001 | 64 ± 1 |
| | TD | 201 ± 2 | 1294 ± 7 | 1010 ± 13 | 0,049 ± 0,006 | 0,060 ± 0,003 | 65 ± 2 |
| CP3 | LD | 296 ± 4 | 1161 ± 11 | 927 ± 12 | 0,075 ± 0,009 | 0,110 ± 0,001 | 62 ± 3 |
| | TD | 210 ± 4 | 1158 ± 8 | 921 ± 16 | 0,064 ± 0,004 | 0,08 ± 0,01 | 55 ± 4 |

présente les résultats du module de Young (E), de l'UTS, de la limite d'élasticité à 0,2% de la déformation plastique ($\sigma_{0,2\%}$), de la déformation au niveau de la contrainte maximale (ϵ_{UTS}), de la déformation à la fracture (ϵ_f) et du coefficient de striction (Z), exprimé par l'équation (2) avec S_0 la section initiale et S_f la section finale.

$$Z = \left(\frac{S_0 - S_f}{S_0} \right) \times 100 \quad (2)$$

Table I-3. Résultats des essais de traction de CP1, CP2 et CP3

| | | E (GPa) | UTS (MPa) | $\sigma_{0.2\%}$ (MPa) | ϵ_{UTS} | ϵ_r | Z (%) |
|-----|----|----------|-----------|------------------------|------------------|---------------|--------|
| CP1 | LD | 200 ± 13 | 1384 ± 22 | 962 ± 6 | 0,09 ± 0,01 | 0,136 ± 0,005 | 46 ± 6 |
| | TD | 219 ± 1 | 1385 ± 2 | 977 ± 3 | 0,083 ± 0,006 | 0,133 ± 0,003 | 44 ± 6 |
| CP2 | LD | 196 ± 8 | 1309 ± 5 | 1022 ± 13 | 0,059 ± 0,004 | 0,061 ± 0,001 | 64 ± 1 |
| | TD | 201 ± 2 | 1294 ± 7 | 1010 ± 13 | 0,049 ± 0,006 | 0,060 ± 0,003 | 65 ± 2 |
| CP3 | LD | 296 ± 4 | 1161 ± 11 | 927 ± 12 | 0,075 ± 0,009 | 0,110 ± 0,001 | 62 ± 3 |
| | TD | 210 ± 4 | 1158 ± 8 | 921 ± 16 | 0,064 ± 0,004 | 0,08 ± 0,01 | 55 ± 4 |

Les éprouvettes peuvent être classées en fonction de la résistance maximale : CP1 > CP2 > CP3, et de la déformation à rupture : CP1 > CP3 > CP2. Il est intéressant de noter que Z ne suit pas la même évolution que l'allongement, puisque CP1 présente l'allongement le plus élevé mais le paramètre Z le plus faible. Inversement, CP2 et CP3 présentent un coefficient de striction élevé, mais l'allongement le plus faible. Cette différence indique une réduction importante de l'épaisseur pendant la striction qui n'est pas détectable par l'extensomètre.

4. Synthèse des résultats et conclusion

Dans ce chapitre, l'importance de la caractérisation métallurgique des aciers CP a été mise en évidence pour expliquer les propriétés mécaniques. Les résultats majeurs de ce chapitre sont résumés dans la **Error! Reference source not found.**

Table I-4. Récapitulatif du pourcentage d'austénite résiduelle mesuré dans les trois nuances d'aciers CP1200.

| | UTS (MPa) | ϵ_r | RA (%) | | | Si (wt%) | Dimension moyenne des lattes (μm) |
|-----|-----------|--------------|-----------------|--------------------|-----|----------|--|
| | | | OM | SEM (morphologie) | EBS | | |
| CP1 | 1385 ± 14 | 0,131± 0,005 | 9 | 18 (lattes +ilôts) | 9,1 | 1,4 | 0,2 ± 0,3 |
| CP2 | 1301 ± 10 | 0,083± 0,006 | Faible quantité | 15 (lattes) | 0,2 | 0,91 | 0,5 ± 0,4 |
| CP3 | 1161 ± 8 | 0,105± 0,001 | 2 | 11 (lattes +ilôts) | 2 | 0,84 | 1 ± 1 |

Ces résultats nous permettent de conclure que :

- Un large éventail de propriétés mécaniques peut être observé sous la désignation CP1200. Dans les trois nuances étudiées, 200 MPa sur l'UTS et une variation de 0,05 sur l'allongement total ont été mesurés entre les valeurs extrêmes. Ces différences peuvent être expliquées par les différences de microstructures.

- Tous les nuances ont révélé la présence d'austénite mais avec deux morphologies différentes : les îlots et les lattes. Cette austénite est développée grâce à la présence de silicium qui retarde la formation de cémentite. Cependant, sa quantité n'assure pas forcément la ductilité du matériau. En effet, il a été souligné dans la littérature que les îlots d'austénite sont plus bénéfiques pour la ductilité, ce que nos expériences tendent à confirmer.

- L'analyse des angles de désorientation à l'aide de l'EBSD révèle deux types de bainite (supérieure et inférieure). Les mesures effectuées permettent de les identifier mais pas de les quantifier. Cependant, l'étude permet de mettre en évidence un angle de 45° entre la ferrite bainitique et l'austénite, ce qui pourrait constituer un obstacle aux mouvements de dislocations et le point de départ de l'endommagement.

- Les mesures de la taille des lattes confirment leur effet sur la résistance mécanique. En effet, le classement de l'UTS ($CP1 < CP2 < CP3$) est inverse à celui de la taille des lattes ($CP3 < CP2 < CP1$).

Les caractéristiques de stabilité thermique de l'acier CP1200 ont été étudiées par analyses DSC et dilatométrie. Trois modifications microstructurales différentes lors du chauffage de la température ambiante à 900 °C sont mises en évidence. Tout d'abord, la décomposition d'austénite résiduelle en ferrite et cémentite est mesurée. Ensuite, la transformation de la ferrite et de la cémentite bainitiques en austénite se produit, puis la microstructure devient complètement austénitique.

Chapter II. Etude des mécanismes de plasticité cyclique des aciers CP1200 et impact d'un chargement thermomécanique

1. Mécanismes de plasticité cyclique des aciers CP1200

Dans ce chapitre, les résultats concernant l'étude des mécanismes de plasticité présents dans les aciers CP1200 sont étudiés. Dans un premier temps, une étude de l'impact de la quantité des dislocations sur l'adoucissement cyclique est menée. Ensuite, les composants de écrouissage cinématique et isotrope sont mesurés et la présence du comportement de Masing dans ces alliages est observé. Le détail des expériences est développé dans le manuscrit de thèse.

1.1. Effet de la densité de dislocation sur l'adoucissement cyclique dans l'acier CP1200

Les courbes cycliques alternées ont été obtenues par la méthode des tests incrémentaux, à l'aide d'un étai. Comme le montre la Figure II-1, des cycles avec des amplitudes de contrainte croissantes ont été appliqués à la nuance CP2. Les résultats ont été acquis avec trois échantillons (t1, t2 et t3), où suffisamment de cycles ont été atteints sans flambement sensible. Les deux premiers tests ont été réalisés avec un programme d'amplitudes de déformation similaire afin de vérifier la répétabilité des mesures, tandis que le troisième a été réalisé avec des niveaux d'amplitudes de déformation plus élevés.

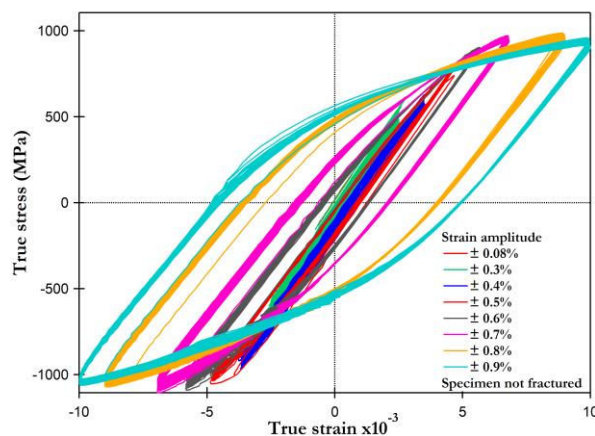


Figure II-1. Courbes de traction cycliques obtenues par la méthode des tests incrémentaux sur le CP2 à des amplitudes de déformation de $\pm 0,08\%$, $\pm 0,3\%$, $\pm 0,4\%$, $\pm 0,5\%$, $\pm 0,6\%$, $\pm 0,7\%$, $\pm 0,8\%$ et $\pm 0,9\%$.

Afin d'observer le durcissement ou l'adoucissement cyclique, la courbe de contrainte-déformation cyclique (CSSC) est présentée à la Figure II-2. Pour évaluer ces résultats, l'amplitude de

contrainte des cycles saturés pour chaque niveau doit être représentée en fonction de l'amplitude de déformation. Cependant, pour ces expériences, même après 100 cycles par niveau, la saturation cyclique n'est plus observée après $\pm 0,4\%$. Par conséquent, les valeurs du dernier cycle pour chaque amplitude de déformation ont été prises en compte.

Pour compléter l'analyse, l'évolution de l'amplitude de contraintes cycliques est affichée en fonction du nombre de cycles.

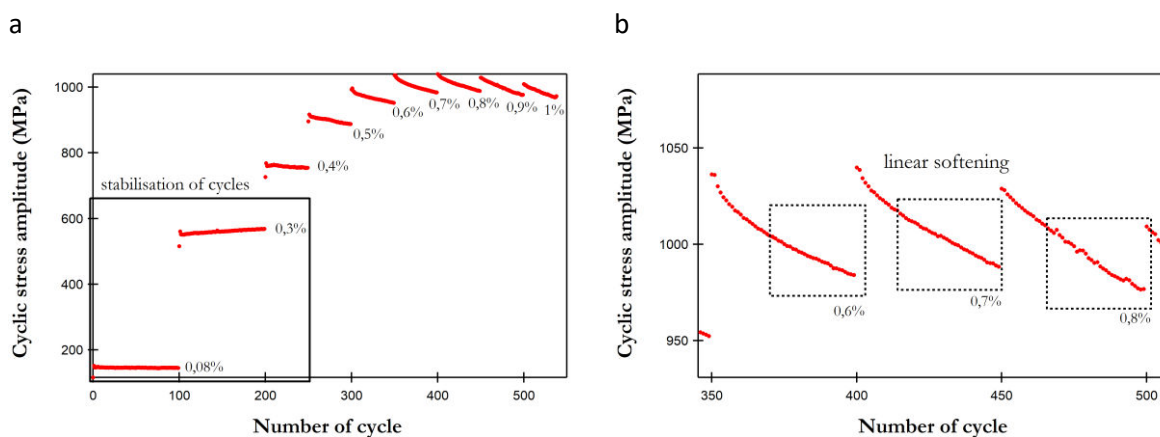


Figure II-2. Détermination de l'adoucissement : (a) Evolution de l'amplitude des contraintes cycliques pendant les tests, (b) Réduction de la contrainte observée lors de l'adoucissement cyclique.

Pour les amplitudes de déformation cyclique comprises entre $\pm 0,08\%$ et $\pm 0,3\%$, une légère augmentation de l'amplitude de contrainte cyclique est perceptible. Cependant, après $\pm 0,4\%$, un adoucissement se produit pendant les premiers cycles. Ces résultats sont en accord avec les travaux de Yoshida et al. [16]. À faible nombre de cycles, les dislocations sont enchevêtrées et inamovibles, entraînant le durcissement du matériau. Néanmoins, dans l'acier bainitique, une grande quantité de dislocations a été observée. Leurs interactions permettent rapidement leur annihilation et la formation d'arrangements de dislocations, ce qui favorise le ramollissement de l'acier. Cependant, la littérature indique une dépendance du durcissement cyclique et du ramollissement à l'amplitude de déformation [17,18]; il est donc nécessaire de tester davantage de conditions expérimentales pour vérifier ces résultats.

1.2. Analyse des structures de dislocations par l'application de la loi de Masing

L'étude de l'adoucissement cyclique révèle l'impact de la forte densité de dislocations et de leur arrangement avec l'amplitude des contraintes. Afin de confirmer cela, le comportement de Masing a été étudié à l'aide de tests incrémentaux. Pour effectuer l'analyse, les cycles en déformations

plastique ont été calculés et les domaines élastiques ont été alignés pour tous les cycles. Toutes les valeurs minimales ont ensuite été coïncidées pour normaliser les courbes cycliques (Figure II-3).

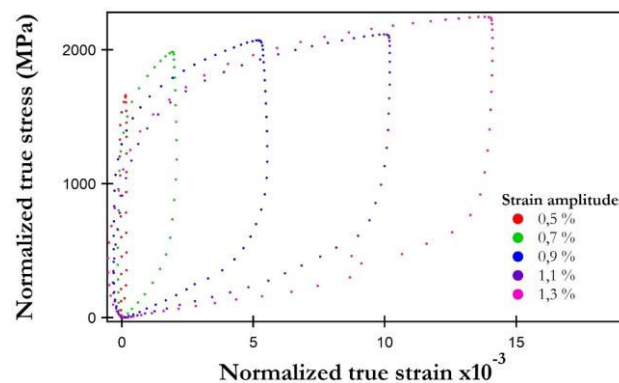


Figure II-3. Vérification de la loi de Masing par la normalisation des courbes cycliques obtenues par des tests incrémentaux sur l'acier CP2.

Avant $\Delta\epsilon/2 = 0,9\%$, la superposition de la contrainte réelle de chargement n'est pas perceptible. Entre $\Delta\epsilon/2 = 1,1\%$ et $\Delta\epsilon/2 = 1,3\%$, on peut observer un chevauchement des parties en traction des courbes. D'après la littérature [19–22], la non-superposition de la contrainte de chargement vraie met en évidence une modification dans l'arrangement des dislocations et le chevauchement de la partie de chargement révèle un arrangement de dislocations similaire pour ces amplitudes de déformation. Pour confirmer cette théorie, une caractérisation microstructurale a été réalisée. Des tests cycliques comprenant 50 cycles ont été effectués avec une contrainte d'amplitude de $\pm 0,5\%$ et $\pm 1\%$ avec un rapport cyclique de -1. Des observations microstructurales ont ensuite été effectuées par EBSD et TEM au centre de ces échantillons.

Les résultats obtenus par EBSD ne révèlent pas beaucoup de différences entre l'échantillon initial et les échantillons qui ont été soumis à une déformation cyclique. Même s'ils avaient été seulement légèrement déformés, le nombre initial de mauvaises orientations dans la bainite serait trop élevé pour que toute différence soit perceptible. Par conséquent, à cette échelle, aucune modification des structures microstructurales n'est visible.

Pour tenter de percevoir ces changements microstructuraux et le non-respect de la loi de Masing, des analyses MET ont été effectuées (**Error! Reference source not found.**).

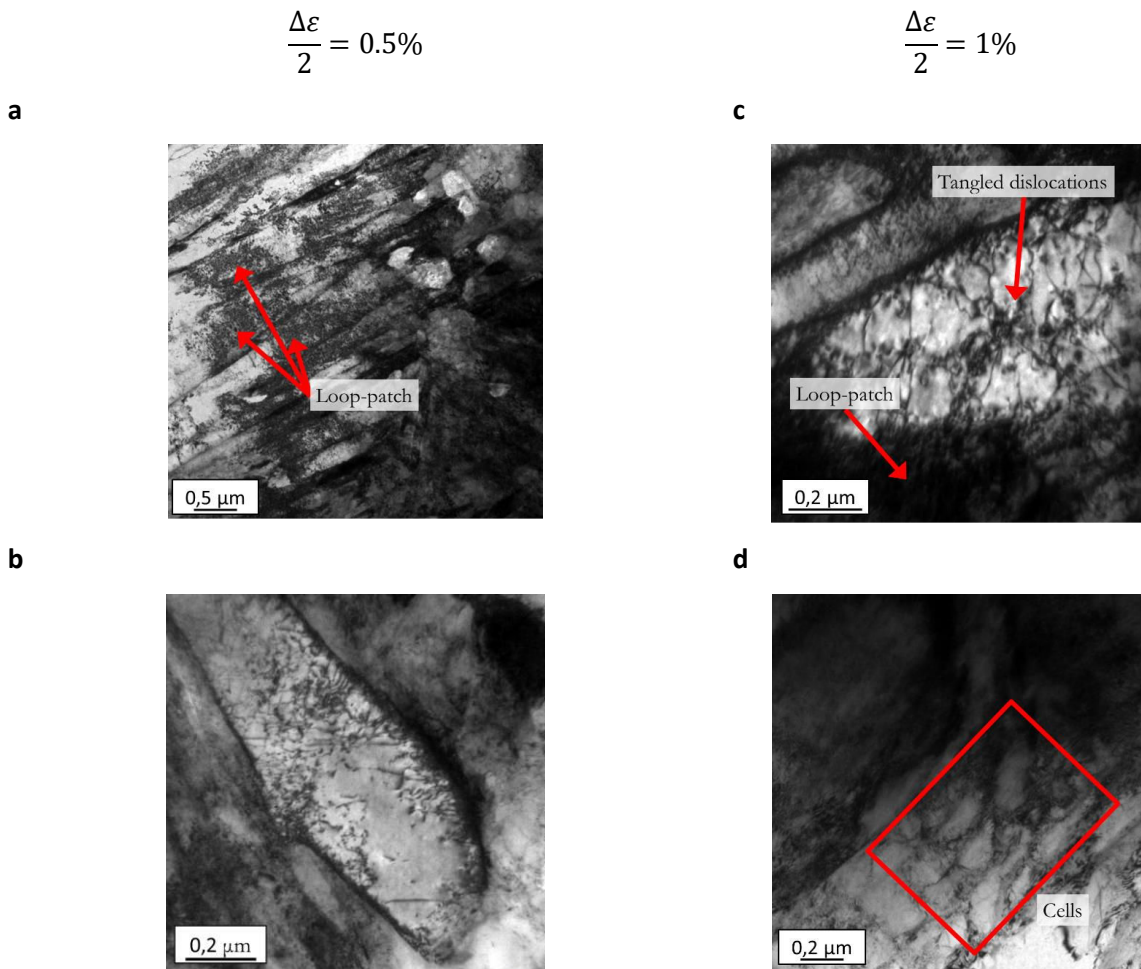


Figure II-4. Images MET après (a), (b) 50 cycles à une amplitude cyclique de 0.5% montrant l'enchevêtrement des dislocations et (c), (d) 50 cycles à une amplitude cyclique de 1% exposant la présence de cellules.

Des dislocations enchevêtrées ont été observés dans les microstructures après une déformation cyclique ($\pm 0,5\%$). Ces caractéristiques étaient également présentes dans l'échantillon au stade initial. Pour l'échantillon déformé à une amplitude de déformation de 1%, la formation de cellules est observable. Ces résultats sont en accord avec les travaux de Shih et al. [20].

1.3. Etude des interactions des dislocations par l'analyse de l'écroissage isotrope et cinématique

L'évolution des composants cinématiques et isotropes a été analysée en fonction de la déformation plastique (**Error! Reference source not found.**). À faible déformation plastique cumulée, une réduction du durcissement isotrope et une augmentation du durcissement cinématique peuvent être notées. Cependant, lorsque l'amplitude de déformation plastique atteint 0,2%, une stabilisation des deux composants du durcissement est observée. La réduction du durcissement isotrope et l'augmentation du durcissement cinématique indiquent l'influence significative des interactions à

longue distance sur les propriétés mécaniques du CP2. Conformément à la caractérisation microstructurale effectuée au Chapitre I de cette synthèse de thèse, les interactions à longue distance qui ont un impact sur le durcissement cinématique pourraient être induites par le nombre élevé de dislocations dans la microstructure initiale et la présence élevée de joints de grains en raison des lattes minces. Pour vérifier ces hypothèses, des essais similaires pourraient être effectués sur des aciers bainitiques avec une taille de latte différente.

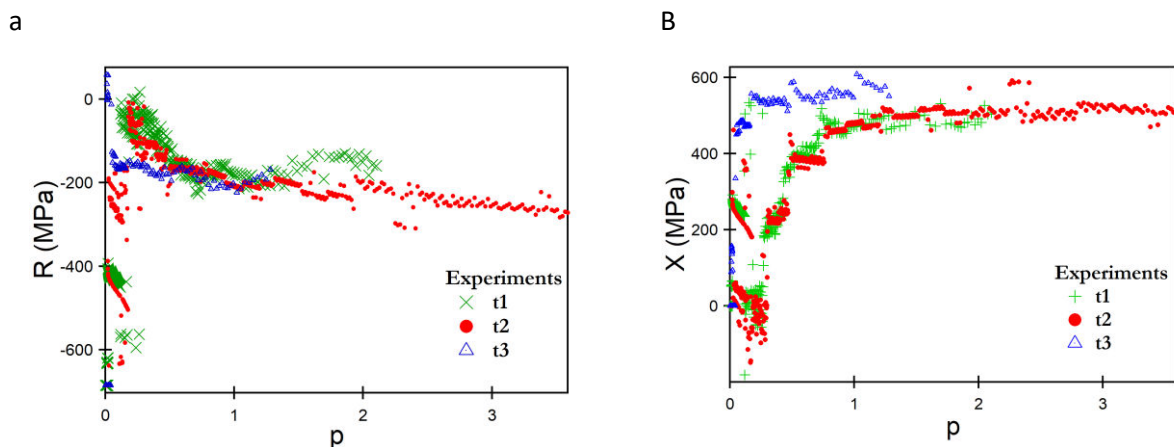


Figure II-5. Evolution de l'érouissage isotrope (a) et cinématique (b) en fonction de la déformation plastique cumulée

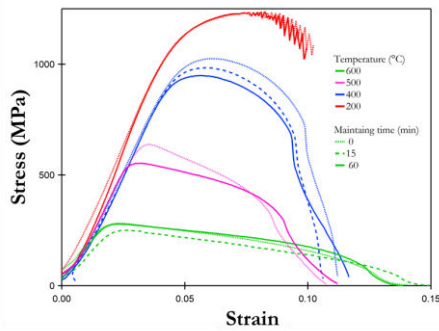
2. Impact de la température sur les propriétés en traction

Dans cette section, la stabilité thermique des propriétés mécaniques de l'acier CP1200 est étudiée dans une plage de températures allant de 200 °C à 600 °C. La température maximale n'excédant pas A_{c1} , aucune austénitisation n'a eu lieu pendant les essais. Ainsi, toutes les conclusions concernent la microstructure bainitique.

2.1. Influence de la température et du temps de maintien sur les propriétés mécaniques

Pour étudier le comportement thermomécanique du CP2, des essais de traction ont été réalisés sur un simulateur thermomécanique (Gleeble) à des températures comprises entre 200 °C et 600 °C et à différents temps de maintien inférieurs à 1 heure. Afin de simplifier la désignation des essais de traction effectués à haute température, l'acronyme HT est utilisé. Tous les résultats de traction sont présentés à la Figure II-6-a.

a



B

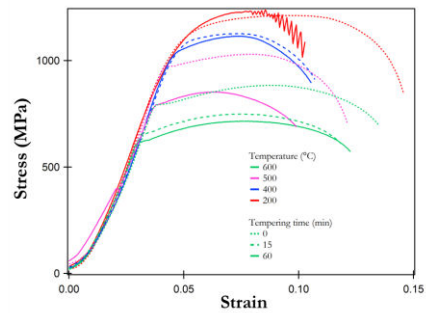


Figure II-6. (a) Tests de traction effectués à différentes températures [200 °C – 600 °C]; (b) Tests de traction effectués après un revenu à différentes températures [200 °C – 600 °C].

Les courbes de traction en dents de scie observées à 200 °C contrastent avec les courbes obtenues aux températures plus élevées. Cette observation est caractéristique de l'effet Portevin-Le Chatelier. Dans les aciers, cet effet peut être expliqué par une diffusion de carbone qui arrête le déplacement des dislocations [9,23]. La libération des dislocations entraîne une diminution significative de la contrainte, ce qui crée des fluctuations sur les courbes de traction. Ce phénomène étant complexe et dépendant de la vitesse de déformation et de la température, il n'a pas été approfondi au cours de ce projet. À des températures allant jusqu'à 400 °C, une diminution de la contrainte est mise en évidence par une augmentation de la température et du temps de maintien (Figure II-7). Les effets de viscosité et la modification de la microstructure peuvent expliquer cette réduction. Pour dé-corréler ces deux paramètres, des essais de traction ont été réalisés à température ambiante (RT) après un revenu similaire à HT (Figure II-6-b). Les tests de RT après revenu à différentes températures ont permis d'identifier la perte de contrainte résultante d'une modification de la microstructure des échantillons. A HT, une diminution de la résistance peut être identifiée à la suite de l'augmentation de la température. Pour comparer les résultats des tests HT et RT, les contraintes maximales sont représentées en fonction de la température et du temps de revenu en Figure II-7.

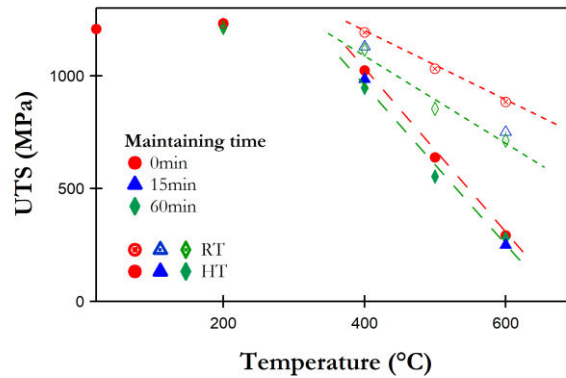


Figure II-7. Evolution de la contrainte maximale en fonction du temps de maintien pour les essais effectués à température ambiante et à hautes températures.

Pour tous les tests, une légère augmentation de la résistance est observée entre les échantillons testés à température ambiante et à 200 °C. A 400 °C, une diminution significative de l'UTS est détectée. Cependant, la diminution de la force est moins significative dans les tests effectués à température ambiante. À une température de 600 °C sans temps de revenu, une différence de 600 MPa dans l'UTS est mesurée. Ces différences représentent l'impact de la viscoplasticité sur les propriétés étudiées, qui est plus significative à 600°C qu'à 400°C. Un autre point à noter est qu'aucune modification de l'UTS n'est observée pour les essais à HT avec l'augmentation du temps de maintien, alors que pour les essais à température ambiante, une réduction significative est observée.

2.2. Bilan de l'analyse thermomécanique

Les résultats thermomécaniques de cette étude révèlent une diminution de la résistance mécanique au-dessus de 400 °C. Cette réduction des propriétés mécaniques s'explique par deux phénomènes : les mécanismes de viscoplasticité et la modification de la microstructure de l'acier. À la température ambiante, la plasticité est régie par le glissement des dislocations, alors que les mécanismes de diffusion peuvent être activés à la suite d'une augmentation de la température. Selon D. Hull et D.J. Bacon [24], la force (ΔF^*) nécessaire à une dislocation pour surmonter un obstacle peut être divisée en une énergie mécanique (τ^*V^*) et une énergie thermique (ΔG^*) (voir Équation (6)):

$$\Delta F^* = \tau^*V^* + \Delta G^* \quad (3)$$

Les travaux de Hull et Bacon présentent l'évolution de la contrainte de cisaillement nécessaire pour surmonter les obstacles en fonction de la température (Figure II-8). La contrainte de cisaillement est séparée en deux composantes : la contrainte interne (τ_G) qui n'est pas ou peu affectée par la température et la contrainte effective (τ^*) qui est totalement supprimée après une température critique (T_c). Une contrainte effective est induite par des interactions à courte portée, qui peuvent être

surmontées par une activation thermique. Les interactions à longue distance qui caractérisent la contrainte interne sont des barrières trop importantes pour être affectées par l'activation thermique.

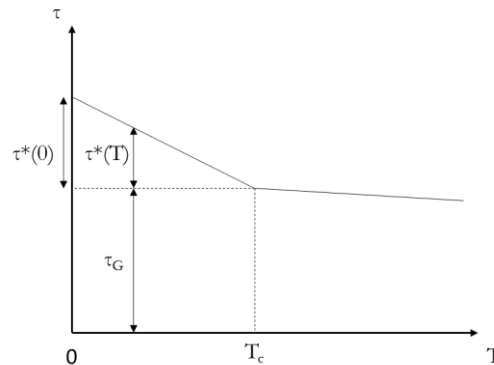


Figure II-8. Evolution de la contrainte de cisaillement en fonction de la température [24].

Avant T_c , on observe une réduction à partir de $\tau^*(0)$, qui est la contrainte nécessaire pour surmonter les obstacles à 0 K. Ce paramètre inclut la contrainte de Peierls-Nabarro, définie comme la résistance des atomes au mouvement des dislocations à 0 K. A la température T , la contrainte de cisaillement est réduite à $\tau^*(T)$, ce qui implique une augmentation de l'énergie thermique pouvant s'expliquer par la vibration des atomes favorisée par la température. De plus, cette vibration atomique accrue facilite la montée des dislocations. Celle-ci est caractérisée par le déplacement d'une dislocation dans un autre plan de glissement du fait de la création ou de l'annihilation de lacunes [24]. Ce mécanisme est donc encouragé par la diffusion de lacunes ou par la diffusion d'atomes interstitiels, toutes deux favorisées par la température. L'activation de la montée des dislocations facilite le mouvement des dislocations, réduisant ainsi la résistance et augmentant la ductilité du CP2.

La modification de la microstructure est un deuxième phénomène survenu. Selon la littérature [14,25–27], différentes étapes peuvent être observées au cours du processus de revenu : la décomposition de l'austénite en carbure (ce qui induit une réduction des contraintes mécaniques), avant la relaxation des contraintes internes, et enfin la recristallisation de la bainite en une structure équiaxe sur une longue durée de revenu. Toutes ces modifications microstructurales réduisent les propriétés mécaniques du CP2. Des températures plus élevées augmentent la diffusion et la vibration des atomes, ce qui favorise la formation de carbures et favorise l'activation des mécanismes viscoplastiques.

Dans le chapitre suivant, l'endommagement dans l'acier CP1200 après des sollicitations en traction sur des éprouvettes entaillées est étudié au moyen d'une quantification des vides. On observe que la présence des contraintes internes mesurées précédemment et les modifications de la microstructure dues à la température influencent les mécanismes d'endommagement.

Chapter III. Description et quantification des mécanismes d'endommagement de l'acier CP1200

Ce chapitre présente les résultats de l'endommagement dans les aciers CP1200. L'endommagement a été quantifié en utilisant deux méthodes différentes. Premièrement, la sensibilité des propriétés mécaniques à l'endommagement a été analysée en prenant en compte le concept de contrainte effective introduit par Rabotnov [28,29]. Dans un second temps, une observation microstructurale des vides a été réalisée et leur évolution a été étudiée en fonction de la déformation plastique à différentes températures et de la triaxialité de contraintes. La localisation des vides à l'intérieur de la microstructure a aussi été étudiée pour comprendre les faiblesses et les forces du matériau. Seuls les résultats de cette dernière expérience sont présentés dans ce rapport.

1. Quantification des vides avec l'impact du taux de triaxialité

Les résultats montrent une augmentation importante de la fraction surfacique maximale de vides (se référer au manuscrit de thèse) avec l'augmentation de la déformation plastique à la rupture. La ductilité de l'échantillon favorise alors la formation de vides. Premièrement, des analyses ont été effectuées sur des éprouvettes en traction. La fraction surfacique vide est affichée en fonction de la déformation plastique (Figure III-1-b) et la répartition de la fraction de surface vide à la surface du matériau est présentée à la Figure III-1-a. Le nombre et la surface moyenne des vides ont ensuite été tracés en fonction de la déformation plastique (voir Figure III-1-c-d). Ces paramètres fournissent, respectivement, des informations sur la nucléation et la croissance des vides.

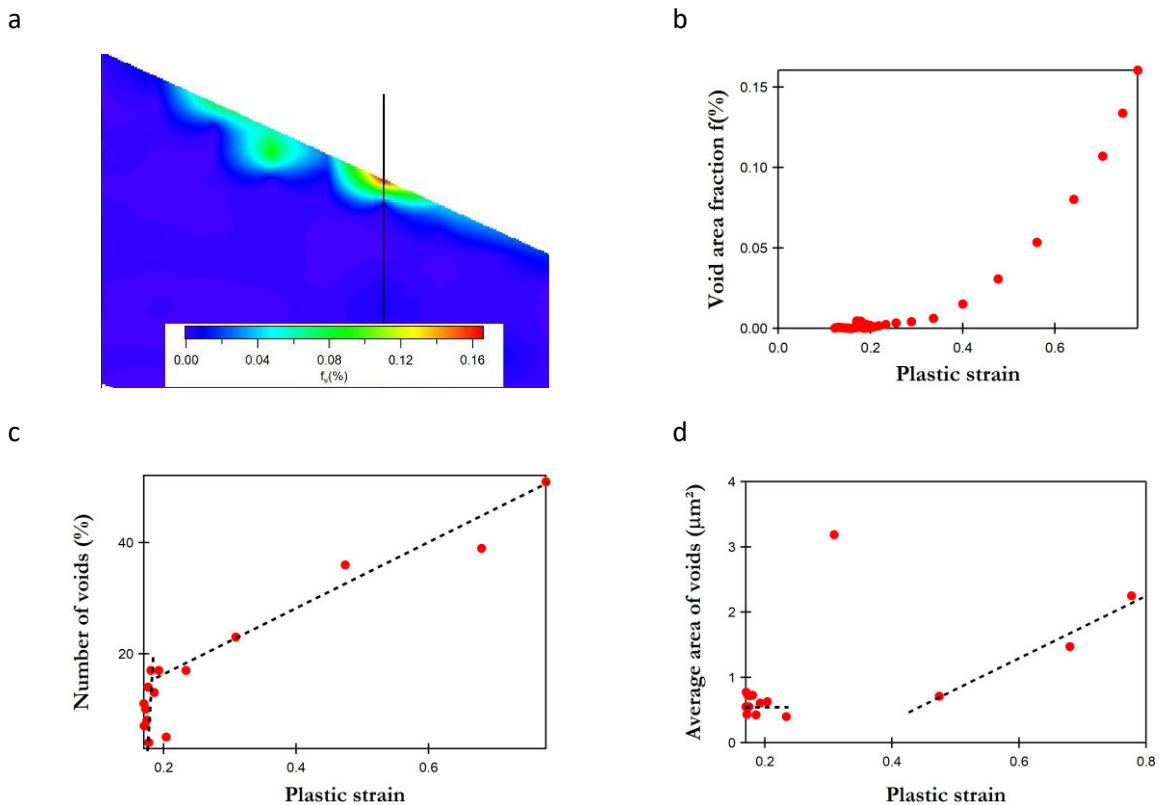
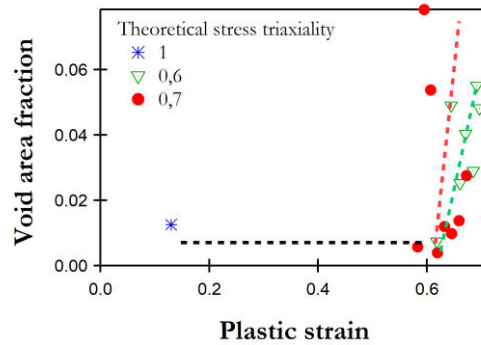


Figure III-1. (a) Cartographie de la fraction surfacique de vides à mi-épaisseur d'une éprouvette de traction; évolution de (b) la fraction surfacique de vides, (c) du nombre, et (d) du diamètre moyen des vides en fonction de la déformation plastique.

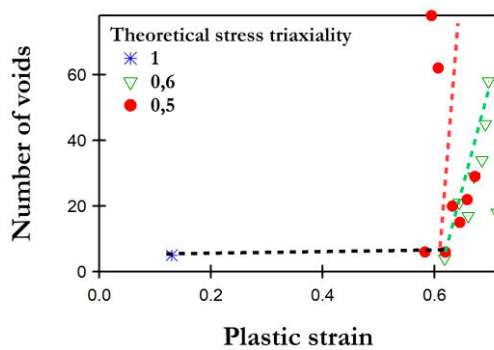
La cartographie de l'endommagement révèle la localisation des vides à l'interception des bandes de cisaillement créées lors de la striction. De plus, en ce qui concerne l'évolution des paramètres de vide, deux étapes peuvent être observées. Pour une déformation plastique de 0,2, ce qui semble être la valeur critique pour l'initiation de l'endommagement, un faible nombre de vides de petites dimensions (en dessous de $1 \mu\text{m}^2$) sont mesurés. Ensuite, au-dessus de ce niveau de déformation plastique, on peut observer une augmentation du nombre de vides, ainsi que des diamètres plus importants. Cependant, la quantité d'endommagement reste faible même en cas de fracture (0,15%). Il est donc possible de conclure que la fracture de l'échantillon est rapide et se produit dès la première apparition des vides.

La croissance, le nombre et la fraction de vide ont également été représentés graphiquement pour les échantillons entaillés à la Figure III-2. Pour η_1 , la déformation plastique mesurée était trop faible pour être mesurée en fonction de la distance de la fracture. Par conséquent, la fraction de surface vide, le nombre de vides et la surface moyenne de vides ne sont représentés qu'à la valeur de déformation plastique maximale.

a



b



c

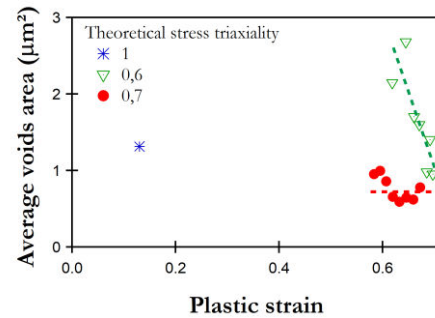


Figure III-2. (a) Fraction surfacique de vides, (b) nombre de vides, et (c) surface moyenne des vides en fonction de la déformation plastique pour différents taux de triaxialité.

Les résultats obtenus pour chaque échantillon montrent une augmentation de la fraction, de la croissance et du nombre de vides avec la déformation plastique. En ce qui concerne l'évolution de la fraction de surface vide, $\eta_{0,5}$ et $\eta_{0,6}$ présentent une contrainte critique similaire (0,6), après quoi un développement rapide des vides peut être observé. Pour η_1 , la fraction surfacique de vide est inférieure, ce qui est cohérent avec la faible ductilité observée lors des essais de traction. Ce manque de ductilité réduit le développement de vides. Il est donc possible de supposer qu'une transition entre fracture ductile et fragile se produit à un taux triaxialité des contraintes comprise entre 1 et 0,6. Cependant, des expériences supplémentaires avec un taux de triaxialité de contrainte intermédiaire doivent être réalisées pour confirmer cette hypothèse.

De plus, le nombre de vides est assez similaire pour $\eta_{0,5}$ et $\eta_{0,6}$ et une quantité plus faible de vides a été mesurée pour η_1 . Cependant, pour $\eta_{0,6}$ et η_1 , la superficie moyenne de vide est d'environ $1,5 \mu\text{m}^2$. Des valeurs légèrement plus élevées de la surface de vides moyenne sont mesurées pour $\eta_{0,5}$. Par conséquent, la croissance des vides s'accélère avec le taux de triaxialité, η_1 présentant des zones vides similaires pour une contrainte plastique inférieure à $\eta_{0,5}$ et $\eta_{0,6}$. Cette observation est conforme au modèle de Rice et Tracey, qui prédit une augmentation de la croissance des vides avec le taux de

triaxialité. Néanmoins, il est possible de conclure que les microstructures des aciers CP1200 ne permettent pas un développement important de l'endommagement, car elles présentent de faibles valeurs pour la fraction surfacique, la croissance et le nombre de vides. Une étude complémentaire sur la localisation dans ces échantillons a montré que pour tous les taux de triaxialité, l'endommagement se forme à l'interface entre les lattes de bainite.

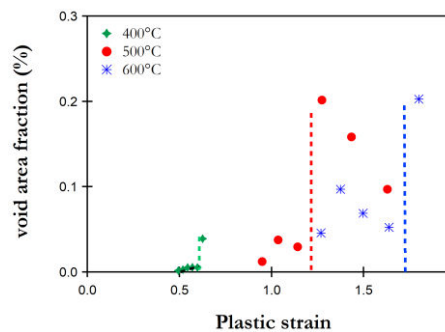
2. Influence de la température sur l'évolution de l'endommagement

Comme indiqué au Chapitre II, les propriétés mécaniques de l'acier CP1200 sont fortement modifiées par une augmentation de la température. Par conséquent, les variations de température pourraient également influencer sur les contraintes à la rupture et les mécanismes d'endommagement.

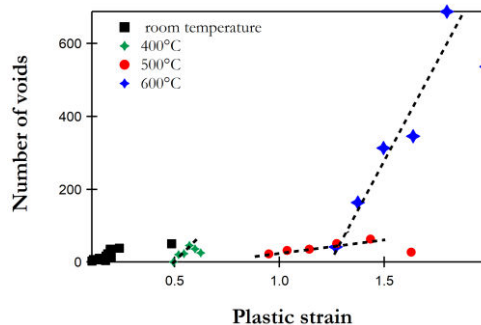
2.1. Influence des sollicitations mécaniques à haute température sur l'évolution de l'endommagement

Selon les résultats précédents, l'évolution de l'endommagement est modifiée par une augmentation de la température. Après avoir obtenu ce résultat, comme précédemment, la fraction surfacique de vide, le nombre et la croissance des vides ont été étudiés en fonction de la déformation plastique (Figure III-3).

a



b



c

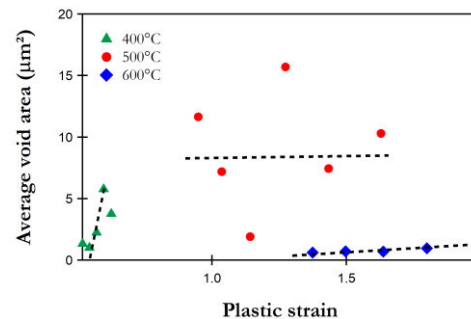


Figure III-3. Evolution (a) de la fraction surfacique des vides, (b) du nombre de vides, et (c) de la croissance des vides en fonction de la déformation plastique pour les éprouvettes de traction ($\eta = 0,33$).

Pour toutes les températures, on peut observer une contrainte critique après laquelle les fractions surfaciques de vide augmentent de manière significative. Les contraintes critiques sont de 0,6, 1,14 et 1,6 pour les températures respectivement de 400 °C, 500 °C, et 600 °C. En ce qui concerne le nombre de vides, on observe une augmentation de ce paramètre avec de la déformation plastique. Cependant, il convient de noter qu'un faible nombre de vides s'est développée en dessous de 500 °C et qu'une augmentation significative de la formation de vides est observable à 600 °C. Enfin, la croissance des vides a été mesurée. Dans la Figure III-3-c, pour que le graphique reste lisible, seules les valeurs moyennes sont représentées. En effet, pour toutes les températures, un écart-type deux fois supérieur à la moyenne a été calculé. Les résultats indiquent qu'à 400 °C, une augmentation de la taille des vides s'est produite en raison d'une contrainte de déformation plastique plus importante, alors qu'à 500 °C, une valeur moyenne d'environ $10 \mu\text{m}^2$, avec une dispersion élevée des résultats, peut être identifiée. Enfin, à 600 °C, la taille moyenne mesurée est d'environ $1 \mu\text{m}^2$. Sur la base de ces résultats, deux étapes différentes peuvent être identifiées. En dessous de 500°C, le nombre de vides augmente légèrement avec la température et une augmentation importante de la superficie moyenne de vide a été mesurée. Le mécanisme de croissance semble être responsable de l'endommagement pour ces températures. À 600 °C, une augmentation significative du nombre de vides peut être observée. De plus, une réduction importante de la zone de vide est mesurée. La nucléation semble devenir le principal mécanisme d'endommagement. Ces résultats suggèrent qu'une transition entre deux mécanismes d'endommagement se produit entre 500 °C et 600 °C.

Des résultats similaires ont été obtenus sur des éprouvettes entaillées avec un taux de triaxialité de 0,5. Les résultats sont disponibles dans le manuscrit de thèse. Un bilan des résultats est présenté dans la Figure III-4.

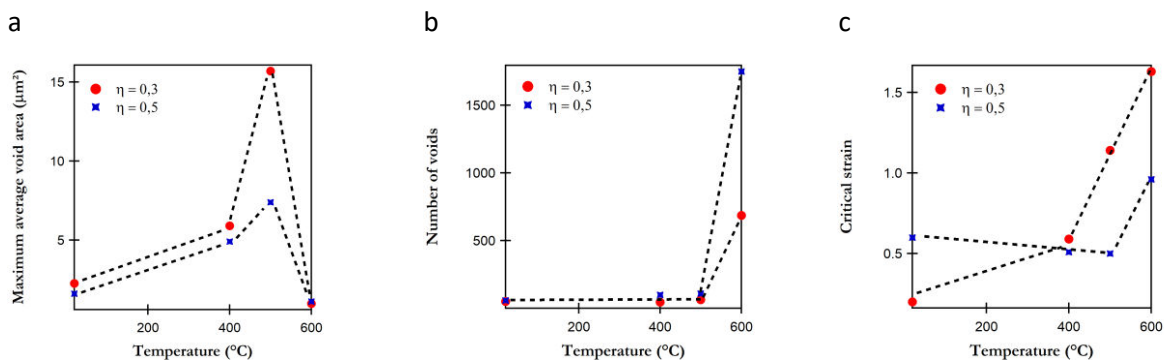


Figure III-4. Evolution (a) de la moyenne maximale des aires des vides, (b) du nombre de vides et (c) de la déformation critique après laquelle la fraction surfacique des vides croient en fonction de la température et du taux de triaxialité ($\eta=0,3$ and $\eta=0,5$).

2.2. Observation de la localisation des vides et de la transformation de la microstructure

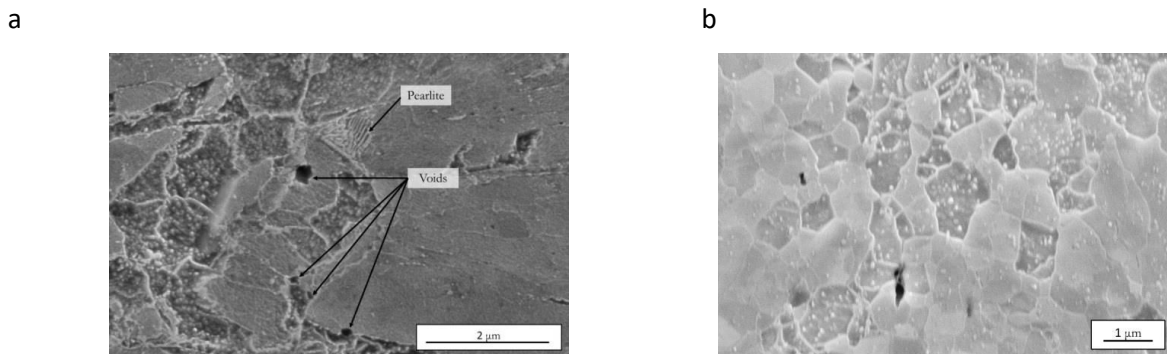


Figure III-5. Exemple de localisation des vides avec l'impact de la température : (a) 400°C et (b) 600°C

Pour tous les échantillons, la nucléation des vides s'est produite aux interfaces entre la ferrite bainitique et l'austénite. Des microstructures similaires à celles observées après les tests de traction à la température ambiante sont observables à 400 °C et à 500 °C. Au contraire, des modifications apportées aux microstructures des échantillons à 600 °C sont remarquables. Par conséquent, pour obtenir des informations supplémentaires sur cette modification, des analyses EBSD des spécimens déformés à 600 °C ont été effectuées. Les cartographies IPF sont présentées à la Figure III-6.

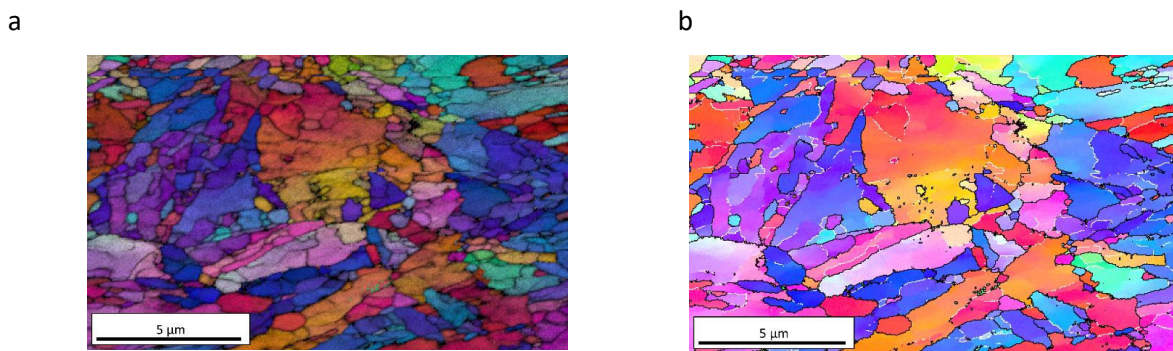


Figure III-6. (a) Figure de pole inverse superposée à l'IQ; (b) IPF avec les joints de grains de faibles désorientations (blanc: 2°–15°) et de fortes désorientations (noir: < 15°) d'une éprouvette de traction déformée à 600°C.

La superposition des cartographies IQ et IPF montrent une microstructure similaire à celle représentée dans les images MEB. Cependant, la cartographie IPF révèle qu'aucune modification de l'orientation cristallographique n'est observable entre ces structures. Ces observations peuvent être expliquées par la recristallisation de la microstructure lors du test de traction effectué à 600 °C. Deux facteurs peuvent avoir influencé cette recristallisation : la température et la contrainte appliquée. Par

conséquent, afin d'explorer l'impact des contraintes sur cette microstructure, une caractérisation métallurgique de la tête de l'échantillon de traction a été réalisée. A cette localisation, où la microstructure était tempérée mais non déformée, aucune modification significative n'est observable sur les images (se référer au manuscrit de thèse).

Il est possible de suggérer l'hypothèse qu'une diffusion du carbone se produit pendant l'essai de traction et que ce carbone conduit à la modification de la microstructure. Il a été noté dans la littérature que les carbures sont une phase fragile et conduisent à une rupture prématurée des aciers bainitiques. Par conséquent, une augmentation du nombre de vides pourrait être expliquée par la formation de carbures. Pour confirmer cette hypothèse, les carbures devraient être identifiés par diffraction réalisée au MET.

3. Synthèse des résultats concernant l'endommagement

Quatre résultats importants peuvent être extraits de ce chapitre :

- L'évolution de l'endommagement a été mesurée par l'étude de l'évolution des vides en fonction de la déformation plastique. Ces résultats mettent en évidence une forte dépendance de la fraction de vide au taux de triaxialité des contraintes et à la déformation plastique. Une réduction du nombre de vides sans modification significative du diamètre moyen a été observée avec l'augmentation de la triaxialité de contrainte. Cependant, pour compléter ces conclusions, il manque une géométrie d'échantillon avec une triaxialité de contrainte intermédiaire.
- Après la quantification des vides, leur localisation dans la microstructure a été étudiée. La plupart d'entre eux sont situés à l'interface entre l'austénite résiduelle et la ferrite bainitique. Ces résultats sont conformes aux études précédentes sur les aciers multiphasés mettant en évidence la nucléation des vides aux interfaces. [4, 45].
- Ensuite, l'influence de la température sur l'endommagement a été étudiée. Une transition intéressante des mécanismes d'endommagement a été observée après 600 °C. En effet, au-dessous de cette température, la principale modification liée à l'élévation de la température est l'augmentation de la contrainte critique où la nucléation des dommages commence à être mesurée. A cette température, aucun impact significatif sur le nombre de vides et la croissance n'est observé. Cependant, une augmentation importante du nombre de vides avec la réduction de la croissance des vides est mise en évidence. Cette modification est liée à la recristallisation dynamique de la microstructure.

Une des problématiques de ce sujet a été de comparer les résultats obtenus concernant les aciers DP1000 et CP1200. À cette fin, la Table III-1 présente un résumé des caractéristiques générales relatives à la mécanique, à la métallurgie et à l'endommagement.

Table III-1. Comparaison des propriétés mécanique et d'endommagement entre les aciers DP1000 et CP1200.

| | DP1000 | CP1200 |
|---|--|---|
| UTS (MPa) | 1040 | 1301 |
| Elongation | 0,8 | 0,8 |
| Température critique | 290 °C | 400 °C |
| Microstructure | Martensite et ferrite | Bainite et RA |
| Modification de la microstructure à haute température | Formation de martensite revenue et adoucissement de la ferrite | Formation de carbures |
| Localisation des vides | Par la rupture de la martensite et aux interfaces des inclusions | Aux interfaces entre la bainite ferritique et l'austénite |
| Localisation des vides sous sollicitations mécaniques à haute températures | Par rupture de la ferrite | A l'interface entre les lattes de bainite |

Conclusion

Les objectifs de cette thèse étaient d'obtenir des informations sur les mécanismes de plasticité et d'endommagement des aciers multiphasés CP1200. Cette étude a été lancée par l'entreprise Faurecia Automotive Seating. Le but était de mieux spécifier leurs exigences concernant les nombreuses propriétés microstructurales et mécaniques des matériaux provenant de différents fournisseurs. Il s'agissait aussi d'acquérir une meilleure compréhension des comportements en plasticité et d'endommagement de ces aciers.

Les principaux résultats obtenus à température ambiante sont les suivants :

- En fonction du fournisseur, une large gamme de propriétés mécaniques et de microstructures a été observée. La volonté était alors de mieux comprendre la relation qui existe entre les propriétés macroscopiques et les aspects microscopiques. Les chapitres I et II démontrent l'impact de la taille des lattes bainitiques et de la présence de l'austénite résiduelle sur les propriétés mécaniques et sur l'endommagement. En effet, les structures bainitiques avec des fines lattes conduisent à une augmentation de la résistance et la présence d'îlots d'austénite résiduelle induit une augmentation de la ductilité.
- L'étude des mécanismes de plasticité analysés par des essais de traction/compression cycliques permet de mettre en évidence le développement de l'écroutissage cinématique causé par les interactions à longue distance des dislocations. Ces tests permettent également de confirmer la présence d'une forte densité de dislocations dans la microstructure initiale par l'apparition rapide d'un adoucissement cyclique pour de faibles déformations plastiques.
- Les dommages sont réduits avec la triaxialité des contraintes à la température ambiante, et les résultats montrent que les vides se localisent à l'interface entre la ferrite bainitique et l'austénite.

De plus, l'étude de la stabilité thermique de l'acier CP1200 permet d'acquérir de nouvelles informations :

- La microstructure est fortement influencée par la température. D'après les expériences de DSC et de dilatométrie, la décomposition de l'austénite en ferrite et en cémentite a lieu à des températures comprises entre 300 °C et 400 °C. À des températures plus élevées (635 °C), la ferrite et la cémentite se transforment en austénite.

- Cette modification microstructurale a un impact sur les expériences de traction. En effet, une réduction importante de la résistance et une augmentation de la déformation à la rupture ont été observées après 400 °C. De plus, la réduction des propriétés de traction a été affectée par des effets viscoplastiques lors d'essais réalisés à haute température.
- Il a été démontré l'impact de la température sur l'endommagement à travers une transition des mécanismes d'endommagement à 600 °C. En dessous de cette température, une forte croissance des vides a été observée. Au-dessus 600 °C, une augmentation importante du nombre de vides a été observée avec un faible développement de la croissance. Ce phénomène est lié à une modification de la microstructure.

Ces résultats permettent d'obtenir des données sur la plasticité et les mécanismes d'endommagement des aciers CP1200. Il serait intéressant de poursuivre l'étude sur ce projet :

- La première amélioration qui pourrait être réalisée est la répétition de toutes les expériences d'analyse de l'endommagement pour acquérir davantage de données statistiques. Avec suffisamment de données, les lois théoriques pourraient être appliquées. De plus, une géométrie d'échantillon supplémentaire de taux de triaxialité entre 0,6 et 1 doit être effectuée pour compléter le graphique de l'évolution de la fraction de surface vide en fonction de la triaxialité des contraintes.
- L'utilisation de la simulation numérique pourrait apporter une valeur ajoutée à ces travaux. Par exemple, la détermination de la triaxialité des contraintes lors d'essais de traction sur une éprouvette entaillée avec l'évolution de la déformation plastique pourrait être obtenue avec plus de précision grâce aux outils numériques. De plus, l'utilisation de simulations numériques pourrait permettre d'appliquer et de vérifier les coefficients de l'écroissage cinématique de la loi de Lemaitre et Chaboche obtenus à l'aide d'essais de traction-compression.
- La modification des microstructures à 600 °C dans des conditions d'essai de traction a été observée mais n'a pas été approfondie. Des expériences complémentaires telles que la traction in situ sous MEB pourraient être réalisées afin de comprendre le phénomène qui conduit à cette modification microstructurale et pourquoi cette structure favorise la nucléation des vides.

Références

- [1] S. Keeler, M. Kimchi, P.J. Mooney, *Advanced High-Strength Steels Application Guidelines Version 6.0, Adv. High-Strength Steels Appl. Guidel.* (2017).
- [2] *An Assessment of Mass Reduction Opportunities for a 2017-2020 Model Year Vehicle Program*, Lotus Engineering Inc., 2010.
- [3] J. Chottin, *Etude de l'endommagement des aciers Dual-Phase : Application au procédé de mise en forme par cambrage*, PhD Thesis, University of Caen, 2011.
- [4] B.L. Bramfitt, *Metals Handbook - Structure/property Relationships in Irons and Steels, Struct. Relatsh. Irons Steels, Desk Edition*, J.R. Davis, 1998, pp. 153–173.
- [5] G. F. Vander Voort, *Etching isothermally treated steels*, *Heat Treat. Prog.* APRIL/MAY 2001 (2001).
- [6] K. Radwański, *Structural characterization of low-carbon multiphase steels merging advanced research methods with light optical microscopy*, *Arch. Civ. Mech. Eng.* 16 (2016) 282–293.
- [7] S. Zajac, V. Schwinn, K.H. Tacke, *Characterisation and Quantification of Complex Bainitic Microstructures in High and Ultra-High Strength Linepipe Steels*, *Mater. Sci. Forum.* 500–501 (2005) 387–394.
- [8] F.G. Caballero, C. Garcia-Mateo, M.K. Miller, *Design of novel bainitic steels: moving from ultrafine to nanoscale structures*, *Jom.* 66 (2014) 747–755.
- [9] H.K.D.H. Bhadeshia, *Bainite in steels: theory and practice*, Third edition, Maney Publishing, Leeds, 2015.
- [10] J.P. Naylor, *The influence of the Lath Morphology on the Yield Stress and Transition Temperature of Martensitic-Bainitic Steels*, *Metall. Trans. A.* 10A (1979) 861–873.
- [11] S. Zajac, J. Komenda, P. Morris, P. Dierickx, S. Matera, F. Penalba Diaz, *Quantitative structure-property relationships for complex bainitic steels*, European commission EU21245, (2005).
- [12] F.G. Caballero, C. Garcia-Mateo, C.G. de Andrés, *Dilatometric study of re-austenitisation of high silicon bainitic steels: Decomposition of retained austenite*, *Mater. Trans.* 46 (2005) 581–586.
- [13] W. Cui, D. San-Martín, P.E.J. Rivera-Díaz-del-Castillo, *Stability of retained austenite in martensitic high carbon steels. Part I: Thermal stability*, *Mater. Sci. Eng. A.* 711 (2018) 683–695.
- [14] N. Luzginova, L. Zhao, J. Sietsma, *Evolution and thermal stability of retained austenite in SAE 52100 bainitic steel*, *Mater. Sci. Eng. A.* 448 (2007) 104–110.
- [15] E. De Moor, S. Lacroix, L. Samek, J. Penning, J.G. Speer, *Dilatometric study of the quench and partitioning process*, *Proceedings of the 3rd International Conference on Advanced Structural Steels*, (2006), pp. 1–6.
- [16] F. Yoshida, T. Uemori, K. Fujiwara, *Elastic–plastic behavior of steel sheets under in-plane cyclic tension–compression at large strain*, *Int. J. Plast.* 18 (2002) 633–659.
- [17] T. Hilditch, H. Beladi, P. Hodgson, N. Stanford, *Role of microstructure in the low cycle fatigue of multi-phase steels*, *Mater. Sci. Eng. A.* 534 (2012) 288–296.
- [18] Q. Zhou, L. Qian, J. Meng, L. Zhao, F. Zhang, *Low-cycle fatigue behavior and microstructural evolution in a low-carbon carbide-free bainitic steel*, *Mater. Des.* 85 (2015) 487–496.
- [19] E. Watanabe, T. Asao, M. Toda, M. Yoshida, S. Horibe, *Relationship between Masing behavior and dislocation structure of AISI 1025 under different stress ratios in cyclic deformation*, *Mater. Sci. Eng. A.* 582 (2013) 55–62.

- [20] C.-C. Shih, N.-J. Ho, H.-L. Huang, The relationship between cyclic stress-strain curve and dislocation structures in cyclically deformed IF steel, (2009) 235–238.
- [21] Y. Li, C. Laird, Masing behavior observed in monocrystalline copper during cyclic deformation, *Mater. Sci. Eng. A.* 161 (1993) 23–29.
- [22] T. Mayer, E. Mazza, S.R. Holdsworth, Parameter evolution in a continuous Masing approach for cyclic plasticity and its physical interpretation, *Mech. Mater.* 57 (2013) 86–96.
- [23] B. Grzegorzczak, A. Kozłowska, M. Morawiec, R. Muszyński, A. Grajcar, Effect of Deformation Temperature on the Portevin-Le Chatelier Effect in Medium-Mn Steel, *Metals.* 9 (2018) 1–13.
- [24] D. Hull, D.J. Bacon, Introduction to dislocations, fifth, Edition BH, 2011.
- [25] M.J. Peet, S.S. Babu, M.K. Miller, H.K.D.H. Bhadeshia, Tempering of Low-Temperature Bainite, *Metall. Mater. Trans. A.* 48 (2017) 3410–3418.
- [26] A. Saha Podder, H.K.D.H. Bhadeshia, Thermal stability of austenite retained in bainitic steels, *Mater. Sci. Eng. A.* 527 (2010) 2121–2128.
- [27] D. Liu, B. Bai, H. Fang, W. Zhang, J. Gu, K. Chang, Effect of tempering temperature and carbide free bainite on the mechanical characteristics of a high strength low alloy steel, *Mater. Sci. Eng. A.* 371 (2004) 40–44.
- [28] J. Lemaitre, A Continuous Damage Mechanics Model for Ductile Fracture, *J. Eng. Mater. Technol.* (1985) 83–89.
- [29] J. Lemaitre, A course on damage mechanics, second, Edition Springer, 1996.
- [30] E. Hug, M. Martinez, J. Chottin, Temperature and stress state influence on void evolution in a high-strength dual-phase steel, *Mater. Sci. Eng. A.* 626 (2015) 286–295.
- [31] L. Ryde, D. Lindell, A. Pichler, J. Garcia Ferrero, Y. Vilander Granbom, E. Werner, A. Fillafer, R. Wesenjak, P. Tsipouridis, A. Nitschke, Micro-scale damage tolerance of AHSS steels as function of microstructure and stress-strain state, European Commission EUR 25863, (2013).

Plasticity and damage mechanisms in specific multiphase steels with bainitic matrix under various mechanical loading paths - Influence of temperature

This PhD work investigates plasticity and damage mechanisms of complex phase steels. The bainitic microstructures of such steels, which feature retained austenite islands, result in these steels exhibiting good formability properties, which are of interest to automotive companies. However, the complexity of these microstructures, which are characterised by a high amount of grain boundaries and a high density of dislocations, influences plasticity and damage mechanisms. In order to estimate the impact of a steel's microstructure on these properties, the investigation of metallurgical features of complex phase steels provided by the company Faurecia is performed. Plasticity mechanisms are then investigated by tension-compression tests to determine the influence of long- and short-range interactions on the motion of dislocations. Thereafter, the evolution of damage within microstructures is analysed at different stress triaxialities in order to obtain the volume area fraction and the number and average diameter of voids as functions of plastic strain. Finally, to examine the thermal stability of these parameters (microstructure, plasticity, and damage), experiments are performed at a range of temperatures between 20°C and 600°C.

Key words: Complex phase steels, damage characterisation, cyclic loading, microstructural analysis

Etude des mécanismes d'endommagement et de plasticité d'acier multiphasés à matrice bainitique sous différents trajets de chargement - Impact de la température

Ce travail de thèse porte sur les mécanismes de plasticité et d'endommagement des aciers complexes phases (CP). La microstructure bainitique de ces aciers permet d'acquérir de bonnes propriétés de formabilité, ce qui intéresse les constructeurs automobiles. Cependant, la complexité de ces microstructures, qui se caractérisent par une grande quantité de joints de grains et une densité élevée de dislocations, influence la plasticité et les mécanismes d'endommagement. Afin d'estimer l'impact de la microstructure, une étude des caractéristiques métallurgiques des aciers à phases complexes est réalisée. Les mécanismes de plasticité sont ensuite étudiés par des tests de tension-compression afin d'étudier les mécanismes d'érouissage du matériau. Ensuite, l'évolution de l'endommagement au sein de la microstructure est analysée à différents taux de triaxialité des contraintes afin d'obtenir la fraction de surfacique des vides, le nombre et le diamètre moyen des vides en fonction de la déformation plastique. Enfin, pour examiner la stabilité thermique de ces paramètres (microstructure, plasticité et endommagement), des expériences sont effectuées dans une plage de températures allant de 20 °C à 600 °C.

Mots clés : Aciers complexes phases, caractérisation de l'endommagement, chargements cycliques, analyse microstructurale